

Tripodal Silanolate Ligands Expand MoX_3 Chemistry Beyond Its Traditional Borders

&

Synthetic Strategies for Diamagnetic Iron Carbenes

Dissertation

Zur Erlangung des akademischen Grades eines
Doktors der Naturwissenschaften
(Dr. rer. nat.)
der Fakultät für Chemie und Chemische Biologie
der Technischen Universität Dortmund

vorgelegt von
Daniel Rütter
geboren am 05.01.1996 in Duisburg

Mülheim an der Ruhr, Juni 2025

Eidesstattliche Versicherung (Affidavit)

Rütter, Daniel

Name, Vorname
(Surname, first name)

231993

Matrikel-Nr.
(Enrolment number)

Belehrung:

Wer vorsätzlich gegen eine die Täuschung über Prüfungsleistungen betreffende Regelung einer Hochschulprüfungsordnung verstößt, handelt ordnungswidrig. Die Ordnungswidrigkeit kann mit einer Geldbuße von bis zu 50.000,00 € geahndet werden. Zuständige Verwaltungsbehörde für die Verfolgung und Ahndung von Ordnungswidrigkeiten ist der Kanzler/die Kanzlerin der Technischen Universität Dortmund. Im Falle eines mehrfachen oder sonstigen schwerwiegenden Täuschungsversuches kann der Prüfling zudem exmatrikuliert werden, § 63 Abs. 5 Hochschulgesetz NRW.

Die Abgabe einer falschen Versicherung an Eides statt ist strafbar.

Wer vorsätzlich eine falsche Versicherung an Eides statt abgibt, kann mit einer Freiheitsstrafe bis zu drei Jahren oder mit Geldstrafe bestraft werden, § 156 StGB. Die fahrlässige Abgabe einer falschen Versicherung an Eides statt kann mit einer Freiheitsstrafe bis zu einem Jahr oder Geldstrafe bestraft werden, § 161 StGB.

Die oben stehende Belehrung habe ich zur Kenntnis genommen:

Official notification:

Any person who intentionally breaches any regulation of university examination regulations relating to deception in examination performance is acting improperly. This offence can be punished with a fine of up to EUR 50,000.00. The competent administrative authority for the pursuit and prosecution of offences of this type is the chancellor of the TU Dortmund University. In the case of multiple or other serious attempts at deception, the candidate can also be unenrolled, Section 63, paragraph 5 of the Universities Act of North Rhine-Westphalia.

The submission of a false affidavit is punishable.

Any person who intentionally submits a false affidavit can be punished with a prison sentence of up to three years or a fine, Section 156 of the Criminal Code. The negligent submission of a false affidavit can be punished with a prison sentence of up to one year or a fine, Section 161 of the Criminal Code.

I have taken note of the above official notification.

Ort, Datum
(Place, date)

Unterschrift
(Signature)

Titel der Dissertation:
(Title of the thesis):

Tripodal Silanolate Ligands Expand MoX₃ Chemistry Beyond Its Traditional Borders
& Synthetic Strategies for Diamagnetic Iron Carbenes

Ich versichere hiermit an Eides statt, dass ich die vorliegende Dissertation mit dem Titel selbstständig und ohne unzulässige fremde Hilfe angefertigt habe. Ich habe keine anderen als die angegebenen Quellen und Hilfsmittel benutzt sowie wörtliche und sinngemäße Zitate kenntlich gemacht.

Die Arbeit hat in gegenwärtiger oder in einer anderen Fassung weder der TU Dortmund noch einer anderen Hochschule im Zusammenhang mit einer staatlichen oder akademischen Prüfung vorgelegen.

I hereby swear that I have completed the present dissertation independently and without inadmissible external support. I have not used any sources or tools other than those indicated and have identified literal and analogous quotations.

The thesis in its current version or another version has not been presented to the TU Dortmund University or another university in connection with a state or academic examination.*

*Please be aware that solely the German version of the affidavit ("Eidesstattliche Versicherung") for the PhD thesis is the official and legally binding version.

Ort, Datum
(Place, date)

Unterschrift
(Signature)

1. Berichterstatter: Prof. Dr. Alois Fürstner
2. Berichterstatter: Prof. Dr. Carsten Strohmann

Die vorliegende Arbeit entstand unter der Anleitung von Prof. Dr. Alois Fürstner in der Zeit von April 2021 bis Juni 2025 am Max-Planck-Institut für Kohlenforschung in Mülheim an der Ruhr. Teile dieser Arbeit wurden bereits veröffentlicht:

D. Rütter, M. van Gastel, M. Leutzsch, N. Nöthling, D. SantaLucia, F. Neese, A. Fürstner, *Inorg. Chem.* **2024**, *63*, 8376-8389.

D. Rütter, N. Nöthling, M. Leutzsch, A. A. Auer, A. Fürstner, *J. Am. Chem. Soc.* **2025**, *147*, 13871-13884.

Die praktischen Arbeiten erfolgten teilweise in Zusammenarbeit mit Dr. William Parisot. NMR-spektroskopische Messungen wurden in Kooperation mit Dr. Markus Leutzsch durchgeführt. Einkristallstrukturanalysen wurden von Dr. Nils Nöthling oder Jörg Rust vorgenommen; Heike Schucht, Elke Dreher oder Lucas Schulte-Zweckel übernahmen hierbei die Probenpräparation. Dr. Maurice van Gastel führte EPR- und UV-Vis-Messungen durch und analysierte die Ergebnisse; darüber hinaus hat er DFT-Rechnungen vorgenommen. SQUID Messungen wurden von Dr. Daniel SantaLucia durchgeführt und ausgewertet. Mößbauer-spektroskopische Messungen wurden von Derya Demirbas durchgeführt. Prof. Dr. Alexander Auer hat DFT-Rechnungen durchgeführt. Cyclovoltammetrie-Messungen wurden von Dr. Alexios Stamoulis durchgeführt und interpretiert. Die beschriebenen Ergebnisse bilden eine vollständige Übersicht über diese gemeinsamen Arbeiten. Die von diesen Mitarbeitern alleinverantwortlich erzielten Ergebnisse wurden als solche an entsprechender Stelle gekennzeichnet.

Danksagung

Zunächst möchte ich meinem Doktorvater und Mentor, Herrn Prof. Dr. Alois Fürstner, für die Möglichkeit danken, meine Doktorarbeit in seinem Arbeitskreis anzufertigen. Die Zeit in seiner Gruppe hat mich nicht nur als Chemiker, sondern vor allem auch als Mensch maßgeblich geprägt. Besonders beeindruckt hat mich hierbei das entgegengebrachte Vertrauen und die eingeräumte Möglichkeit auch Projekte zu verfolgen, die eher etwas außerhalb des typischen Themenspektrums der Fürstner Gruppe liegen. Das Level auf dem Chemie in seiner Gruppe „gelebt“ wird hat mich in meiner Entwicklung massiv beeinflusst. Auch die wöchentlichen Seminare, bei denen ich unter anderem von ihm lernen durfte, welche außergewöhnlichen wissenschaftlichen Errungenschaften von anderen Forschern am Max-Planck-Institut für Kohlenforschung erzielt wurden, habe ich sehr genossen. Für all diese Dinge bin ich ihm zu tiefstem Dank verpflichtet.

Herrn Prof. Dr. Carsten Strohmann möchte herzlich für die Übernahme des Zweitgutachtens danken.

Natürlich gibt es eine Reihe von Personen, die ich während meiner Zeit am Max-Planck-Institut für Kohlenforschung kennengelernt habe und denen ich im Folgenden danken möchte.

Dr. Markus Leutzsch möchte ich für die außerordentlich gute Zusammenarbeit bei unseren gemeinsamen Projekten danken. Seine Fähigkeiten in der fortgeschrittenen NMR-Spektroskopie sind phänomenal und elementarer Baustein bei der Charakterisierung verschiedenster Moleküle innerhalb dieser Doktorarbeit.

Ein anderer extrem wichtiger Kooperationspartner war für mich Dr. Nils Nöthling. Die Qualität seiner Beiträge bei der Analyse verschiedenster Metall-Komplexe innerhalb dieser Doktorarbeit sprechen für sich, insbesondere wenn es hierbei um fast aussichtslose Kristallstrukturanalysen ging. Darüber hinaus möchte ich ihm für seine Freundschaft danken.

Ein besonderer Mensch ist auch Dr. Richard Goddard, welcher über die Jahre hinweg eine Art Mentor für mich geworden ist. Beeindruckend ist für mich hierbei, wie er komplexe Probleme in allen Bereichen der Chemie analysiert. Er ist somit ein Paradebeispiel, an dem sich junge Wissenschaftler orientieren können. Darüber hinaus möchte ich ihm für das Korrekturlesen dieser Arbeit danken.

Dr. William Parisot danke ich für die gute Zusammenarbeit im Rahmen des Eisen-Projekts.

Allen weiteren Kooperationspartnern möchte ich für die gute Zusammenarbeit danken, sie sind im Folgenden genannt: Dr. Maurice van Gastel, Dr. Daniel SantaLucia, Prof. Dr. Alexander Auer und Dr. Alexios Stamoulis.

Ich hatte das Glück, Dr. Jack Sutro während meiner Zeit hier am Institut kennen zu lernen. Ihm möchte ich für seine Freundschaft und die zahlreichen Diskussionen im Bereich der Chemie danken. Die Breite seines Wissensspektrums in allen Bereichen der Wissenschaft und die Art und Weise, wie er komplexe Probleme angeht, sind äußerst beeindruckend und haben mich als Doktorand geprägt. Darüber hinaus danke ich ihm herzlich für das Korrekturlesen dieser Arbeit.

Nepomuk Korber möchte ich für die gemeinsame Zeit hier am Institut danken, während dieser er für mich zu einem Freund geworden ist. Hierbei haben wir voneinander lernen können, sei es bei unseren Vorbereitungen auf gemeinsame Gruppenseminare oder bei der Überwindung von Herausforderungen im Labor. Auch außerhalb des Labors haben wir viel zusammen unternommen, ich werde mich immer gerne an diese Zeit zurückerinnern.

Eine weitere wichtige Person, die natürlich nicht vergessen werden darf, ist Dr. Ricardo Molina Betancourt. Die gemeinsame Zeit in „Box 4“ wird mir immer in schöner Erinnerung bleiben.

Den Technikern Saskia Schulthoff, Christian Wille, Christopher Rustemeier, Yannik Sell, Karin Radkowski und Roswitha Leichtweiß möchte ich dafür danken, dass sie durch ihre Arbeit exzellente Rahmenbedingungen schaffen, um wissenschaftliche Forschung zu betreiben. Besonders hervorzuheben sind hierbei Saskia Schulhoff und Christian Wille, zwei Techniker, auf die stets Verlaß ist und die beeindruckende Fähigkeiten im Labor besitzen.

Einen extrem wichtigen Beitrag haben auch die Mitarbeiter der analytischen Abteilungen am Institut geleistet. Besonderer Dank gilt Heike Schucht, Lucas Schulte-Zweckel, Jörg Rust, Elke Dreher und Markus Kochius für die gewissenhafte Bearbeitung zahlreicher Analysenaufträge.

Dr. Julius Hillenbrand möchte ich für seine Freundschaft danken. Er hat mir besonders in meiner Anfangszeit in der Gruppe geholfen und dient mir als Vorbild, wie ein Wissenschaftler schwierige Projekte durch die Erarbeitung von systematischen Lösungsansätzen vorantreiben sollte. Darüber hinaus habe ich unsere gemeinsamen Rennradtouren sehr genossen.

Den anderen Mitgliedern der Rennrad-Gruppe möchte ich an dieser Stelle natürlich auch danken und namentlich erwähnen: Dr. Simon Spohr, Dr. Raphael Zachmann, Dr. Michael Buchsteiner, Dr. Tobias Biberger und Dr. Sorin Rosca. Insbesondere möchte ich hierbei Dr. Simon Spohr und Dr. Raphael Zachmann danken, die mir während meiner Anfangszeit als Leitfiguren dienten.

Weiterhin möchte ich Thilo Bender und Daniel Isak für die Zeit am Institut und die vielen wissenschaftlichen Diskussionen danken. Unser gemeinsamer Besuch der BOSS Konferenz in Liège wird mir in schöner Erinnerung bleiben. Daniel Isak möchte ich darüber hinaus für das gewissenhafte Korrekturlesen dieser Arbeit danken. Ich werde unsere morgendlichen Kaffeepausen vermissen.

Dr. Mingxu Cui möchte ich für das Korrekturlesen dieser Arbeit danken.

Den jetzigen und ehemaligen Mitgliedern von „Box 4“ möchte ich für die Zusammenarbeit danken, besonderer Dank gilt hierbei: Luis Renken, Clément Rein, Djung Sue Jeon, Dr. Nikolai Rossouw, Dr. Marco Mijangos, Dr. Robin Weiss, Dr. Tomas Saiegh und Dr. Zhanchao Meng.

Allen aktuellen und ehemaligen Mitarbeitern der Arbeitsgruppe Fürstner möchte ich für die angenehme Arbeitsatmosphäre danken. Besonders hervorheben möchte ich hierbei: Noah Richter, Andrea Tomio, Albert Hermann, Dr. Stephan Hess, Dr. Lorenz Löffler, Dr. Fabio Caló, Dr. Mira Holzheimer, Dr. Juan Carlos Babón Molina, Dr. Thomas Varlet, Quentin Riedl, Paul Moths, Julius Steidele und Dr. Peter Chapple.

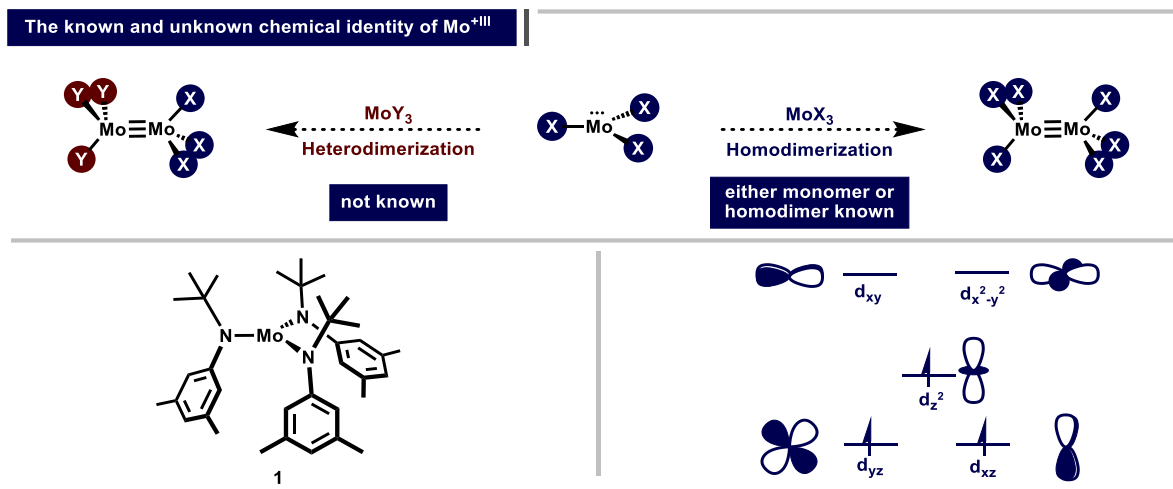
Auch meinen Freunden außerhalb der Arbeit möchte ich für ihre Unterstützung danken; explizit erwähnen möchte ich meine langjährigen Freunde Niklas Weghaus und Lars Müller. Meinen ehemaligen Studienkameraden Tim Oberkirch, Dr. Dustin Jordan und Dr. René Schloots möchte ich auch einen Dank aussprechen.

Mein größter Dank gilt allerdings meiner Familie, ohne deren stetige Unterstützung dieser Weg nicht möglich gewesen wäre. Meinen Eltern und meiner Zwillingsschwester Alicia danke ich ganz besonders. Sie haben mich während meiner gesamten Schulzeit und meines Studiums unermüdlich begleitet und unterstützt. In all dieser Zeit konnte und kann ich mich stets auf ihren Rückhalt verlassen, dafür bin ich ihnen zu tiefstem Dank verpflichtet. Ein besonderer Dank gilt auch meiner Partnerin Lynn für ihre Unterstützung in den vergangenen Jahren. Mit ihrer verständnisvollen und unterstützenden Art hat sie mir geholfen, die Herausforderungen der Promotion zu meistern. Dafür bin ich ihr von Herzen dankbar und freue mich auf all das, was wir in Zukunft gemeinsam erleben werden.

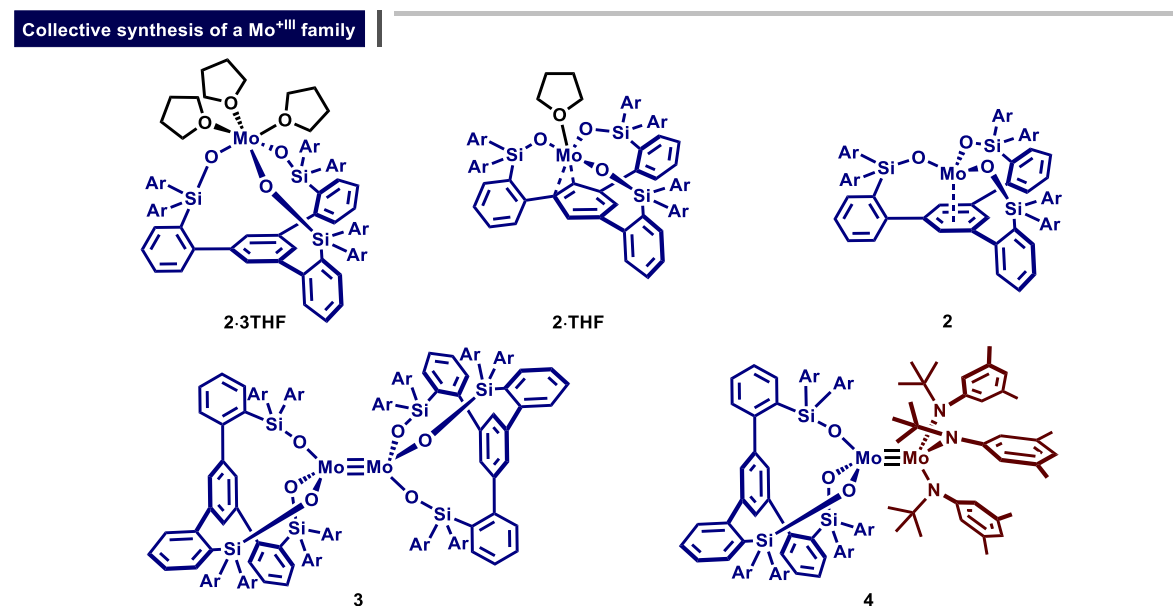
Lynn, Alicia, Mama, Papa und Opa: Ich liebe euch. Euch möchte ich diese Arbeit widmen.

Abstract

Dimer formation is the signature reactivity of Mo^{III} complexes, shaping their unique chemical identity. This proclivity for dimerization stems from the formation of a thermodynamically exceptionally robust $\sigma^2\pi^4$ triple bond, characterized by bonding interactions between the d_z^2 , d_{xz} , and d_{yz} orbitals of two monomeric triradical fragments. While a myriad of homodimeric Mo^{III} complexes are well documented in the literature, their corresponding monomeric complements coordinated by the same ligand have remained elusive.^[1-2] A breakthrough occurred in 1995, when Cummins and co-workers unveiled the synthesis of a stable monomeric Mo^{III} complex **1** featuring three bulky anilide ligands.^[3] This discovery was of utmost importance, as it challenged the long-standing paradigm that Mo^{III} fragments must engage in metal-metal triple bonding. By preventing homodimerization, the energy typically released during the formation of the strong triple bond was essentially “stored”, enabling the resulting highly reactive monomeric complex **1** to engage in a diverse array of three-electron redox processes. Against this backdrop, it is hardly surprising that, to date, neither self-dimerization of **1** nor heterodimerization with other monomeric Mo^{III} fragments has been reported.



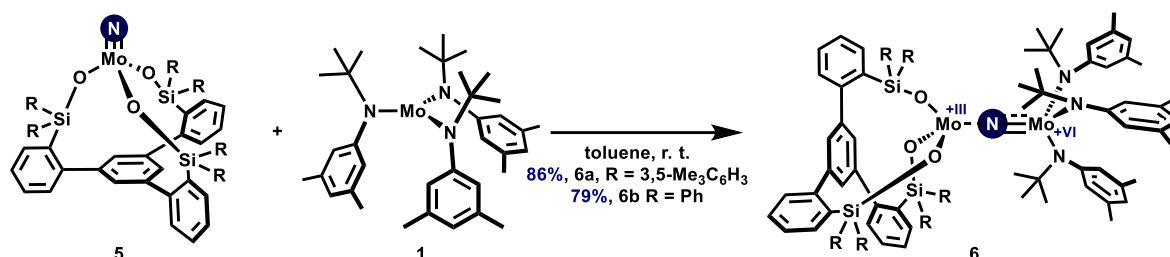
Within this doctoral thesis, the prevailing paradigm was successfully challenged by synthesizing, for the first time, monomeric (**2**, **2·THF**, and **2·3THF**), homodimeric (**3**), and previously unknown heterodimeric (**4**) complexes, all incorporating the same ligand. Notably, the resulting monomer **2·THF** is able to activate small molecules such as N_2O or 1,1-dichloropropane. An in-depth analysis of the electronic structure of the heterodimeric complex was performed using ^{95}Mo NMR spectroscopy and DFT calculations.



Nitrogen atom transfer was tested as an alternative approach toward monomeric Mo^{III} complexes. The required tripod nitrides **5** were synthesized *via* a protonolysis reaction and characterized by a diverse array of analytical tools, including X-ray diffraction, ^{95}Mo , and ^{14}N NMR spectroscopy. When the nitride complexes **5** were treated with the Cummins complex **1** as a potential acceptor, paramagnetic and highly sensitive compounds **6a** and **6b**

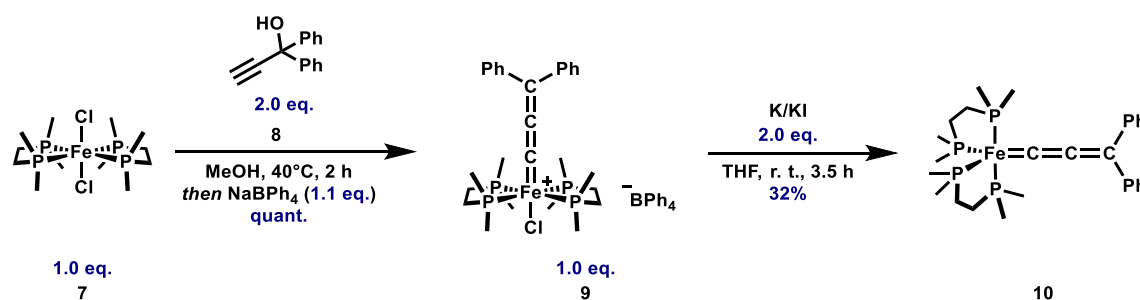
formed instantaneously in each case. Species **6a** and **6b** were characterized by X-ray diffraction analysis, which verified that the bridging nitrogen atom is asymmetrically positioned between both molybdenum fragments. Magnetometry data suggested that complex **6b** is paramagnetic with an $S = 1/2$ state. Our analysis also encompassed DFT as well as EPR spectroscopy. In contrast to prior understanding in the literature (which largely postulates $\text{Mo}^{\text{IV}}\text{-N-Mo}^{\text{V}}$ species), it was established by a Löwdin spin population analysis and EPR spectroscopy that these adducts are best regarded as a Mo^{VI} nitride coordinated to a Mo^{III} fragment.

Incomplete nitrogen atom transfer



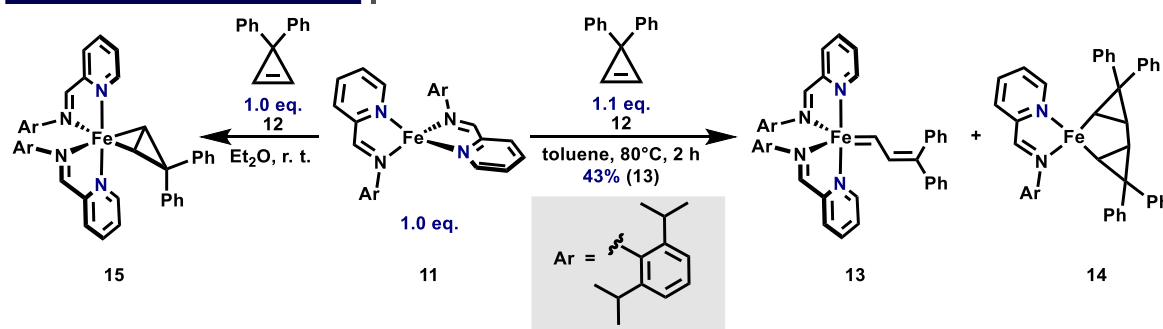
In the second part of this thesis, various strategies for the synthesis of iron carbenes were explored. One of these approaches utilized the activation of propargylic alcohols with $\text{dmpe}_2\text{FeCl}_2$ (**7**), followed by reduction with K/KI to give a formally zero-valent Fe allenylidene **10**. This complex was characterized using X-ray crystallography, NMR spectroscopy, elemental analysis, and mass spectrometry.

Synthesis of iron allenylidenes



Another approach that goes beyond established synthetic blueprints for iron carbenes is the Binger rearrangement strategy.^[4] It involves the formal electrocyclic ring-opening of a strained cyclopropene to generate an alkenyl iron carbene. Although this strategy had previously been explored for iron complexes, it was found to suffer from a dominant side reaction: oxidative cyclization of two cyclopropenes with an iron center to form a metallacyclopentane. We overcame this limitation through the judicious choice of the iron precursor IP_2Fe (**11**) (IP = iminopyridine). Depending on the reaction conditions, either the η^2 -cyclopropene complex **15** or carbene **13** was obtained. It is worth noting that carbene formation competes with oxidative cyclization to give **14**, as both complexes were identified in the same reaction mixture. For complex **13**, conventional analytical tools were complemented by ^{57}Fe NMR spectroscopy, a technique that is highly challenging due to the unfavorable properties of the ^{57}Fe nucleus.

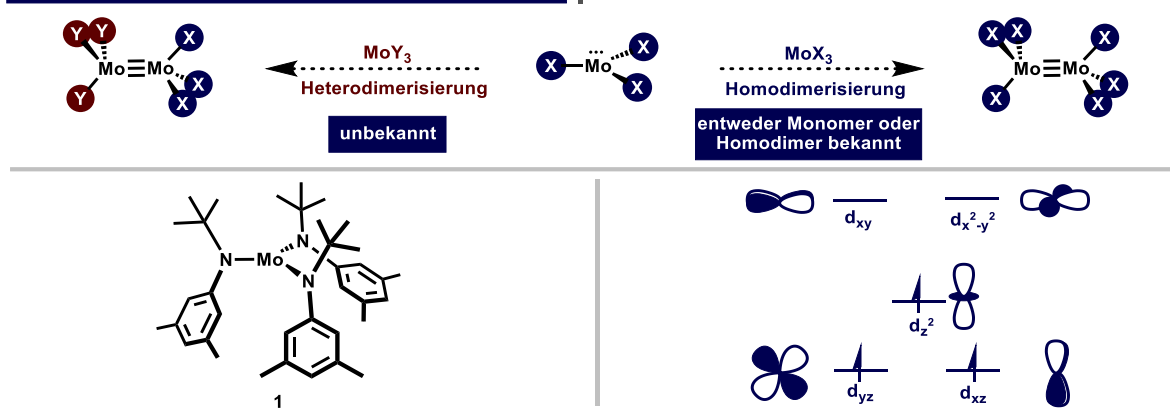
A novel strategy toward iron carbenes



Inhalt

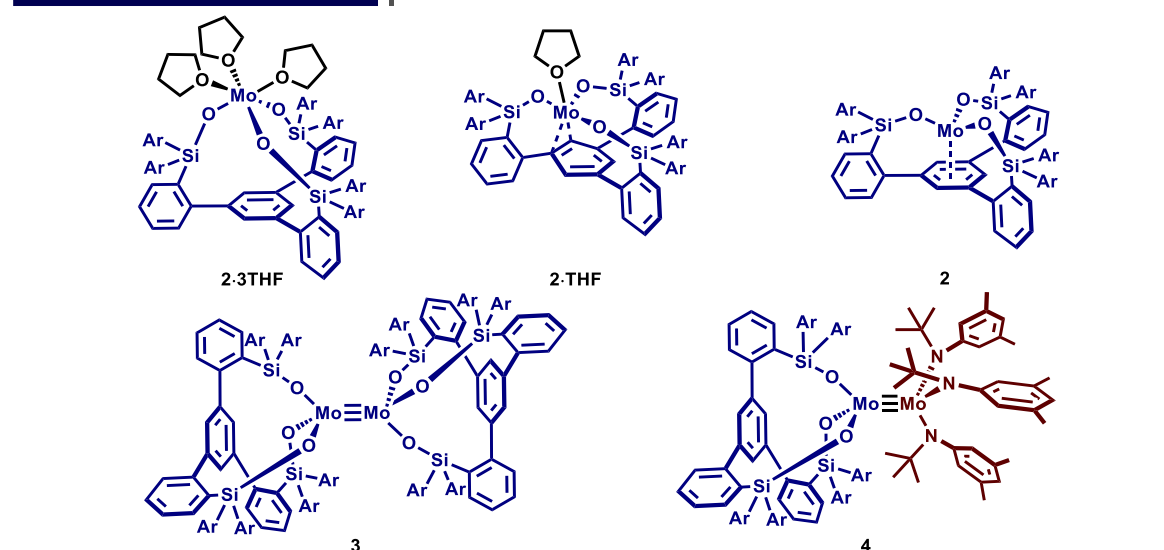
Die Bildung von Dimeren ist die charakteristische Reaktivität von Mo^{III} -Komplexen und prägt daher ihre einzigartige chemische Identität. Die Neigung zur Dimerisierung ist auf die Bildung einer thermodynamisch außergewöhnlich robusten $\sigma^2\pi^4$ -Dreifachbindung zurückzuführen, die Wechselwirkungen zwischen den d_{z^2} -, d_{xz} - und d_{yz} -Orbitalen zweier monomerer Triradikale umfasst. Während eine Vielzahl homodimerer Mo^{III} -Komplexe in der Literatur gut dokumentiert ist, sind die entsprechenden monomeren Komplekte, welche den gleichen Liganden tragen, bislang nicht bekannt.^[1-2] Ein Durchbruch gelang allerdings im Jahr 1995, als Cummins und Mitarbeiter die Herstellung des stabilen monomeren Mo^{III} -Komplexes **1** mit drei Anilid-Liganden vorstellten.^[3] Diese Entdeckung war von äußerster Wichtigkeit, da das Paradigma in Frage gestellt wurde, dass Mo^{III} -Fragmente zwangsläufig Dreifachbindungen zwischen Metallen ausbilden müssen. Durch die Verhinderung der Homodimerisierung wird die Energie, die normalerweise bei der Bildung der starken Dreifachbindung freigesetzt würde, effektiv „gespeichert“. Dadurch kann der resultierende hochreaktive monomere Komplex **1** eine Vielzahl an drei-Elektronen-Redoxprozessen eingehen. Daher ist es nicht verwunderlich, dass bisher weder eine Selbstdimerisierung von **1** noch eine Heterodimerisierung mit anderen monomeren Mo^{III} -Fragmenten bekannt ist.

Die bekannte und unbekannte chemische Identität von Mo^{III}



Im Rahmen dieser Dissertation wurde dieses vorherrschende Paradigma erfolgreich in Frage gestellt. Erstmals wurden monomere (**2**, **2·THF**, and **2·3THF**), homodimere (**3**) sowie bislang unbekannte heterodimere (**4**) Komplexe synthetisiert, die alle denselben Liganden enthalten. Dabei ist bemerkenswert, dass das resultierende Monomer **2·THF** in der Lage ist, kleine Moleküle wie N_2O oder 1,1-Dichlorpropan zu aktivieren. Eine Analyse der elektronischen Struktur des Heterodimers erfolgte mittels ^{95}Mo -NMR-Spektroskopie und DFT-Berechnungen.

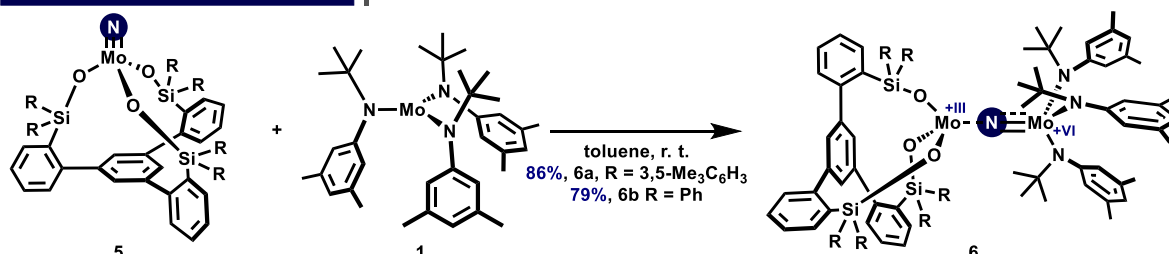
Kollektive Synthese einer Mo^{III} -Familie



Stickstoffatomtransfer wurde als alternativer Ansatz zur Synthese von monomeren Mo^{III} -Komplexen getestet. Die hierfür erforderlichen tripodalen Nitride **5** wurden durch eine Protonolyse-Reaktion synthetisiert und durch eine Vielzahl von Analysemethoden charakterisiert, darunter Röntgenbeugung, ^{95}Mo - und ^{14}N -NMR-Spektroskopie. Bei Reaktion der Nitridkomplexe **5** mit **1** als potenziellem Akzeptor bildeten sich in jedem Fall sofort paramagnetische

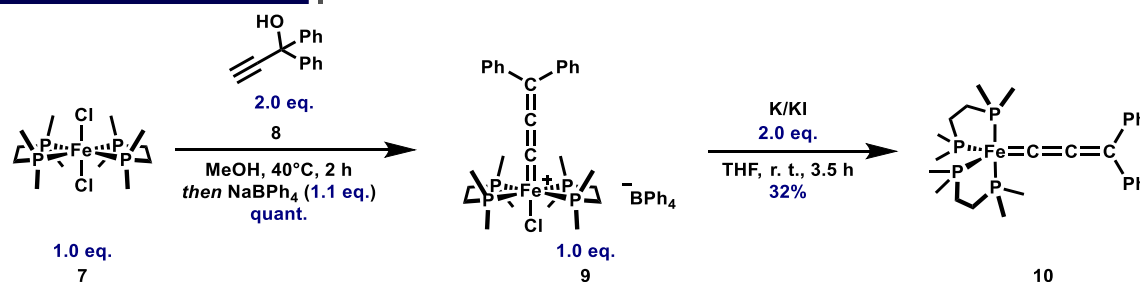
und hochempfindliche Spezies **6a** und **6b**. Diese wurden durch Kristallstrukturanalyse charakterisiert, wobei eine asymmetrische Positionierung des Brückenstickstoffatoms zwischen den beiden Molybdänfragmenten nachgewiesen wurde. Magnetometrische Daten zeigen, dass Komplex **6b** paramagnetisch ist und einen $S = 1/2$ -Spinzustand aufweist. Unsere Analyse umfasste darüber hinaus DFT-Berechnungen sowie EPR-Spektroskopie. Im Gegensatz zu den bisherigen Erkenntnissen in der Literatur (die weitgehend $\text{Mo}^{\text{IV}}\text{-N-Mo}^{\text{V}}$ -Spezies postulieren) konnte mittels Löwdin-Spinpopulationsanalyse und EPR-Spektroskopie gezeigt werden, dass diese Addukte am treffendsten als ein Mo^{VI} -Nitridfragment beschrieben werden, dass an ein Mo^{III} -Fragment koordiniert ist.

Unvollständiger Stickstoffatomtransfer



Im zweiten Teil dieser Arbeit wurden verschiedene Strategien zur Synthese von Eisen-Carbenen untersucht. Einer dieser Ansätze basierte auf der Aktivierung von propargylischen Alkoholen mit $\text{dmpe}_2\text{FeCl}_2$ (**7**), gefolgt von einer Reduktion mit K/KI, um einen formal null-valenten Fe^0 -Allenyliden-Komplex **10** bilden. Dieser Komplex wurde mittels Kristallstrukturanalyse, NMR-Spektroskopie, Elementaranalyse und Massenspektrometrie charakterisiert.

Synthese von Eisen-Allenylidenen



Ein weiterer Ansatz, welcher über etablierte Syntheserouten für Eisen-Carbene hinausgeht, ist die sogenannte Binger-Umlagerungsstrategie.^[4] Dieser Ansatz basiert auf der electrocyclischen Ringöffnung eines gespannten Cyclopropens zur Bildung eines alkenylischen Eisen-Carbens und wurde bereits in früheren Arbeiten für Eisenkomplexe untersucht, allerdings stellte sich heraus, dass eine Nebenreaktion vorherrscht: die oxidative Cyclisierung von zwei Cyclopropenen mit dem Eisen-Komplex. In dieser Arbeit wurden durch die gezielte Wahl der Eisen-Verbindung IP_2Fe (**11**) (IP = Iminopyridin) als Ausgangsverbindung in Abhängigkeit von den Reaktionsbedingungen entweder der η^2 -Cyclopropen-Komplex **15** oder das Alkenyl-Carben **13** erhalten. Die Carbenbildung konkurrierte dennoch mit der oxidativen Cyclisierung zu **14**, da beide Komplexe in der gleichen Reaktionsmischung identifiziert werden konnten. Bei der Charakterisierung von Komplex **13** wurden konventionellen Analysemethoden durch die ⁵⁷Fe-NMR-Spektroskopie ergänzt, welche aufgrund der ungünstigen Eigenschaften des ⁵⁷Fe-Kerns als äußerst anspruchsvoll gilt.

Eine neuartige Synthesestrategie für Eisen-Carbene

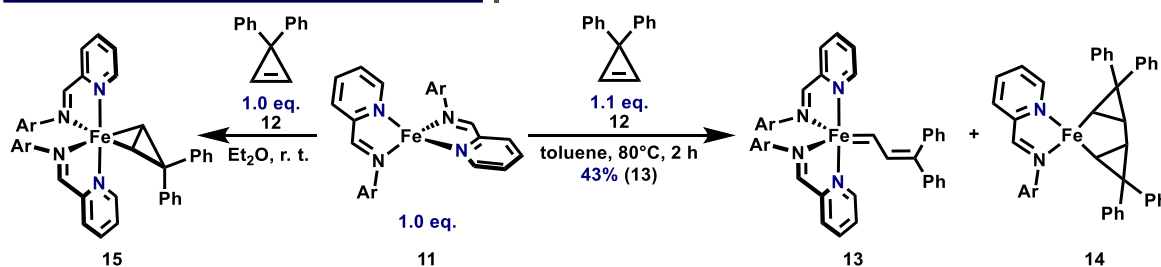


Table of Contents

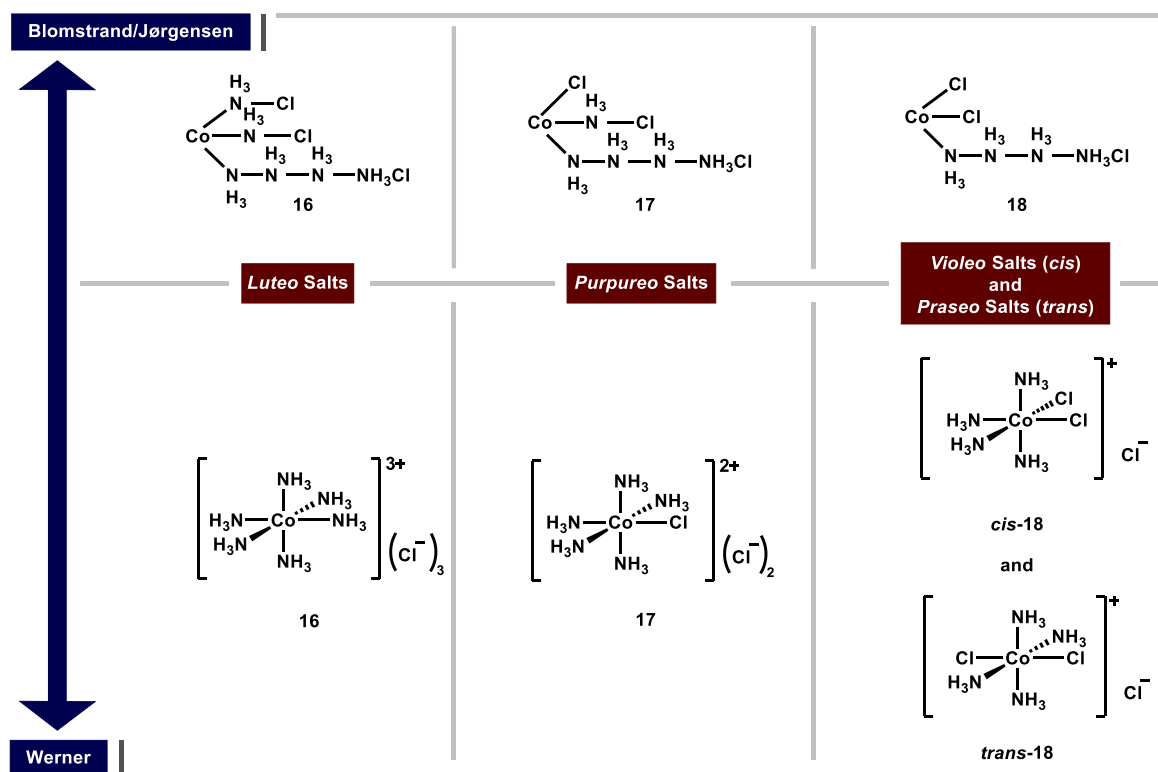
1	Tripodal Silanolate Ligands Expand MoX ₃ Chemistry Beyond Its Traditional Borders.....	1
1.1	Introduction: The Discovery of Dimeric Mo ^{+III} Complexes and Their Status in Coordination Chemistry.....	1
1.2	Introduction: The Chemistry of Monomeric Mo ^{+III} Complexes	17
1.3	Aim	30
1.4	Results.....	32
	Synthesis Of A Heterodimeric Mo ^{+III} Complex With Monodentate Ligands	34
	Design of a Sterically Demanding Silanolate Ligand Leading to the Isolation of a Complete Mo ^{+III} Family.....	37
	Synthesis and Electronic Structure of a Bridged Molybdenum Nitride	53
1.5	Summary (Part 1)	68
2	Synthetic Strategies for Diamagnetic Iron Carbenes	72
2.1	Introduction: From Ziegler's Mülheim Polyethylene Process to Olefin Metathesis.....	72
2.2	Introduction: Toward Iron-Catalyzed Olefin Metathesis.....	84
2.3	Aim	89
2.4	Results.....	91
	Attempted α -H abstraction	91
	Synthesis of Fe allenylidenes	93
	Accessing Iron Carbenes <i>via</i> the Binger Rearrangement Strategy.....	96
2.5	Summary (Part II)	109
3	Experimental Section	111
3.1	General.....	111
3.2	Tripodal Silanolate Ligands Expand MoX ₃ Chemistry Beyond Its Traditional Borders.....	113
3.3	Synthetic Strategies for Diamagnetic Iron Carbenes	135
4	Bibliography.....	142
5	Appendix.....	150
5.1	Overview of Tools	150
5.2	Supporting Crystallographic Information	151

I Tripodal Silanolate Ligands Expand MoX₃ Chemistry Beyond Its Traditional Borders

I.1 Introduction: The Discovery of Dimeric Mo^{+III} Complexes and Their Status in Coordination Chemistry

Until Alfred Werner pioneered the field of coordination chemistry with his landmark paper in 1893,^[5] the relatively young discipline of inorganic chemistry was facing an existential crisis. This was predominantly because the concept of valence, commonly utilized in organic chemistry, could not adequately explain the properties of inorganic complexes.^[6-7]

This is evident in the prevailing theory at the time, the *complex ion chain theory* developed by Christian W. Blomstrand and further investigated by Sophus M. Jørgensen (Scheme 1). As stated in the theory, ammonia complexes of metal halides are represented as chains. This description ensured that the valence of each atom is taken into account, much as organic chemists treated carbon-based molecules.^[6, 8-9] However, the limitations of the approach became apparent through simple experimental observations.^[5] When the *luteo* salt [Co(NH₃)₆]Cl₃ (**16**) was reacted with three equivalents of silver nitrate, three equivalents of silver chloride were formed. This experimental outcome was consistent with the *complex ion chain theory*, as it was hypothesized that the chlorides were only weakly bound to the ammonium residue, which enabled their precipitation as silver chloride. When one molecule of ammonia was removed, the *purpureo* salt of cobalt [Co(NH₃)₅]Cl₂ (**17**) was obtained. In this compound, only two chlorides behaved as ions. The remaining chloride was believed to be tightly bound to the cobalt atom, consistent with the proposed theory. Similarly, the removal of another ammonia molecule yielded the *violeo* and *praseo* salts, the *cis* and *trans* isomeric forms of [Co(NH₃)₄]Cl₃ (**18**), which are distinguishable by their distinct colors (purple and green). Consistent with the *complex ion chain theory*, only one chloride behaved as an ion.

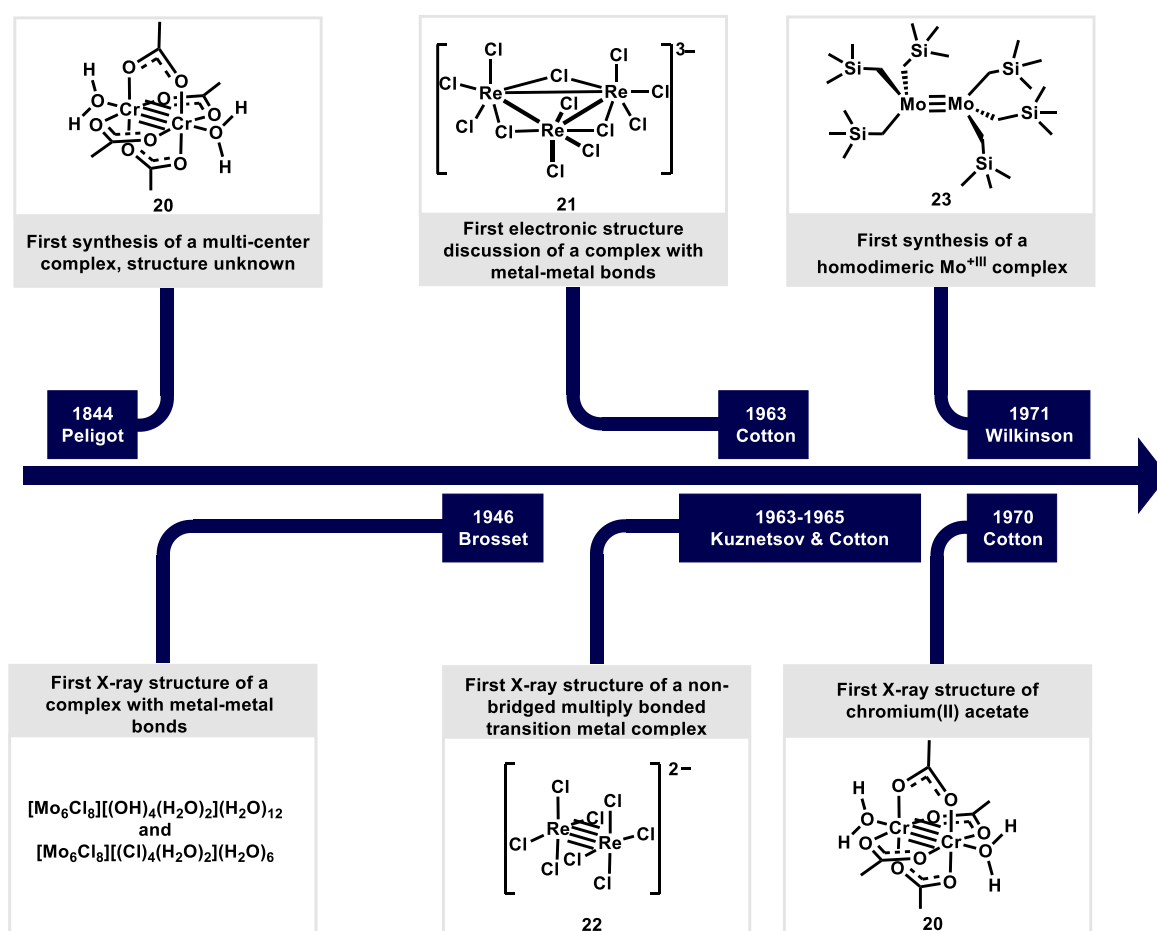


Scheme 1. Top: The *complex ion chain theory* by Blomstrand/Jørgensen. Bottom: Werner's concept of coordination chemistry.

In 1963, the laboratory of F. Albert Cotton discovered that $\text{Cs}[\text{ReCl}_4]$ is a trinuclear cluster with three rhenium atoms connected in a triangular arrangement (Scheme 3). This finding indicated that $\text{Cs}[\text{ReCl}_4]$ should better be interpreted as $\text{Cs}_3[\text{Re}_3\text{Cl}_{12}]$ (**21**) and marked a milestone in the field, because it not only included a single crystal structure determination, but also the first discussion of the electronic structure of a metal-metal bond.^[1, 13-14]

Another key advancement was the X-ray structural analysis of the $[\text{Re}_2\text{Cl}_4]^{2-}$ anion **22**, which was the first example of a transition metal complex containing a multiple bond without additional bridging ligands (Scheme 3). Seminal studies by Kuznetsov and Cotton independently reported the X-ray analysis of the $[\text{Re}_2\text{Cl}_4]^{2-}$ anion, revealing an exceptionally short Re–Re bond length (2.22 Å). In this compound both rhenium atom are connected by a $\sigma^2\pi^4\delta^2$ quadruple bond.^[1, 15-16]

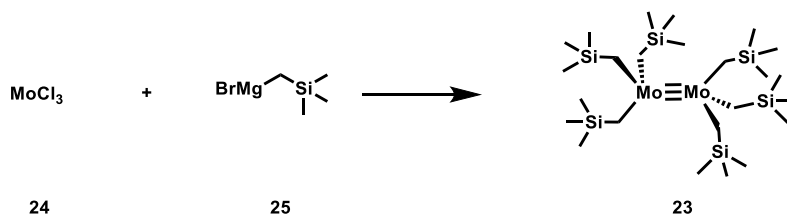
Another groundbreaking achievement was made in 1971, when Wilkinson and his group reported the preparation of the first homodimeric Mo^{III} complex **23** (Scheme 3).^[1, 17]



Scheme 3. Milestones in the evolution of metal-metal bonded compounds in coordination chemistry. Note: Complex **21** is connected by double bonds (not shown for the sake of clarity).

This finding was particularly important because, in a preceding publication, it had been erroneously reported that this compound must be the monomeric complex $\text{Mo}(\text{CH}_2\text{SiMe}_3)_4$.^[18] Fortunately, Wilkinson and co-workers managed to resolve this misassignment by utilizing X-ray diffraction.^[17] The initial synthesis of $\text{Mo}_2(\text{CH}_2\text{SiMe}_3)_6$ (**23**) was achieved by the reaction of a molybdenum trihalide and $\text{Me}_3\text{SiCH}_2\text{MgBr}$ (**25**).^[1, 17] Later, a related procedure was reported to produce the dimer in a yield of 25%, starting from MoCl_3 (Scheme 4).^[19]

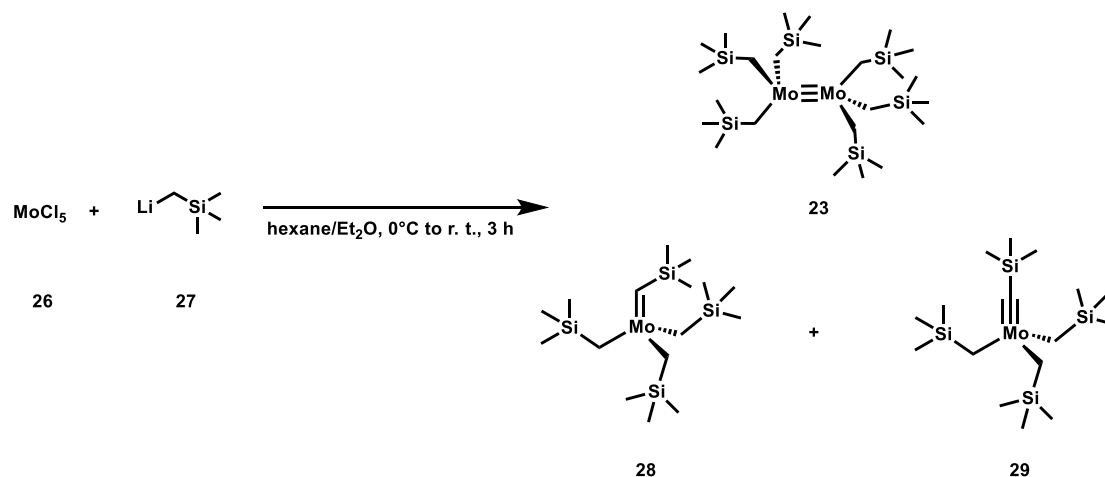
Wilkinson, 1971



Scheme 4. The initial synthesis of **23** by Wilkinson.

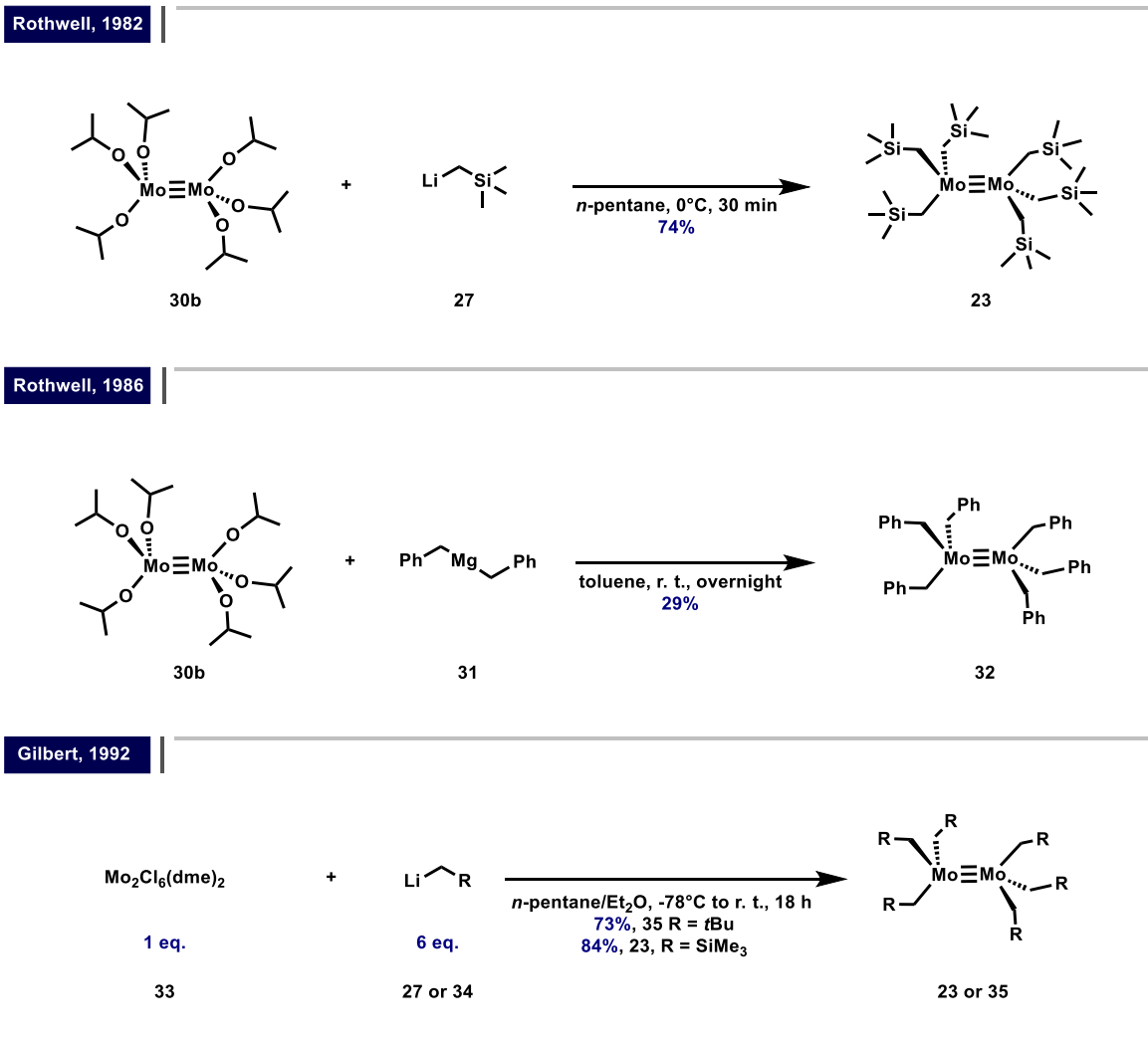
Salt metathesis reactions involving molybdenum halides are notoriously complex and often accompanied by redox processes and C–H activation pathways (Scheme 5). This complexity is exemplified by the work of Chisholm and Wilkinson: The reaction of MoCl_5 (**26**) with $\text{LiCH}_2\text{SiMe}_3$ (**27**), for instance, yielded three distinct products: the dimeric complex **23**, the paramagnetic Mo^{+V} alkylidene **28**, and the diamagnetic alkylidyne **29**.^[1, 19] In this transformation, the alkylidene is formed *via* an α -hydrogen abstraction pathway, reminiscent of the first Schrock carbene synthesis.^[20] In contrast, the formation of the alkylidyne **29** is more intricate, as it requires a one-electron oxidation. Redox processes are also essential for the formation of the dimer. Notably, comparisons can be drawn to observations by Fürstner, where alkylidyne dimerization, mediated by 2-butyne, gave rise to the formation of a dimeric Mo^{+III} complex.^[21]

Chisholm/Wilkinson, 1981



Scheme 5. The synthesis of the first homoleptic Mo^{+III} dimer **23** from MoCl_5 (**26**), and side products.

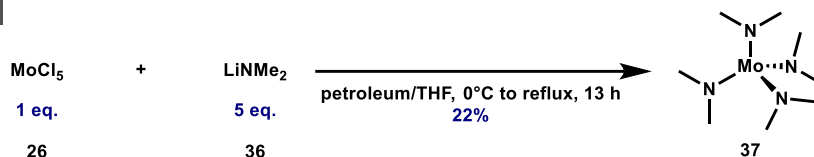
A second entry into homoleptic $X_3Mo\equiv MoX_3$ alkyl complexes is based on the reaction of the homoleptic alkoxide dimer **30b** with an alkyl lithium or a Grignard reagent (Scheme 6).^[1, 22-23] This method significantly improved the yield of complex **23**, usually obtained in low yields ($\leq 25\%$), to as high as 74%. It is worth noting that the yield was only moderate when this approach was adopted for the benzyl derivative **32**. A third pathway emerged with Gilbert's discovery that the reaction of $Mo_2Cl_6(dme)_2$ (**33**) with $LiCH_2tBu$ (**34**) or $LiCH_2SiMe_3$ (**27**) generates the corresponding alkyl substituted dimers **35** and **23**, with yields of 73% and 84%, respectively.^[24]



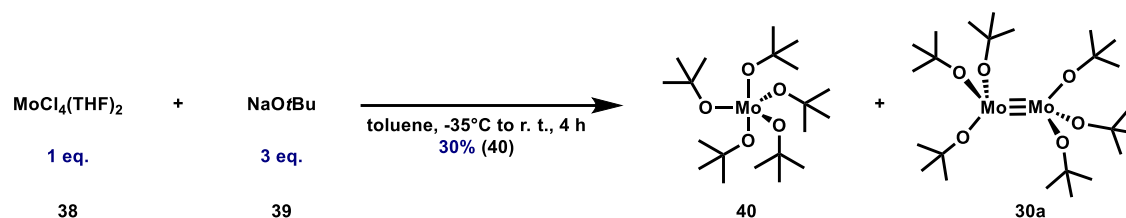
Scheme 6. Subsequent approaches for the synthesis of Mo^{III} alkyl dimers.

In the years following the initial disclosure, the field of dimeric Mo^{III} chemistry thrived under the pioneering efforts of Malcolm H. Chisholm and his research group. This scientific success story in molybdenum chemistry commenced in 1971 with the isolation of a homoleptic Mo^{IV} complex **37**, which was first reported to form upon treatment of $MoCl_5$ (**26**) with $LiNMe_2$ (**36**) (Scheme 7).^[25] Remarkably, another homoleptic molybdenum complex, $Mo(OtBu)_5$ (**40**), was only recently isolated by Fürstner through the reaction of $MoCl_4(THF)_2$ (**38**) with $NaOtBu$ (**39**).^[26] In this reaction, the homoleptic species **40**, along with the known dimer **30a**, is formed as the result of a disproportionation.

Chisholm, 1971



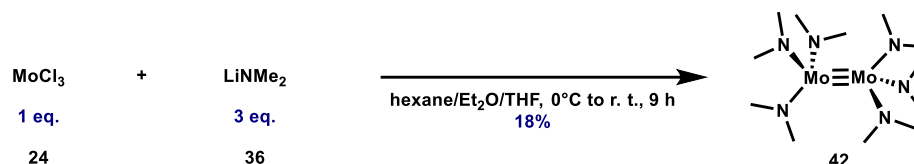
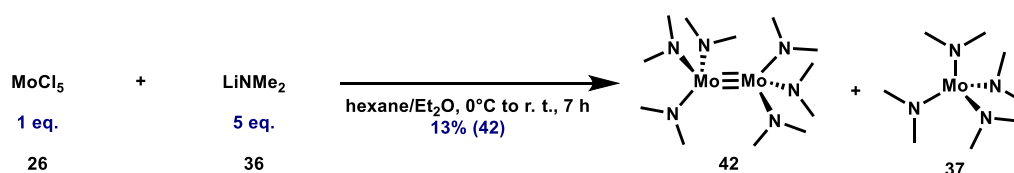
Fürstner, 2020



Scheme 7. Examples of routes to homoleptic Mo^{IV} amide and Mo^{V} alkoxide complexes.

During the same decade, Chisholm laid the groundwork for the expansion of Mo^{III} chemistry by synthesizing the offspring of the alkyl dimers, the homoleptic amide and alkoxide analogues: $(\text{Me}_2\text{N})_3\text{Mo}\equiv\text{Mo}(\text{NMe}_2)_3$ (**42**) and $(t\text{BuO})_3\text{Mo}\equiv\text{Mo}(\text{OtBu})_3$ (**30a**).^[27-28] For the synthesis of **42**, he reported two routes: The first route involved the reaction of MoCl_5 (**26**) with LiNMe_2 (**36**), a procedure reminiscent of the synthesis of the monomeric analogue $\text{Mo}(\text{NMe}_2)_4$ (**37**). This similarity explains the consistent formation of significant amounts of **37** as a by-product *via* this route. Fortunately, it was possible to separate the two compounds *via* fractional sublimation. The second route entailed the addition of MoCl_3 (**24**) to a mixture of LiNMe_2 (**36**) in hexane, Et_2O and THF at 0°C to furnish the desired species in 18% yield. By strictly adhering to this protocol, the formation of $\text{Mo}(\text{NMe}_2)_4$ (**37**) was suppressed to trace quantities (Scheme 8).^[25, 29]

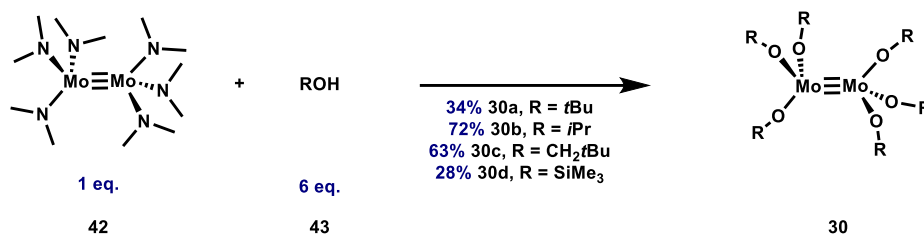
Chisholm, 1974-1976



Scheme 8. The initial protocols for the synthesis of complex **42**.

The homoleptic Mo^{+III} alkoxide and silanolate dimers were initially synthesized by simple protonolysis with the corresponding alcohol starting from complex **42** (Scheme 9).^[1, 28, 30-31] Alcohols, such as MeOH or EtOH, which are not sufficiently bulky, reacted with Mo₂(NMe₂)₆ (**42**) to yield tetranuclear clusters Mo₄(OR)₁₆.^[1]

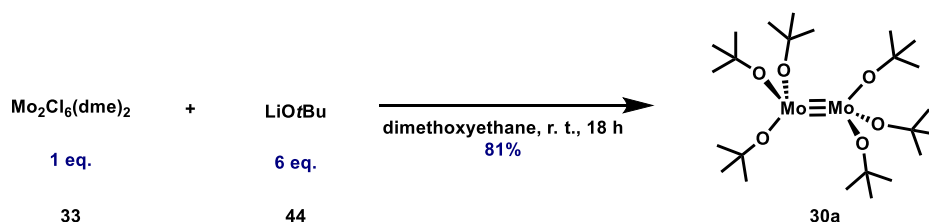
Chisholm, 1974-1977



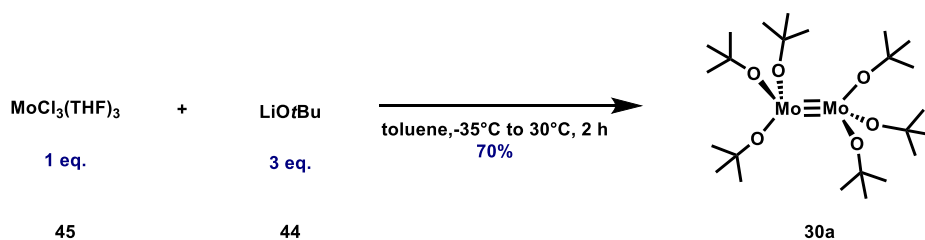
Scheme 9. Original route to dimeric Mo^{+III} alkoxide complexes.

In the following years, however, alternative procedures were established (Scheme 10). Gilbert and Cummins, for instance, explored the reaction of Mo₂Cl₆(dme)₂ (**33**) and MoCl₃(THF)₃ (**45**) with LiOtBu (**44**) to produce the desired species in 81% and 70% yield, respectively.^[24, 32] The analogous tungsten amides and alkoxides were prepared by reaction of WCl₄, WCl₆ or NaW₂Cl₇(THF)₅ with alkali metal amides or alkoxides, respectively.^[1, 33-34]

Gilbert, 1992



Cummins, 1996

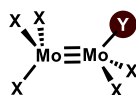


Scheme 10. Improved routes to dimeric alkoxide and silanolate Mo^{+III} complexes.

Beyond the homoleptic X₃Mo≡MoX₃ complexes, a wealth of heteroleptic variants have been disclosed in the literature, typically made by partial ligand exchange from homoleptic Mo^{+III} complexes (Scheme 11). Among these, X₂YMo≡MoX₃ compounds, obtained by exchange of a single ligand, are exceptionally rare.^[35-38] Most prominent are X₂YMo≡MoYX₂ compounds which exhibit a symmetrical 1,2-pattern.^[1] By contrast, less frequently encountered are compounds of the type X₂YMo≡MoX₃, the corresponding unsymmetrical 1,1-isomer.^[35-36, 39] While these 1,2- and 1,1-substituted complexes generally resist thermal isomerization, exceptions exist in which isomerization can be triggered by H₂NMe₂Br or

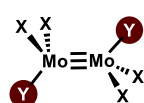
facilitated by the use of a trisilanol ligand.^[40-41] Heteroleptic compounds of the type $\text{Mo}_2\text{X}_3\text{Y}_3$ appear to be extremely rare. They have been inferred as intermediates in ligand exchange studies or were isolated as unsymmetrical phosphine adducts $\text{LX}_2\text{YMo}\equiv\text{MoY}_2\text{XL}$.^[42-43]

$\text{Mo}_2\text{X}_3\text{Y}$ complexes

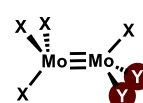
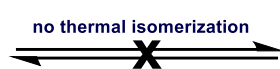


rare

$\text{Mo}_2\text{X}_4\text{Y}_2$ complexes

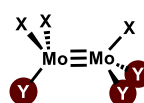


1,2-pattern
well-known

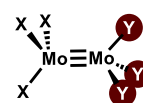


1,1-pattern
rare

$\text{Mo}_2\text{X}_3\text{Y}_3$ complexes



1,1,2-pattern
rare

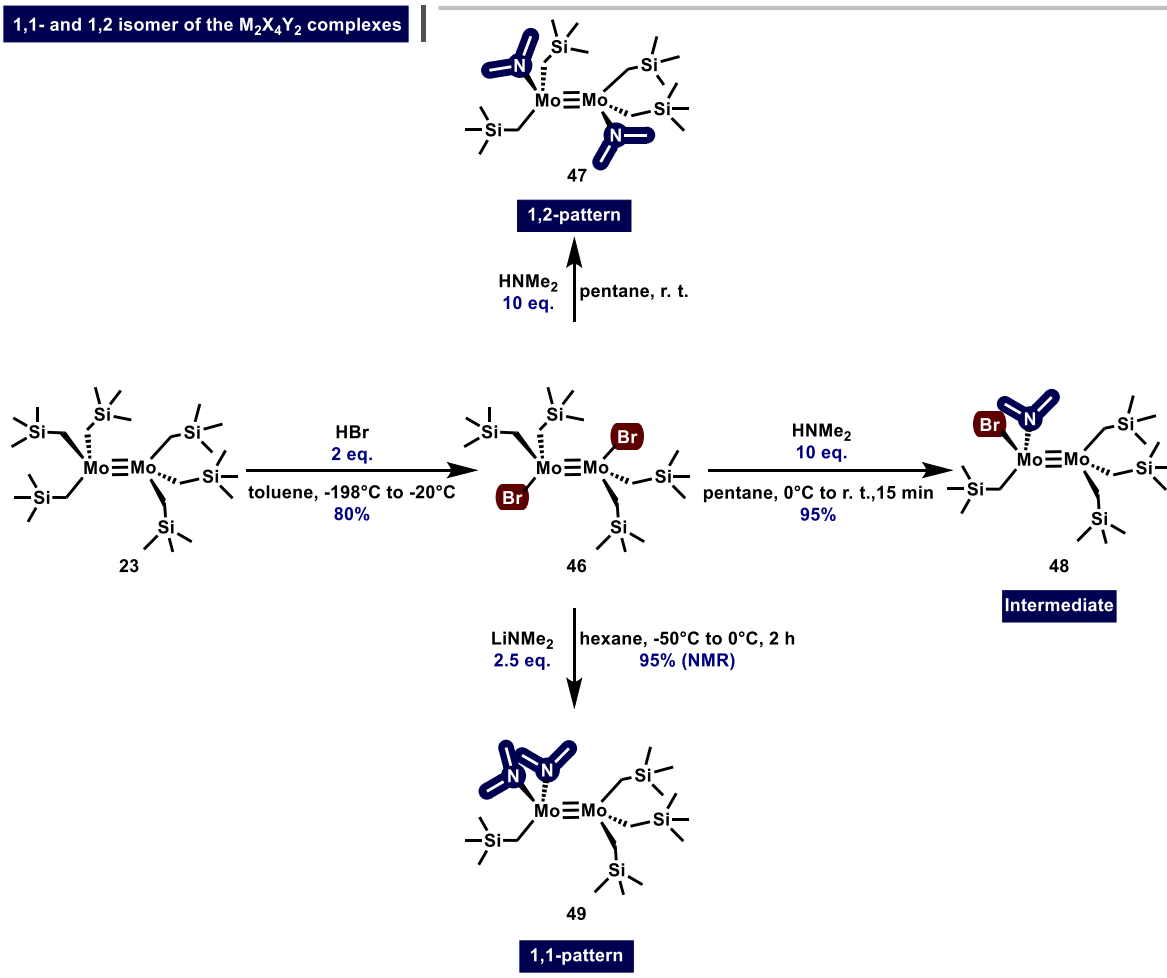


1,1,1-pattern
unknown

Scheme 11. Known, rare and unknown heteroleptic complexes of dimeric Mo^{III} complexes.

The relationship between the 1,1- and the 1,2-isomer is vividly illustrated by the following example, extensively studied by Chisholm (Scheme 12).^[35-36, 40] Treatment of $\text{Mo}_2(\text{CH}_2\text{SiMe}_3)_6$ (**23**) with HBr (2 eq.) in toluene at -198°C yielded the 1,2-isomeric species **46** in 80% yield. Upon reaction of complex **46** with an excess of HNMe_2 (10 eq.) at room temperature, the 1,2-isomeric species **47** was formed. It was later discovered that this transformation proceeds *via* an intermediate complex **48**, which Chisholm managed to isolate by careful control of the reaction conditions.^[40] The corresponding bis-amide species of the 1,1-isomer **49** was formed by reacting the precursor with a slight excess of LiNMe_2 at -50°C .

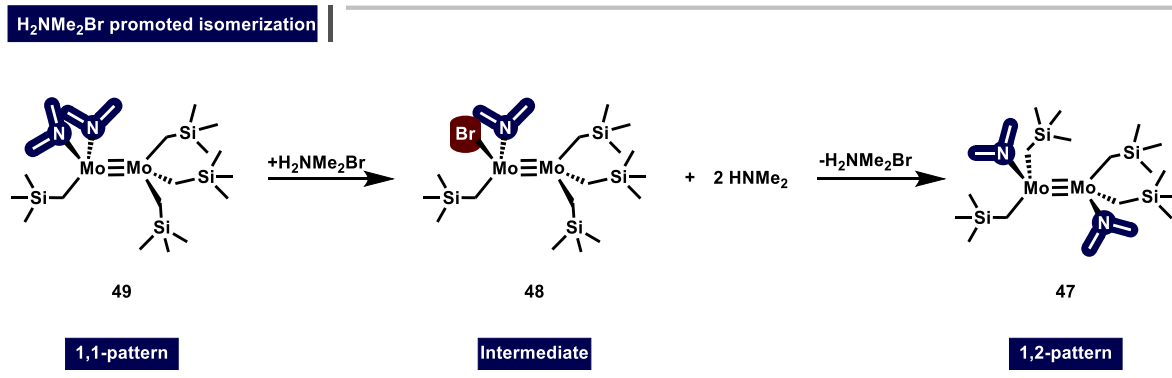
1,1- and 1,2 isomer of the $M_2X_4Y_2$ complexes



Scheme 12. The synthesis of various 1,1- and 1,2- $M_2X_4Y_2$ isomers.

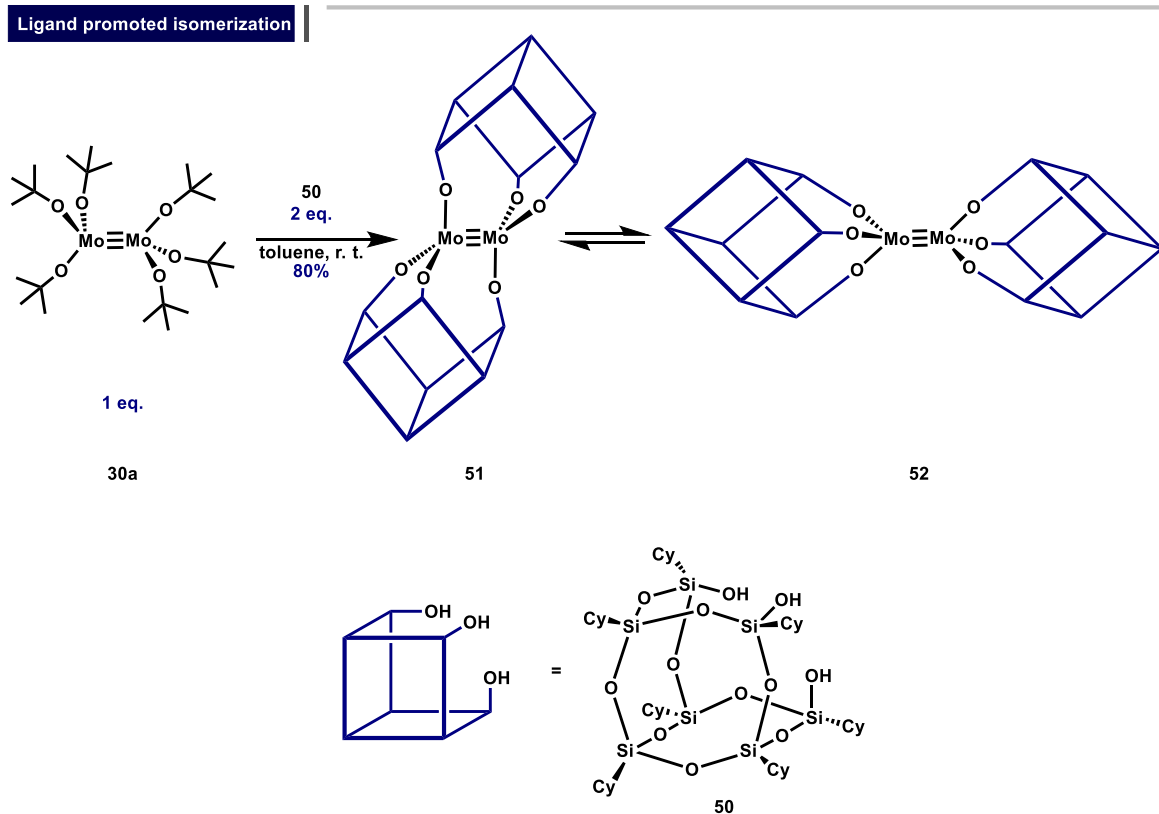
Chisholm also demonstrated that complex **47** and **49** indeed do not undergo thermal isomerization ($>100^\circ C$) due to a prohibitively high kinetic barrier.^[36, 40] However, he discovered that H_2NMe_2Br can catalyze the isomerization of the 1,1- to the 1,2-isomer (Scheme 13). As a possible mechanism, he suggested that the 1,1-isomeric form **49** initially reacts with H_2NMe_2Br to form complex **48**, the intermediate species. In turn, the formerly released $HNMe_2$ then reacts with complex **48**, leading to the formation of the 1,2-isomeric form **47**.

H_2NMe_2Br promoted isomerization



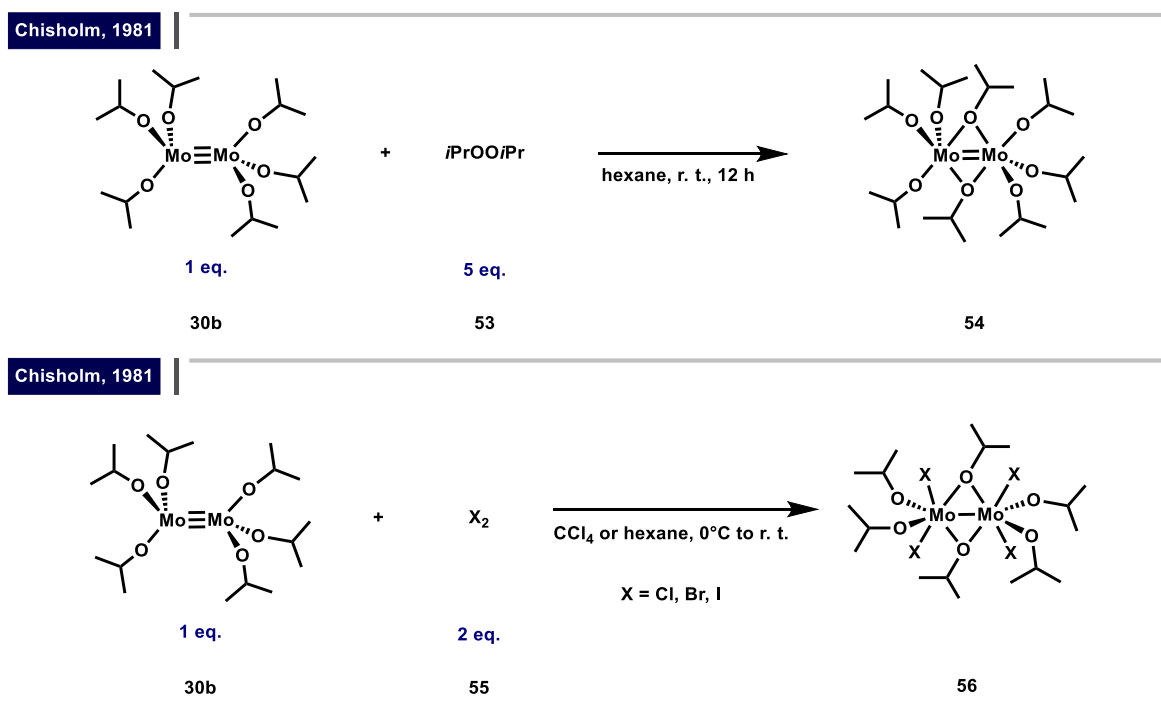
Scheme 13. Mechanistic rationale for the H_2NMe_2 catalyzed isomerization.

The isomerization from the 1,1- to the 1,2-isomeric form can also be facilitated by the use of a trisilanol ligand, as reported by Chisholm. In this case, the reaction of $(t\text{BuO})_3\text{Mo}\equiv\text{Mo}(\text{OtBu})_3$ (**30a**) with trisilanol **50** resulted in the formation of a new species. In the solid state, this species was ascertained by X-ray crystallography as complex **51**. However, in solution, a highly dynamic equilibrium exists. Based on VT NMR data, it was proposed that **51** is in equilibrium with the symmetric species **52** (Scheme 14).^[41]



Scheme 14. Isomerization of a $\text{Mo}_2\text{X}_4\text{Y}_2$ complex facilitated by a trisilanol ligand.

Besides substitution reactions, dimers of Mo^{+III} feature a wide range of remarkable reactivity. These dimeric Mo^{+III} complexes can engage in redox reactions, as exemplified by the reaction of Mo₂(OiPr)₆ (**30b**) with *i*PrOO*i*Pr (**53**) to yield Mo₂(OiPr)₈ (**54**); a compound originally synthesized by the reaction of Mo(NMe₂)₄ with HO*i*Pr (Scheme 15).^[44-46] In contrast, other peroxides, such as *t*BuOO*t*Bu did not react with compound **30b**, nor did the related dimer Mo₂(O*t*Bu)₆ (**30a**) produce the desired Mo^{+IV} species upon reaction with any of the provided peroxides. Additionally, Mo₂(OiPr)₆ (**30b**) was found to react with iodine, bromine, or chlorine to give the corresponding Mo^{+V} species **56**. In this complex, the Mo–Mo interaction is best described as a single bond.^[46]



Scheme 15. Redox reactions of dimeric Mo^{+III} complexes to give double and single bonded Mo dimers.

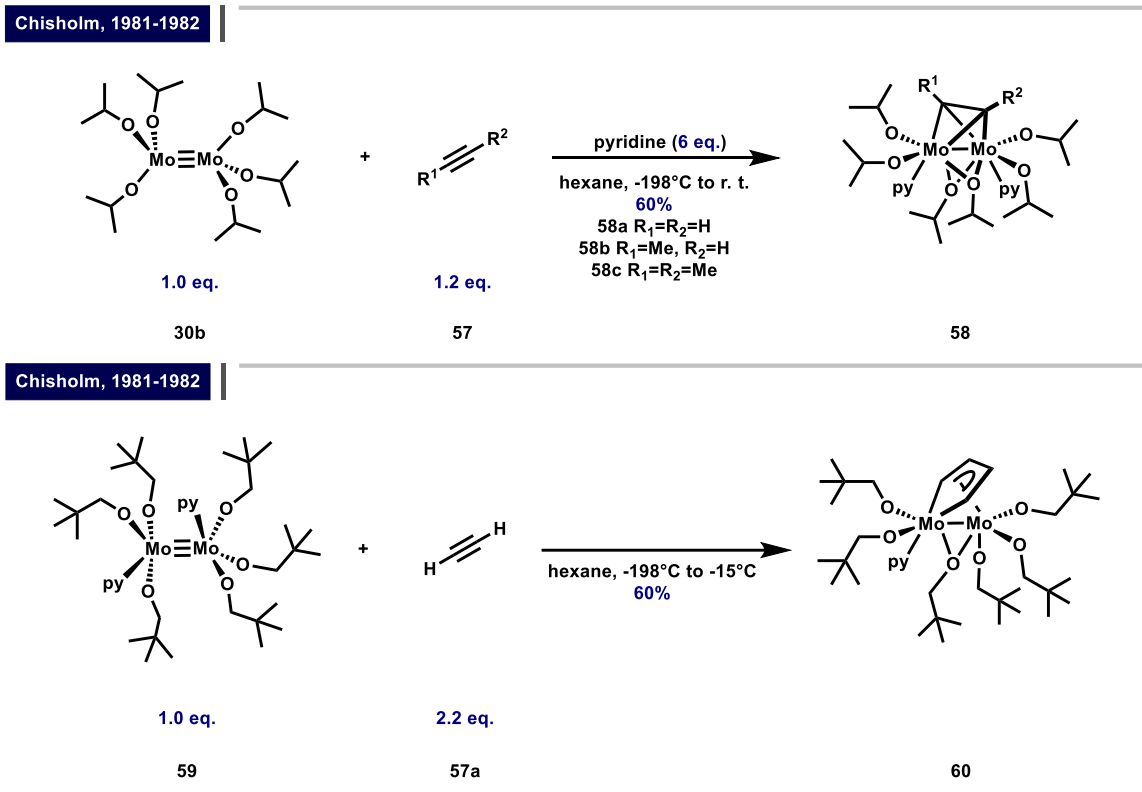
Mo^{+III} and W^{+III} complexes are renowned for their remarkable reactivity toward alkynes. One of the earliest reported examples involved the reaction of (*i*PrO)₃Mo≡Mo(O*i*Pr)₃ (**30b**) with acetylene, which initially led to rapid oligomerization.^[47-48]

Notwithstanding these results, Chisholm proposed that the introduction of a donor ligand might permit the isolation of a transient reaction intermediate. In 1981, his group succeeded in isolating such an acetylene adduct **58a** by employing pyridine as the donating ligand (Scheme 16). The strategy was later extended to prepare propyne and 2-butyne adducts of type **58**. Additionally, it was found that the pyridine adduct **59** reacts with acetylene to yield an acetylene adduct. Upon reaction of this adduct with another equivalent of acetylene, the metallacyclopentadiene complex **60** was formed, marking the first step of an oligomerization process.

Complexes **58** and **60** were also found to catalyze the cyclotrimerization of alkynes. For instance, complex **58** (5 mol%) was capable of catalyzing the cyclotrimerization of acetylene to furnish benzene in low yield. Similarly, complex **60** catalyzed the cyclotrimerization of acetylene in low yield, however, in this case the formation of large amounts of polyacetylene was noted.

Within the Chatt-Dewar-Duncanson formalism, alkyne coordination to dimeric Mo^{+III} complexes can be described as two extremes. In the first scenario, the ligation can be interpreted as an oxidative addition, where the alkyne acts as a [R–C–C–R]⁴⁻ or [R–C–C–R]²⁻ bridging ligand, leading to a singly bonded dimeric Mo^{+V} or a doubly bonded dimeric Mo^{+IV} complex, respectively. Alternatively, if one assumes the

presence of the adduct model within the Chatt-Dewar-Duncanson formalism, the oxidation state of the Mo atom remains unchanged upon coordination of the alkyne. In complex **60**, the bonding situation is best described as a metallacyclopentadiene fragment coordinated to the second molybdenum center.



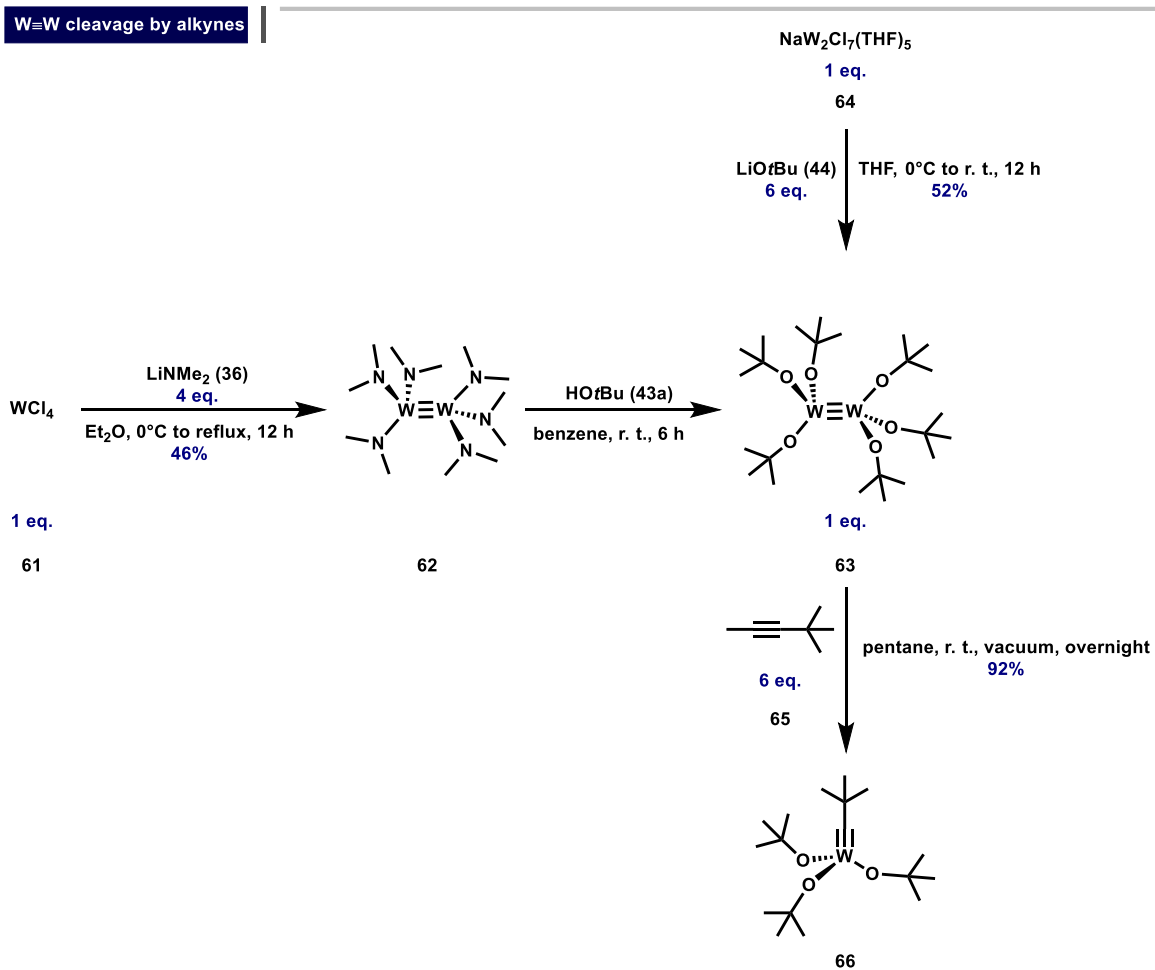
Scheme 16. Isolated intermediates in the cyclotrimerization and oligomerization of alkynes mediated by dimeric Mo^{+III} complexes.

In the years following Chisholm's original discovery, Richard Schrock's group set out to explore the cleavage reaction of alkynes with dimeric W^{+III} complexes, aiming to develop a novel strategy for synthesizing W^{+VI} alkylidynes.^[49-50] This approach would later be known as the Schrock "Chop Chop" reaction (Scheme 17).^[1]

Similar to the synthesis procedure for dimeric Mo^{+III} complexes, the initial synthesis of the tungsten analogues commenced with the reaction of WCl₄ (**61**) with LiNMe₂ (**36**) to yield the corresponding dimeric W^{+III} complex **62**.^[33, 51] This was followed by a ligand exchange, where protonolysis with HOtBu (**43a**) generated the W^{+III} alkoxide complex **63**, although the yield for this step was not reported.^[52]

An improved strategy for the synthesis of W₂OtBu₆ (**63**) was based on Schrock's observation that when WCl₄ (**61**) is reduced with one equivalent of Na/Hg in THF, a compound with the formal composition W₂Cl₆THF₄ is obtained.^[53] Upon reaction with LiOtBu, the alkoxide dimer **63** is formed.^[49] Notably, this transformation may also be carried out as a one-pot procedure.^[34, 54-55] Later Chisholm discovered NaW₂Cl₇THF₅ (**64**), another useful precursor for the synthesis of dimeric W^{+III} compounds. In the same report, Chisholm reported the synthesis of W₂OtBu₆ (**63**), achieving a yield of 52%.^[34]

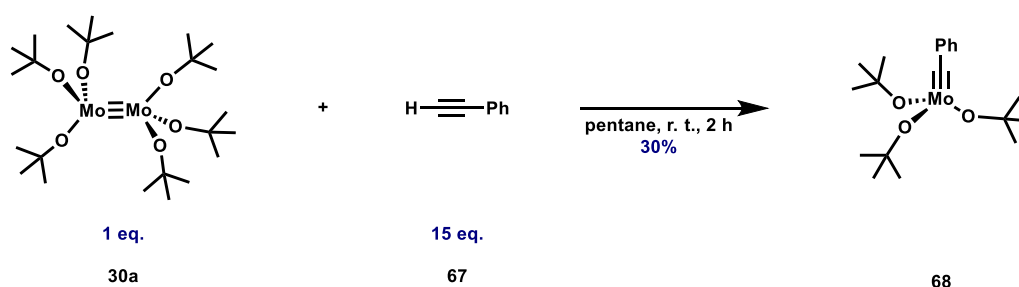
The key step in this strategy involved metathesis of dimer **63** with an alkyne such as **65**, resulting in the formation of the neopentylidyne complex **66**. Likewise, it has been demonstrated that metathesis with nitriles such as acetonitrile or benzonitrile is feasible, yielding a 1:1 mixture of an alkylidyne and a nitrido complex.^[49-50]



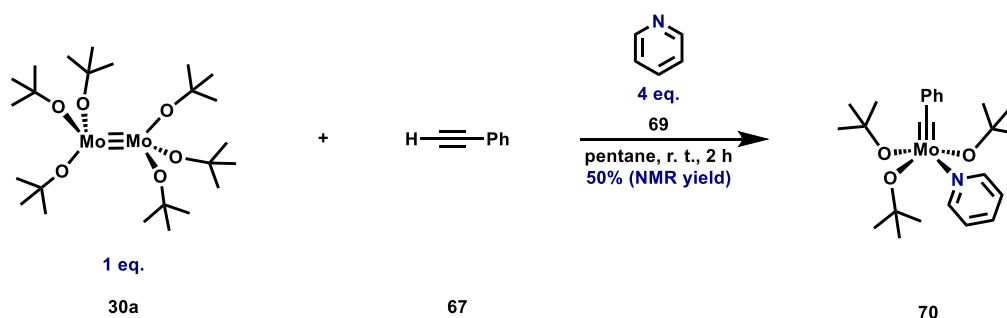
Scheme 17. Schrock's "Chop Chop" reaction.

A comparable approach for the preparation of Mo^{+VI} alkyldynes has not been established. In contrast, dimeric Mo^{+III} complexes do not react with any internal alkyne. However, Schrock discovered that phenylacetylene, a terminal alkyne, undergoes metathesis with (tBuO)₃Mo≡Mo(OtBu)₃ (**30a**) yielding the corresponding benzylidyne **68** as the sole isolable product in 30% yield (Scheme 18).^[56] It was not possible to identify the methylidyne, which presumably can decompose *via* bimolecular coupling to regenerate (tBuO)₃Mo≡Mo(OtBu)₃ (**30a**) together with the release of acetylene, which would then oligomerize in the presence of **30a**.^[47-48, 56] When the reaction was repeated in the presence of quinuclidine or pyridine, a 1:1 mixture of the corresponding benzylidyne and methylidyne adducts was obtained, which is a strong indication for a metathetic cleavage of the Mo≡Mo triple bond.

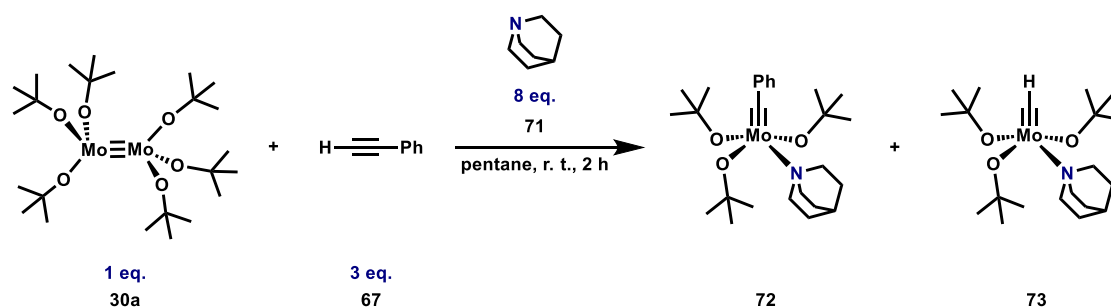
Schrock, 1984



Trapping with pyridine



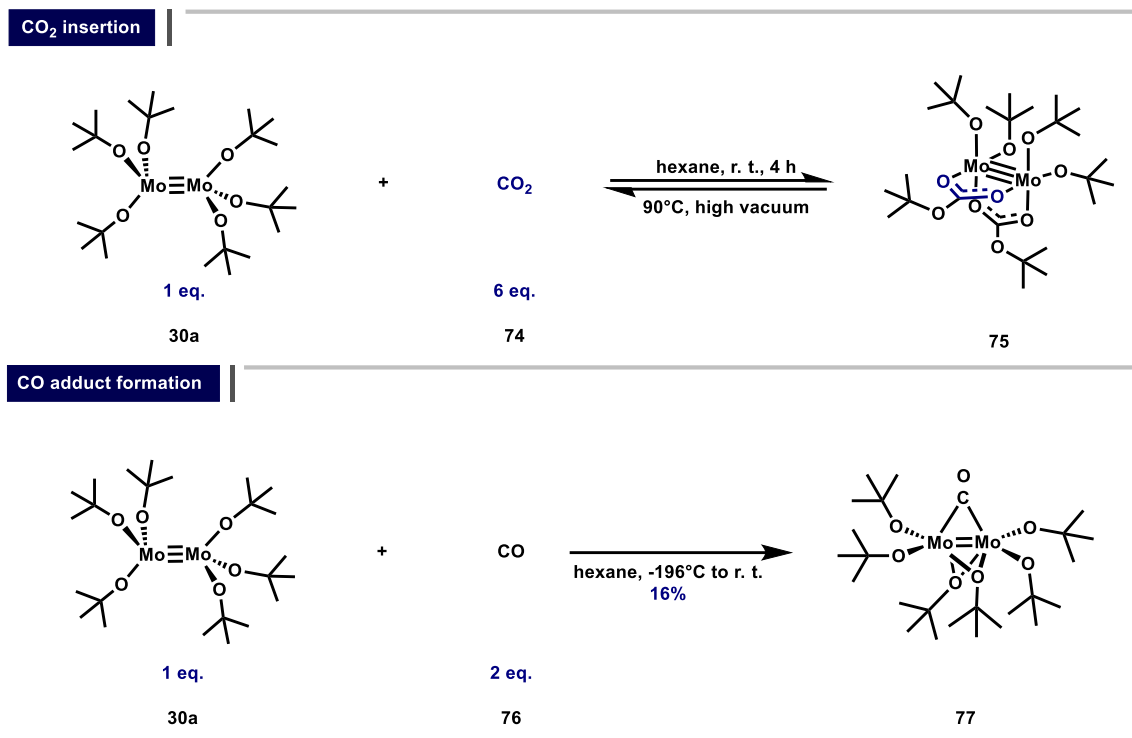
Trapping with quinuclidine



Scheme 18. The reaction of (tBuO)₃Mo≡Mo(OtBu)₃ (**30a**) with phenylacetylene and trapping of products with donor ligands.

Dimeric Mo^{+III} complexes also undergo reversible reactions with CO and CO₂ (Scheme 19).^[57-58] Cotton and Chisholm discovered that when Mo₂(OtBu)₆ (**30a**) is exposed to CO₂ at room temperature, two equivalents of CO₂ insert into two of the metal-alkoxide bonds, yielding complex **75** as blue crystals. This transformation is reversible: upon heating of complex **75** to 90°C *in vacuo*, CO₂ is released, regenerating the original complex. Subsequently, Cotton and Chisholm found that **30a** forms adducts with CO.

However, precise control of the reaction conditions is crucial; otherwise, disproportionation occurs, leading to the formation of $\text{Mo}(\text{CO})_6$ and $\text{Mo}(\text{OtBu})_4$.



Scheme 19. Reactions of $\text{Mo}_2(\text{OtBu})_6$ (**30a**) with CO_2 (**74**) and CO (**76**).

Because of their interesting electronic structure, dimeric Mo^{III} complexes have been extensively studied by multiple research groups.^[1, 59-61] Qualitatively, the triple bond can be described as an interaction between the d_{z^2} orbitals that form the σ bond, while interactions between the pairs of d_{xz} and d_{yz} orbitals lead to the formation of the two π bonds (Figure 1).^[1]

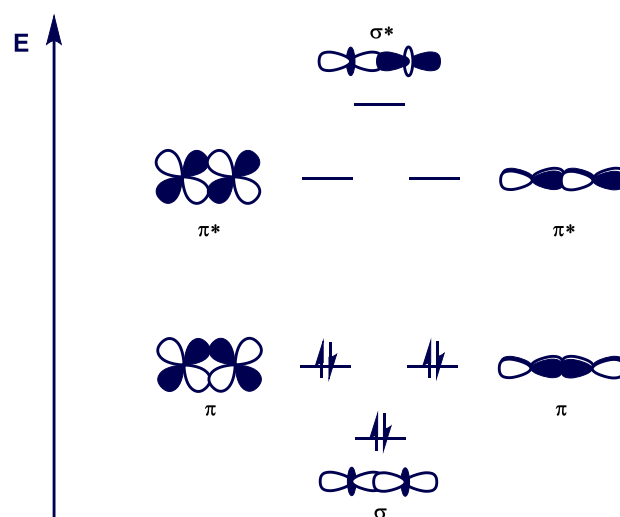


Figure 1. General and qualitative MO scheme for dinuclear Mo^{III} complexes.

In a combined experimental and theoretical approach, Cotton utilized photoelectron spectroscopy to study the compounds $\text{Mo}_2(\text{OtBu})_6$ (**30a**), $\text{Mo}_2(\text{NMe}_2)_6$ (**42**) and $\text{Mo}_2(\text{CH}_2\text{tBu})_6$ (**35**) and performed calculations on their simplified counterparts $\text{Mo}_2(\text{OH})_6$, $\text{Mo}_2(\text{NH}_2)_6$ and $\text{Mo}_2(\text{CH}_3)_6$ (Figure 2).^[59]

For $\text{Mo}_2(\text{OH})_6$, the HOMO mainly consists of contributions from the bonding Mo–Mo π orbitals, along with a minor amount of δ^* character. Energetically below this, the HOMO–1 is primarily of Mo–Mo σ character, while the oxygen lone pair p orbitals are located at still lower energies.

In $\text{Mo}_2(\text{NH}_2)_6$, the ordering of the metal-metal σ - and π -bonding orbitals remains largely unchanged; however the HOMO is now composed of ligand based lone pair p orbitals. This shift in energy aligns with the fact that nitrogen is less electronegative than oxygen. M–N bonding orbitals from the amido ligands appear between the M–M bonding π and σ orbitals, composed of nitrogen based 2p orbitals that actively participate in M–N π -bonding interactions.

$\text{Mo}_2(\text{CH}_3)_6$ represents a unique case: Here, the HOMO remains predominantly Mo–Mo π in character yet exhibits significant δ^* -antibonding contributions, weakening the π -bonding interaction. Energetically below this, Mo–C σ -bonding orbitals mix with Mo–Mo σ^* -antibonding orbitals. A similar orbital to the HOMO appears at a lower energy level, again followed by an M–C σ -bonding orbital primarily derived from ligand based p orbitals and Mo–Mo σ^* -antibonding orbitals. Further below, Mo based δ orbitals mix with ligand based p orbitals and metal centered π^* -antibonding orbitals, which describes the strong σ -donor interaction of the alkyl ligands with molybdenum-based orbitals. The Mo–Mo σ -bonding orbital resides at an even lower energy level.

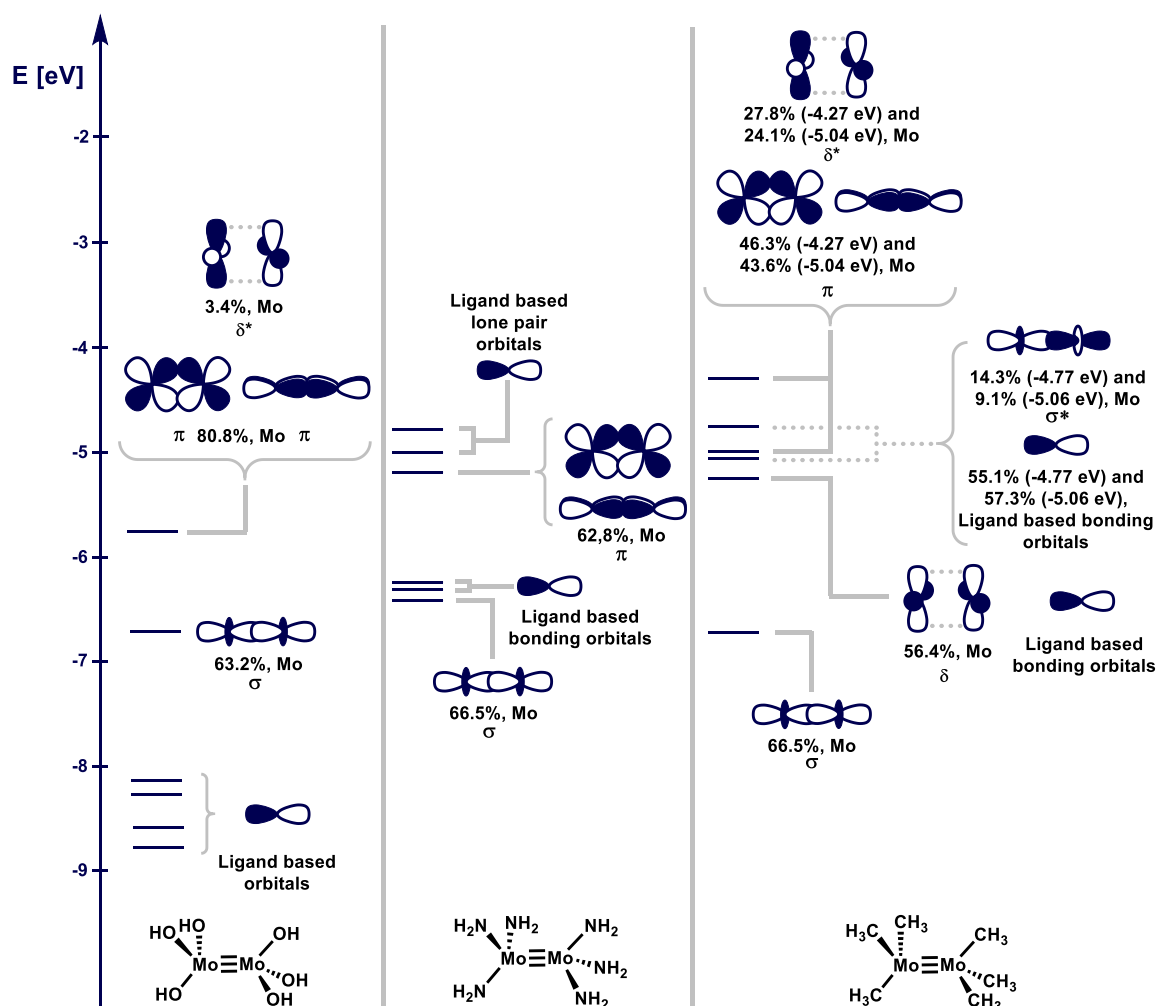
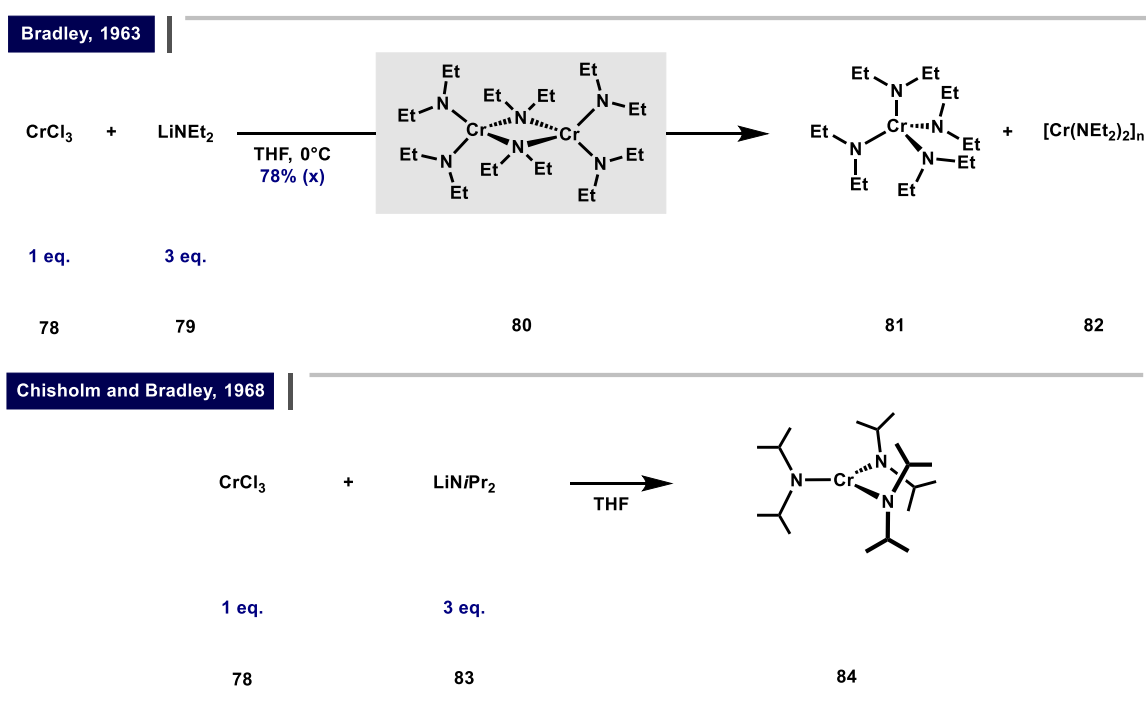


Figure 2. Quantitative molecular orbital scheme showing the most important orbitals of $\text{Mo}_2(\text{OH})_6$, $\text{Mo}_2(\text{NH}_2)_6$ and $\text{Mo}_2(\text{CH}_3)_6$.

1.2 Introduction: The Chemistry of Monomeric Mo^{+III} Complexes

Among the elements in the chromium group, Mo^{+III} and W^{+III} complexes strongly favor metal-metal triple bond formation, a trait conspicuously absent in chromium analogues.^[62] Instead, Cr^{+III} complexes, particularly those with diethylamido ligands, exist as dimers in solution, featuring bridging amido ligands but lacking a direct metal-metal triple bond (Scheme 20).^[63] Against this backdrop, it is notable that the utilization of the N(Et)₂ ligand led to the formation of triply bonded and thermally stable Mo^{+III} and W^{+III} complexes. However, attempts to use the NiPr₂ ligand were unsuccessful for W^{+III}.^[29, 33, 51]

Despite their apparent stability in solution, Cr^{+III} complexes are highly susceptible to disproportionation, yielding homoleptic, tetracoordinate Cr^{+IV} amido complexes **81** and polymeric Cr^{+II} species **82**.^[64-65] However, the isolation of a stable trigonal-planar Cr^{+III} monomer **84** became possible through careful ligand selection. This challenge was first met by Chisholm and Bradley in 1968, who reported the isolation of the first three-coordinate Cr^{+III} complex. Coordinated by three NiPr₂ ligands, this complex was analyzed utilizing single X-ray diffraction and magnetometry, confirming both its monomeric nature and the existence of three unpaired electrons.^[66-67]



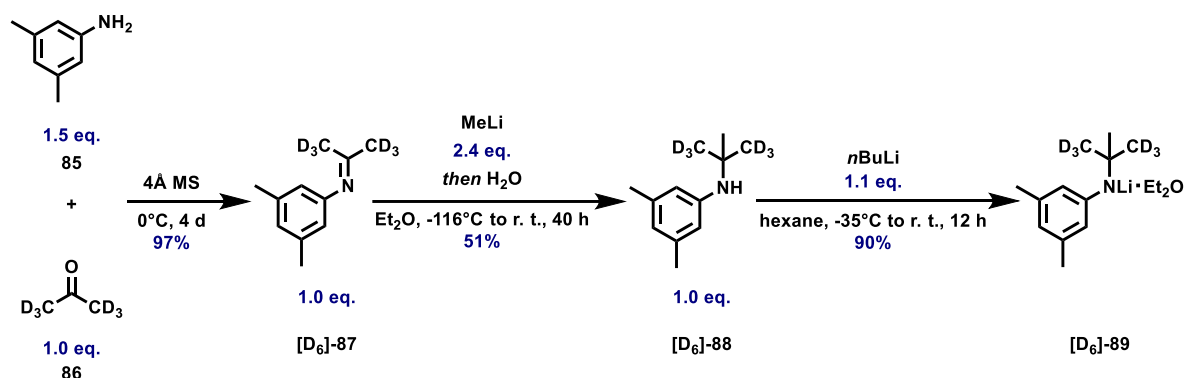
Scheme 20. Cr^{+III} does not show a high proclivity for triple bond formation and is susceptible to disproportionation.

To reconcile the chemistry of Cr^{+III} and that of its heavier group six counterparts, Mo^{+III} and W^{+III}, Christopher C. Cummins, who had just started his independent career at MIT, set out to craft a sterically demanding anilide ligand; one that would enable the isolation of the first trigonal-planar Mo^{+III} complex.^[3, 62] Cummins' ligand design was guided by simple but strategic criteria. Firstly, the ligand should be composed of carbon-based building blocks and lack β -hydrogens in order to avoid common decomposition pathways. Additionally, the ligand should feature one spherical substituent (*t*Bu group) and one planar substituent (3,5-Me₂C₆H₃) to enhance intramolecular packing effects and, ultimately enable the isolation of a C₃-symmetric species. A final strategic design element was the incorporation of deuterium labels into the ligand to facilitate the analysis of the resulting paramagnetic product using NMR spectroscopy.^[62]

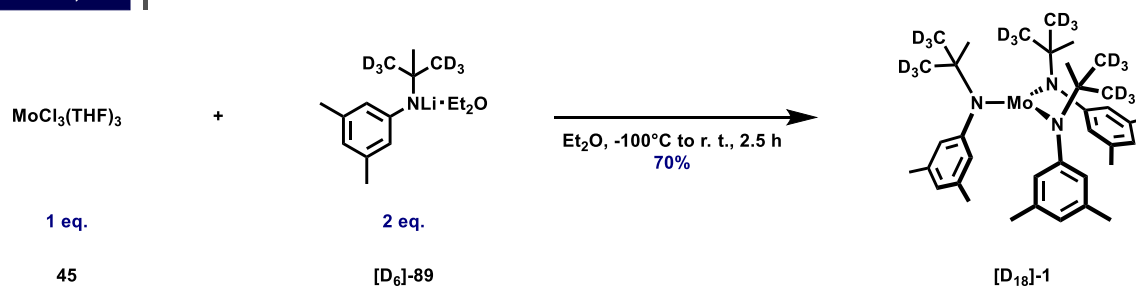
The synthesis of the ligand commenced with the condensation of aniline **85** with [D₆]-acetone (**86**), yielding the desired imine [D₆]-**87** in 97%.^[68] Subsequent steps involved addition into the imine with

MeLi, followed by deprotonation of the resulting aniline **[D₆]-88** to give the lithium anilide **[D₆]-89** in 90% yield. The final synthesis of the monomeric complex **[D₁₈]-1** proceeded *via* the reaction of lithium anilide **[D₆]-89** with MoCl₃(THF)₃ (**45**) under an atmosphere of N₂ to yield the desired monomer in 70% yield after crystallization under an atmosphere of argon (Scheme 21).^[3]

Ligand design



Cummins, 1995



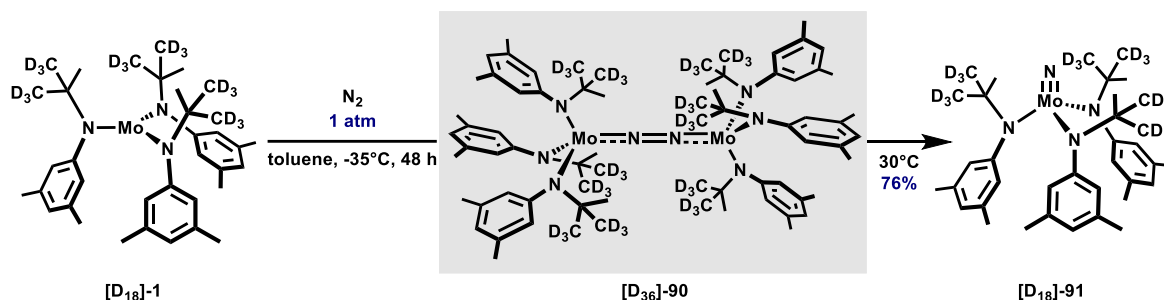
Scheme 21. The synthesis of the Cummins complex **[D₁₈]-1** enabled by careful ligand design.

Initially, crystallization of the compound was attempted at -35°C in Et₂O under an atmosphere of N₂. Strikingly, the deep red solution rapidly turned deep purple within just 45 min. Intrigued by this observation, the crystallization batch was analyzed by ²H NMR spectroscopy, revealing that the original signal at 64 ppm had disappeared, replaced by a single signal at 14 ppm.^[69]

Fascinated by this unexpected behavior, the authors repeated the experiment at -35°C in toluene and tracked the reaction by ²H NMR spectroscopy. Within 48 h, conversion to the new species took place. After warming to 30°C, the purple color faded away within several hours, giving rise to the formation of a golden solution, from which only the diamagnetic terminal nitrido complex **[D₁₈]-91** could be identified and subsequently isolated in 76% yield.^[70]

These results pointed to an extraordinary conclusion: the purple species had to be the paramagnetic Mo–N₂–Mo complex **[D₃₆]-90** (Scheme 22). Most remarkably, this study represented the first report of a homogeneous system that was capable of cleaving dinitrogen's exceptionally strong triple bond. In subsequent studies, the purple Mo–N₂–Mo intermediate **[D₃₆]-90** was characterized by EXAFS structural studies and SQUID experiments and later by X-ray diffraction.^[70-71] It was also found that this cleavage reaction proceeds through a *zig-zag* transition state.^[72] Such reactivity was entirely unprecedented and defined a landmark discovery in the field of nitrogen activation chemistry.^[73]

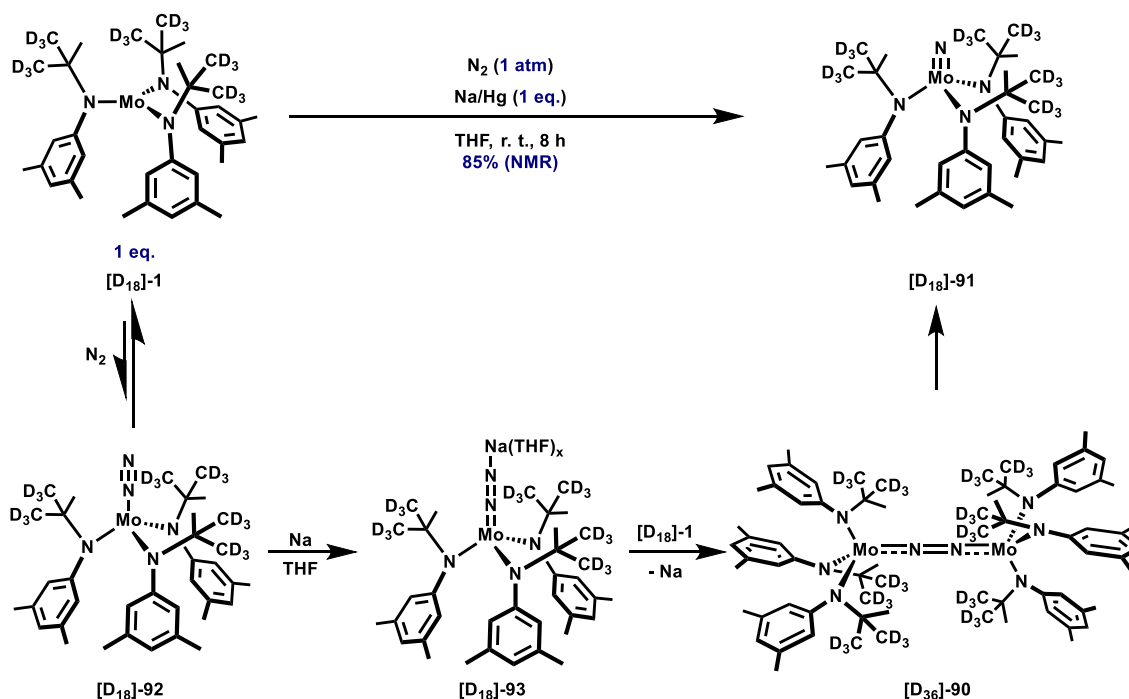
N₂ cleavage



Scheme 22. Complex **[D₁₈]-1**, the first homogenous system to cleave the strong triple bond of dinitrogen in a stoichiometric fashion.

The rate of N₂ cleavage can be enhanced through a redox-catalyzed binding strategy reported by Peters and Cummins.^[74] Initially, N₂ coordination results in the formation of an elusive Mo–N₂ complex **[D₁₈]-92**, which subsequently undergoes one-electron reduction with Na to afford a highly reactive Mo–N₂–Na species **[D₁₈]-93**. This intermediate is subsequently trapped by an additional equivalent of the Cummins complex **[D₁₈]-1**, promoting the formation of the Mo–N₂–Mo species while regenerating elemental Na (Scheme 23). Under strictly controlled conditions, the Mo–N₂–Mo species **[D₁₈]-93** was isolated and further intercepted by electrophiles such as TMSCl or MeOTs.

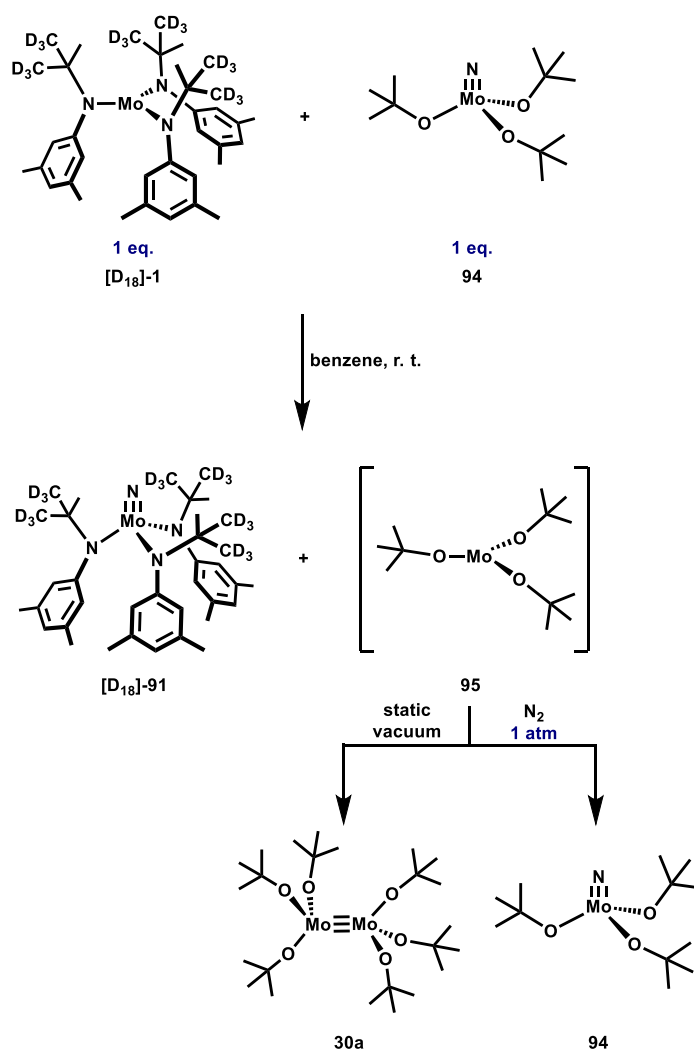
Redox-catalyzed N₂ binding



Scheme 23. Redox-catalyzed binding of N₂ facilitates N₂ cleavage by **[D₁₈]-1**.

Another strategy to enhance the rate of N₂ cleavage encompassed the utilization of the nitrido complex **94**.^[32, 75] It was demonstrated that **[D₁₈]-1** reacts efficiently with nitride **94** through a three-electron redox process (Scheme 24). During this transformation, the nitrogen atom of nitride **94** is transferred to complex **[D₁₈]-1**, generating nitride **[D₁₈]-91** along with the transient monomeric intermediate **95**. This highly reactive monomeric species can in turn bind and cleave N₂, leading to the formation of nitride **94**. Notably, when the same experiment was conducted under exclusion of N₂, the known dimer **30a** along with nitride **[D₁₈]-91** was formed. The participation of the monomeric intermediate **95** was also supported by ¹⁵N labelling studies.

Nitrogen atom transfer coupled with N₂ cleavage



Scheme 24. Nitrogen atom transfer between **[D₁₈]-1** and **94** efficiently enhances the rate of N₂ cleavage.

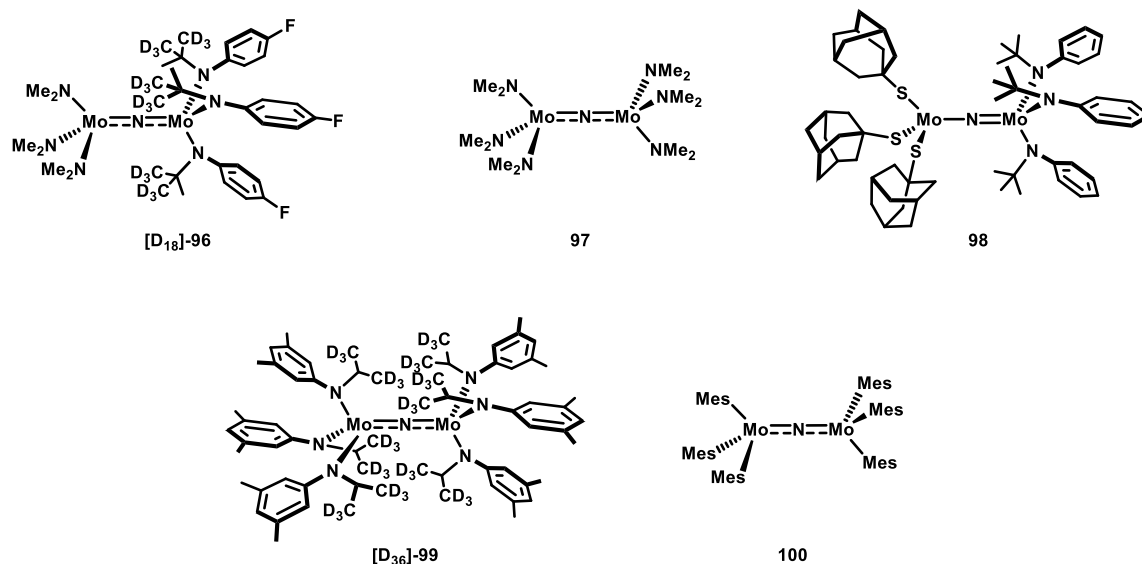
Shortly thereafter, Cummins successfully isolated several intermediates of this nitrogen atom transfer process. The first such product resulting from an incomplete nitrogen atom transfer was obtained by reaction of N≡Mo(NMe₂)₃ with a fluorinated version of the Cummins complex Mo(N(*t*Bu)(Ar^F))₃ (Ar^F = *p*-C₆H₄F), affording complex **[D₁₈]-96** in 74% yield. This complex was further characterized by X-ray diffraction and an Evans magnetic susceptibility measurement, indicating the presence of one unpaired electron (Scheme 25).^[76]

In contrast, the symmetric bridged nitride **97** was made by complete nitrogen atom transfer from $\text{N}\equiv\text{Mo}(\text{NMe}_2)_3$ to $\text{Mo}(\text{N}(t\text{Bu})(\text{Ph}))_3$, whereby the resulting elusive monomeric intermediate $\text{Mo}(\text{NMe}_2)_3$ was presumably captured by unreacted nitride $\text{N}\equiv\text{Mo}(\text{NMe}_2)_3$. The resulting bridged nitride **97** crystallized as a 1:1 co-crystal with the known dimer $\text{Mo}_2(\text{NMe}_2)_6$ (**42**).^[76]

Another intriguing example includes complex **98**, reported by Agapie and Cummins. This complex is also unsymmetrical, as manifested in the different Mo–N bond lengths. It was tentatively assigned as an $[\text{S}_3]\text{Mo}^{\text{IV}}\text{--N--Mo}^{\text{V}}[\text{N}_3]$ complex, where the Cummins fragment constitutes the more oxidized component. This situation may also be explained in view of the stronger donating amide ligands, which enhance $\text{N}_3\text{M--N}$ π -backbonding from the Cummins fragment. Subsequently, this bonding situation was supported by DFT calculations on the heavily truncated system $(\text{HS})_3\text{Mo--N--Mo}(\text{NH}_2)_3$.^[77-79]

Additional examples include complex **[D₃₆]-99** and **100**, which were obtained by N_2 cleavage from the monomer or the Mo–N₂–Mo complex, respectively. The resulting nitride then was captured by not yet reacted starting complex.^[80-81]

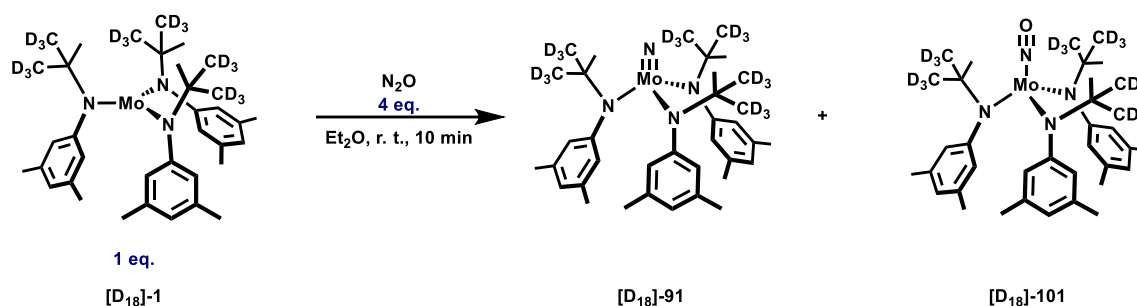
Selected examples of Mo–N–Mo complexes



Scheme 25. Overview of selected literature known Mo–N–Mo complexes.

Complex **[D₁₈]-1** also activates other small molecules, with the most prominent being N_2O . Notably, complex **[D₁₈]-1** selectively cleaves the stronger N–N bond, furnishing a 1:1 mixture of nitride **[D₁₈]-91** and nitrosyl complex **[D₁₈]-101** (Scheme 26).^[3] Kinetic experiments were conducted to investigate whether the cleavage mechanism involves a homobimetallic intermediate or proceeds *via* monometallic cleavage with concomitant release of NO.^[82] The overall cleavage reaction was found to follow first-order kinetics with respect to both, the starting Mo^{III} complex **[D₁₈]-1** and N_2O . It was determined that the formation of a Mo–N₂O adduct was the rate determining step and the generation of an elusive homobimetallic species must occur after the rate-determining step. Additional kinetic experiments for the formation of the nitrosyl complex **[D₁₈]-101** from **[D₁₈]-1** and NO as well as the utilization of $\text{Cr}(\text{NiPr}_2)_3$ (**84**) as a potential NO trapping agent in competitive binding studies further supported a homobimetallic pathway over monometallic N–N bond scission *via* NO release.

N₂O cleavage

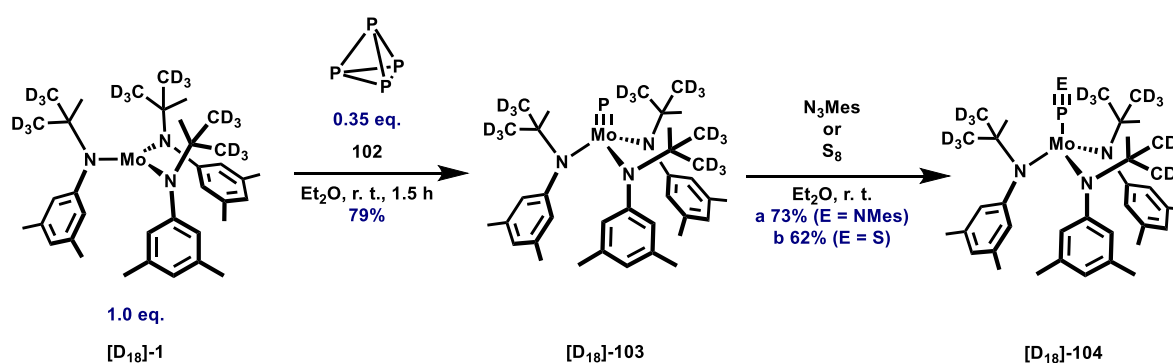


Scheme 26. Complex [D₁₈]-1 cleaves the N–N bond in N₂O selectively to furnish a 1:1 mixture of nitride [D₁₈]-91 and nitrosyl complex [D₁₈]-101.

The Cummins complex [D₁₈]-1 is also capable of cleaving the P–P bond of white phosphorus to furnish the terminal phosphido complex [D₁₈]-103 exclusively (Scheme 27). This complex is isolobal to the terminal nitride [D₁₈]-91 and represented the first example of a terminal transition-metal phosphide. Notably, this discovery coincided with Schrock's report of molybdenum and tungsten phosphides featuring trisamidoamine ligands reported in the same issue of "Angewandte Chemie".^[83-84]

Mechanistically, the fragmentation of P₄ (**102**) proceeds through a rather intricate pathway.^[85] After the initial association of P₄ to the Cummins complex [D₁₈]-1, a simple phosphorus abstraction was ruled out as the route to phosphide formation. Instead, computational investigations support a multistep process: a bimetallic intermediate first generates two equivalents of terminal phosphide complex [D₁₈]-103 alongside P₂. Subsequently, the P₂ fragment is cleaved *via* a bimetallic mechanism that is reminiscent of the bimetallic cleavage of N₂. Subsequent post-functionalization of complex [D₁₈]-103 involved reaction with mesitylazide or elemental sulfur (S₈), affording complexes [D₁₈]-104a and [D₁₈]-104b, respectively.^[84]

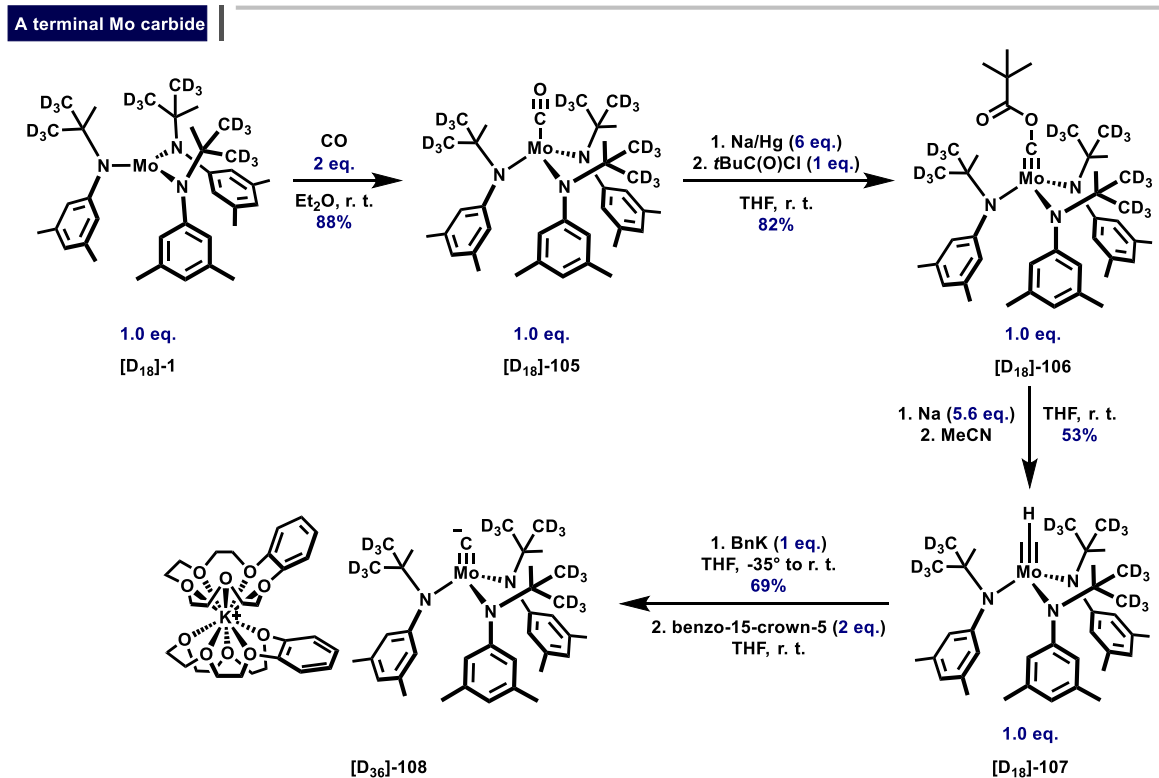
P₄ activation



Scheme 27. Activation of P₄ by [D₁₈]-1 and post-functionalization of the resulting phosphide [D₁₈]-103.

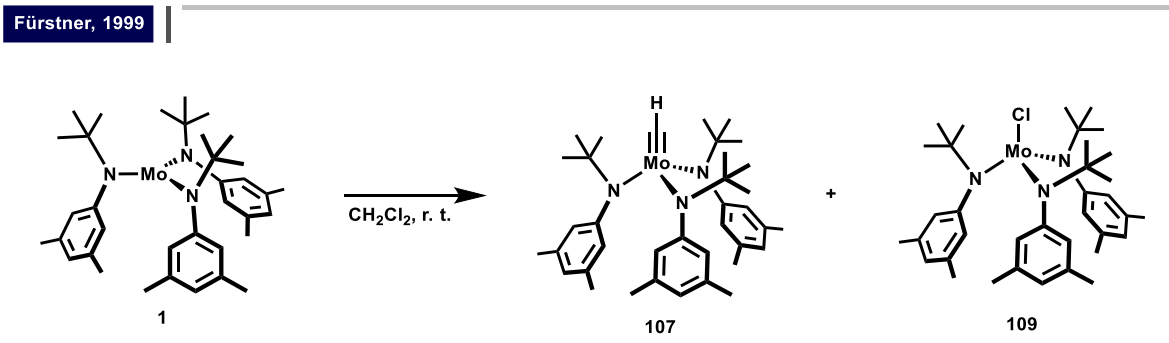
Furthermore, complex [D₁₈]-1 is known to form the CO adduct [D₁₈]-105 upon exposure to CO gas. Reduction of [D₁₈]-105 with Na/Hg, followed by trapping of the generated Mo≡C–O–Na intermediate with pivaloyl chloride, furnished carbyne [D₁₈]-106 in 82% yield. Upon treatment with Na, this complex was converted into three species: a Mo–C–O–Na complex, the methylidyne [D₁₈]-107, and a sodium carbide complex. This mixture was then treated with MeCN, causing the precipitation of complex [D₁₈]-107 in pure form. Subsequent steps involved the deprotonation of complex [D₁₈]-107 with benzyl

potassium, leading to the formation of a bridging carbide dimer, still coordinated to cationic potassium. Upon treatment of this dimer with benzo-15-crown-5, it was possible to isolate the targeted terminal Mo^{+VI} carbide **[D₁₈]-108** and analyze it by single crystal X-ray diffraction (Scheme 28).^[86]



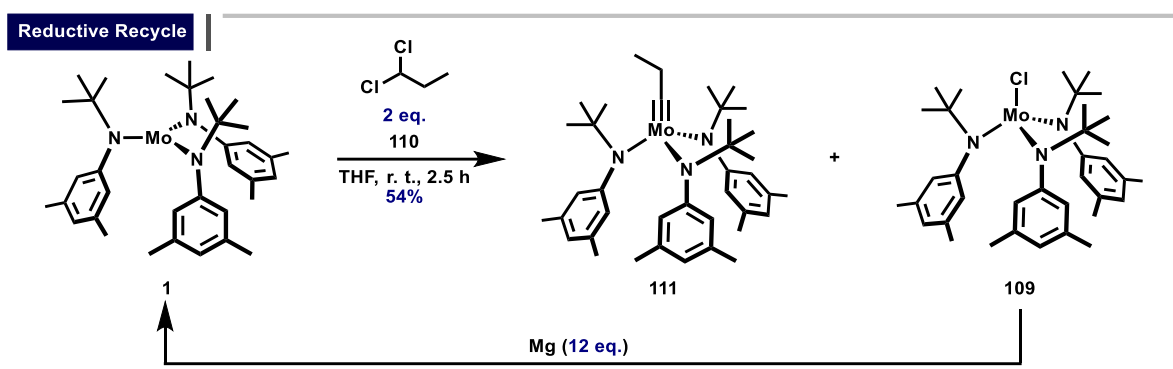
Scheme 28. Synthesis of the terminal Mo carbide **[D₁₈]-108**.

Another remarkable reactivity was unexpectedly discovered by Fürstner (Scheme 29).^[87-88] Upon dissolution of the non-deuterated Cummins complex **1** in CH₂Cl₂, a mildly exothermic reaction occurred. The reaction mixture was thoroughly analyzed by NMR spectroscopy, revealing the formation of methylidyne **107** and one (or more) paramagnetic complexes. Mass spectrometry further indicated that one of the (paramagnetic) products was the chloride complex **109**, a conclusion further confirmed by its independent synthesis from **1** and chlorine gas, as well as by single-crystal X-ray diffraction analysis. However, the most spectacular finding was the discovery that the *in situ* generated mixture of **107** and **109** serves as an efficient and functional group tolerant catalyst system for alkyne metathesis. This remarkable discovery ultimately paved the way for alkyne metathesis to become a valuable strategic asset in both natural product total synthesis and material science.^[89-91]



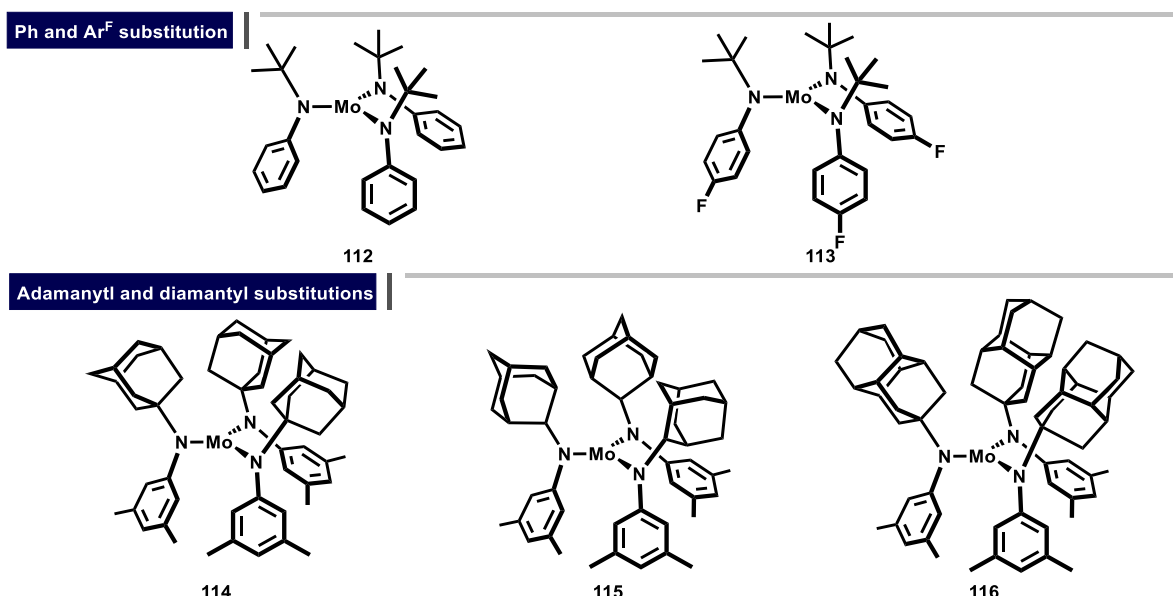
Scheme 29. Utilization of the Cummins complex **1** as a precursor to a highly effective system for alkyne metathesis.

Several years after the initial discovery, the group of Jeffrey S. Moore re-evaluated this approach and refined it by using other *gem*-substituted dihalides, such as 1,1-dichloropropane, to furnish the corresponding alkylidyne **111** and chloride complex **109** (Scheme 30). Subsequently, it was hypothesized that a reducing agent, such as magnesium, would lead to one-electron reduction of the chloride complex **109**, thus regenerating the Cummins complex **1**. The regenerated Cummins complex **1** in turn would then react again with the *gem*-dichloride, ultimately leading to an enrichment of the crude product in alkylidyne **111**. This approach is indeed very fruitful and is now known as the “reductive recycle approach”, yielding alkylidyne **111** in 54% yield.^[92-94]



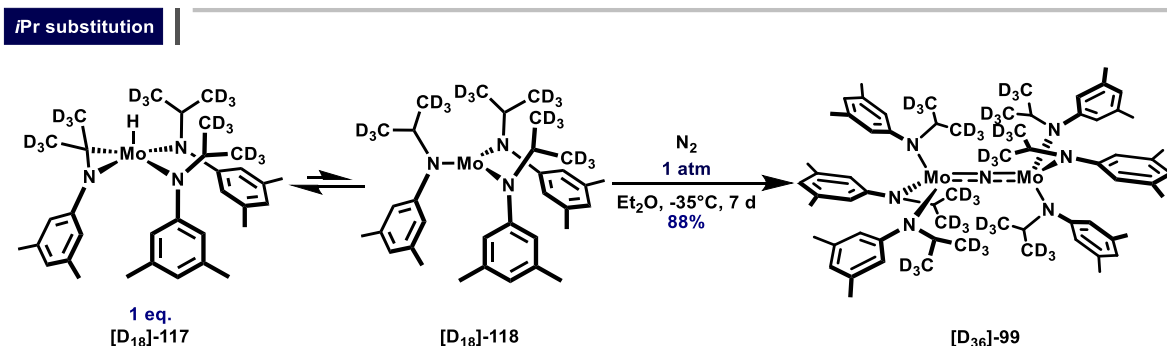
Scheme 30. Moore’s reductive recycle approach.

Beyond the prototypical Cummins complex **1**, a variety of differently substituted derivatives have been developed over the years. These monomeric siblings also rely on sterically demanding anilide ligands to prevent dimerization. The first such variation involved the substitution of the 3,5-Me₂C₆H₅ group with a Ph group.^[70] Further modifications included the introduction of fluorinated Ar substituents (Scheme 31).^[76, 87-88] Formal replacement of the *t*Bu group have also been explored. Examples involved the utilization of adamantyl-substituted ligands in place of *t*Bu.^[74, 82] Notably, both all 1- and all 2-adamantyl substitutions have been prepared. Complex **115** does coordinate N₂; the resulting adduct was trapped by reduction with Na in THF to form the Mo–N₂–Na complex. However, N₂ cleavage does not occur, as the exceedingly bulky adamantyl groups prevent the formation of the required bimetallic Mo–N₂–Mo complex on steric grounds. Even bulkier versions have been prepared based on a diamantyl substitution.^[95]



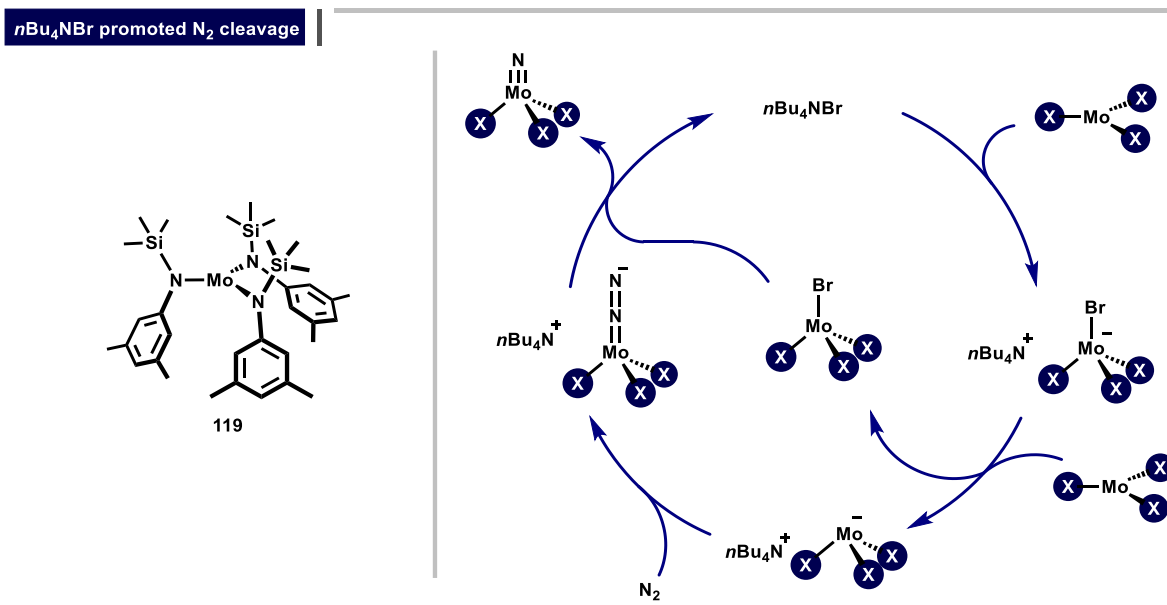
Scheme 31. Monomeric Mo^{III} complexes based on Ph and Ar^F = *p*-C₆H₄F substitution.

Replacing *t*Bu by *i*Pr, led to the formation of a cyclometalated Mo^{+V} complex [D₁₈]-117 via β C–H oxidative addition.^[80] This oxidative addition, however, is reversible, allowing the system to remain very active in N₂ cleavage through intermediacy of the monomeric complex [D₁₈]-118 formed by migratory insertion. As the product, the bridged nitride [D₃₆]-99 was formed (*vide supra*). This complex subsequently also served as the starting point for the synthesis of a Mo^{+VI} alkylidyne.^[96-97]



Scheme 32. *i*Pr substituted monomeric Mo^{+III} complexes undergo reversible β-H elimination and also cleave N₂.

Only recently, the Shi group reported the synthesis of a monomeric Mo^{+III} complex in which the *t*Bu group was replaced by a TMS group.^[98-99] However, under standard conditions, this modification did not coordinate N₂. Instead, N₂ cleavage was achieved through a catalytic disproportionation approach using catalytic *n*Bu₄NBr. In this case, complex **119** reacted with *n*Bu₄NBr, yielding a Mo^{+IV} bromide and a monoanionic Mo^{+II} species. This species exhibits a quintet state and was found to favor N₂ coordination more strongly than its Mo^{+III} precursor which has a S = 3/2 state. Once generated, this complex further reacted with the Mo^{+IV} bromide to form a Mo–N₂–Mo complex, releasing *n*Bu₄NBr. This was followed by cleavage of the strong N–N bond, ultimately yielding a Mo^{+VI} nitride species.



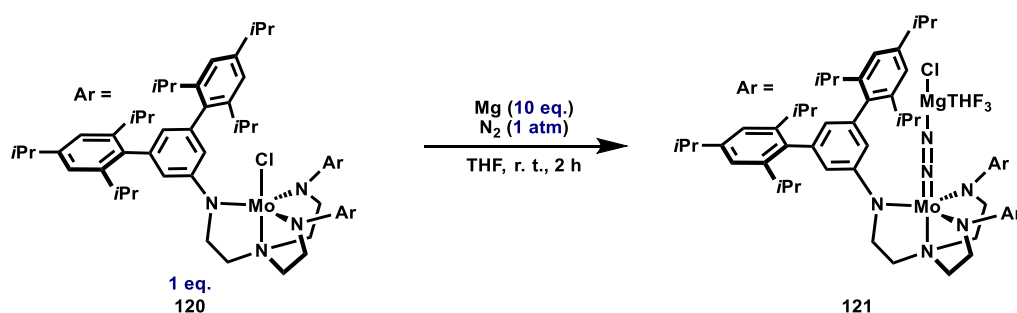
Scheme 33. Shi's disproportionation approach facilitates the N₂ cleavage by **119**.

Prompted by the outstanding reactivity profile of the Cummins complex **1**, other groups set out to stabilize monomeric Mo^{+III} complexes using various blueprints. The first such complex utilized the exceedingly bulky trisamidoamine ligand developed by the Schrock group.^[100] While numerous ligand variations have since been explored, the most prominent remains the classical HIPT

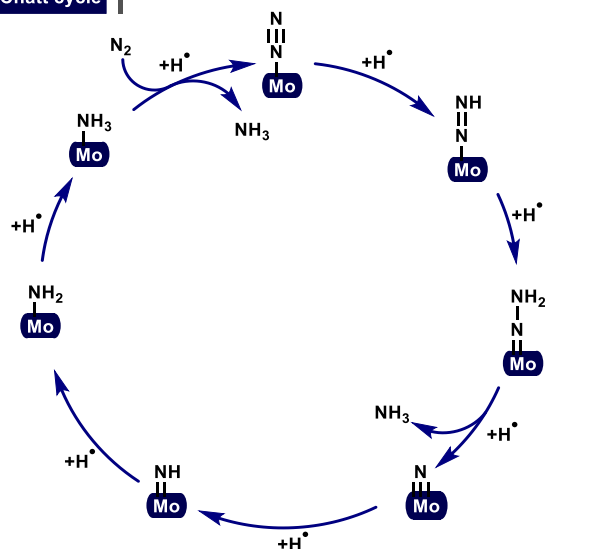
(HexaIsoPropylTerphenyl) substituted ligand, which enabled the first catalytic homogenous synthesis of ammonia from dinitrogen (Scheme 34).^[101-104]

The synthesis of the complex commenced with the reaction of a Mo^{+IV} chloride complex **120** with magnesium in THF under N₂ to afford a Mo^{+II} dinitrogen complex **121**, coordinated by a Mg(THF)₃Cl fragment. Subsequent treatment with ZnCl₂ furnished the targeted Mo^{+III} N₂ complex **122** in 80% yield over two steps. This complex was then utilized in the catalytic reduction of N₂ to NH₃ *via* PCET (Proton-coupled electron transfer) following the Chatt cycle, using Cp*₂Cr as the reductant and a lutidinium salt as the mild acid, achieving a turnover number of 4.^[101, 105-107] Notably, the use of extremely bulky ligands was a deliberate strategy, as replacing the HIPT substituent with less sterically demanding groups led to the isolation of a Mo–N₂–Mo complex, in which N₂ cleavage did not occur. This was attributed to the *trans* effect of the basal nitrogen atom, which likely inhibited N–N bond scission (Scheme 34).^[108]

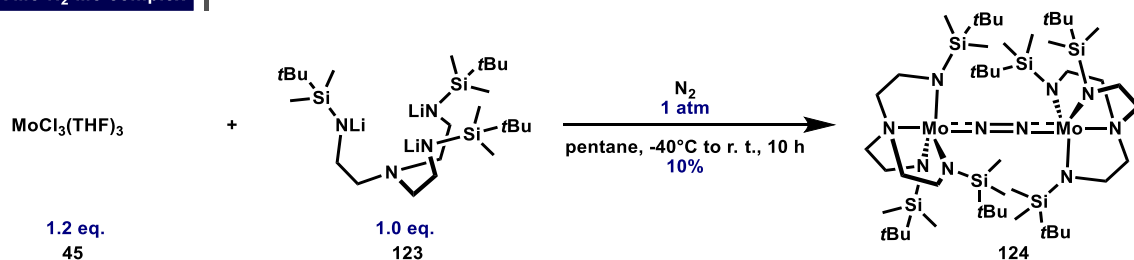
The Schrock/Yandulov system



The Chatt cycle



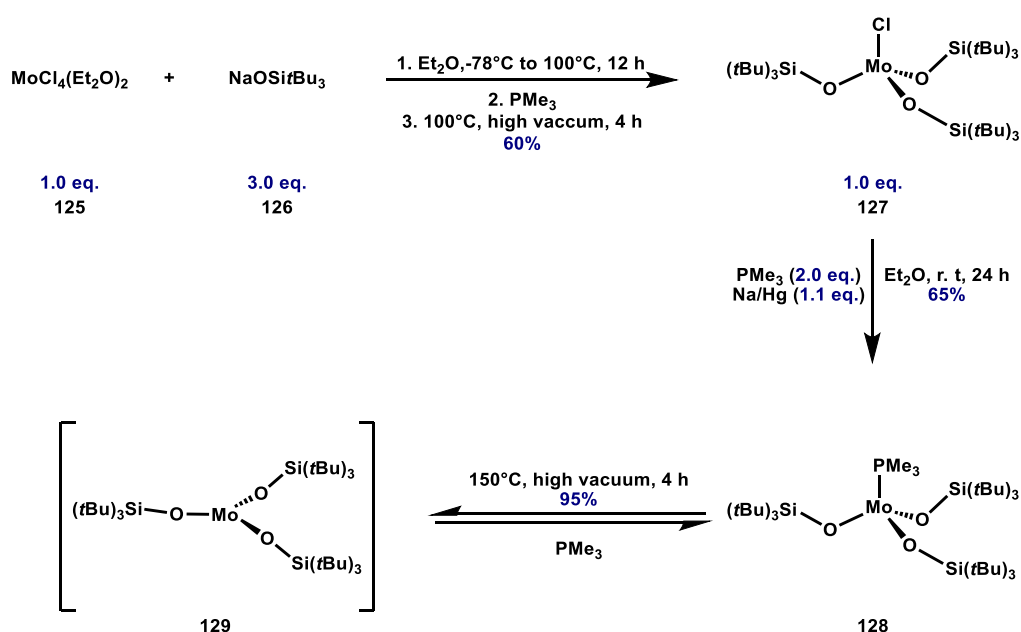
A Mo–N₂–Mo complex



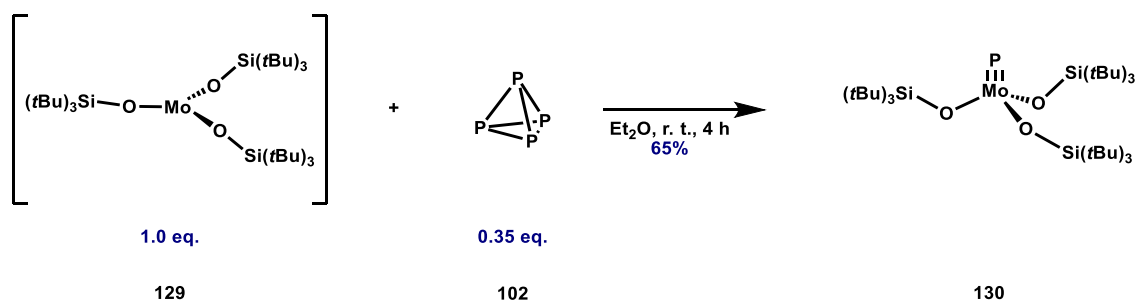
Scheme 34. Schrock's Mo^{+III} system enabled the first homogenous catalytic reduction of N₂ to NH₃.

Another (presumably) trigonal planar Mo^{+III} complex was reported by Wolczanski and co-workers.^[109-110] Complex **129** activates small molecules such as white phosphorus but fails to react with N₂. The synthesis of this complex began with the reaction of MoCl₄(Et₂O)₂ (**125**) and NaOSi^tBu₃ (**126**) in Et₂O to give the Mo^{+IV} chloride complex **127** in 60% yield. Subsequent one-electron reduction of complex **127** with Na/Hg promoted in the presence of PMe₃ furnished the PMe₃ adduct **128**. Upon heating complex **128** as a solid to 150°C under high vacuum for several hours, the (presumably) trigonal planar Mo^{+III} complex was formed in excellent yield (Scheme 35). However, an accurate structural analysis was not possible. Instead, the structure was proposed based on SQUID magnetometry data, which indicated the presence of three unpaired electrons. Furthermore reactivity studies revealed the reversible formation of a PMe₃ adduct, for which an X-ray structure was reported. Notably, the reaction of the related precursor MoCl₄(THF)₂ (**38**) with NaOSi^tBu₃ (**126**) gave a dimeric species Cl(OSi^tBu₃)₂Mo≡Mo(OSi^tBu₃)₂Cl.^[109]

The Wolczanski system



P₄ activation

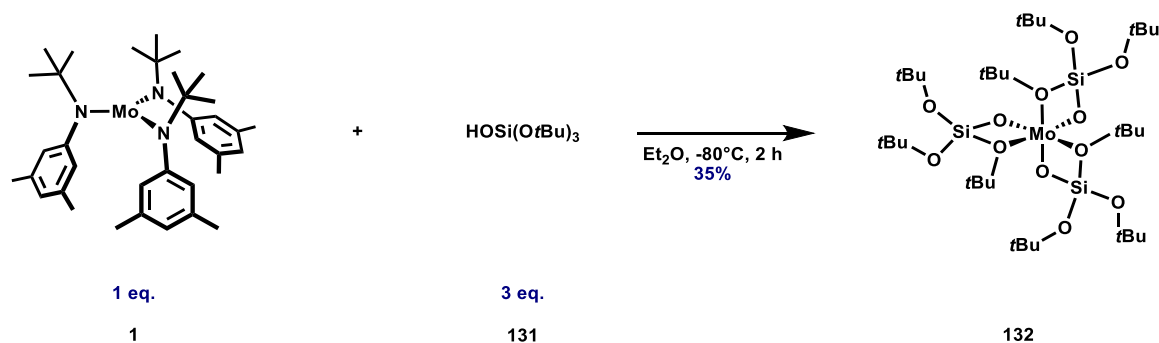


Scheme 35. The Wolczanski system is capable of cleaving P₄.

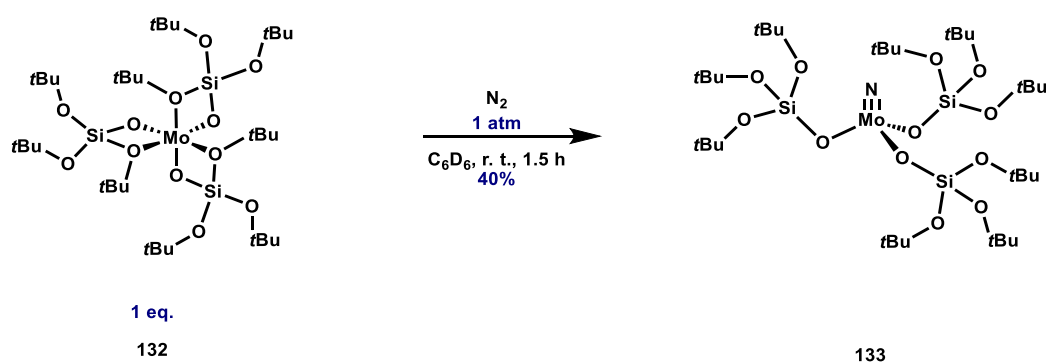
In 2019, Copéret and co-workers reported ligand exchange reactions of the Cummins complex **1** with hemilabile trisalkoxy silanolate ligands **131** to give an octahedral monomeric species **132** in 35% yield (Scheme 36).^[111] Unlike previous systems, dimerization was not prevented by steric encumbrance, but

by the κ^2 -binding of the ligands. This system proved to be extremely active for the coordination and cleavage of N_2 , resulting in immediate formation of a purple $Mo-N_2-Mo$ intermediate. Upon warming to room temperature, complete conversion to the nitrido complex **133** was observed. Beyond the cleavage of N_2 , complex **132** also activates other small molecules such as N_2O , P_4 , and CO_2 .

The Copéret system



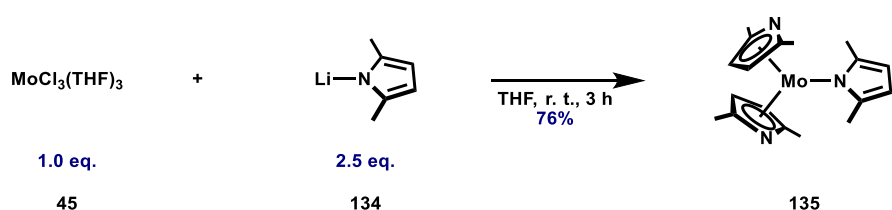
N_2 cleavage



Scheme 36. The Copéret system is capable of cleaving the strong triple bond in N_2 with remarkable efficiency.

Another monomeric complex was reported by Schrock and Wampler (Scheme 37).^[112] Originally discovered in 2008, this system was not reported to exhibit a rich small molecule activation chemistry. However, its protonation with strong acids and reduction with KC_8 were described in the same publication. The limited reactivity could potentially be attributed to the fact that the complex has 17 VE, making it nearly electronically saturated. In complex **135**, three pyrrolide ligands coordinate to the Mo^{+III} center, with one binding in η^1 and two of them in η^5 fashion. Complex **135** can be synthesized from both $MoCl_3(THF)_3$ and $MoCl_4(THF)_2$, with yields as high as 76%.

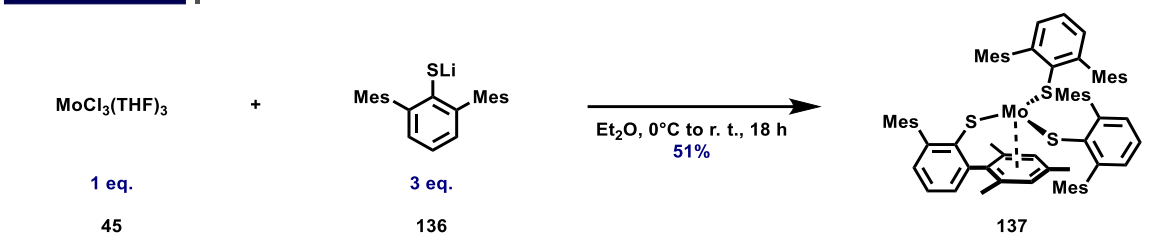
The Schrock/Wampler system



Scheme 37. Complex **135** is a 17 VE complex with pyrrolide ligands binding with different hapticities.

The final monomeric complex presented in this chapter, was reported in 1998 by Power and co-workers.^[113] This system was synthesized by the reaction of $\text{MoCl}_3(\text{THF})_3$ (**45**) with *in situ* generated lithium thiolate **136** to give the η^6 -arene complex **137** in 51% isolated yield (Scheme 38).

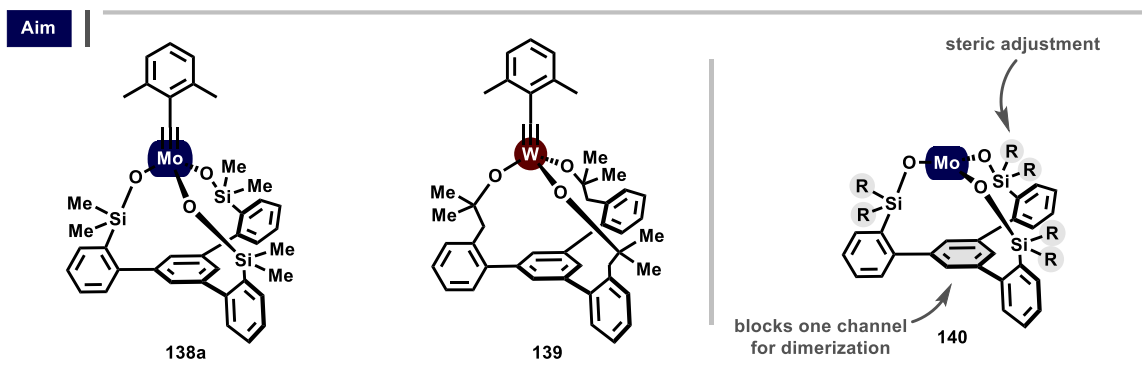
The Power system



Scheme 38. The Power system.

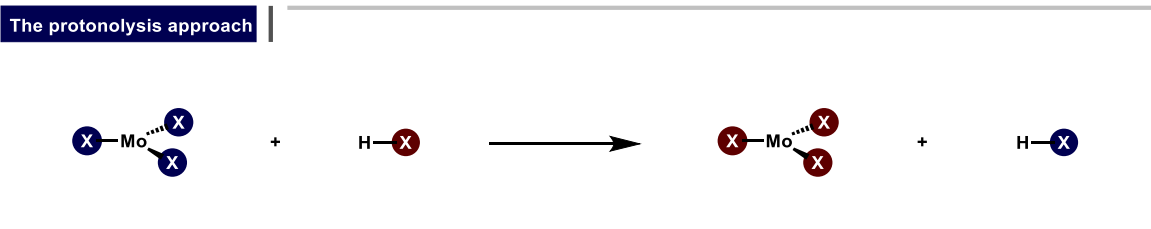
1.3 Aim

The aim of this section of the doctoral thesis was to explore tripodal silanolates and alkoxides as ligands in low-valent molybdenum chemistry. Originally designed to harness the power of highly reactive and functional group tolerant Mo^{+VI} alkylidynes for alkyne metathesis,^[21, 114-118] these ligands were envisioned to facilitate the isolation of rare and highly reactive monomeric Mo^{+III} complexes of type **140** (Scheme 39). The utilization of the ligand was strategic, as one face was already blocked by the basal phenyl ring of the tripodal ligand, and therefore systematic adjustment of the steric parameters of the R groups on the silanolate or alkoxide ligand should enable the isolation of a monomeric species. If the ligand was not sufficiently sterically demanding, the respective dimeric product was to be expected.



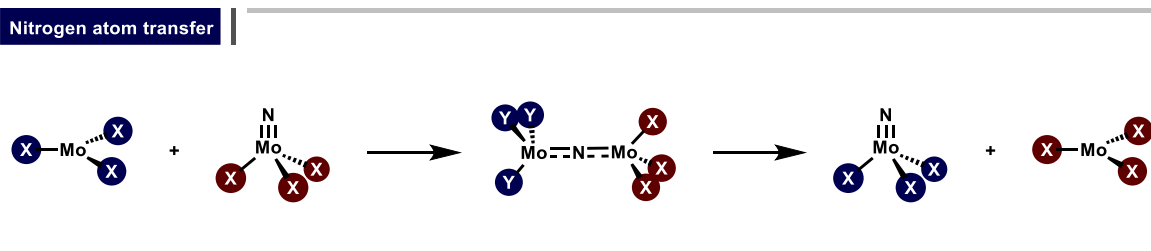
Scheme 39. Tripodal ligands were envisioned to facilitate the isolation of rare monomeric Mo^{+III} complexes.

Various strategies for the preparation of monomeric Mo^{+III} complexes were evaluated, with two primary approaches being selected. The first, a protonolysis reaction, had already been successfully employed in the synthesis of the Copéret system, a system that also features silanolate ligands (Scheme 40).^[111]



Scheme 40. A protonolysis approach as a strategy for the synthesis of a monomeric Mo^{+III} complex.

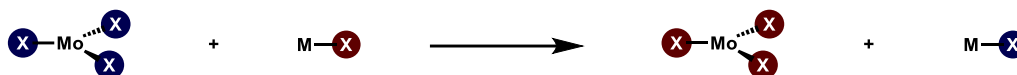
The second strategy involved a nitrogen atom transfer. Such a transfer process would require the synthesis of a previously unknown nitrido complex bearing a tripodal ligand. We regarded this strategy as potentially promising, as the more strongly donating amide ligands in the Cummins complex would lead to enhanced π -backbonding and hence facilitate the transfer from the less donating silanolate-ligated fragment (Scheme 41).^[32, 76, 78]



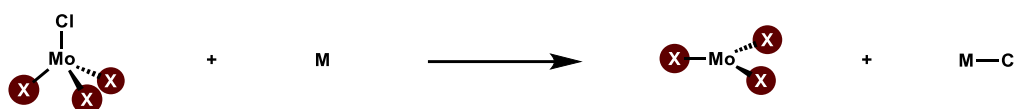
Scheme 41. Nitrogen atom transfer as a strategy for the synthesis of a monomeric Mo^{+III} complex.

Other potential strategies were also considered, which encompassed a salt metathesis reaction using a $\text{Mo}^{+\text{III}}$ halide precursor or the reduction of a $\text{Mo}^{+\text{IV}}$ chloride complex (Scheme 42).^[3, 119] However, the salt metathesis reaction posed significant limitations: as already mentioned in the introduction, salt metathesis reactions involving molybdenum complexes are highly intricate.^[19] On top of this, the tripodal nature of the ligand would arguably further complicate this approach. In contrast, the reduction strategy hinged on the availability of a $\text{Mo}^{+\text{IV}}$ chloride complex, which, like its $\text{Mo}^{+\text{III}}$ counterparts, is challenging to synthesize.

Salt metathesis



One-electron reduction

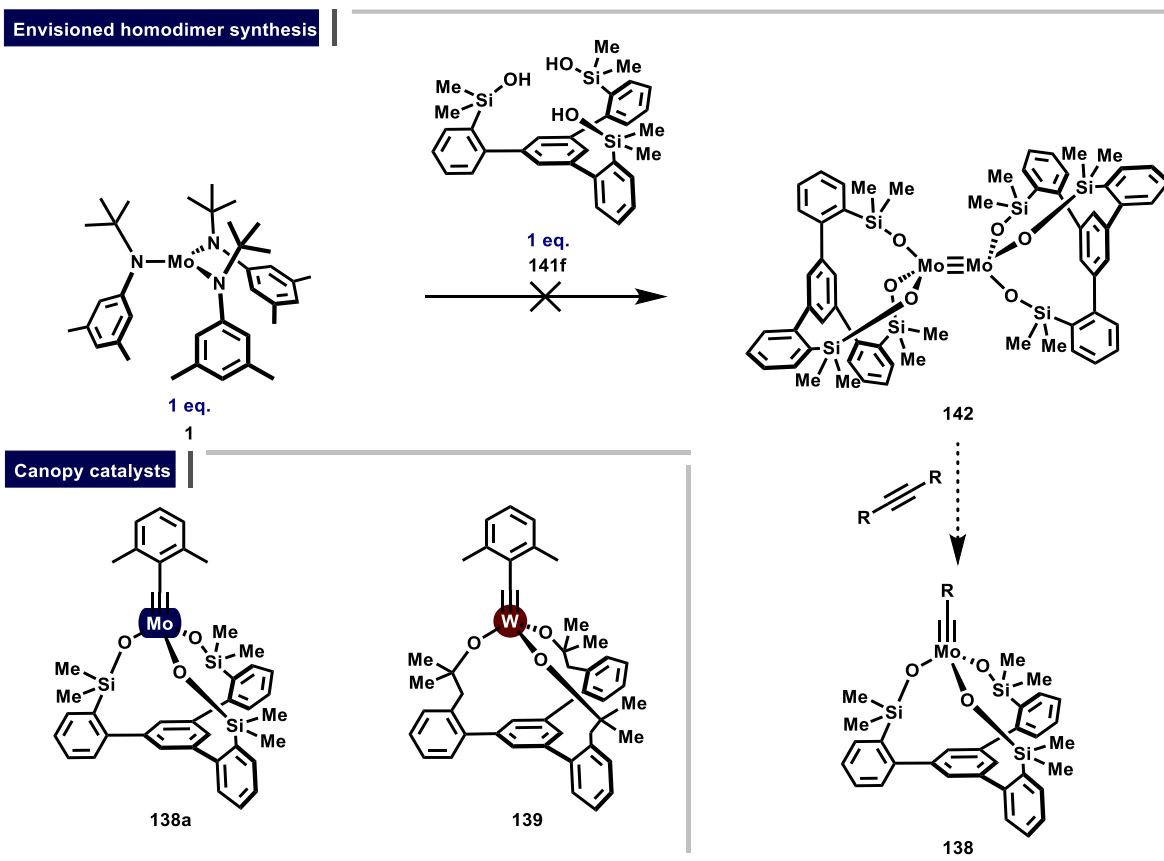


Scheme 42. Other synthetic strategies toward monomeric $\text{Mo}^{+\text{III}}$ complexes.

1.4 Results

The research in this thesis originated from work in the Fürstner group on the synthesis of alkyne metathesis catalysts; we reasoned that homodimeric Mo^{VI} complexes could serve as valuable synthetic precursors for Mo^{VI} alkyldynes through their reaction with internal or terminal alkynes. As mentioned in the introduction, such a cleavage reaction is not a widely established strategy for Mo^{VI} alkyldyne synthesis, unlike in the case of their W^{VI} congeners, where it represents the method of choice.^[1, 49-50, 56] If this cleavage reaction were feasible for molybdenum, it could significantly advance the development of even more efficient alkyne metathesis catalysts.

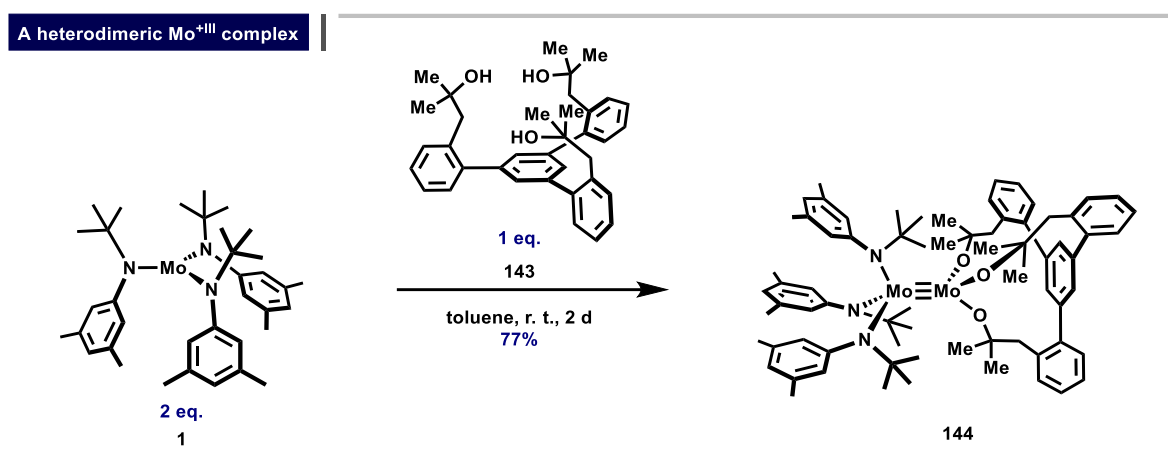
Synthetic approaches toward such homodimeric complexes initially comprised ligand exchange reactions between the respective tripodal silanols **141** or alcohols **143** and $\text{Mo}_2(\text{OtBu})_6$ (**30a**). However, this strategy turned out to be rather intricate, and no well-defined species were obtained. As a result, the monomeric Cummins complex **1** was subsequently considered as a suitable precursor for dimer formation. It was hypothesized that after initial ligand exchange, the resulting monomeric fragment would be highly reactive and, depending on the substituents R on the silanolate or alkoxide ligand, dimerization might subsequently occur. Despite these efforts, initial experimental investigations were unsuccessful (Scheme 43). For instance, when employing ligand **141f**, at the time the preferred ligand for the alkyne metathesis catalysts in our group, only ill-defined oligomeric species were obtained. In contrast, shifting our focus to tripodal alcohol **143**, which had originally been designed for the tungsten alkyldyne series, gave more satisfactory results (Scheme 43).^[120]



Scheme 43. Envisioned homodimer synthesis and Mo^{VI} and W^{VI} based canopy catalysts for alkyne metathesis.

Initial experiments consisted of reacting a 1:1 mixture of ligand **143** and complex **1**, yielding a well-defined species with a notably complex ^1H NMR spectrum. Moreover, only half of the ligand had reacted, while complex **1** was completely consumed during the reaction. HRMS analysis of the product mixture indicated that one of the products had the composition $[\text{C}_{72}\text{H}_{93}\text{Mo}_2\text{N}_3\text{O}_3]^+$. This led to an extraordinary conclusion: rather than forming the intended homodimer, a complex **144** incorporating the intact Cummins complex **1** might have formed.^[120]

To validate this finding, the stoichiometry was adjusted to a 1:2 ligand to starting complex ratio, which ultimately enabled the isolation of the product in 77% yield (Scheme 44). Utilizing a wide array of analytical tools, including X-ray diffraction and NMR spectroscopy, complex **144** was fully characterized, confirming its unique structure. Complex **144** represents the first-ever heterodimeric Mo^{III} complex of its kind and in addition it contained the intact Cummins fragment. For the first time in the long-standing history of Mo^{III} chemistry, it was demonstrated that the monomeric Cummins complex **1** can indeed engage in metal-metal triple bonding. The resulting Mo–Mo bond (2.2955(7) Å) was unusually long yet robust. The Newman projection of **144** shows that the O–Mo–Mo–N torsion angle (39.6°) is far away from the idealized staggered conformation (60°).^[120]



Scheme 44. The synthesis of a heterodimeric Mo^{III} complex **144** incorporating the intact Cummins fragment and bearing a tripodal alkoxy ligand.

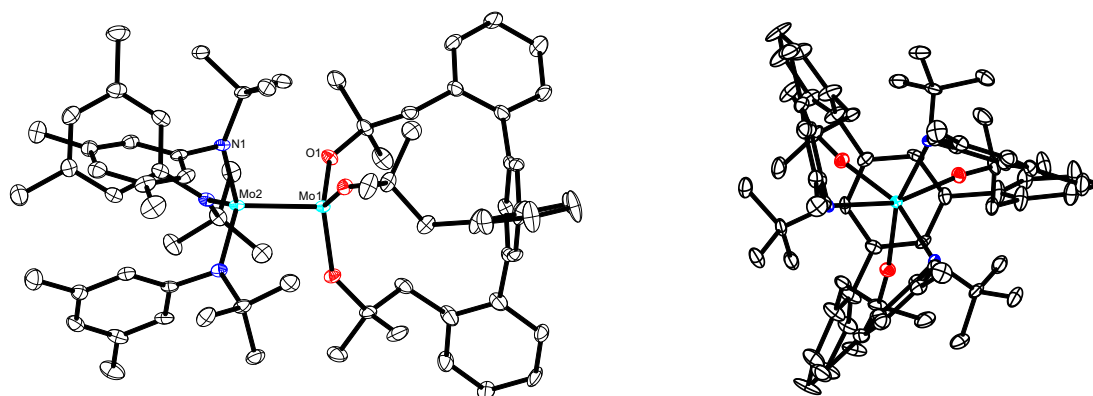
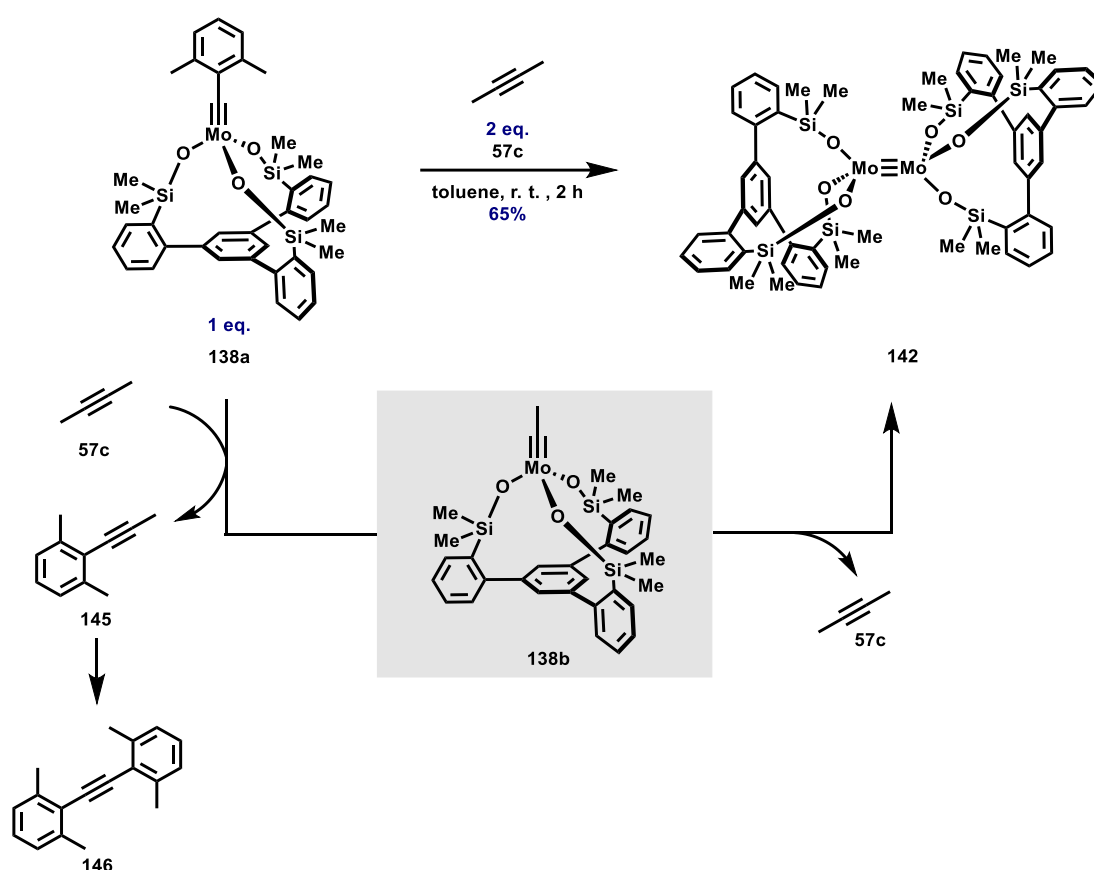


Figure 3. Single crystal structure analysis of the heterodimeric complex **144**. Left: side view. Right: projection along the threefold crystallographic Mo–Mo axis. Hydrogen atoms, disordered parts, and solvent molecules in the unit cell are not shown for clarity.

Pertinent to these results, J. Nepomuk Korber afterward set out to investigate possible decomposition pathways of the state-of-the-art alkyne metathesis catalyst system **138a**. While this system exhibited extremely high activity, its lifetime was rather short. During metathesis experiments, alkyne **146** was

observed, implying a potential decomposition pathway *via* the bimolecular coupling of two alkyldynes **138a**. To probe this hypothesis, he reacted complex **138a** with 2-butyne and successfully isolated the dimeric species **142**. Although an X-ray structure analysis was not obtained, the highly characteristic NMR spectroscopic fingerprints ($\delta_{\text{Mo}} = 2631.5$ ppm), along with the HRMS data and elemental analysis, proved the isolated species to be the homodimeric complex **142**, which is the same homodimer that was initially targeted through ligand exchange experiments. This result led to the intriguing conclusion that rather than simple Mo–Mo triple bond cleavage, the microscopic reverse constitutes the preferred pathway.^[21, 121]

Homodimer formation *via* alkyldyne coupling



Scheme 45. A homodimeric complex **142** formed *via* coupling of two alkyldyne complexes.

Synthesis Of A Heterodimeric Mo^{+III} Complex With Monodentate Ligands

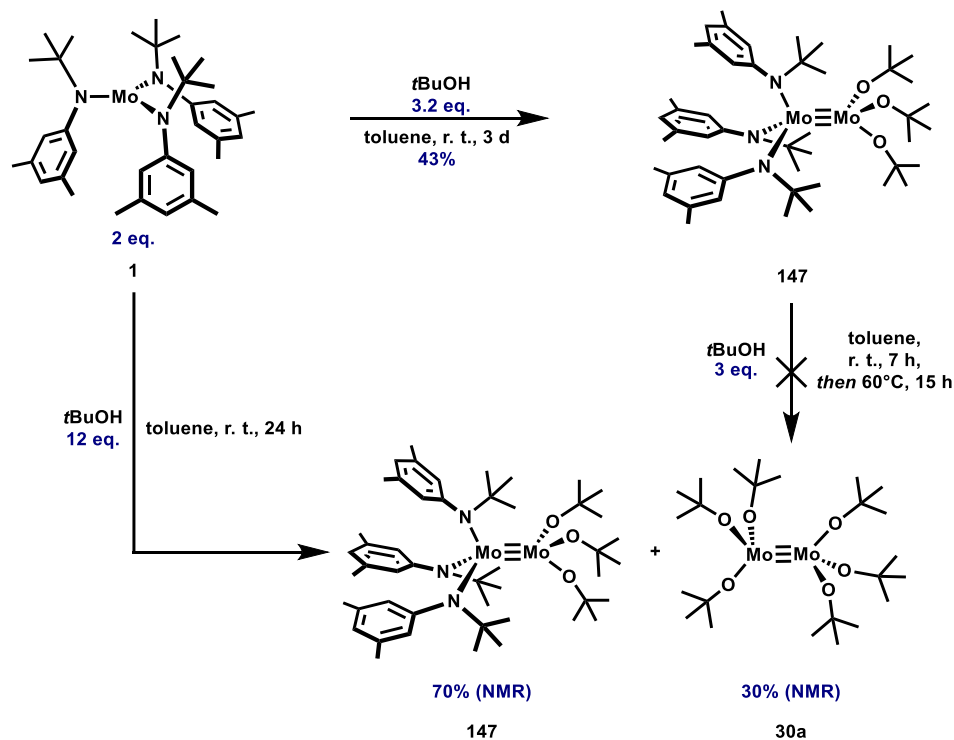
We decided to unravel the intricacies of this heterodimerization process while simultaneously designing a modified tripodal ligand that could enable the isolation of a monomeric Mo^{+III} complex. To probe whether the tripodal ligand motif was essential, the reaction of the Cummins complex **1** with monodentate alcohols was initially explored. Given that the tripodal ligand **143** essentially consists of *t*BuO⁻ subunits tethered by a tripodal ligand backbone, it was reasoned that using simple *t*BuOH as the reaction partner in a protonolysis reaction with complex **1** could yield the corresponding heterodimer. The outcome of this experiment would determine if heterodimerization was a consequence of the unique tripodal ligand framework or not. With this hypothesis in mind, a solution of **1** was mixed with *t*BuOH and left to react in toluene at room temperature for 3 d. Upon inspection of the crude NMR data, the formation of a single new product alongside a large amount of the aniline by-product was evident.

Crystallization from HMDSO afforded the desired heterodimer **147** in 43% isolated yield, with the modest yield primarily attributed to the high solubility of complex **147** in common organic solvents (Scheme 46).

With a considerable amount of purified heterodimer **147** in hand, an attempt was made to convert it into the known homodimer **30a** using *t*BuOH. Surprisingly, even after a prolonged reaction time at room temperature, no conversion to the homodimer took place. Raising the temperature to 60°C did not lead to any improvement. This was a striking result, as one of Chisholm's original protocols for the preparation of $(t\text{BuO})_3\text{Mo}\equiv\text{Mo}(\text{OtBu})_3$ (**30a**) relied on the protonolysis of $(\text{Me}_2\text{N})_3\text{Mo}\equiv\text{Mo}(\text{NMe}_2)_3$ (**42**) with *t*BuOH (*vide supra*).^[30] The inability to form the known homodimer *via* protonolysis from either **1** or **147** hinted at a deeper mechanistic puzzle. It appeared that once protonolysis of **1** with *t*BuOH occurs, the resulting monomeric fragment $(t\text{BuO})_n((t\text{Bu})(\text{Ar}))\text{N}_m\text{Mo}$, $n+m = 3$) is so reactive that it immediately traps any remaining Cummins complex **1** to form the heterodimeric species **147**. Notably, the monomeric and elusive species $\text{Mo}(\text{OtBu})_3$ (**95**) had previously been proposed to form through nitrogen atom transfer, as explained in the Introduction.^[32] Once generated, the heterodimeric species **147** exhibits exceptionally high kinetic stability toward further substitution by *t*BuOH, thereby impeding the formation of the thermodynamic product, the homodimer **30a**.

Equally revealing was an experiment in which an excess of *t*BuOH was reacted with the Cummins complex **1**, leading to a mixture of products in which complex **147** constituted the major and homodimer **30a** the minor component. This result strongly suggests a kinetic preference for heterodimer formation, with the experiments collectively indicating that the protonolysis reaction is rate determining, followed by a rapid heterodimerization step.

Heterodimerization with *t*BuOH



Scheme 46. Protonolysis of **1** with *t*BuOH favors heterodimerization over homodimerization.

The structure of heterodimer **147** was fully assigned by NMR spectroscopy. Key were ROESY cross peaks between the H-2↔H-4 protons of the *Ot*Bu and *Nt*BuAr moieties, confirming that both ligand spheres belong to the same C₃-symmetrical molecule. At room temperature, the N–Ar signals were broadened, indicating an increased rotational barrier. Upon cooling, these signals sharpened, allowing for a more accurate characterization of the compound at 233 K. The coalescence temperature for the H-6↔H-6' exchange was observed around 333 K, allowing an estimate of the N–Ar rotational barrier to be in the order of $\Delta G^{\ddagger}_{TC} \approx 12.5$ kcal/mol (Figure 4).

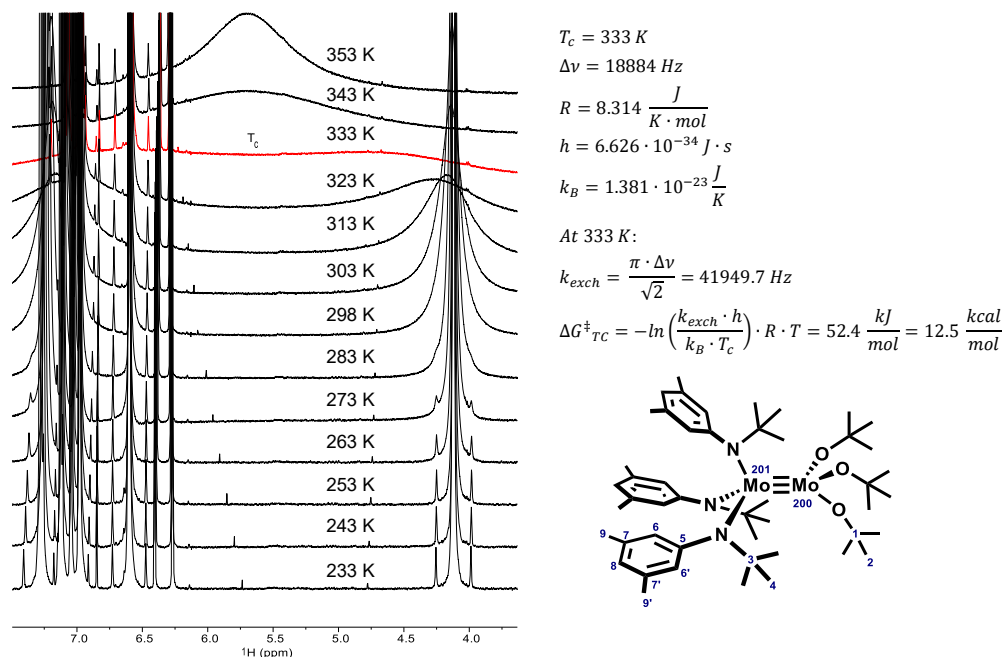


Figure 4. ¹H NMR spectra of complex **147**: [D₈]-toluene, 233 K–353 K, 600 MHz. Coalescence temperature of the H-6/H-6' exchange and estimation of the rotational barrier about the N–Ar bond.

Remarkably, the aromatic proton H-6 is highly shielded, resonating at $\delta_{\text{H}} = 4.12$ ppm. This dramatic shift can be attributed to the anisotropic ring current effect, where the Ar moiety of a neighboring anilide ligand influences proton H-6. This interpretation aligns very well with observations made in the crystal structure of **147**, in which H-6 (highlighted in yellow with the crystallographic numbers H2, H14 and H26) is positioned directly above the plane of the aryl ring (Figure 5).

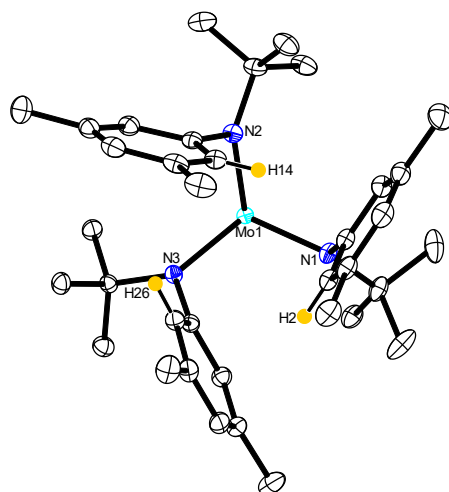


Figure 5. Single crystal structure analysis of the heterodimeric complex **147**; view along the Mo–Mo axis; the Mo(*Ot*Bu)₃ fragment is not shown for clarity, H-atoms (apart from H2, H14, and H26) and solvent molecules in the unit cell are not shown for clarity.

Interestingly, the Mo–Mo bond length (2.2944(2) Å) is nearly identical to that of its tripodal counterpart **144** (2.2955(7) Å). This suggests that the elongation of the Mo–Mo bond does likely not originate from the peculiar tripodal ligand framework but rather arises from steric repulsion between the alkoxide ligands and the highly sterically demanding anilide ligands of the Cummins fragment (Figure 6).

Notably, the O–Mo–Mo–N torsion angles (32.57°, 33.35°, 34.72°) deviate significantly from the ideal 60° staggered “ethane-like” conformation. This distortion is even more pronounced compared to the O–Mo–Mo–N torsion angle (39.59°) of its tripodal analogue **144**.

The coordination geometry around the oxygen-ligated molybdenum atom falls between trigonal-pyramidal and tetrahedral, as indicated by the average Mo1–Mo2–O bond angle (100.3°). In contrast, the nitrogen ligated Mo atom more closely resembles a tetrahedron than a trigonal pyramid, as seen in the average Mo2–Mo1–N bond angle (106.1°). This divergence may result from steric clashes between the N-*t*Bu and *Ot*Bu groups, as well as efficient packing of the N–Ar groups.

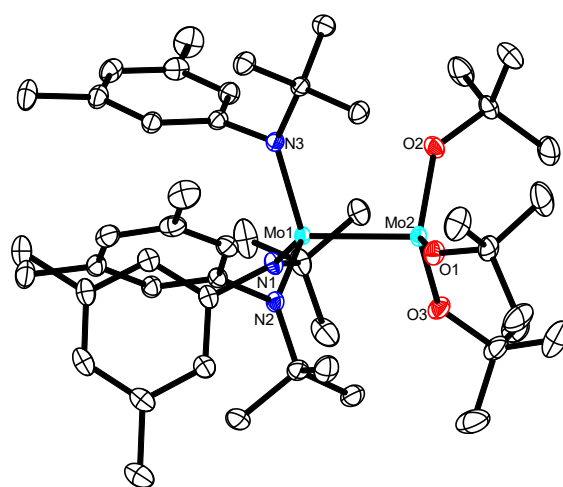


Figure 6. Single crystal structure analysis of the heterodimeric complex **144**. H-atoms and solvent molecules in the unit cell are omitted for clarity.

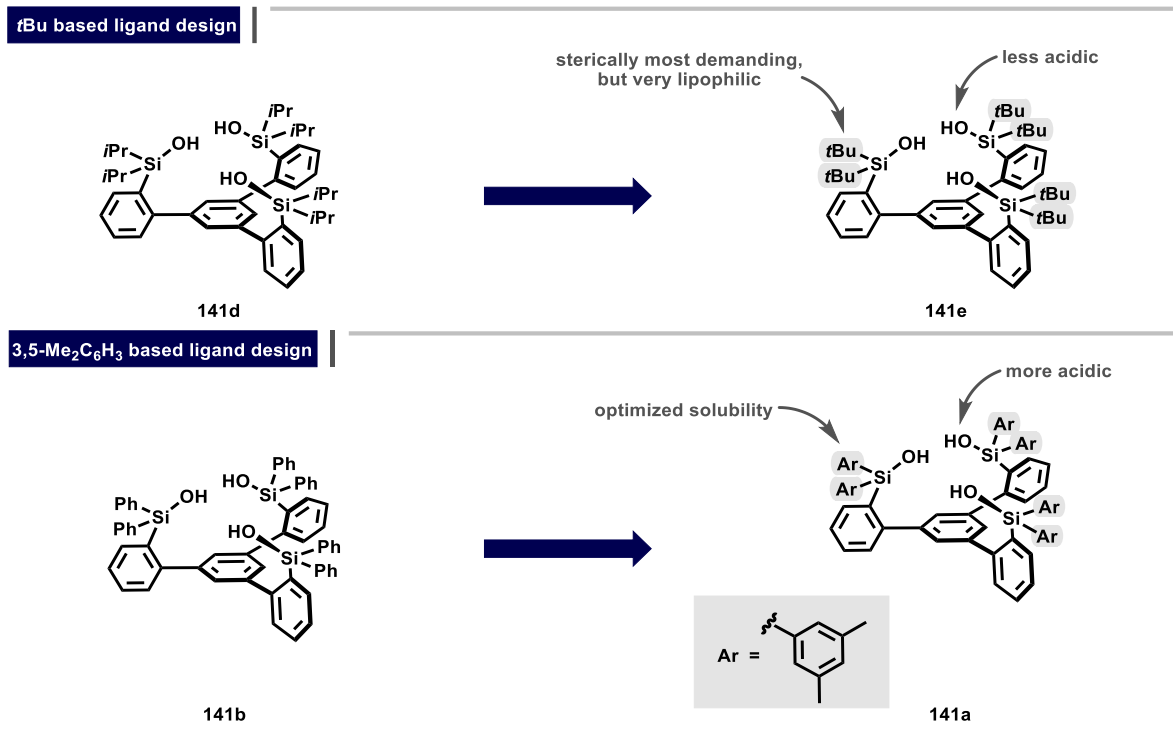
Design of a Sterically Demanding Silanolate Ligand Leading to the Isolation of a Complete Mo^{+III} Family

Next, we aimed to design a ligand that could enable the isolation of a corresponding monomeric Mo^{+III} complex. As stated previously, this ligand needed to be sterically highly demanding to prevent dimerization. Our ligand design encompassed two different strategies (Scheme 47).

The first strategy was to install *t*Bu groups on the silicon atoms. Previous attempts in our group at synthesizing ligand **141e** had failed, so devising a novel approach would be necessary. A related ligand was compound **141d**, bearing *i*Pr groups on the silicon atom, which was at that point the bulkiest ligand of this type reported by our group. Yet, both of these ligands are alkyl substituted silanols, hence they are somewhat less acidic; a potential ligand exchange *via* protonolysis would be slow and challenging. Moreover, the resulting product would likely be highly lipophilic and overly soluble in common organic solvents, complicating purification and separation from the aniline by-product.

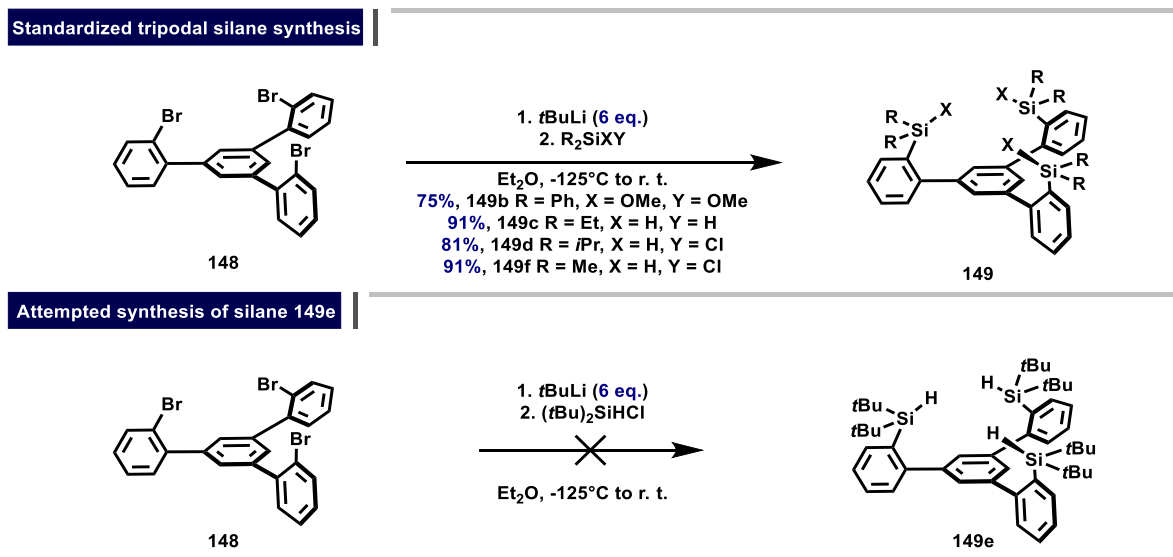
A solution to this problem encompassed the utilization of aryl substituted silanols. Such silanols exhibit a significantly enhanced acidity and a reduced lipophilicity. While the compounds bearing the Ph-substituted ligand **141b** had previously been shown to form aggregates in solution and were extremely challenging to solubilize, we envisioned that the use of 3,5-Me₂C₆H₃ groups would not only prevent

aggregation, but also slightly enhance solubility.^[114] Additionally, the more encumbered 3,5-Me₂C₆H₃-groups were expected to inhibit dimerization more effectively than standard Ph rings.



Scheme 47. Envisioned ligand design strategies.

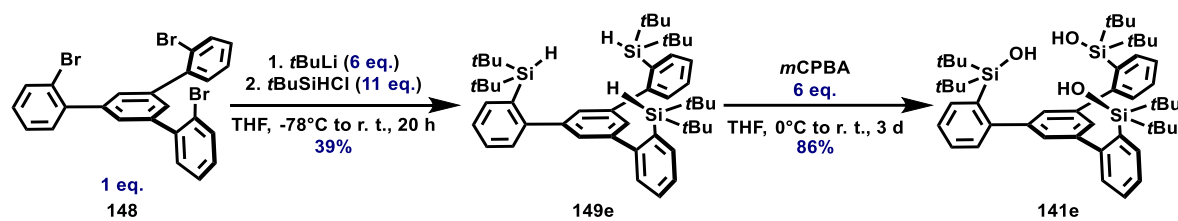
The standard protocol for the synthesis of the tripodal silanol ligands featured a two-step procedure: the initial synthesis of the respective silane or methoxysilane **149** (X = H, OMe), followed by oxidation (for silanes) or hydrolysis (for methoxysilanes).^[114-116] The silane/methoxysilane synthesis commenced with lithium/halogen exchange of **148** with *t*BuLi in Et₂O at -125°C, followed by subsequent reaction of the triorganolithium intermediate with a chlorosilane or a dimethoxysilane to afford the corresponding products **149** in up to 91% yield (Scheme 48). However, this protocol proved ineffective for the synthesis of silane **149e**. Under these conditions, the *in situ* generated organolithium species exhibited no reactivity toward (tBu)₂SiHCl in Et₂O, failing to produce the desired silane **149e**.



Scheme 48. Top: Literature protocol for the synthesis of the tripodal silanes **149**. Bottom: Failed attempt to synthesize silane **149e**.

A brief review of the literature suggested that simply switching the solvent from Et₂O to THF could be sufficient to achieve the desired reaction.^[122] Indeed, this proved to be correct, enabling the isolation of silane **149e** in 39% yield (Scheme 49). The low yield was due to the formation of substantial amounts of unidentified side products. Subsequent oxidation with *m*CPBA in THF furnished the targeted silanol **141e** in 86% yield.

Synthesis of silanol **141e**



Scheme 49. Synthesis of the sterically demanding silanol **141e**.

NMR analysis confirmed that silane **149e** adopts a C_3 -symmetric conformation, a finding further supported by single crystal X-ray diffraction analysis of a crystal grown *via* slow evaporation of a solution in *n*-pentane (Figure 7).

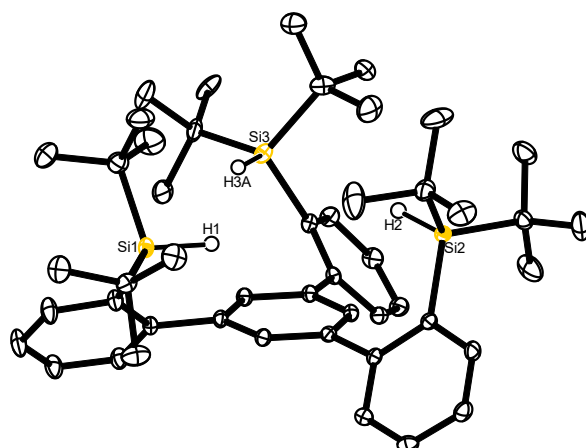
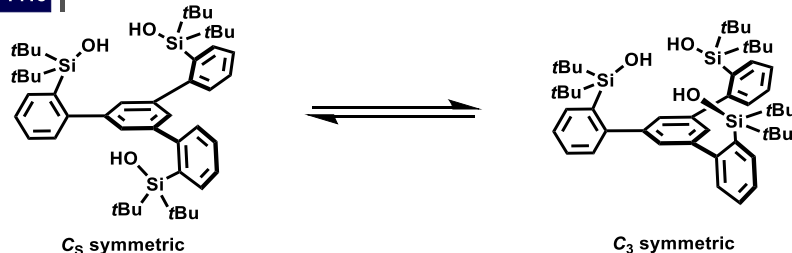


Figure 7. Single crystal structure of **149e**. H-atoms (except the ones of the Si–H groups), minor disordered parts, and solvent molecules in the unit cell are not shown for clarity.

In contrast to silane **149e**, the derived silanol **141e** exhibited a broad ¹H NMR spectrum at 298 K, indicative of rapid exchange between two rotamers (Scheme 50 and Figure 8). Upon cooling, these signals sharpened to two sets of signals, revealing a dynamic equilibrium between a mixture of C_3 - and a major C_s -symmetric species. However, heating the solution of **141e** to 353 K led to averaging of the two rotamers on the NMR timescale, consistent with the NMR spectrum of a C_3 -symmetric species.

Rotamers of silanol **141e**



Scheme 50. Dynamic equilibrium between the C_s - and C_3 -symmetric rotamers.

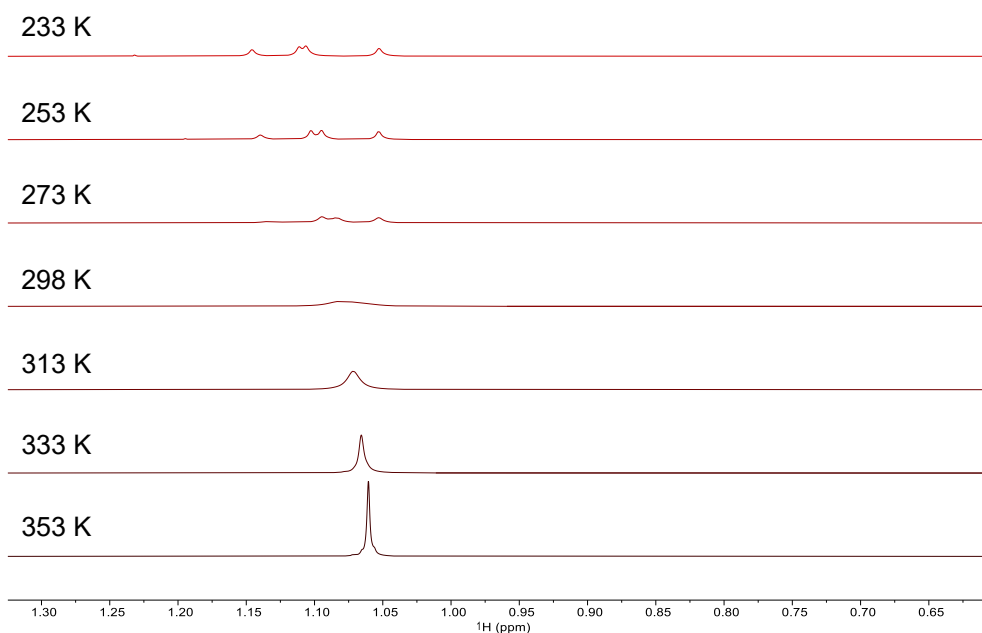


Figure 8. VT NMR experiment of ligand **141e**: [D₈]-toluene, 233 K–353 K, 600 MHz.

Single crystal structure analysis of a crystal grown from a saturated HMDSO solution of **141e** at -20°C confirmed the presence of the C_s -symmetric rotamer in the solid state (Figure 9). Notably, one molecule of water was encapsulated by the tripodal silanol **141e** through hydrogen bonding, which could be removed by storing a solution of silanol **141e** over activated molecular sieves.

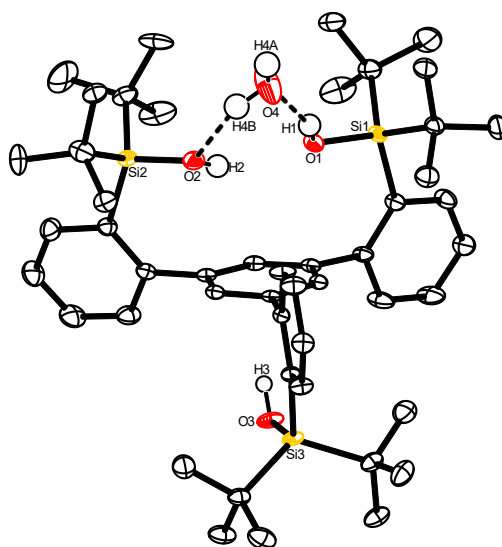
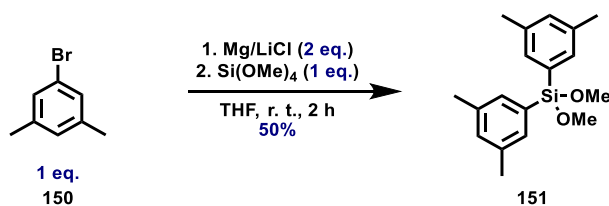


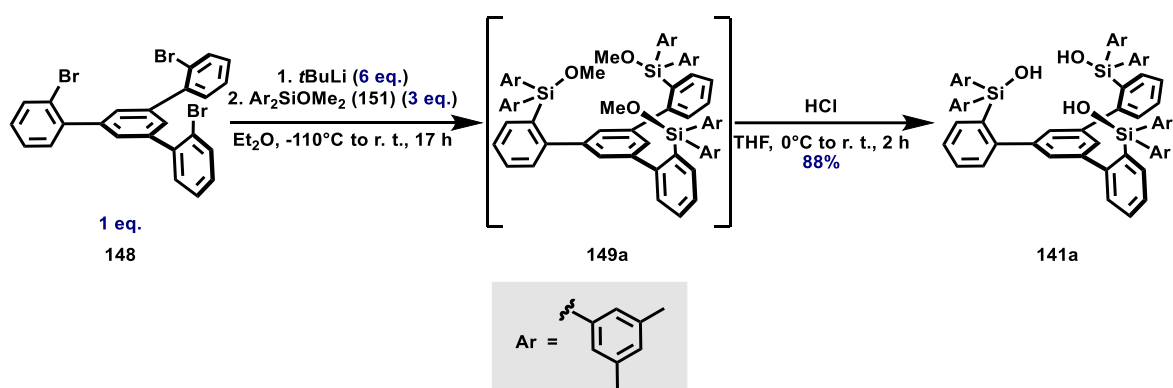
Figure 9. Single crystal structure of **141e**. H-atoms (except the ones of the Si–OH groups), disordered parts, and solvent molecules in the unit cell are not shown for clarity.

The synthesis of the other targeted ligand **141a** began with the reaction of $\text{Si}(\text{OMe})_4$ and an *in situ* generated Grignard reagent to give dimethoxysilane **151** in 50% yield after distillation. Subsequent reactions transformed this dimethoxysilane **151** into methoxysilane **149a** via the standardized lithium/halogen exchange protocol. The resulting methoxysilane **149a** was not isolated but was directly hydrolyzed with concentrated HCl in THF to afford the desired silanol **141a** in 88% yield over two steps. This silanol, according to NMR spectroscopy, exhibits a typical C_3 -symmetric conformation in solution at 298 K.

Synthesis of dimethoxysilane 151



Synthesis of silanol 141a



Scheme 51. Synthesis of silanol **141a** bearing 3,5-Me₂C₆H₃ groups.

Thus, the stage was set to test our hypothesis and attempt the anticipated protonolysis between each of the two new ligands and the Cummins complex **1**. While ligand **141e** showed no reactivity, even at elevated temperatures, the reaction of the more acidic and slightly less sterically encumbered ligand **141a** with the Cummins complex **1** proceeded remarkably fast. Small-scale experiments with a 1:1 mixture of ligand **141a** and complex **1** in THF, a solvent in which ligand **141a** displayed superior solubility, indicated complete consumption of both starting materials within a few minutes.

Nevertheless, no well-defined product was observed. Instead, ¹H NMR spectroscopy revealed only a broad and featureless spectrum, suggesting the formation of a highly dynamic species. Moreover, the paramagnetic nature of the envisaged monomeric Mo^{+III} species would inherently complicate its characterization *via* NMR spectroscopy. However, when the reaction was repeated on a significantly larger scale, the isolation of a well-defined species became possible. Upon concentration of the reaction mixture *in vacuo*, an orange crystalline product began to precipitate. The supernatant was filtered off and stored in the freezer at -20°C to give a second crop of product.

A single-crystal X-ray diffraction experiment confirmed its identity as a monomeric, octahedral Mo^{+III} complex **2·3THF**, where the Mo^{+III} center is ligated by a tripodal silanolate and three THF ligands. Unfortunately, obtaining other analytical data and a yield for compound **2·3THF** was not possible, as all attempts to dry the complex *in vacuo* led to decomposition, indicated by a color change from orange to dark red.

The only arguably comparable species is the Copéret system **132**, which also adopts the *fac* isomeric form. Furthermore, the crystal structure of **2·3THF** unambiguously proves that the molybdenum atom does not interact with the basal phenyl ring of the tripodal ligand, as indicated by the 4.08 Å separation between the Mo atom and the basal phenyl plane (Figure 10).

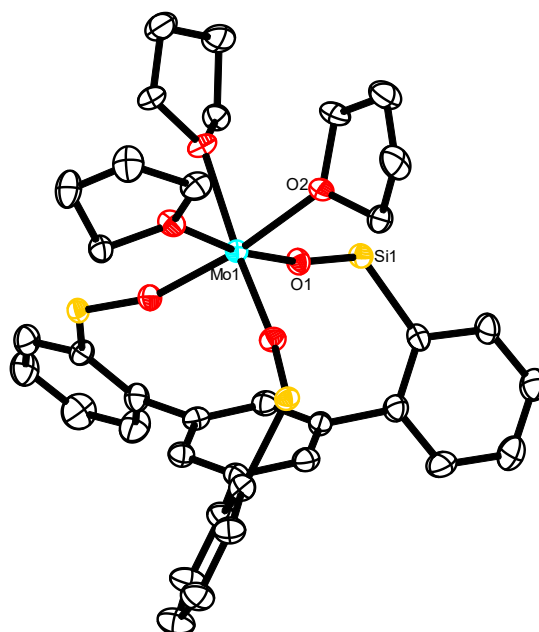
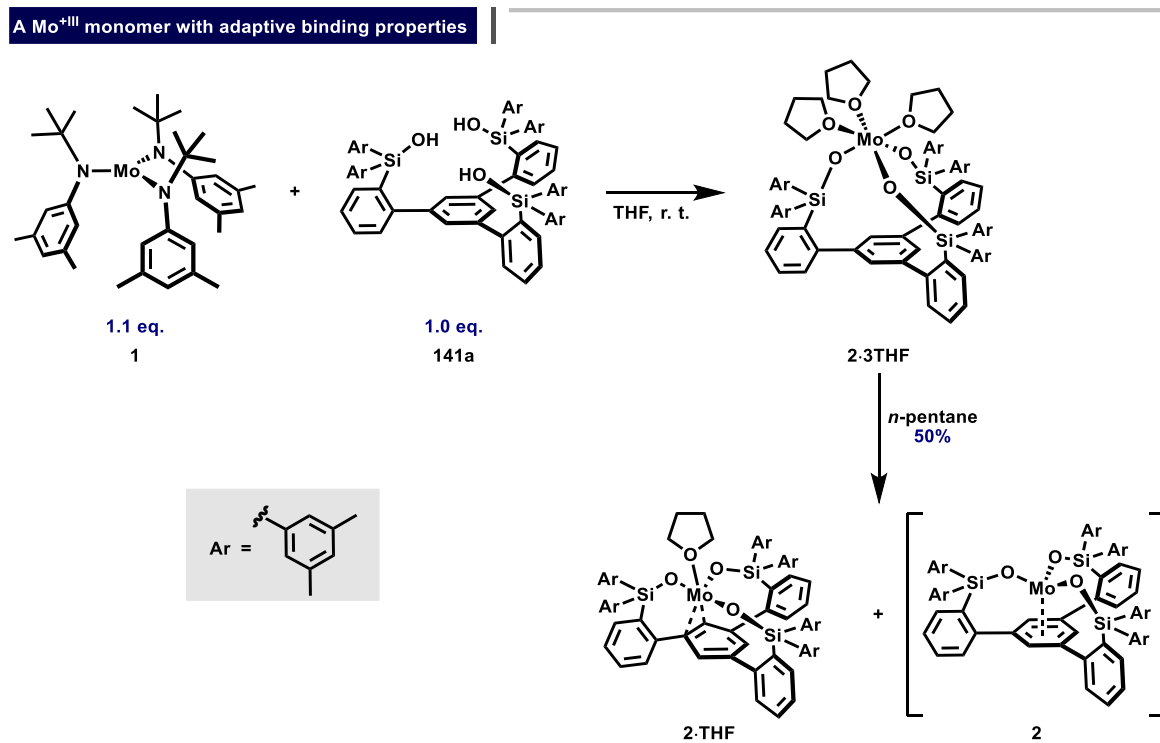


Figure 10. Truncated crystal structure of complex **2·3THF**. The 3,5-Me₂C₆H₃ groups and H-atoms are not shown for clarity.

Similarly, washing of **2·3THF** with *n*-pentane resulted in the formation of a deep red solution, from which dark red crystals formed over time, leaving behind an almost colorless supernatant. The crystals were dried *in vacuo* at room temperature to give complex **2·THF** in 50% yield. A sample obtained in this manner was suitable for elemental analysis, which was apparently consistent with the mono-THF adduct (Scheme 52).



Scheme 52. Monomeric Mo^{+III} complexes with a tripodal silanolate ligand feature adaptive binding properties.

Strikingly, the X-ray structure analysis revealed a far more complex composition, rendering the structural determination highly challenging. Although the crystals were relatively large and optically suitable, their diffraction pattern was of only medium quality. This limitation could be attributed to

multiple disorders that became evident during the refinement process. Our structural model suggested a multi-component crystal consisting of three distinct chemical species. The predominant species, accounting for an occupancy of approximately 90%, was identified as the mono-THF adduct **2**·THF which binds in a η^2 fashion to the basal phenyl ring. The second species identified with certainty was the THF-free complex **2**, which binds in a η^6 fashion to the basal phenyl ring, exhibiting an occupancy of $\approx 3\%$. Due to the low occupancy of **2**, it was not possible to localize the atomic positions with high accuracy. Notably, 9 different crystals from various batches were investigated by single-crystal X-ray diffraction at different temperatures (between 100 and 253 K); in all cases complex **2**·THF represented the major species. In order to shed light on the individual components, the structure obtained from the X-ray diffraction experiment was optimized using DFT. A superposition of the experimental and calculated structure of **2** shows a good agreement; together with the distance of the Mo atom to the basal phenyl ring (1.726 Å), it is reasonable to assign it as a η^6 arene complex (Figure 11). However, a third component, which is also present, could not be modeled accurately, although the assignment as a bis-THF species appears plausible.

Comparison of the structures **2**·3THF, **2**·THF, and **2** reveals another remarkable feature: Usually known to support tetrahedral to trigonal pyramidal coordination spheres, this tripodal ligand showcases sufficient flexibility and adaptability to support varying coordination spheres, oxidation states, and binding modes and therefore can adopt for the needs of a given central metal. This is evident from the varying positions of the central metal in the three crystal structures: in **2**·3THF the Mo atom is located 1.05 Å above the plane defined by the oxygen atoms of the silanol ligand, in **2**·THF it is approximately located in this plane, and in **2** it is located below this plane.

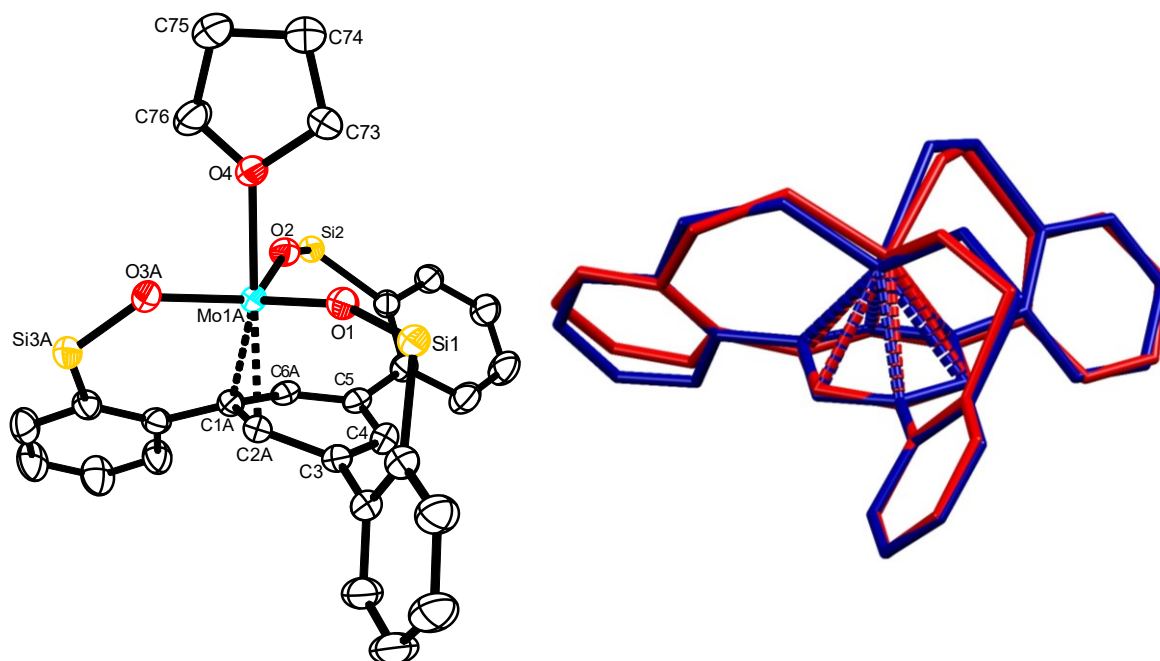


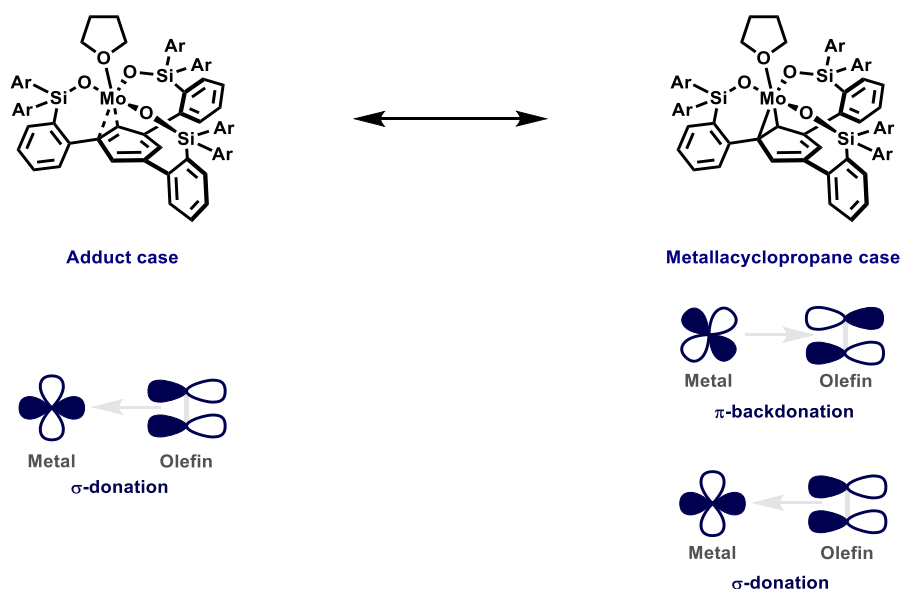
Figure 11. Left: Truncated crystal structure of **2**·THF. Right: Superposition of the truncated experimental (blue) and calculated (red) structure of **2** in the solid state. The 3,5-Me₂C₆H₃ groups and H-atoms are not shown for clarity.

The compelling geometric features of complex **2**·THF mandate further inspection. The most striking and arguably most intriguing property of **2**·THF is the ability of the Mo atom to activate the basal phenyl ring beneath it and bind to it in an η^2 mode. This interaction leads to a partial loss of aromaticity in the phenyl ring, which results in distortion and can be interpreted using the Chatt-Dewar-Duncanson model.^[123]

In this formalism, two extreme bonding scenarios can be imagined (Scheme 53). The adduct case involves only σ donation from the π -bonding orbital of one olefin ligand to a d-orbital of the metal atom, preserving the oxidation state of the metal. Conversely, in the metallacyclopropane extreme case, this σ donation is counterbalanced by π -backdonation from a d orbital of the metal center into the π^* orbital of the olefin ligand, formally resulting in a two electron oxidation of the metal. Differentiating between these cases can be achieved through analytical methods such as NMR spectroscopy or X-ray diffraction. NMR spectroscopy provides insights *via* the $^1J_{H,C}$ coupling constant, which exhibits an angular dependence. As the hybridization shifts from sp^2 to sp^3 , the coupling constant decreases, indicating a larger degree of metallacyclopropane character. However, in our case, this tool was not suitable due to the paramagnetism of the complex.

Instead, X-ray diffraction can unveil the bonding situation in complex **2**·THF by examining the C–C bond length of the bound ligand. In complex **2**·THF, the C1A–C2A (1.466(3) Å) and C4–C5 (1.438(3) Å) bonds are notably more elongated than the C3–C4 (1.351(3) Å) and C5–C6A (1.375(4) Å) bonds. This asymmetry indicates a partial loss of aromaticity, along with a significant degree of metallacyclopropane character, which is also evident from the relatively short Mo1A–C1A (2.276(2) Å) and Mo1A–C2A (2.224(2) Å) distances. The results indicate that the “true” oxidation state of complex **2**·THF may be intermediate between Mo^{+III} and Mo^{+V} .

Adduct or metallacyclopropane?

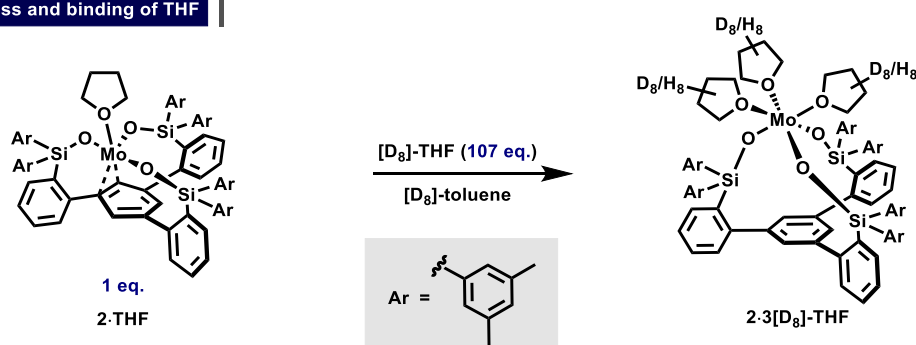


Scheme 53. The Chatt-Dewar-Duncanson model can be applied to complex **2**·THF to describe its bonding characteristics.

The notion that a monomeric Mo^{+III} complex binds THF is remarkable, given that the original Cummins complex **1** is known not to coordinate THF, PEt_3 , or pyridine.^[62] Consequently, it is not considered a Lewis acid, despite the metal center being highly electron deficient. Two factors may contribute to this property: First, the strongly donating anilide ligands compensate the electron deficiency at the metal center. Second, the Cummins complex is sterically shielded, allowing only small rod-like molecules to enter its coordination sphere. In contrast, the trisilanolate ligand of complex **2** is less donating, therefore rendering the metal more Lewis acidic.^[115, 117] Additionally, the complex is arguably less sterically demanding than the ligands of the Cummins complex **1**.

The loss of THF between **2·3THF** and **2·THF** is reversible: addition of $[D_8]$ -THF to **2·THF** in $[D_8]$ -toluene can be tracked by means of 2H NMR spectroscopy (Scheme 54). At 233 K two new broad signals were found at 47 and 34 ppm. Over time, single crystals precipitated from this sample. The crystals appeared homogenous under the microscope and a determination of the unit cell proved it to be the corresponding tris-adduct.

Reversible loss and binding of THF

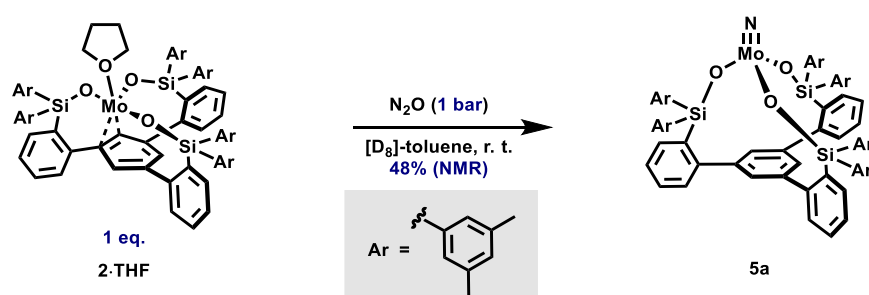


Scheme 54. 2H NMR spectroscopy supports reversible $[D_8]$ -THF binding to complex **2·THF**.

Complex **2·THF** also activates small molecules. The addition of N_2O resulted in an immediate color change from deep red to a golden solution. Analysis of the reaction mixture using an internal standard revealed that nitride **5a** had formed in a 48% NMR yield (Scheme 55). The independent synthesis and characterization are explained in Scheme 68. Strikingly, no nitrosyl complex was observed.

This latter observation could have two reasons: First, a potential nitrosyl complex might have opened the tripodal ligand framework, resulting in the formation of oligomeric Mo nitrosyl complexes. Similar behavior has been observed with pyridine and molybdenum alkylidynes.^[21] However, any attempts to detect such species *via* mass spectrometry were met with failure. Second, in contrast to the original Cummins complex **1**, the coordination of N_2O may not be the rate-determining step but instead proceeds rapidly. Monometallic cleavage of N_2O would then lead to the formation of nitride **5a**, accompanied by NO release.

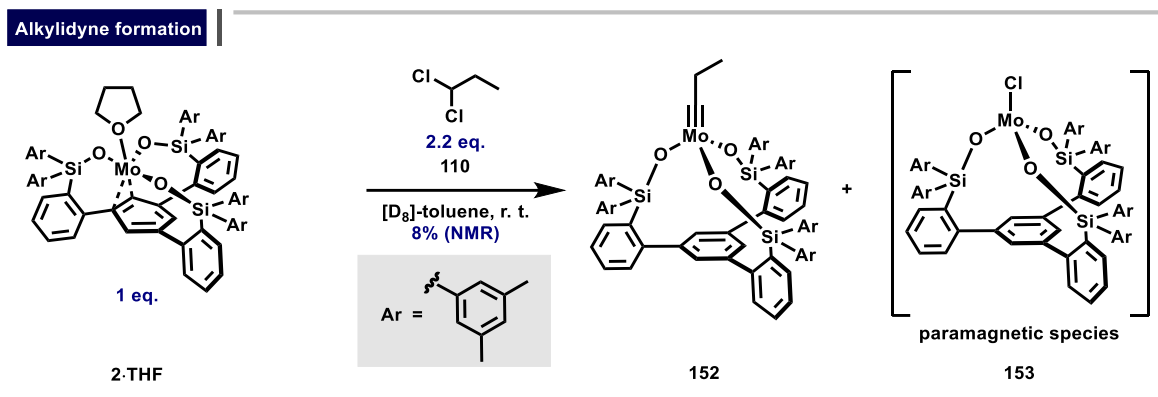
N_2O cleavage



Scheme 55. N–N Cleavage of N_2O results in the formation of nitrido complex **5a**.

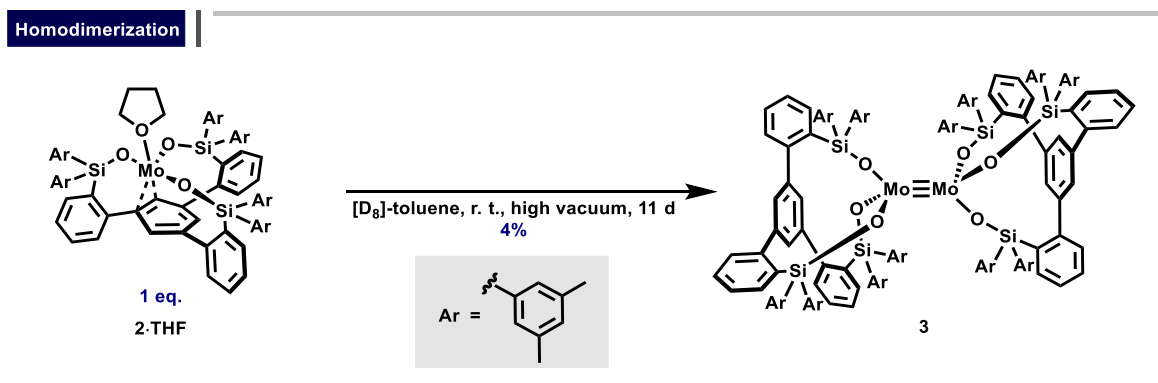
Complex **2·THF** not only activates N_2O but also reacts with 1,1-dichloropropane to afford the corresponding alkylidyne **152** (Scheme 56). In contrast to the cleavage reaction with N_2O , the NMR spectrum of this reaction mixture exhibits a broad background, indicating the formation of several other (oligomeric) species. Despite these challenging conditions, it was possible to fully assign the targeted Mo^{+VI} alkylidyne *via* NMR spectroscopy and determine the yield to be in the range of 10%. Key to the assignment was the characteristic ^{13}C NMR shift of $\delta_C = 322.8$ ppm. Additionally, paramagnetic signals

were observed which might correspond to the Mo^{+IV} chloride complex **153**. Mass spectrometric analysis of the crude reaction mixture further supported the formation of such species.



Scheme 56. Reaction of **2·THF** with 1,1-dichloropropane gives the Mo^{+VI} alkyidyne **152**.

Next, we sought to investigate whether the THF free adduct can be formed selectively. We hypothesized that repeated removal of the toluene solvent might promote the selective formation of the η⁶-arene complex **2** *via* co-evaporation of the THF ligand. After three dissolution/vacuum cycles, the residue was dissolved again in toluene. After several days, large single crystals separated from this solution. These crystals were insoluble in a variety of common organic solvents, preventing the acquisition of NMR data. A single-crystal X-ray diffraction experiment revealed that these crystals were not the η⁶-arene complex **2**, but rather a homodimeric complex **3**, formed in a low yield of 4%. Additional analytical tools, including elemental analysis and mass spectrometry, supported the assignment as **3** (Scheme 57).



Scheme 57. Formation of a sterically crowded homodimer **3**.

This was an unprecedented yet rewarding result, as it marked the first observation of a pair of monomeric and homodimeric Mo^{+III} complexes carrying the same ligand. The crystal structure of **3** revealed an exceptionally long Mo–Mo bond (2.2873(3) Å), comparable to the bond length of the heterodimeric complexes **144** and **147** (*vide supra*). The ligand sphere in **3** is highly congested, and it was also evident that the 3,5-Me₂C₆H₃ groups packed tightly within this environment. This observation might also explain the low isolated yield of **3**. While a high kinetic barrier exists for dimerization due to the crowded ligand environment, once this kinetic barrier is overcome, the dimer could be stabilized not only by the strong Mo–Mo triple bond but also by the attractive non-covalent interactions between the 3,5-Me₂C₆H₃ groups.

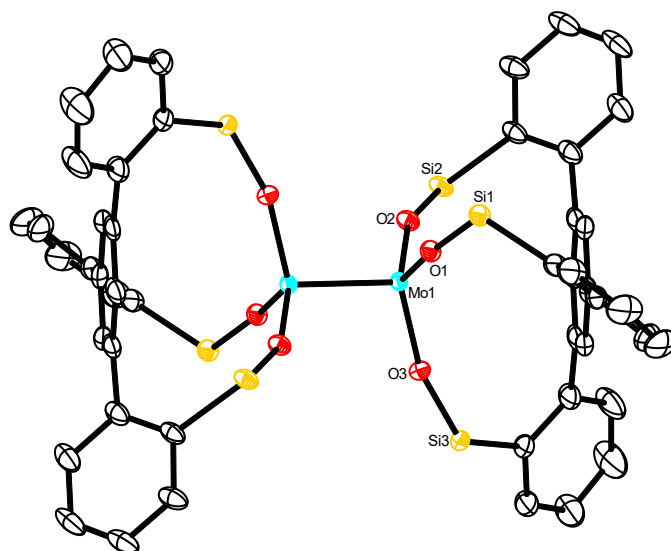
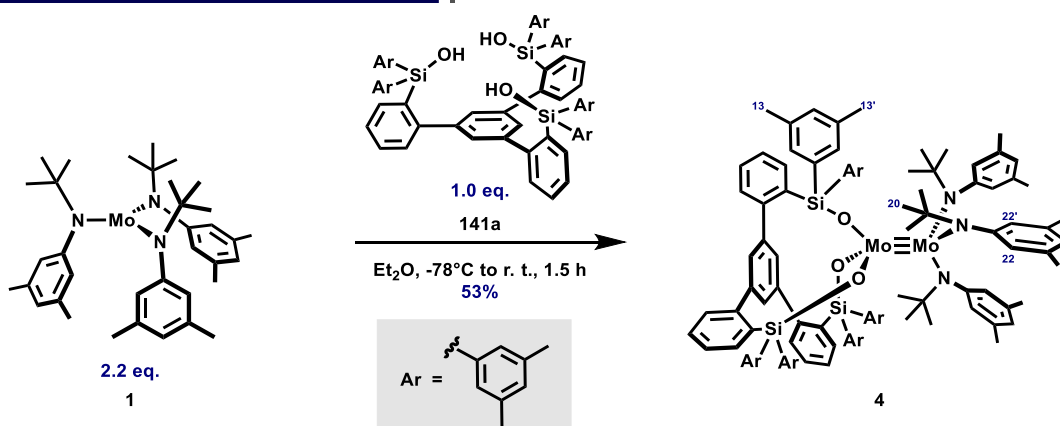


Figure 12. Truncated crystal structure of **3**. The 3,5-Me₂C₆H₃ groups and H-atoms are removed for clarity.

This result suggested that the use of a weaker donor solvent than THF might lead to the isolation of either the monomer **2**, homodimer **3**, or the novel heterodimer **4**. Initial test reactions indicated the formation of a diamagnetic and soluble species. Certain spectroscopic fingerprints closely resembled those of the previously observed heterodimers **144** and **147**. The NMR spectra appeared highly complex due to the presence of diastereotopic protons in the ligand framework. Particularly indicative was a signal at $\delta_{\text{H}} = 3.57$ ppm, a distinct shift similar to that observed in the other heterodimers, likely caused by the anisotropic ring current effect influencing the aromatic proton H-22. Furthermore, ROESY cross peaks between protons H-13 \leftrightarrow H-20 and H-13' \leftrightarrow H-20 allowed the two sets of ligand spheres to be assigned to the same complex. Additionally, the observed ¹⁵N NMR shift ($\delta_{\text{N}} = -129$ ppm) differed significantly from that of the free aniline ligand (-289 ppm). Upon adjustment of the stoichiometry, the heterodimer was ultimately isolated in 53% yield.

A Mo^{III} heterodimer with a tripodal silanolate ligand



Scheme 58. A heterodimeric complex incorporating the Cummins fragment and a tripodal silanolate ligand.

The NMR data was complemented by an X-ray structure analysis of an orange single crystal grown by slow evaporation from a solution in Et₂O (Figure 13). While heterodimerization occurred significantly faster than the homodimerization of complex **2**·THF, analysis of the X-ray structural data revealed an exceptionally long Mo–Mo triple bond (2.3440(3) Å). In fact, this triple bond is by far the longest observed between two unbridged Mo^{III} centers each with CN = 4 (CN = Coordination number) known

to date. Nevertheless, complex **4** proved to be remarkably stable, as the corresponding monomers were never observed once heterodimerization had occurred.

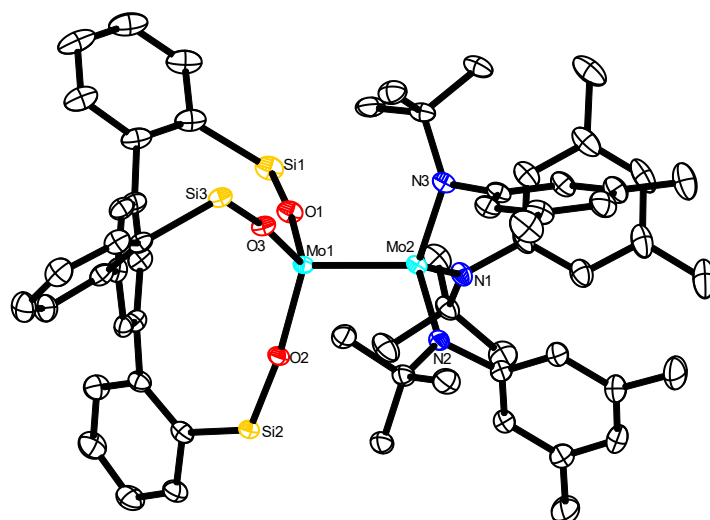
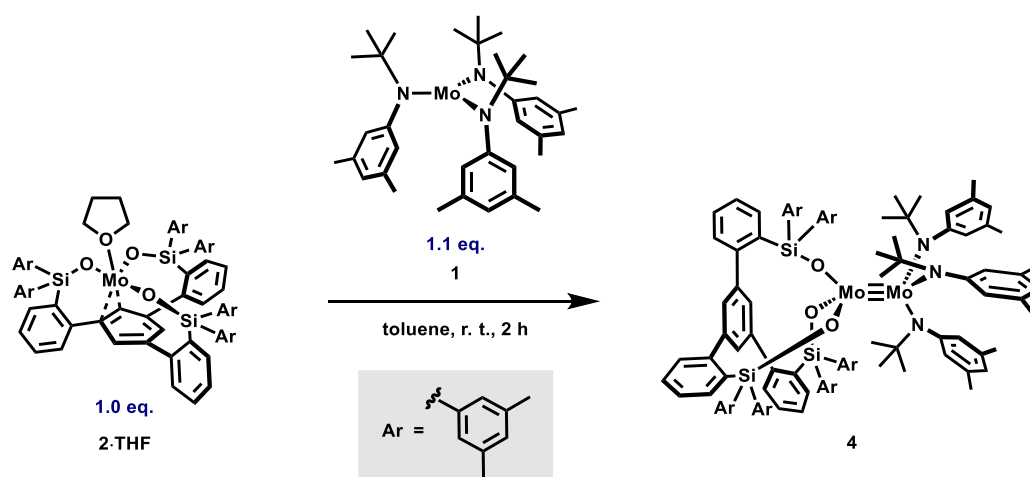


Figure 13. Truncated crystal structure of complex **4**. The 3,5-Me₂C₆H₃ groups, H-atoms and disordered parts are not shown for clarity.

A mixture of complex **2**·THF and complex **1** in [D₈]-toluene also converted smoothly into the corresponding heterodimer **4** (Scheme 59).

A Mo^{+III} heterodimer with a tripodal silanolate ligand



Scheme 59. Heterodimerization by mixing of the monomeric species **2**·THF and **1**.

Notably, synthetic efforts with ligand **141a** enabled the first collective synthesis of a monomer, its corresponding homodimer, and a heterodimer, a compound class which is completely unprecedented in the literature. The ability to isolate both the monomeric and the dimeric forms using the same ligand is remarkable, as typically only one species forms due to steric factors, preventing both from coexisting.

Next, we studied these heterodimeric Mo^{+III} complexes *via* ⁹⁵Mo NMR measurements, a tool previously established for investigating the electronic character of Mo^{+VI} alkylidynes.^[116, 124] A parameter that clearly distinguished our heterodimers from previously reported dimeric Mo^{+III} species was their significantly elongated Mo–Mo triple bond. This was evident from a comparison of the X-ray structural parameters of the heterodimers with literature-known complexes in the CSD that contained an unbridged Mo≡Mo

unit, with each molybdenum atom having a coordination number of 4 (Figure 14). Consequently, we were interested in determining whether a correlation exists between the experimental bond length and the observed ^{95}Mo NMR shift.

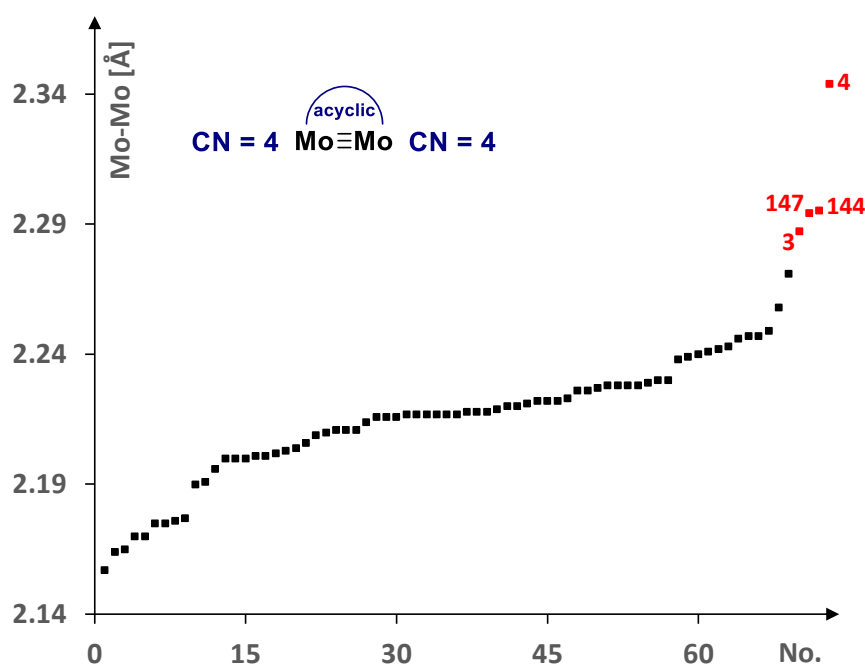


Figure 14. Plot of Mo–Mo bond length of complexes in the CSD that comprise an unbridged Mo–Mo unit with CN = 4 for each molybdenum atom.

Obtaining high-quality ^{95}Mo NMR data is inherently challenging because of the nature of the ^{95}Mo isotope: a quadrupolar $S = 5/2$ nucleus with a low gyromagnetic ratio and a natural abundance of ca. 15.9%. For these heterodimeric complexes in particular, the asymmetry between both molybdenum atoms and the large ligand sets will render these measurements even more challenging, especially for the extremely large heterodimer **4** ($M = 1789$ g/mol).

Despite these obstacles, previous efforts in obtaining ^{95}Mo NMR shifts for a number of smaller homodimeric Mo^{III} complexes have delivered valuable benchmarks.^[125-126] For instance, shifts for homodimeric amide and alkoxide species were observed around 2400-2700 ppm. In contrast, the homodimeric alkyl complexes are significantly more deshielded and resonate at approximately 3600-3700 ppm, which aligns well with the observation of Cotton that truncated Mo_2X_6 alkyl complexes possess a unique electronic structure in comparison to their amide or alkoxide counterparts (*vide supra*).^[59]

The ^{95}Mo NMR measurements of the heterodimeric complexes **4** and **147** at 333 K were successful. For complex **147**, two signals were observed. The broader signal at 3127 ppm was tentatively assigned to the MoN_3 unit due to the broader line width of other known Mo amido complexes (see Figure 22). The sharper signal at 3260 ppm was consequently assigned to the MoO_3 unit (Figure 15).

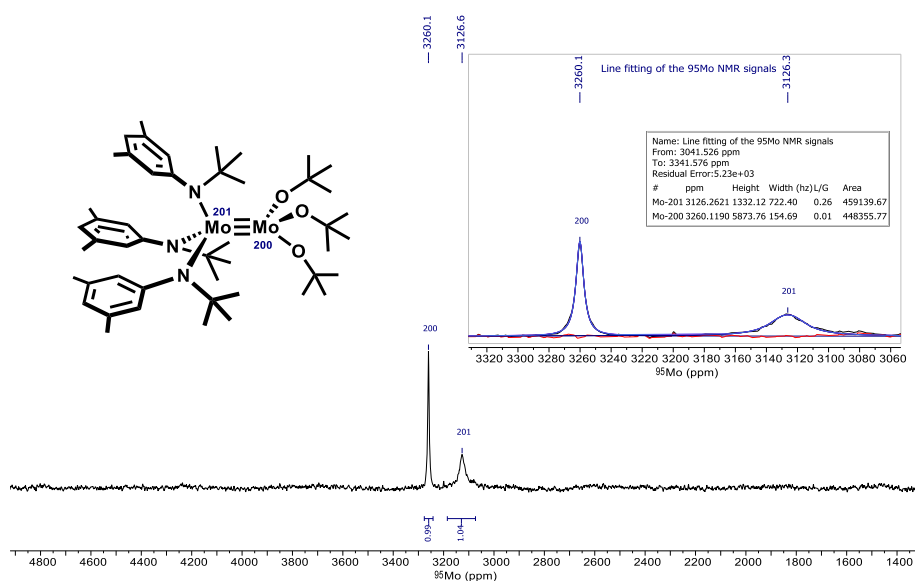


Figure 15. ^{95}Mo NMR spectrum of **147** in $[\text{D}_8]$ -toluene at 333 K. In collaboration with Dr. Markus Leutsch.

For the much larger heterodimeric species **4**, only one broad signal was observed, even after an extensive acquisition time of 5 d. This signal was tentatively assigned to the MoO_3 unit, while the signal of the MoN_3 unit was presumably broadened by the influence of the quadrupolar ^{14}N nucleus to such a degree, that it could not be observed. The much broader signal for **4**, in comparison with the relatively sharper signal set of **147**, aligns well with the assumption that a larger ligand environment entails extensive line broadening (Figure 16).

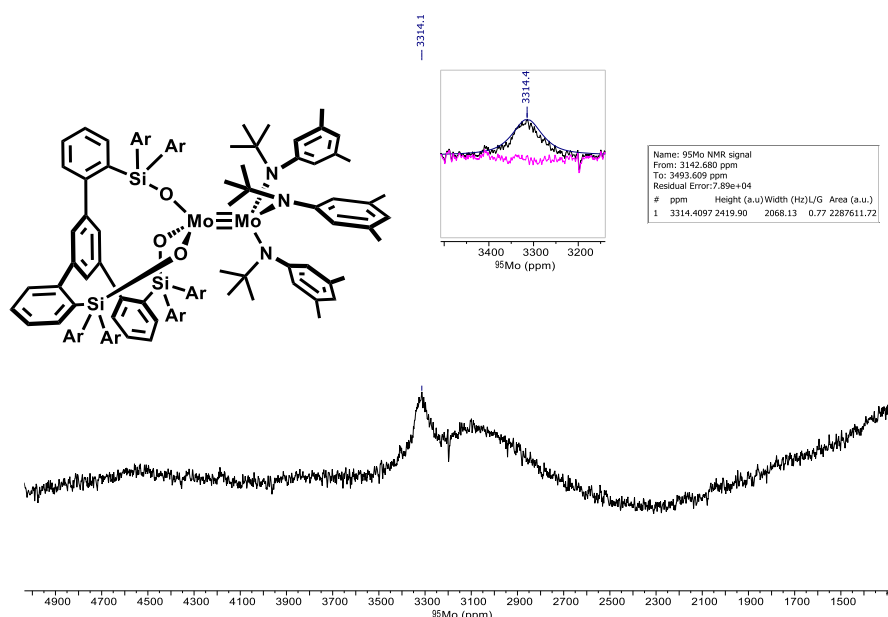


Figure 16. ^{95}Mo NMR spectrum of **4** in $[\text{D}_8]$ -toluene at 333 K. In collaboration with Dr. Markus Leutsch.

Initially, it was assumed that the highly deshielded ^{95}Mo NMR shifts arise from the elongated $\text{Mo}-\text{Mo}$ triple bonds of both heterodimeric species. Qualitatively, an elongation of the $\text{Mo}-\text{Mo}$ triple bond would lead to less electronic density in the triple bond, and therefore one could conjecture about a deshielded ^{95}Mo NMR shift. However, this assumption proved to be incorrect. $\text{Mo}_2\text{CH}_2t\text{Bu}_6$ (**35**) (2.1654(3) Å, 3695 ppm) has one of the shortest $\text{Mo}-\text{Mo}$ triple bond lengths known to date, yet exhibits an even more deshielded signal than the heterodimers **4** and **147**.

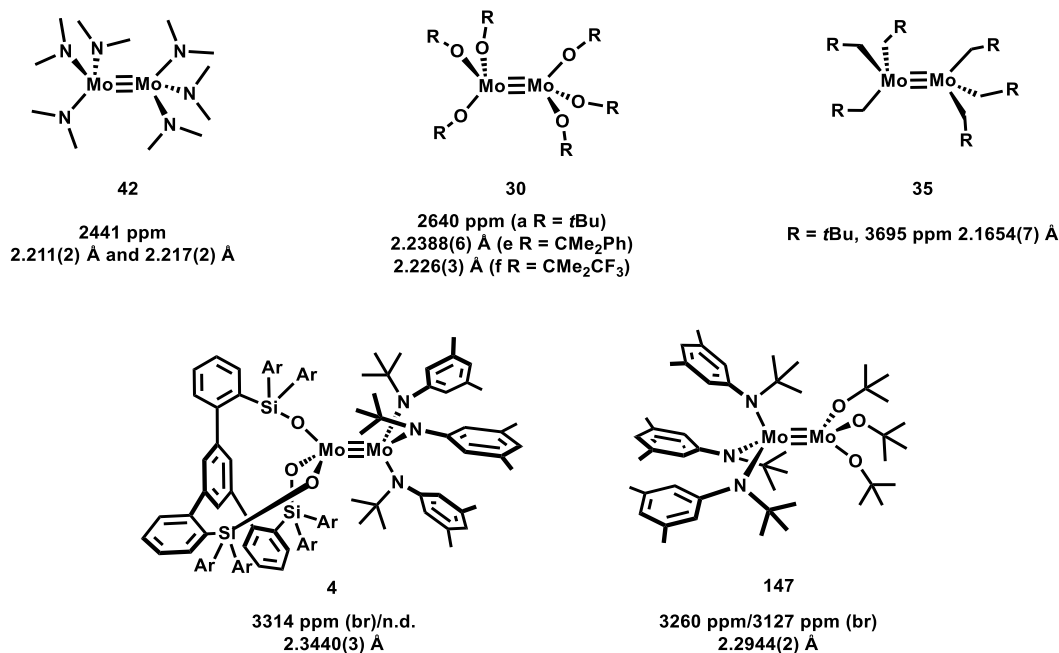


Figure 17. Comparison of Mo–Mo bond length and ^{95}Mo NMR shifts of known Mo^{+III} dimers and the heterodimeric complexes. ^{95}Mo NMR shifts (**23**,^[126] **30a**,^[26] and **35**^[126]) and Mo–Mo bond lengths (**30e**,^[127] **30f**,^[128] **35**,^[129] and **42**^[29]) were taken from the literature.

Perplexed by these data, we turned our attention to a computational analysis, including the determination of the NMR shielding tensor. We sought not only to gain a detailed electronic structure analysis of **30a**, **35** and **42** as well as of the heterodimers **4** and **147**, but we also aimed at validating our calculations by comparison to the experimental shifts. With the calculated shielding tensor in hand, we could examine if there is a correlation between the (paramagnetic) shielding along the Mo–Mo triple bond axis and the Mo–Mo bond length. With the chosen level of theory (TPSSH/def2-TZVPP (SARC-ZORA-TZVPP for Mo) and CPCM(toluene) using geometries optimized at the B3LYP/def2-TZVP D3BJ CPCM(toluene) we first calculated the NMR shielding of all selected compounds and compared the calculated isotropic shielding to the experimental ^{95}Mo NMR shift. We obtained a good correlation ($R^2 = 0.9093$) between the calculated and the experimental data (Figure 18).

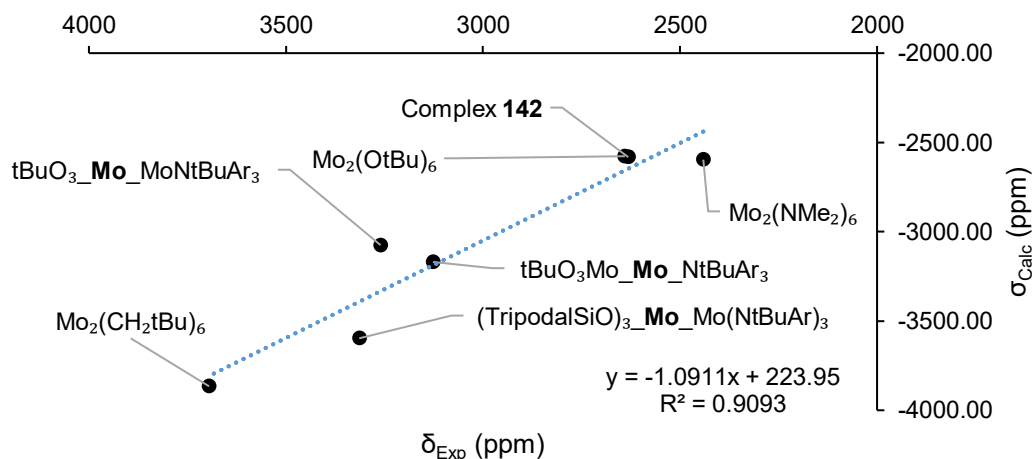


Figure 18. Correlation between the experimental NMR chemical shift and the calculated isotropic shielding.

Despite these efforts, a conclusive correlation between the (paramagnetic) shielding along the Mo–Mo bond axis and the bond length was not found. Therefore, we examined the electronic structure of these complexes more closely and were able to elucidate why no relationship exists between the paramagnetic shielding tensor and the bond length.

In the most simplified picture, one might assume that the triple bond, formed by the d_z^2 , d_{xz} , and d_{yz} orbitals, corresponds to the HOMO-2, HOMO-1, and HOMO. However, as explained in the introduction, this view is oversimplified. Therefore, it is essential to consider the most influential factor for the electronic structure of these complexes, the ligand type.

Indeed, it was found that only $\text{Mo}_2(\text{OtBu})_6$ (**30a**), a complex carrying alkoxide ligands, reflects the simplistic view, in which the d_z^2 , d_{xz} , and d_{yz} orbitals constitute the HOMO-2, HOMO-1, and HOMO, respectively. In contrast, for $\text{Mo}_2(\text{NMe}_2)_6$ (**42**), which carries more π -donating amide ligands, the nitrogen based lone pair p orbitals constitute the HOMO and HOMO-1. While these orbitals do not contribute to the Mo–Mo triple bond interaction, they significantly influence the paramagnetic ^{95}Mo NMR shielding tensor. The Mo–Mo triple bond interaction in this complex is instead described by the HOMO-2, HOMO-3, and HOMO-4.

$\text{Mo}_2(\text{CH}_2t\text{Bu})_6$ (**35**), a complex bearing purely σ -donating alkyl ligands, represents a special case. Here, the triple bond interaction corresponds to the HOMO, HOMO-1, and HOMO-2. However, the HOMO describes the σ -type interaction between the d_z^2 orbitals of the two Mo^{III} fragments, while the interaction between the d_{xz} and the d_{yz} orbital occur at slightly lower energy. This observation is particularly interesting when compared to its truncated version $\text{Mo}_2(\text{CH}_3)_6$, as described in the introduction, where the σ orbital formed by the d_z^2 orbital interaction is found below the π -bonds derived from the d_{xz} and d_{yz} orbital (*vide supra*).^[59]

For the heterodimer **4**, a normal ordering of orbitals was observed, in which the π -bonding orbitals constitute the HOMO and HOMO-1, while the σ bond is described by the HOMO-2. The latter exhibits extensive mixing of the d_z^2 orbital with amide ligand-based p orbitals. Notably, in heterodimer **4**, the triple bonds are strongly polarized toward the MoN_3 fragment.

This comparative analysis reveals why a correlation between paramagnetic shielding tensor and bond length is missing. While the HOMO of $\text{Mo}_2(\text{OtBu})_6$ (**30a**) has π character ($\Delta E_{\text{HOMO-LUMO}} = 3.3$ eV), the HOMO of $\text{Mo}_2(\text{NMe}_2)_6$ (**42**) is ligand based ($\Delta E_{\text{HOMO-LUMO}} = 3.9$ eV), and the HOMO of $\text{Mo}_2(\text{CH}_2t\text{Bu})_6$ (**35**) has σ character ($\Delta E_{\text{HOMO-LUMO}} = 3.8$ eV). Although the HOMO of **4** has π character, this heterodimer presents yet another distinct case, as its frontier orbitals are strongly polarized toward the MoN_3 fragment ($\Delta E_{\text{HOMO-LUMO}} = 2.7$ eV). Despite the fact that the average energy of the frontier orbitals of the heterodimer is higher (-4.8 eV) compared to the homodimers (-5.0 eV (**30a**), -5.1 eV (**42**) and -5.5 eV (**35**)), the absence of correlation between these energies and the paramagnetic ^{95}Mo NMR shielding tensor suggests a more complex relationship.

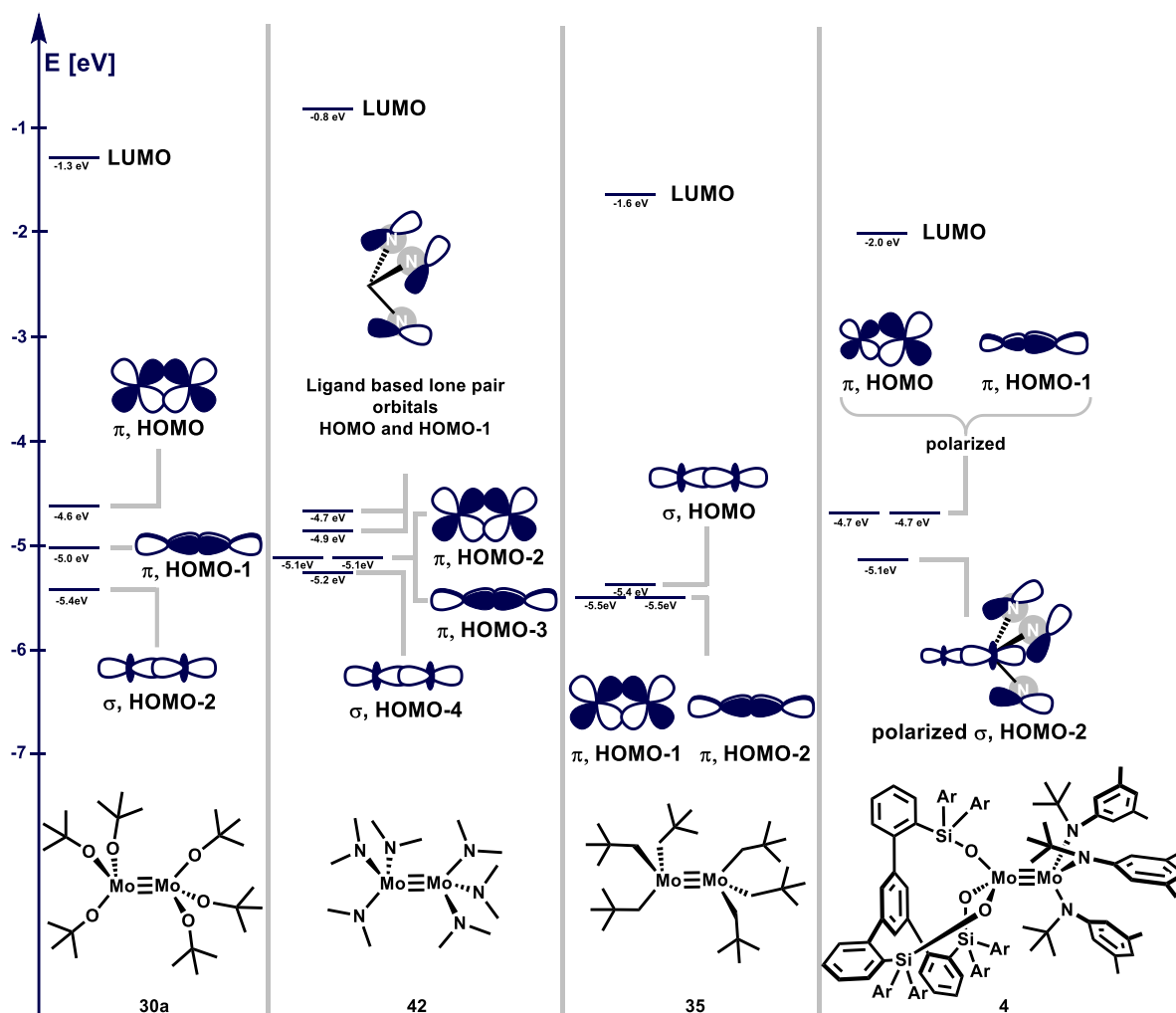
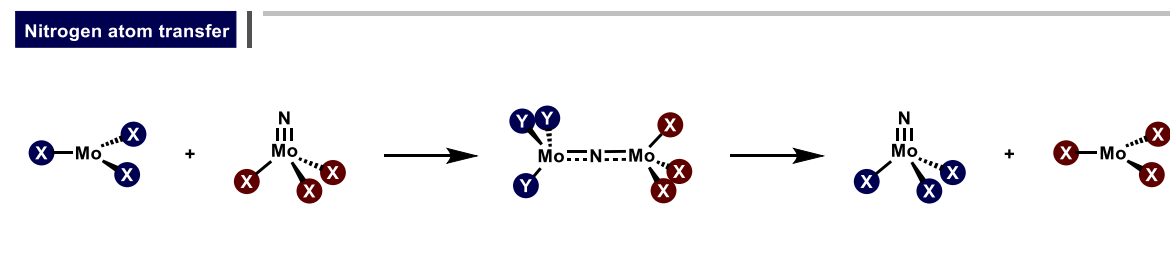


Figure 19. Quantitative MO scheme of the frontier orbitals of complexes **30a**, **42**, **35**, and **4**. In collaboration with Prof. Alexander Auer.

Synthesis and Electronic Structure of a Bridged Molybdenum Nitride

With the successful isolation of the monomeric, homodimeric, and heterodimeric form *via* the protonolysis approach, we turned our attention to our second strategy: the nitrogen atom transfer approach (Scheme 60). The anticipated complete transfer process features an overall three-electron redox event. As outlined in the introduction, such complete transfer is, however, known to be partially driven by the formation of either a homodimeric Mo^{III} dimer with a thermodynamically robust triple bond, or, if performed under N_2 , the formation of a thermodynamically stable nitrido complex *via* N_2 cleavage with the elusive monomeric fragment.^[32]

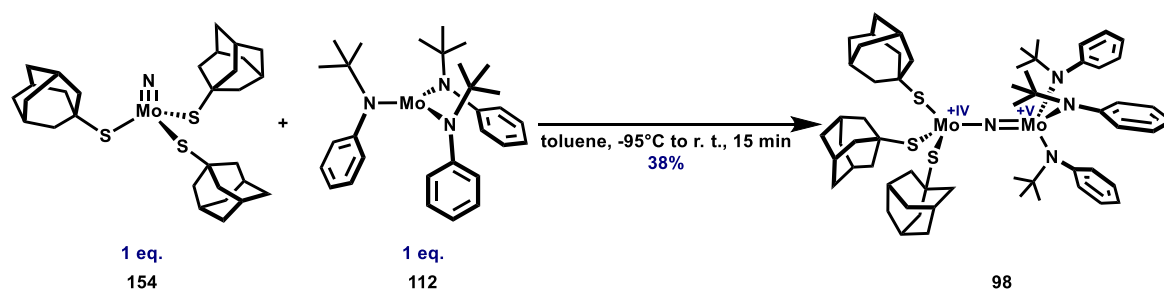


Scheme 60. Nitrogen atom transfer as a strategy for the synthesis of a monomeric Mo^{III} complex.

Several bridging nitrides resulting from incomplete nitrogen atom transfer have been isolated in the past, and efforts have been made to assign the oxidation states of the molybdenum atoms. In symmetric Mo–N–Mo complexes, the nitrogen atom is evenly distributed between the two molybdenum fragments, leading to a formal oxidation state of +4.5 for each molybdenum atom. However, in unsymmetric complexes, the situation is different.

For example, $\text{AdS}_3\text{Mo–N–Mo}(\text{N}(\text{tBu})(\text{Ph}))_3$ (**98**), obtained from the reaction of nitride **154** with monomer **112**, was tentatively assigned as an $[\text{S}_3\text{Mo}^{+\text{IV}}\text{–N–Mo}^{+\text{V}}[\text{N}_3]]$ complex (Scheme 61). This assignment was based on differences in bond lengths observed in the X-ray structure analysis (1.882(7) Å ($\text{S}_3\text{Mo}^{+\text{IV}}\text{–N}$) vs. 1.771(7) Å ($\text{N}_3\text{Mo}^{+\text{V}}\text{–N}$)) and was later supported by a DFT investigation of a largely simplified $(\text{HS})_3\text{Mo–N–Mo}(\text{NH}_2)_3$ model complex.^[77-78]

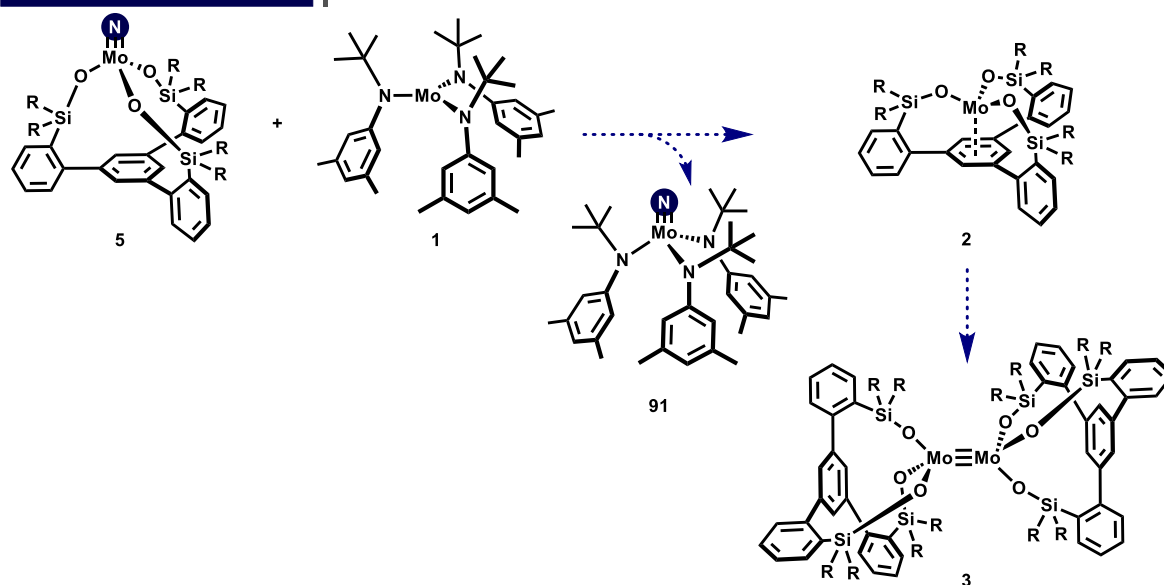
Cummins' unsymmetrical Mo–N–Mo complex



Scheme 61. Cummins' unsymmetrical Mo–N–Mo complex featuring thiolate and amide ligands.

Attempting the nitrogen atom transfer with nitrido complexes **5** and the Cummins complex **1** appears highly plausible. From a qualitative perspective, silanolates are weaker donors than amides, and therefore the $\text{N}_3\text{Mo–N}$ fragment should exhibit a stronger nitride bond than the $(\text{SiO})_3\text{Mo–N}$ fragment due to enhanced π -backbonding in the former. An additional driving force could be the trapping of the elusive trigonal-planar $\text{Mo}^{+\text{III}}$ fragment by the basal phenyl ring of the tripodal silanolate to form the previously identified η^6 -arene complex **2** (for $\text{R} = 3,5\text{-Me}_2\text{C}_6\text{H}_3$). Another possibility would be the formation of the homodimer **3** (Scheme 62).

Envisioned nitrogen atom transfer

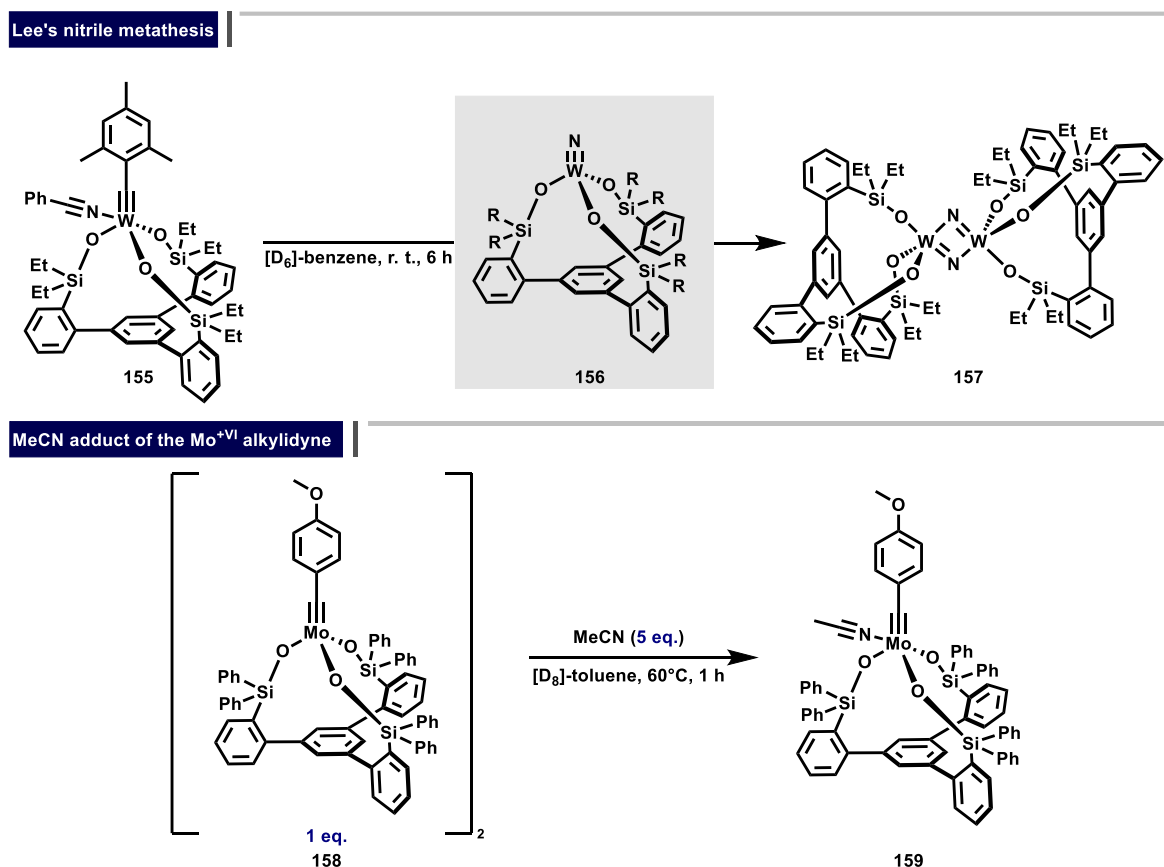


Scheme 62. Envisioned nitrogen atom transfer with the Cummins complex **1** as the acceptor.

Our initial efforts were directed toward devising viable strategies to obtain the nitrido complexes **5**, the key components for attempting nitrogen atom transfer with the Cummins complex **1**. A question that arose was whether these nitride complexes would adopt a common terminal nitride structure or whether they exist as dimeric species.

It is worth noting that Lee and co-workers had recently disclosed the synthesis of a dimeric tungsten nitride **157** carrying the tripodal silanolate ligand decorated with Et substituents on the silicon atom. This nitride was obtained *via* nitrile metathesis, reacting an alkyldiyne with benzonitrile (Scheme 63).^[130] The synthesis of molybdenum nitrides, however, usually fails by this approach, because the reverse reaction, the metathesis of alkynes with nitrides to form alkyldiynes, is typically favored.^[131-133]

The Mo-based canopy catalyst generation is known to coordinate acetonitrile, forming adduct **159**. In contrast to its tungsten congeners, complex **159** is stable at 60°C, and the conversion to the corresponding nitride has never been observed.^[114]



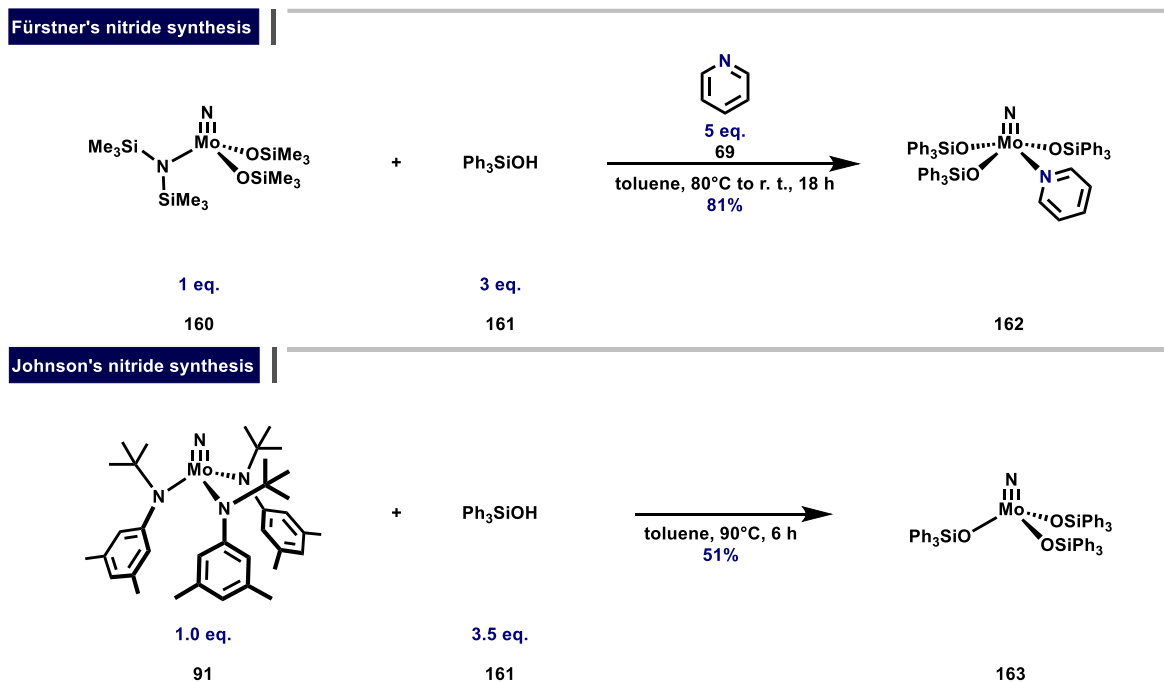
Scheme 63. Top: Lee's nitrile metathesis. Bottom: Fürstner's first crystal structure of the canopy catalyst was enabled by MeCN coordination.

Therefore, we decided to evaluate other strategies. Of particular interest were established routes to nitride complexes incorporating Ph_3SiO^- as ancillary ligands, given that the parent Ph-substituted tripodal silanolate ligand **141b** essentially is composed of three Ph_3SiOH units tethered by a 1,3,5-phenyl linker.

Pioneering work by Fürstner and co-workers employed $\text{Mo}(\text{NTMS}_2)(\text{OTMS})_2$ (**160**) as the starting complex. Originally, this complex was explored as a candidate in the catalytic ring-closing metathesis of alkynes. However, it proved to be entirely inactive. Upon screening a library of different additives, Ph_3SiOH (**161**) proved competent, to impact catalytic activity. Attempts to isolate or identify complex **163** from a stoichiometric ligand exchange between $\text{Mo}(\text{NTMS}_2)(\text{OTMS})_2$ (**160**) and Ph_3SiOH (**161**)

failed. Only after the addition of exogenous pyridine to the mixture was it possible to isolate the pyridine adduct **162** in 81% yield.^[133] This discovery not only established silanolates as ancillary ligands in catalytic alkyne metathesis, but also laid the foundation for the development of air-stable alkyne metathesis catalyst systems.^[134-136]

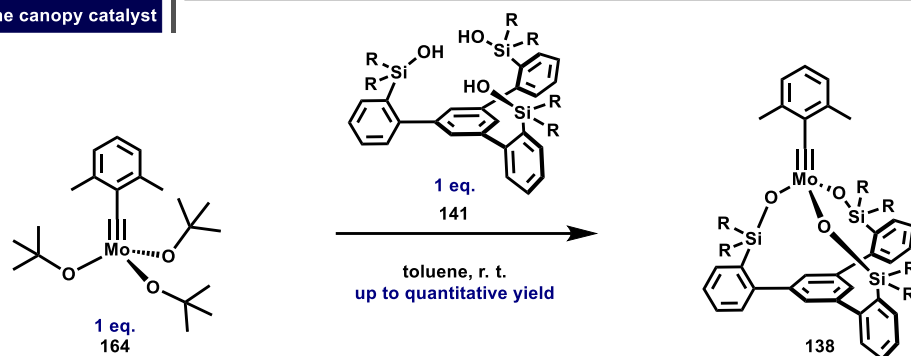
An alternative approach was presented by Johnson and co-workers, who successfully achieved the synthesis of $\text{N}\equiv\text{Mo}(\text{OSiPh}_3)_3$ (**163**) starting from **91**. However, the reaction required high temperatures (90°C) and yielded only moderate amounts of the resulting product.^[137] Notably, no crystal structure analysis was obtained for complex **163**.



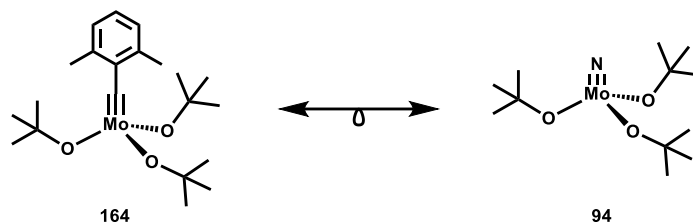
Scheme 64. Selected literature known examples for the synthesis of Mo^{+VI} nitride complexes with silanolates as ancillary ligands.

Given the limitations posed by the existing approaches, we sought to develop an alternative strategy inspired by improved protocols for synthesizing molybdenum alkylidynes with tripodal silanolates. In this refined procedure, $\text{ArC}\equiv\text{Mo}(\text{OtBu})_3$ (**164**) served as the precursor, undergoing protonolysis with a variety of differently substituted tripodal silanols to furnish the corresponding alkylidynes **138** in good to excellent yields.^[114, 116] As nitrido complexes are isolobal^[138] to alkylidyne complexes, we hypothesized that employing $\text{N}\equiv\text{Mo}(\text{OtBu})_3$ (**94**) as the precursor in a protonolysis reaction might yield the desired nitrido species.

Synthesis of the canopy catalyst



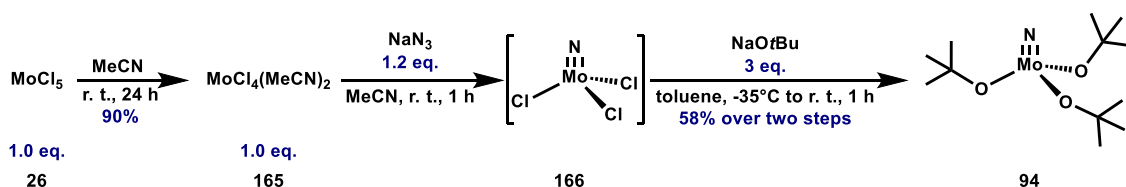
Isolobal analogy



Scheme 65. Top: Synthesis of the canopy catalysts. Bottom: Alkyldynes are isolobal to nitrides.

Therefore, we set out to prepare nitride **94** according to Chisholm's literature protocol.^[75] Stirring of MoCl_5 (**26**) in MeCN led to the precipitation of $\text{MoCl}_4(\text{MeCN})_2$ (**165**) in pure form in 90% isolated yield. In the subsequent multi-step process, **165** was reacted with NaN_3 in MeCN to form an intermediate species **166**. Solvent exchange to toluene, followed by reaction with NaOtBu at low temperatures, gave the desired nitride **94** in 58% isolated yield after recrystallization from toluene.

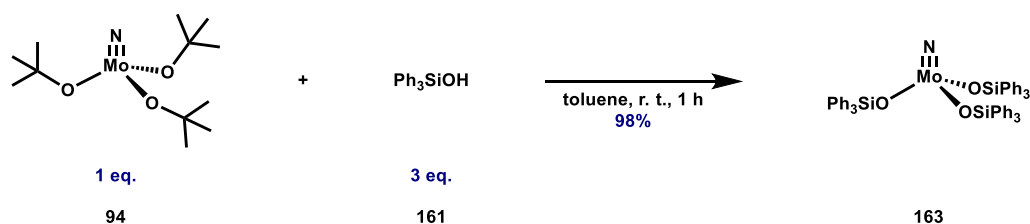
Synthesis of $\text{N}=\text{Mo}(\text{OtBu})_3$



Scheme 66. The literature known synthesis of **94** by Chisholm's protocol.

The anticipated ligand exchange using $\text{N}=\text{Mo}(\text{OtBu})_3$ (**94**) as the precursor proved to be a general method. In our first foray, we prepared the known complex **163** in excellent yield by this method at room temperature. Notably, repeated removal of the toluene solvent was essential to drive the ligand exchange to completion, likely due to the co-evaporation of *t*BuOH (Scheme 67).

Synthesis of $\text{N}=\text{Mo}(\text{OSiPh}_3)_3$



Scheme 67. An improved approach for the synthesis of **163**.

Nitride **163** was unequivocally identified by comparison of its NMR spectroscopic fingerprints with the literature data.^[137] Although the authors in the original article stated that all attempts at growing single crystals suitable for X-ray diffraction had failed, we decided to attempt crystallization again. After examining various conditions, it was found that large single crystals suitable for X-ray diffraction could be grown by slow diffusion of *n*-pentane into a benzene solution of **163** (Figure 20).

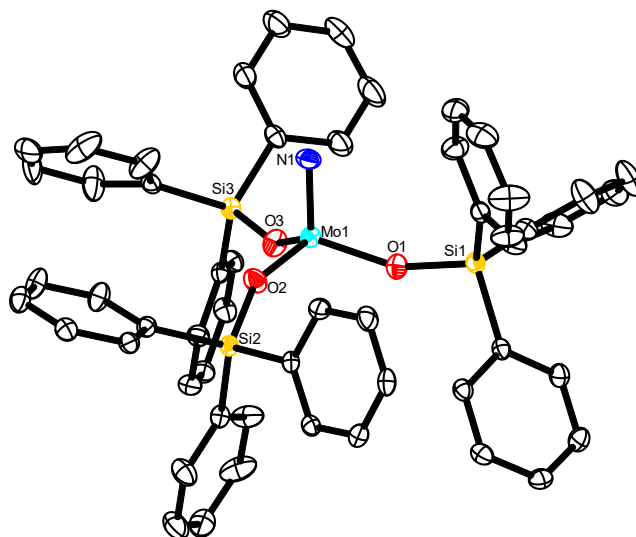
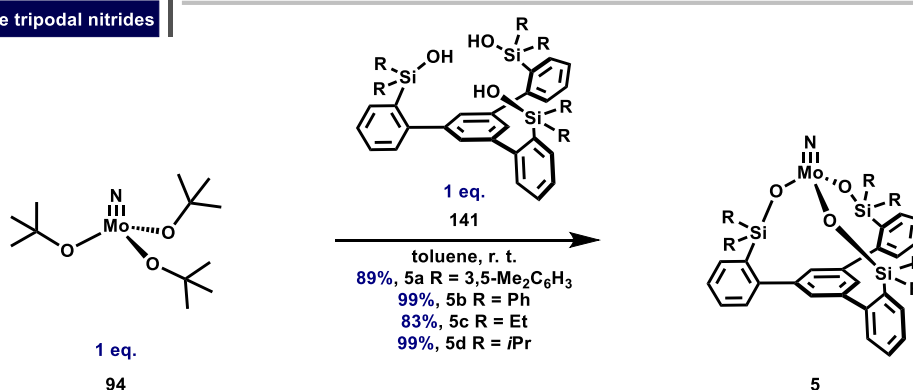


Figure 20. Single crystal structure of **163**. H-atoms and disorders are not shown for clarity.

Next, we synthesized the tripodal nitrides **5** in good to excellent yields (Scheme 68). While complexes **5a**, **5c**, and **5d** exhibited sharp NMR signals at 298 K, complex **5b** had to be heated to 333 K which led to sharpening of the signals. The broad signals at 298 K could originate from the presence of aggregates at 298 K, which break up at higher temperatures; this hypothesis is further supported by the low solubility of **5b** at room temperature.^[114]

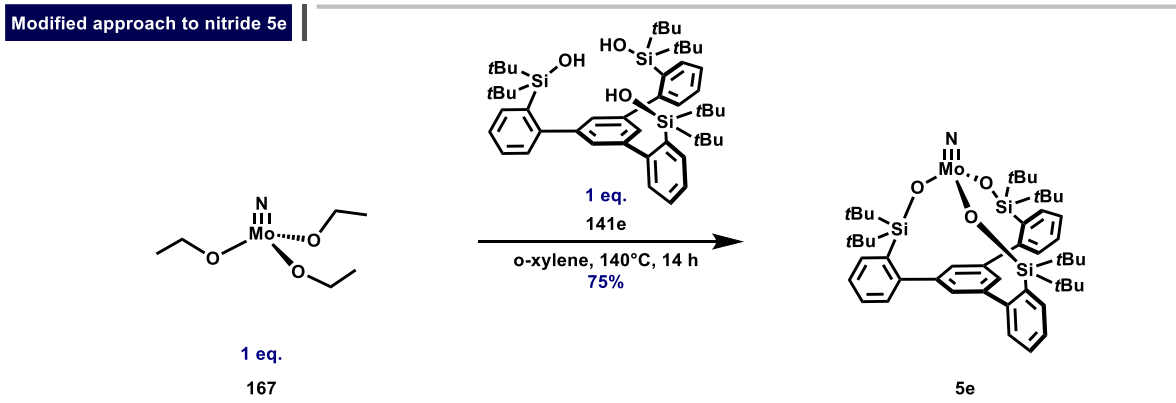
Synthesis of the tripodal nitrides



Scheme 68. Synthesis of tripodal nitrides **5** via protonolysis.

The synthesis of **5e** starting from $\text{N}\equiv\text{Mo}(\text{OtBu})_3$ (**94**) was also attempted. Small-scale NMR experiments in $[\text{D}_8]$ -toluene at 60°C indicated the formation of a product resulting from incomplete protonolysis. Upon heating of this mixture to 100°C, the desired C_3 -symmetrical species was identified and fully assigned. However, this transformation was not clean, as a substantial amount of non-identified side products was also formed. To address this challenge, a modified protocol was required for the synthesis of the sterically hindered complex **5e**. After extensive screening of other nitride precursors, the smaller precursor $\text{N}\equiv\text{Mo}(\text{OEt})_3$ (**167**) was found to enable the complete and clean protonolysis with the bulky ligand **141e**. The optimized protocol necessitated high temperatures (140°C) and a switch to the higher-

boiling solvent *o*-xylene. Using this refined approach, complex **5e** was obtained in 75% yield after recrystallization from toluene/HMDSO (Scheme 69).



Scheme 69. The synthesis of the sterically demanding nitride **5e** was achieved by a modified strategy.

Colorless single crystals of **5d** suitable for X-ray diffraction were obtained by slowly cooling a saturated solution of compound **5d** in Et₂O from 20°C to 5°C. The crystal structure analysis confirmed the presence of a C₃-symmetric terminal nitride (Figure 21).

Notwithstanding the extreme lipophilicity of complex **5e**, single crystals were successfully grown by slowly cooling a solution of **5e** in Et₂O from 20°C to -20°C. X-ray structure analysis revealed that compound **5e** is also C₃-symmetric and contains a terminal nitride ligand (Figure 21).

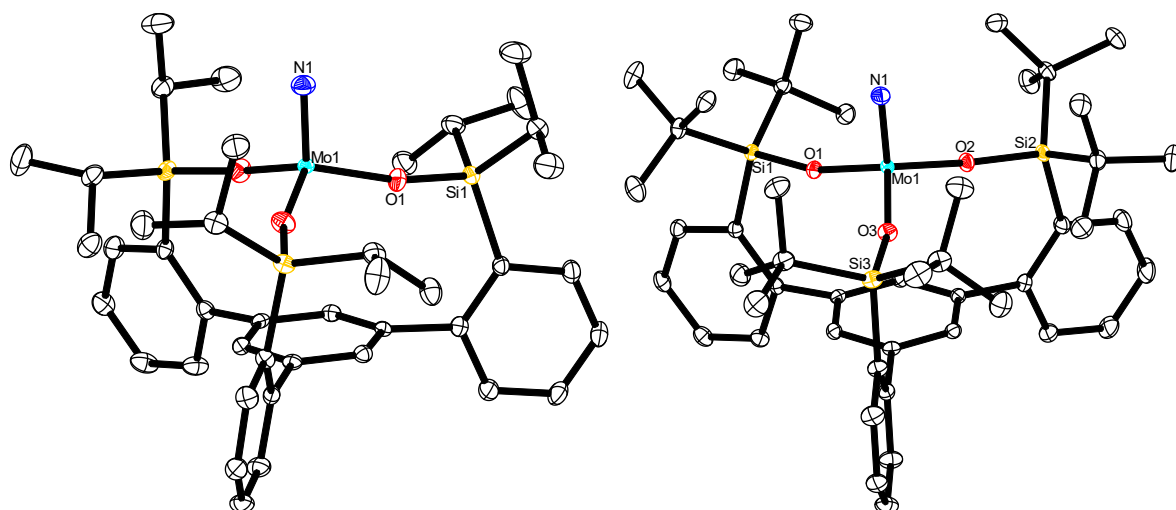


Figure 21. Left: Crystal structure of **5d**. Right: Crystal structure of **5e**. H-atoms and solvent molecules are not shown for clarity.

While a single crystal structure analysis has so far not been obtained for complex **5c**, ⁹⁵Mo NMR spectroscopy together with ¹⁴N NMR spectroscopy, unequivocally confirmed its monomeric nature. The observed ⁹⁵Mo NMR shifts of complexes **5a-e** are very similar ($\delta_{\text{Mo}} = 116$ ppm to 121 ppm). As complexes **5d** and **5e** are monomeric according to X-ray diffraction analysis, the existence of dimeric nitrides for the other nitrides **5**, reminiscent of Lee's dimeric tungsten nitride **157**, seems highly unlikely.

In contrast, N≡Mo(OSiPh₃)₃ (**163**) resonates at much lower field ($\delta_{\text{Mo}} = 159$ ppm). As expected, a markedly different ligand type exerts the most drastic influence on the ⁹⁵Mo NMR shift. While N≡Mo(O*t*Bu)₃ (**94**) resonates at $\delta_{\text{Mo}} = 55$ ppm, the corresponding amides exhibit highly deshielded signals ($\delta_{\text{Mo}} = 393$ ppm for N≡Mo(NMe₂)₃ (**168**) and $\delta_{\text{Mo}} = 389$ ppm for N≡Mo(N(*t*Bu)(Ar))₃ (**91**)). Notably, complex **91** had to be measured at 333 K, as the nitrogen ligated molybdenum atom gave rise to significant line broadening at lower temperatures.

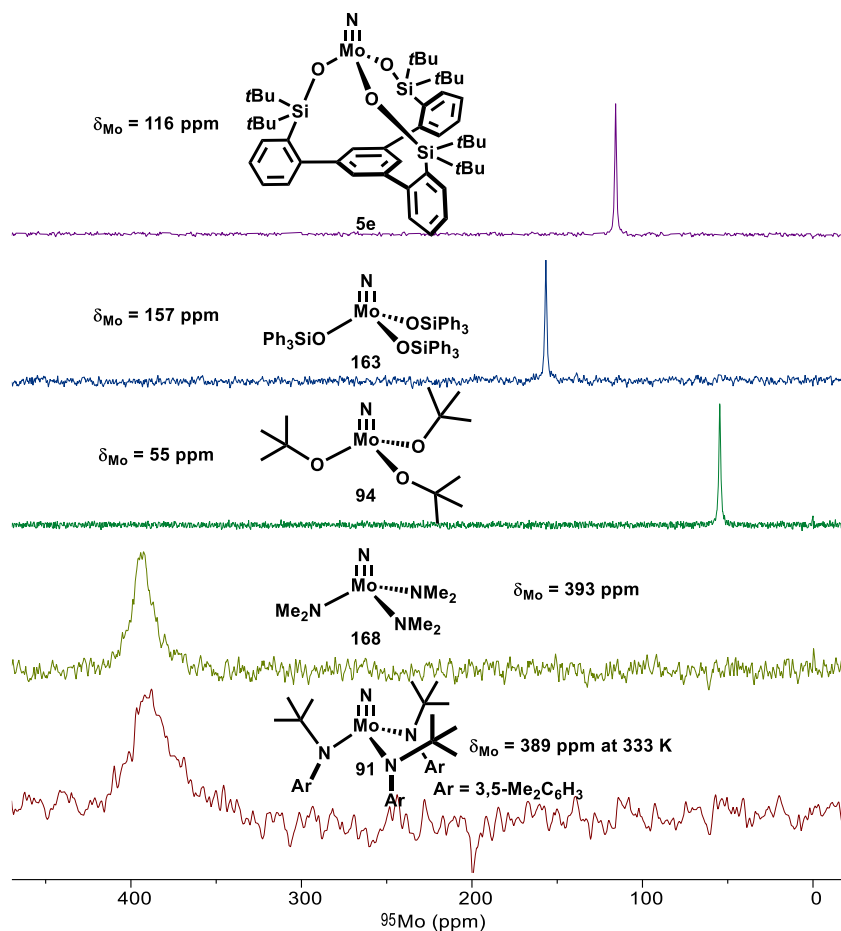


Figure 22. Stacked ^{95}Mo NMR spectra in $[\text{D}_8]$ -toluene at 298 K (except **91**) of selected Mo nitrides. In collaboration with Dr. Markus Leutzsch.

Inspection of the crystal structures revealed why the shift of the tripodal nitrides is confined to a remarkably narrow range and why the signal of $\text{N}\equiv\text{Mo}(\text{OSiPh}_3)_3$ (**163**) is significantly deshielded. In complex **163**, two silanolates are pointing upward while one is oriented downward. In contrast, the tripodal ligand enforces a rigid all-downward conformation (Figure 23). This constraint is accompanied by a notable linearization of the Mo–O–Si linkage (for **5e** $165.60(8)^\circ$, $165.60(9)^\circ$, and $168.14(9)^\circ$). In comparison, the bond angles in **163** are more bent ($148.06(9)^\circ$, $153.62(10)^\circ$, and $154.64(9)^\circ$).

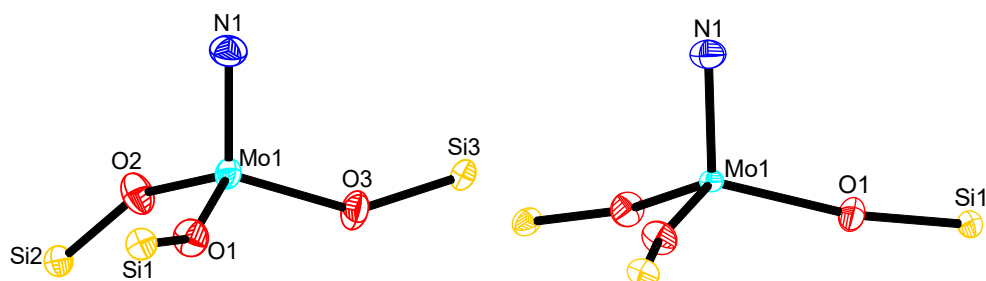
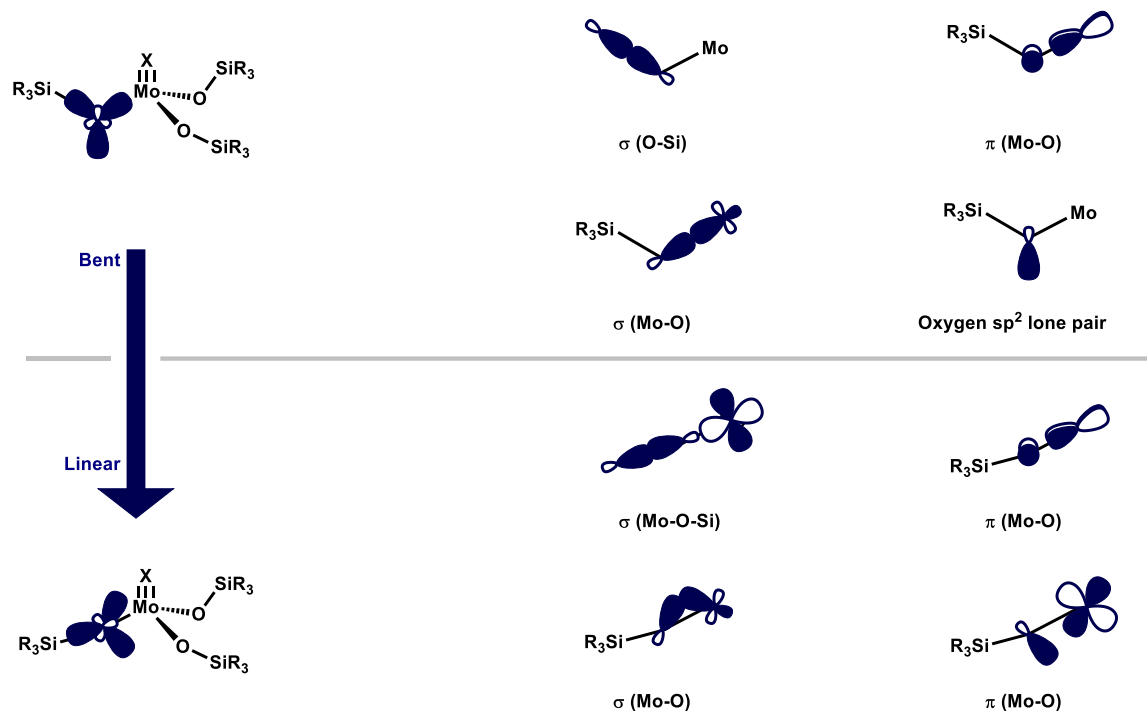


Figure 23. Left: The $\text{N}\equiv\text{MoX}_3$ cone of **163**. Right: The $\text{N}\equiv\text{MoX}_3$ cone of **5d**.

This linearization effect was recently observed by Fürstner for tripodal alkylidynes and studied in a collaborative work with Neese.^[116] The bonding interaction of the essentially sp^2 -hybridized oxygen atom with the metal center involves both σ - and π -bonding interactions (Scheme 70). For small Mo–O–Si angles, the key orbital interactions include the Mo–O σ -bonding interaction, the Mo–O π -bonding

interaction, and the O–Si σ -bonding interaction, complemented by an sp^2 based non-bonding lone-pair orbital. As the Mo–O–Si angle increases, this linkage becomes more linear, leading to an additional Mo–O π -bonding interaction between the formerly sp^2 -based lone-pair orbital and a metal-based d orbital. However, this linearization results in reduced orbital overlap for the more dominant σ -bonding interaction. It is worth speculating that the distinct ^{95}Mo NMR shifts of the tripodal nitrides **5** at least in part originate from the linearization of the Mo–O–Si unit in the tripodal ligand architecture.



Scheme 70. Top: Key orbital interactions for the bent Mo–O–Si linkage in Mo alkylidynes. Bottom: Key orbital interactions for the linear Mo–O–Si linkage in Mo alkylidynes (X = CR). Reproduced from the original publication.^[117] Likely also valid for X = N.

To gain a more comprehensive understanding of the nitride complexes, we turned our attention to ^{14}N NMR spectroscopy. Although the ^{14}N nucleus is quadrupolar and therefore might be affected by line broadening, it has a high natural abundance; hence no expensive labelling, as for ^{15}N NMR spectroscopy, is required. This technique has previously been used to study a wide array of nitrogen-ligated transition metal complexes.^[139-144] At the outset, successful measurements appeared plausible, as the line broadening caused by the quadrupolar nucleus would likely be partially compensated by the highly symmetric nature of all the complexes.

While ^{95}Mo NMR spectroscopy is a valuable and sensitive tool for probing the electronic characteristics of Mo^{+VI} nitrides, the ^{14}N NMR shielding of the nitride ligand is rather insensitive to the nature of the co-ligands on the molybdenum central atom. All complexes exhibit signals within a similar range (Figure 24).

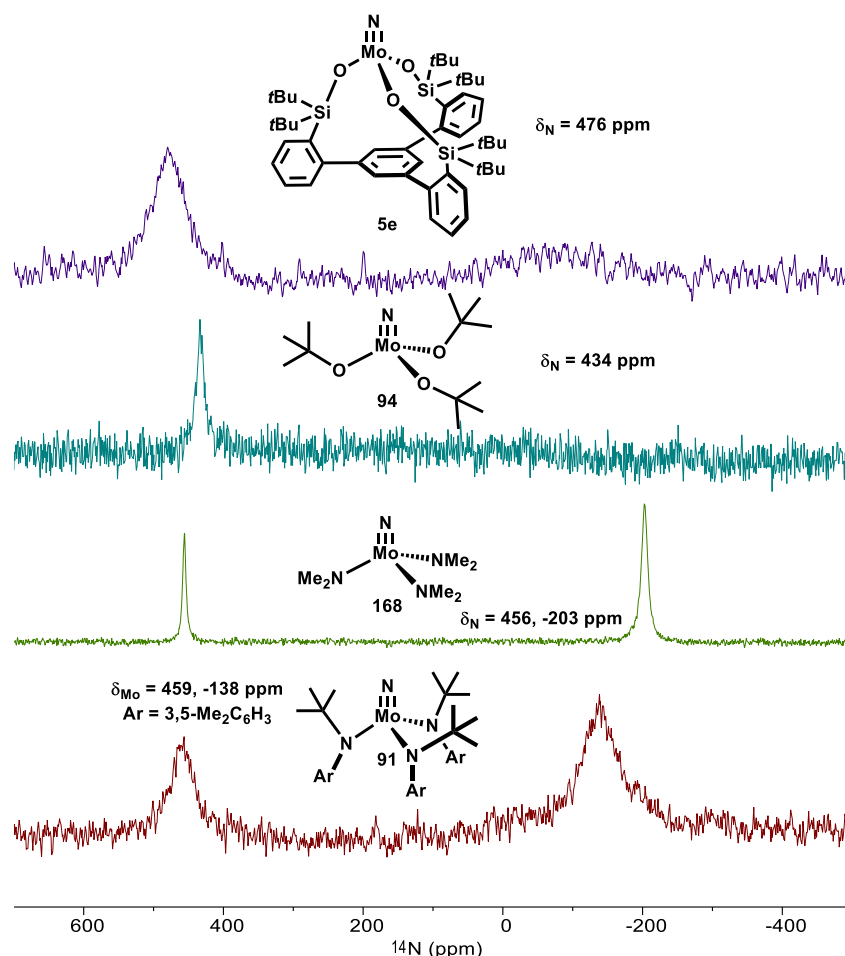
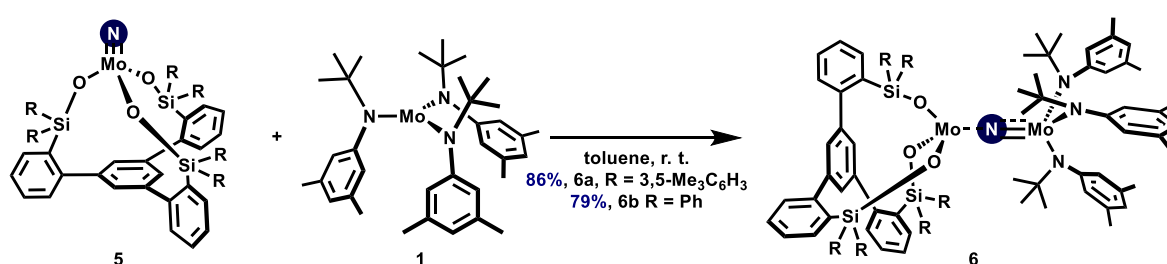


Figure 24. Stacked ^{14}N NMR spectra in $[\text{D}_8]$ -toluene at 333 K of selected Mo nitrides. In collaboration with Dr. Markus Leutzsch.

With the fully characterized nitrides at hand, we turned our attention to the projected nitrogen atom transfer, using the Cummins complex **1** as the potential acceptor. While experiments with a 1:1 mixture of either of the bulky nitrides **5c** and **5d** and the Cummins complex led to a reaction, the resulting green solid product was insoluble in common organic solvents. A complete shutdown of reactivity was observed when complex **5e** was utilized as the donor, likely due to its sterically demanding nature. However, the reactions of both nitrides **5a** and **5b**, which carry bulky aromatic substituents on the Si linkers, with the Cummins complex **1** proceeded smoothly and were accompanied by an instantaneous color change to black. It was possible to isolate the corresponding bridged Mo–N–Mo complexes in 86% (**5a**) and 79% (**5b**) yield, respectively (Scheme 71). All attempts to convert these species to the monomeric or dimeric complexes, either under thermal conditions or by adding a Lewis base, failed.

Incomplete nitrogen atom transfer



Scheme 71. Incomplete nitrogen atom transfer leading to the formation of **6**.

Both complexes were analyzed using X-ray structure determination. Since both structures are very similar, only the structure of **6b** is shown and discussed (Figure 25), while the other structure is reported in the Supporting Crystallographic Information. As expected, the Mo–N–Mo unit exhibits a linear geometry ($178.56(18)^\circ$); yet a distinct asymmetry is evident ($(1.838(3) \text{ \AA})$ Mo1–N1 and $(1.808(3) \text{ \AA})$ Mo2–N1). The apparent weakening of the Mo1–N1 bond supports the hypothesis that the tripodal silanolate is a weaker donor than the anilide ligand, thereby enhancing π backdonation in the Mo2–N1 fragment. This asymmetry, in fact, reminiscent of what had been observed in complex **98**, where the thiolate ligands exhibit reduced donor capacity compared to the anilide ligands. The coordination geometry about each molybdenum atom is closer to trigonal-pyramidal than tetrahedral and the $\text{O}_3\text{Mo–N–MoN}_3$ moiety exhibits a staggered conformation.

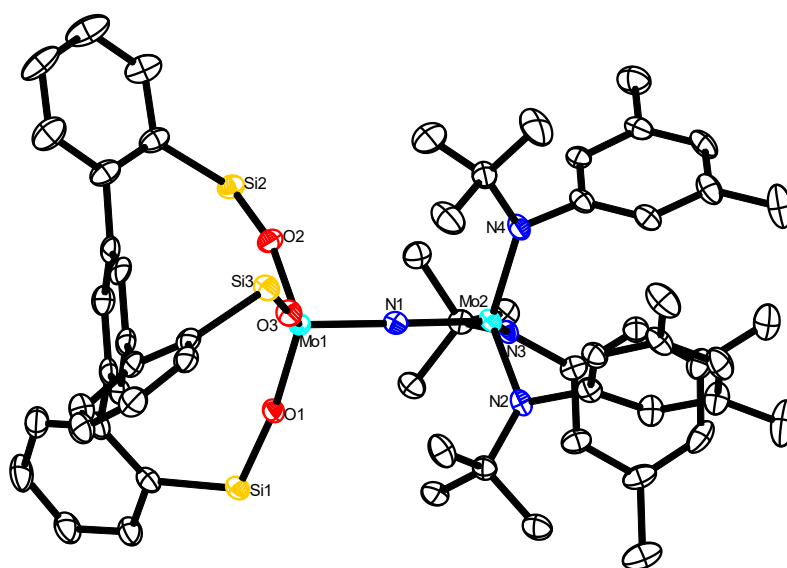
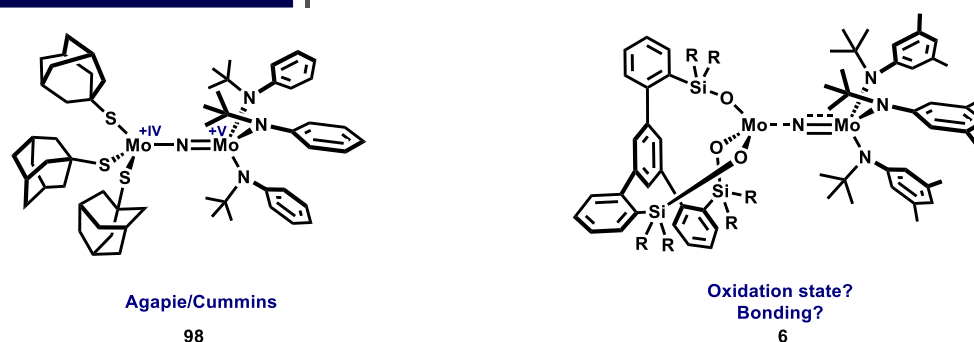


Figure 25. Truncated crystal structure of complex **6b**. The Ph groups, H-atoms and solvent molecules are not shown for clarity.

As mentioned previously, a number of Mo–N–Mo complex has already been reported in the literature. Especially in the case of unsymmetric ligand patterns, questions about the actual bonding situation and consequently the oxidation state of each molybdenum atom arise. For instance, in $\text{AdS}_3\text{Mo–N–Mo}(\text{N}(t\text{Bu})(\text{Ph}))_3$ (**98**), the oxidation state of each molybdenum atom was tentatively assigned to be $[\text{S}_3]\text{Mo}^{+IV}\text{–N–Mo}^{+V}[\text{N}_3]$, based on the different Mo– μN bond lengths (*vide supra*).^[78] This suggestion was subsequently supported by B nard, who performed calculations on a heavily truncated version.^[77] We decided to revisit this proposal by a combined experimental and theoretical approach in collaboration with the group of Prof. Frank Neese (Scheme 72).

Electronic structure of Mo–N–Mo complexes



Scheme 72. Revisiting the electronic character of unsymmetric Mo–N–Mo complexes.

Despite their paramagnetism, the structure of both complexes **6a** and **6b** could be assigned using 1D and 2D NMR spectroscopy. A solution magnetic susceptibility measurement *via* the Evans method revealed the presence of one unpaired electron in complex **6b** (Table 1, Table 2, and Figure 26). The obtained value ($\mu_{\text{eff}} = 2.16(6) \mu_{\text{B}}$ at 298 K) was corrected for the purity of complex **6b**, which was determined to be $90.3\% \pm 1.0\%$ using 1,2,4,5-tetramethylbenzene as an internal standard. The measured susceptibility is consistent with the spin-only value of one unpaired electron ($1.73 \mu_{\text{B}}$). It should be emphasized that the value obtained *via* the Evans method is not corrected for temperature-independent paramagnetism (TIP).

Table 1. Parameters used in the determination of the effective magnetic moment μ_{eff} *via* Evans method.

F_{spectrometer} (Hz)	600200000	
c (mol/L)	0.00664	$\pm 5.00\%$
M (g/mol)	1633.03	
χ_{D} (cm³/mol)	$-8.17 \cdot 10^{-4}$	$\pm 10.00\%$
c (g/L)	10.85	

Table 2. Parameters obtained *via* the Evans method.

T (K)	ΔF_1 (Hz)	ΔF_2 (Hz)	ΔF (Hz)	χ_{m} (l/g)	χ_{m} (cm³/mol)	χ_{P} (cm³/mol)	μ_{eff} (μ_{B})
298	18.84	19.40	19.12 ± 0.40	$7.01 \cdot 10^{-10}$	$1.14 \cdot 10^{-3} \pm 6.20 \cdot 10^{-5}$	$1.96 \cdot 10^{-3} \pm 1.02 \cdot 10^{-4}$	2.16 ± 0.06

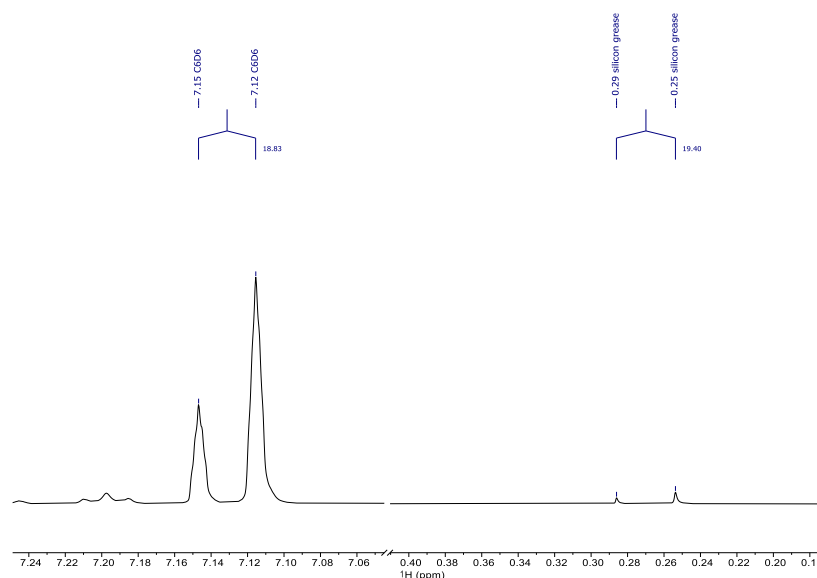


Figure 26. ¹H NMR spectrum of **6b** for the determination of μ_{eff} using the Evans method: [D₆]-benzene, 298 K, 600 MHz. In collaboration with Dr. Markus Leutzsch.

SQUID magnetometry data further corroborated that the same spin state persists in the solid state. Starting at $1.53(6) \mu_B$ (2.00 K) the curve of the $\chi_P T$ value plotted against the temperature sharply increases, reaching $1.56(6) \mu_B$ (6.16 K). Beyond this point, measurements from 6.16 K to 300 K revealed that compound **6b** exhibits pronounced TIP, as evidenced by the steady, linear rise in the $\chi_P T$ value with increasing temperatures. The value of $2.01(7) \mu_B$ recorded at 300 K aligns well with the $2.16(6) \mu_B$ obtained *via* the Evans method at 298 K. Upon correction for TIP, the refined value at 300 K is $1.55(6) \mu_B$, corresponding to $g_{\text{avg}} = 1.89$. This deviation from the value of a free electron ($g = 2.002319$) can be attributed to the presence of spin-orbit coupling.

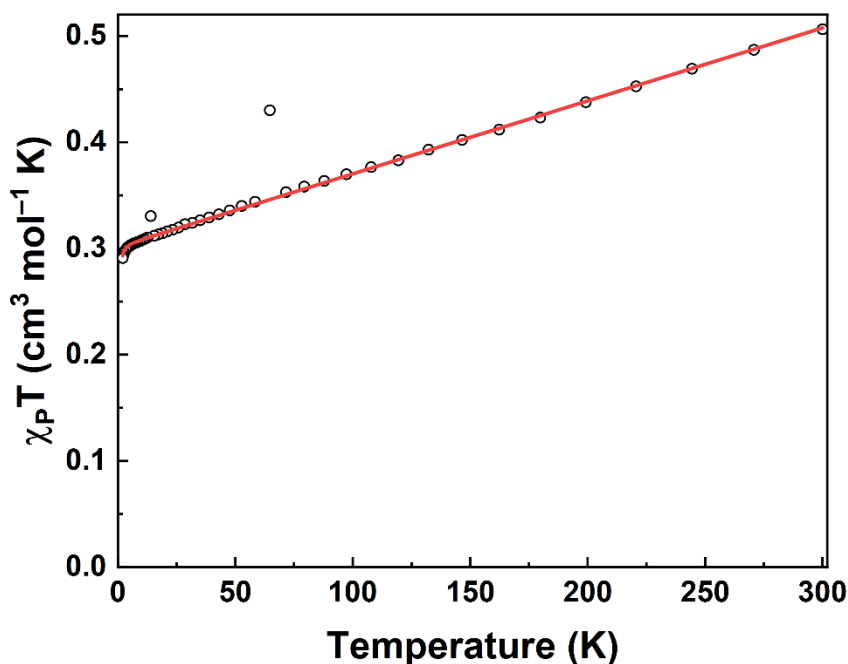


Figure 27. Direct current paramagnetic susceptibility data for **6b** from 2.00 to 300 K (black dots) and fit to the data with the spin Hamiltonian model (red trace). The outliers at 13.96 and 64.65 K were excluded from the model. Fit parameters: 9.7% $S = 0$ (diamagnetic) impurity (fixed based on the 90.3% reported NMR purity), TIP = $0.0006866 \text{ cm}^3 \text{ mol}^{-1}$, $g_{\text{avg}} = 1.89$, residual = 0.00198. In collaboration with Dr. Daniel SantaLucia.

To elucidate the electronic structure of complex **6b**, we resorted to DFT calculations (B3LYP functional, def2-TZVP basis set, effective core potentials at the molybdenum atoms). Initially, it was determined whether complex **6b** should be classified as a $\text{Mo}^{+\text{IV}}/\text{Mo}^{+\text{V}}$ system with three unpaired electrons, where a high-spin ($S = 1$) $4d^2$ $\text{Mo}^{+\text{IV}}$ center is antiferromagnetically coupled to an $S = 1/2$ $4d^1$ $\text{Mo}^{+\text{V}}$, or whether it is more aptly described as containing only one unpaired electron (either $\text{Mo}^{+\text{III}} / \text{Mo}^{+\text{VI}}$ or $\text{Mo}^{+\text{IV}}/\text{Mo}^{+\text{V}}$ with $S = 0$ for $\text{Mo}^{+\text{IV}}$). Computational results favored an $S = 1/2$ state over a local $\text{Mo}^{+\text{IV}}$ high-spin configuration.

An in-depth bonding analysis necessitates the consideration of 11 valence electrons. Five LMOs (localized molecular orbitals) and one SOMO (singly occupied molecular orbital) were identified as quintessential for describing the electronic structure of **6b** (Figure 28). The σ orbital is delocalized across the entire Mo–N–Mo fragment, representing a three-centered, two-electron bond, while the μN 2s orbital describes a nitrogen-centered lone pair. Two additional LMOs were unequivocally established to be $\text{Mo}^{[\text{N}]}-(\mu\text{N})$ π -bonding orbitals. The final doubly occupied orbital corresponds to a $\text{Mo}^{[\text{O}]}-(\mu\text{N})$ π -bonding interaction, which also exhibits a $\text{Mo}^{[\text{N}]}-(\mu\text{N})$ π -antibonding character.

The SOMO orbital contains the unpaired electron, which is asymmetrically distributed across the Mo–N–Mo unit. A Löwdin spin population analysis (0.91 $\text{Mo}^{[\text{O}]}$, 0.02 $\text{Mo}^{[\text{N}]}$ and 0.08 μN) revealed that

this unpaired electron is predominantly localized on the Mo^[O] atom, suggesting that this fragment is best seen as either low-spin Mo^{+III} or as Mo^{+V}. Given that the formal bond orders of Mo^[N]- μ N and Mo^[O]- μ N amount to 2.5 and 0.5, respectively, a description as a [O₃]Mo^{+III}-N-Mo^{+VI}[N₃] complex is considered more likely.

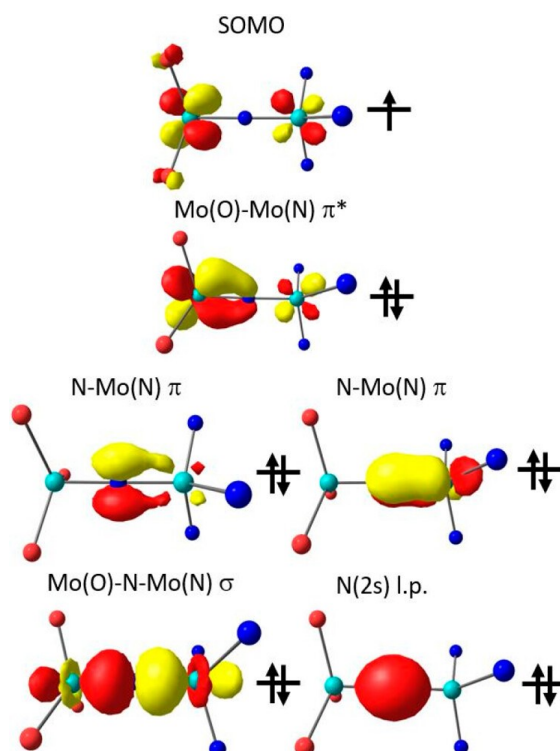


Figure 28. SOMO of **6b** and the five LMOs of the Mo^[N]-(μ N)-Mo^[O] core of this complex showing the σ and π bonds with the bridging ligand and a Mo-Mo π^* bond. Atom color code: light blue for molybdenum, blue for nitrogen, and red for oxygen. In collaboration with Dr. Maurice van Gastel.

To substantiate the proposed oxidation state, complex **6b** was analyzed by EPR spectroscopy (Figure 29). The recorded EPR spectrum appeared relatively broad and featureless yet revealed a distinct pattern. This EPR spectrum exhibited one positive g-shift ($g_z = 2.24$) and two negative g-shifts ($g_x = 1.77$ and $g_y = 1.83$).

In general, negative g-shifts are expected when an electron is promoted from the SOMO to a higher-lying orbital, whereas positive g-shifts are observed when an electron is promoted from a doubly occupied orbital into the SOMO. To illustrate these scenarios, one might consider cases where only a single type of promotion is allowed.

One such example is Cu^{+II}, where the only viable promotion of the electron is from a lower-lying orbital into the SOMO, consequently leading to positive g-shifts. Conversely, in Mo^{+V} complexes, the electron can only be promoted from the SOMO into a higher-lying empty orbital, solely resulting in negative g-shifts. As complex **6b** exhibits one positive and two negative g-shifts, it must be interpreted as a Mo^{+III}/Mo^{+VI} species.

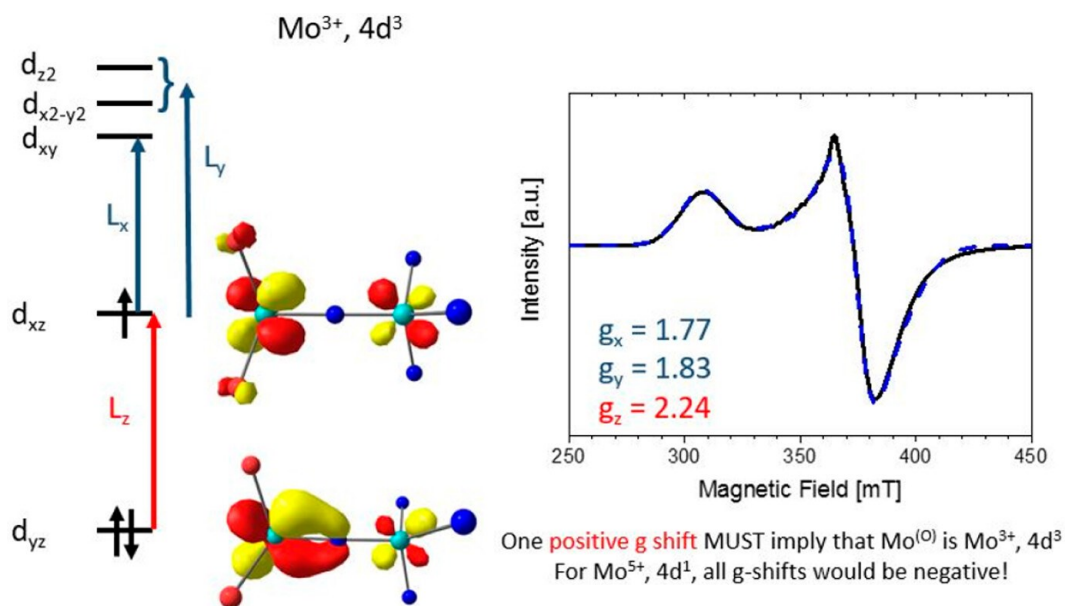
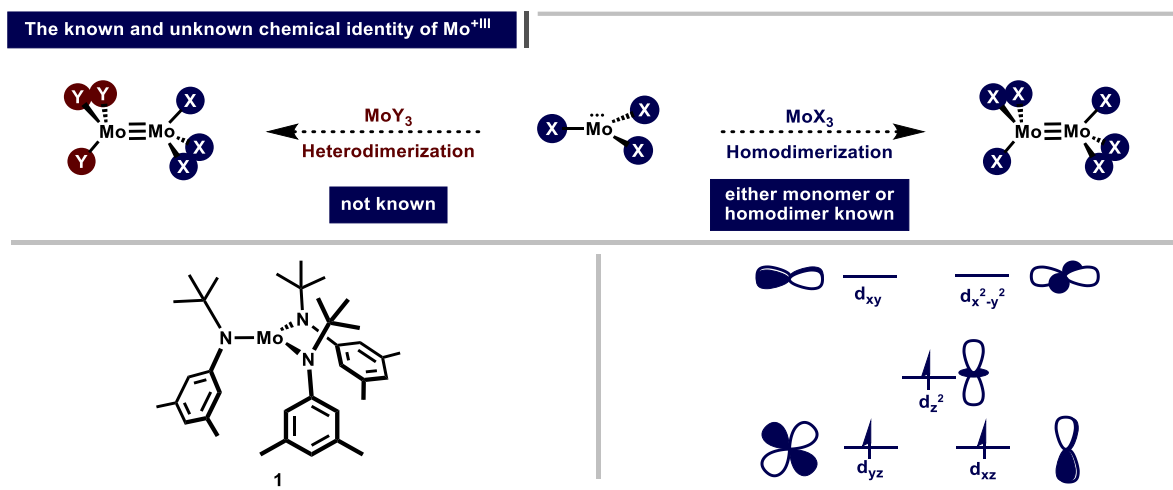


Figure 29. Continuous wave (cw) EPR spectrum of a 4.2 mM frozen solution of **6b** in toluene. Experimental conditions: $T = 10 \text{ K}$, $\nu = 9.629 \text{ GHz}$, $P_{\text{mw}} = 2 \text{ mW}$, modulation amplitude 0.5 mT. Also included is an Easyspin simulation (dotted line) with parameters $g = 1.77, 1.83, 2.24$. Given the sensitivity of the complex, a spin quantification resulted in a spin concentration of 3.3 mM. Also included is a schematic overview of the $[\text{O}_3]\text{Mo}$ 4d orbitals relevant for rationalizing the observed g shifts. In collaboration with Dr. Maurice van Gastel.

1.5 Summary (Part I)

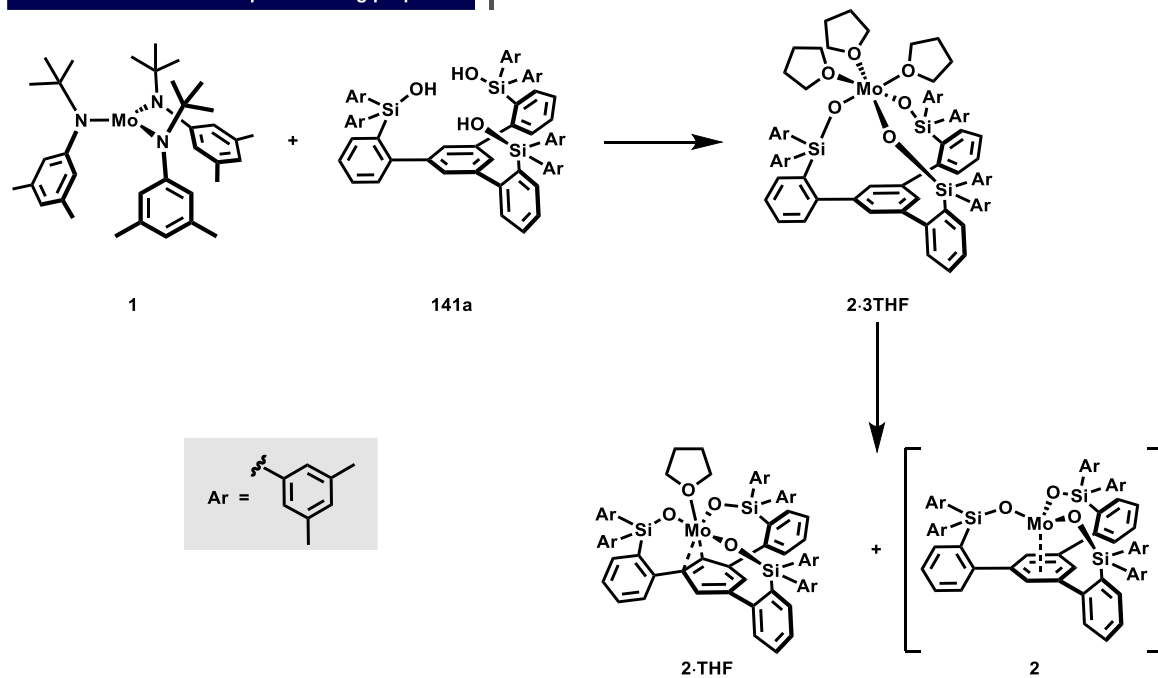
Dimer formation is the signature reactivity of Mo^{III} complexes, shaping their unique chemical identity. This tendency arises from the formation of a thermodynamically strong $\sigma^2\pi^4$ triple bond, which involves bonding interactions between the d_{z^2} , d_{xz} , and d_{yz} orbitals of two monomeric triradical fragments. While numerous homodimeric Mo^{III} complexes are well-known, their corresponding monomeric complements coordinated by the same ligand have remained elusive.^[1-2] A breakthrough occurred in 1995, when Cummins and co-workers unveiled the synthesis of a kinetically stable monomeric Mo^{III} complex **1** featuring three bulky anilide ligands.^[3] This discovery was of utmost importance, as it challenged the long-standing paradigm that Mo^{III} fragments must engage in metal-metal triple bonding. By obviating homodimerization, the energy typically released during the formation of the strong triple bond was essentially “stored”, enabling the resulting highly reactive monomeric complex **1** to engage in a wide array of three-electron redox processes. Against this backdrop, it is hardly surprising that, to date, neither self-dimerization of **1** nor heterodimerization with other monomeric Mo^{III} fragments has been reported (Scheme 73).



Scheme 73. Top: Relationship between monomeric, homodimeric, and heterodimeric Mo^{III} complexes. Bottom left: Structure of the Cummins complex **1**. Bottom right: Simplified representation of the d-orbital splitting of a trigonal-planar Mo^{III} fragment.

Aiming to isolate a monomeric Mo^{III} complex, we designed a bulky tripodal silanolate ligand. The novel ligand showcased remarkable adaptive binding properties, enabling the formation of three distinct monomeric complexes. The first is **2·3THF**, in which the Mo^{III} center remains entirely disengaged from the underlying arene system. The other two species, **2·THF** and **2**, feature an interaction of the Mo^{III} center with the basal arene moiety of the tripodal silanolate ligand in either an η^2 or a η^6 fashion, depending on the number of coordinating solvent molecules (Scheme 74). Notably, **2·THF** activates small molecules such as N_2O or 1,1-dichloropropane.

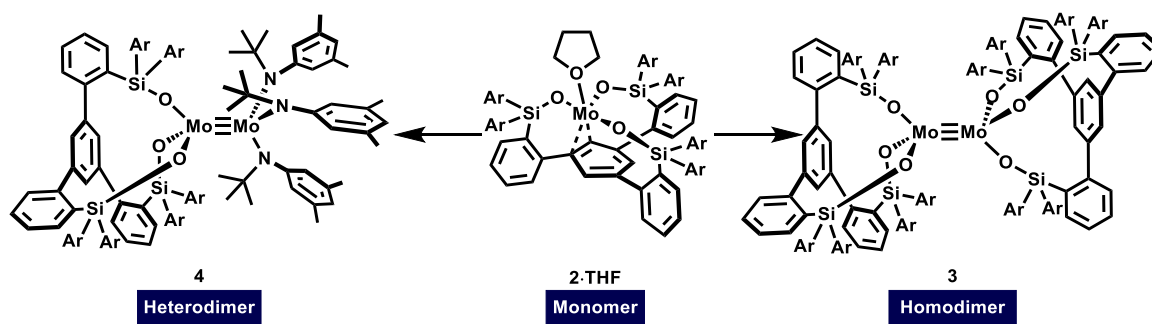
A Mo^{+III} monomer with adaptive binding properties



Scheme 74. Monomeric Mo^{+III} complexes with a tripodal silanolate ligand feature adaptive binding properties.

Next, we challenged the longstanding doctrine in Mo^{+III} chemistry that either the monomer or the dimer is formed. For the first time, monomeric (**2**, **2·THF**, and **2·3THF**), homodimeric (**3**), and heterodimeric (**4**) complexes, all incorporating the same ligand, were synthesized (Scheme 75). The formation of heterodimer **4** is without precedent, as such X₃Mo≡MoY₃ species were previously unknown in the literature. Notably, complex **4** features by far the longest triple bond between two unbridged Mo^{+III} centers, each with CN = 4 (CN = coordination number). Although the triple bond is unusually long, it is remarkably robust: once formed, its monomeric building blocks were never observed. Complex **4** incorporates the exceedingly bulky Cummins complex **1** as one of its subunits, an astounding observation, given that metal-metal bonding had never previously been observed for complex **1**.

A complete ensemble of Mo^{+III} complexes

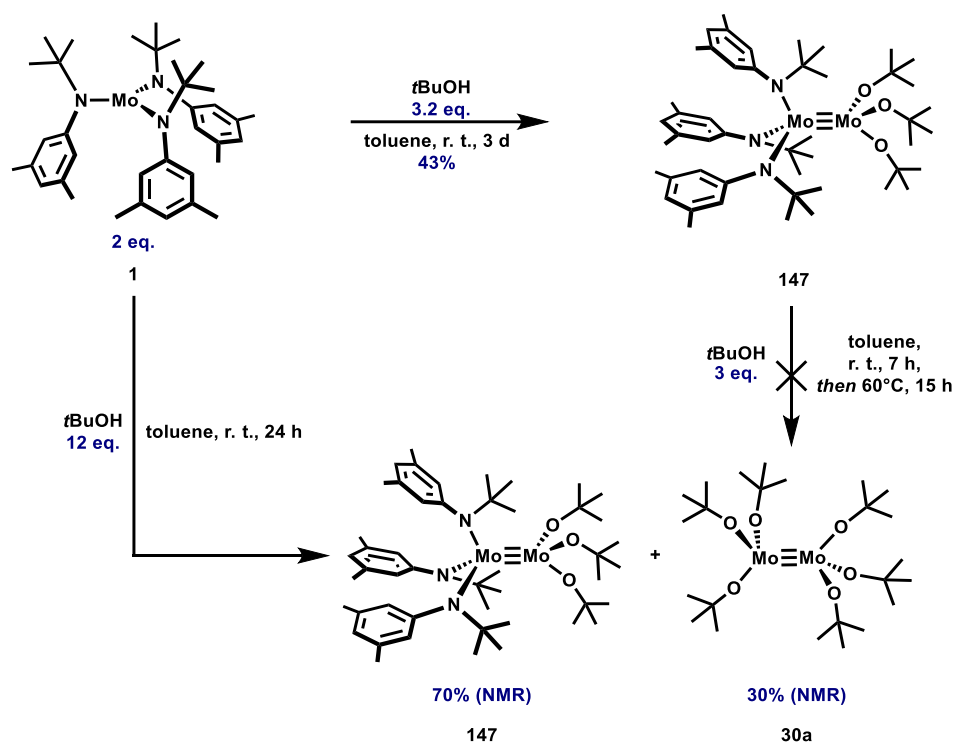


Scheme 75. A complete ensemble of homodimeric, monomeric, and heterodimeric Mo^{+III} complexes.

This intricate and unprecedented heterodimerization process was not caused by the peculiar tripodal ligand, as the use of simple *t*BuOH as the protonolysis reagent also resulted in the formation of a heterodimeric complex **147**. A series of experiments indicated that the heterodimerization was a kinetically driven process. Since all heterodimeric complexes exhibited unusually long yet robust triple bonds, these species were also studied by ⁹⁵Mo NMR spectroscopy, complemented by computational

studies of their electronic structures. Notably, no correlation was found between the paramagnetic shielding tensor and the Mo–Mo bond length. Since the paramagnetic shielding tensor is innately linked to the frontier orbitals *via* the Ramsey equation, the surrounding ligands were found to play a pivotal role. Depending on their nature, some ligand-based orbitals displayed energies comparable to the σ and π -bonding orbitals. While these ligand-based orbitals do not contribute directly to the Mo–Mo bond, they influence the paramagnetic shielding tensor.

Heterodimerization with *t*BuOH

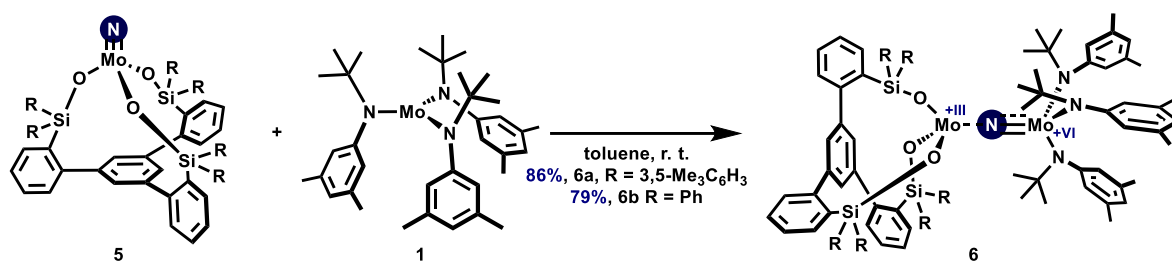


Scheme 76. Protonolysis of **1** with *t*BuOH favors heterodimerization over homodimerization.

Nitrogen atom transfer was subsequently explored as another conceivable entry into low-valent molybdenum(III) chemistry. In a first step the novel nitrides **5** were synthesized and characterized by means of X-ray crystallography, ^{95}Mo and ^{14}N NMR spectroscopy. Upon reaction of selected nitrides with the Cummins complex **1** as the acceptor, paramagnetic and highly sensitive bridged nitrides **6** were formed.

A detailed picture of the electronic structure was sought by a combination of experimental and computational tools, including SQUID magnetometry, EPR spectroscopy, and a Löwdin spin population analysis. In contrast to prior understanding in the literature, it was found that the unsymmetric Mo–N–Mo complex **6b** is actually a $[\text{O}_3]\text{Mo}^{\text{III}}\text{--N--Mo}^{\text{VI}}[\text{N}_3]$ species, which is in stark contrast to the literature known species **98** described as a $[\text{S}_3]\text{Mo}^{\text{IV}}\text{--N--Mo}^{\text{V}}[\text{N}_3]$ complex (Scheme 77).

Incomplete nitrogen atom transfer



Scheme 77. Incomplete nitrogen atom transfer leading to the formation of **6**.

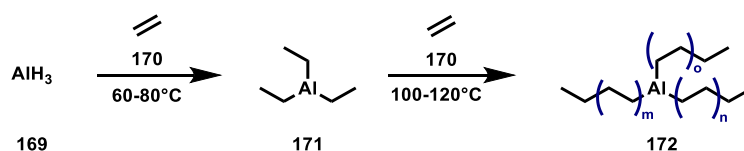
2 Synthetic Strategies for Diamagnetic Iron Carbenes

2.1 Introduction: From Ziegler's Mülheim Polyethylene Process to Olefin Metathesis

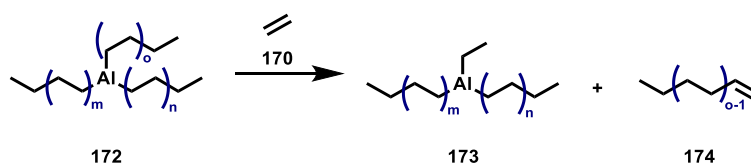
One of the breakthroughs that arguably initiated the explosive growth of modern organometallic chemistry can be traced back to the Mülheim process for producing low-pressure polyolefins. This process was discovered by Karl Ziegler, who was then director of the Max-Planck-Institut für Kohlenforschung.^[145-147]

The origins of this discovery lie in fundamental observations made in the realm of organoaluminum chemistry. Ziegler found that organoaluminum hydrides such as AlH_3 (**169**), at 60-80°C, undergo stepwise insertion of ethylene to sequentially yield AlEtH_2 , AlEt_2H , and ultimately AlEt_3 (**171**). At elevated temperatures (100-120°C) insertion into Al-C bonds also becomes possible. However, controlled synthesis of $\text{Al}(n\text{Bu})_3$ could not be achieved, as all Al-C bonds are equally reactive. Consequently, before the final *n*-butyl ligand is formed, insertion may already proceed from an existing *n*-butyl group to an *n*-hexyl group, resulting in a statistical mixture of organoaluminum species **172**.^[148] This method, known as the "Aufbau" ("chain-growth") reaction, is an oligomerization process. Ziegler stated that this approach could produce paraffins with molecular weights of up to 2500-3000 g/mol upon hydrolysis, but no true polyethylene was formed which typically exhibits polymer weights of ≥ 20000 -30000 g/mol. The "limited" molecular weight was attributed to a side reaction, that Ziegler termed "Übertragungs" ("chain-transfer") reaction. After approximately 100 consecutive ethylene insertion steps, the growing organoaluminum species **172** underwent β -hydride elimination, releasing an oligomer **174**, accompanied by insertion of the ethylene molecule into the newly formed Al-H bond.^[148] Ziegler initially believed that this limitation was a fundamental constraint, concluding that the synthesis of true polyethylene was unattainable by this method (Scheme 78).^[149]

The Aufbau reaction



The Übertragungs reaction

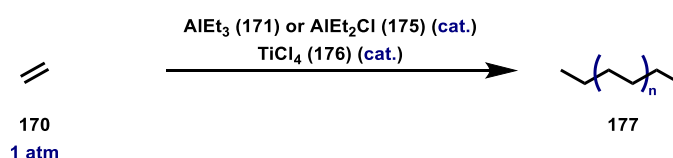


Scheme 78. The "Aufbau" ("chain-growth") and the "Übertragungs" ("chain-transfer") reaction.

At the end of the year 1952, Erhard Holzcamp, one of his doctoral students, made an intriguing observation. Upon repeating the Aufbau reaction under standard conditions (AlEt_3 (**171**), 100 atm of ethylene at 100°C), he found that no paraffin was formed, but rather he recovered AlEt_3 (**171**) along with 1-butene. As this reaction had been performed many times before, this was a striking observation. After an extensive investigation, the origin of this unexpected reactivity was identified. Nickel-catalyzed hydrogenations had been performed before in the employed autoclave. Before performing the Aufbau reaction, the doctoral student had carefully washed the autoclave with nitric acid and subsequently phosphate containing detergent, thus forming trace amounts of nickel phosphate. Upon reaction with

AlEt_3 (**171**), colloidal Ni was formed.^[148] This colloidal nickel together with traces of acetylene in the ethylene, suppressed the formation of oligomeric organoaluminum species, only leading to the dimerization of ethylene to form 1-butene.^[147] This effect was subsequently called the “Nickel effect”.^[150] Subsequently, Ziegler tasked Heinz Breil, then a diploma student at the institute, with a systematical screening of the periodic table in order to determine whether other transition metal additives could similarly influence the course of the Aufbau reaction. Initially, this approach was not very fruitful: Breil found that only platinum and cobalt additives exhibited effects comparable to those of nickel compounds. However, under his standard conditions (AlEt_3 (1 eq.), transition metal additive (0.01 eq.), and ethylene (100-150 atm) at 100-110°C), he eventually made a spectacular discovery that would fundamentally change catalysis research. On October 26, 1953, as the result of a reaction using $\text{Zr}(\text{acac})_4$ as the transition metal additive, he was able to isolate solid white polyethylene. Further investigations revealed that TiCl_4 (**176**) was the most effective co-catalyst and that other organoaluminum species such as AlEt_2Cl (**175**) also were viable initiators. It was subsequently demonstrated that efficient polymerizations could even occur at ambient ethylene pressure, which ultimately led to the development of the Ziegler process as it is known today (Scheme 79).^[146-148, 151]

The Mülheim polyethylene process

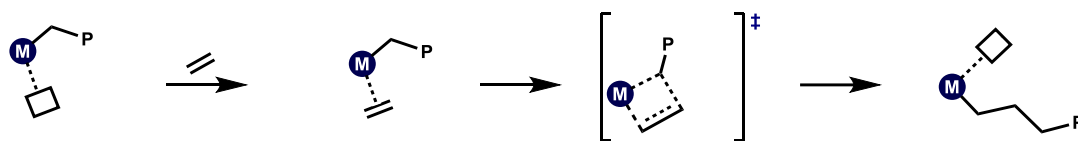
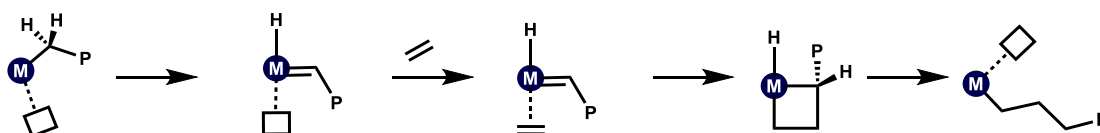


Scheme 79. The Mülheim polyethylene process discovered by Karl Ziegler.

Ziegler informed Montecatini, an Italian company, of his findings, as he had a licensing agreement with them regarding his work on organoaluminum chemistry. Giulio Natta, a chemist closely associated with this company, used the information about Ziegler’s newly discovered heterogeneous catalyst system to investigate the polymerization of other olefins. Whereas Heinz Martin, a student in Ziegler’s laboratory, demonstrated that the Ziegler system not only copolymerizes ethylene and propylene, but also polymerizes propylene, it was Giulio Natta who discovered that the polymerization of propylene occurs stereospecifically and therefore yielded crystalline isotactic polypropylene.^[151] Both, Ziegler and Natta were jointly awarded the Nobel Prize in Chemistry in 1963; Karl Ziegler for the discovery of an entirely new method for the polymerization of olefins, and Giulio Natta for the discovery that the Ziegler catalyst system enables the stereoregular polymerization of propylene into crystalline isotactic polypropylene.^[147, 151]

Today, the most widely accepted mechanism for the Ziegler catalysis is the Cossee-Arlman mechanism (Scheme 80).^[152-159] Accordingly, the olefin initially binds to the metal center, followed by insertion into the metal-alkyl bond.

However, several years after Ziegler’s groundbreaking discovery, other laboratories found that modified Ziegler-type catalyst systems could also polymerize certain cyclic olefins, not only yielding products derived from an insertion polymerisation, but also producing polymers that arise from ring-opening metathesis polymerization (ROMP).^[145, 160-161] These observations led to the proposal of the Rooney-Green mechanism, in which a transition-metal alkylidene hydride is initially generated by a 1,2-hydride shift, followed by a [2+2] cycloaddition of the olefin to form a metallacyclobutane. Subsequently, C–H reductive elimination leads to the formation of the saturated polymer product.^[162]

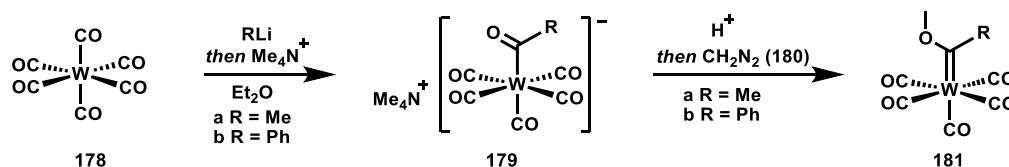
Cossee-Arlman mechanism**Green-Rooney mechanism**

Scheme 80. Selected mechanisms for the Ziegler process. P = polymer chain.

The potential involvement of metal carbenes as intermediates in the ROMP of cyclic olefins using certain Ziegler-type catalyst systems was not recognized at the time, as transition metal carbenes were considered elusive species in 1960. The Rooney-Green mechanism was proposed almost 20 years later, during a period of intense debate over the mechanism of the olefin metathesis reaction.^[162-170] Nevertheless, this example compellingly illustrates the interconnection between the fields of Ziegler catalysis and olefin metathesis.

Another important example is the Phillips Petroleum process, in which molybdenum- or tungsten-based catalysts converted propylene into ethylene and butylene.^[171] The origin of the name “olefin metathesis” dates back to 1967, when Nissim Calderon discovered that a combination of WCl_6 , ethanol, and $EtAlCl_2$ catalyzed the scrambling of internal olefins; a reaction he named “olefin metathesis” in the same publication.^[161, 172]

In fact, the first transition metal carbene was isolated in 1964 by Ernst Otto Fischer at the Technical University of Munich, following his tremendous contributions to the structural elucidation of ferrocene in 1952, alongside Wilkinson, Woodward, and others.^[173-177] The synthesis of the first carbene began with the nucleophilic attack of $PhLi$ or $MeLi$ on the CO ligand of $W(CO)_6$ (**178**), followed by cation exchange to precipitate the NMe_4 salt **179**. Protonation with acid and subsequent treatment with CH_2N_2 , yielded carbene **181** (Scheme 81).^[178-179] Related carbene complexes (with $M = Cr, Mo, W, \dots$) were discovered, typically featuring neutral co-ligands and heteroatoms bonded to the carbene carbon. This class of carbenes later became known as Fischer carbenes.

The first Fischer carbene

Scheme 81. The synthesis of the first Fischer carbene **181**.

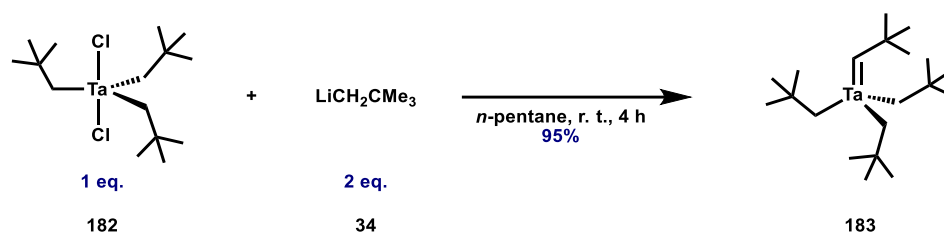
Only a few years later, Richard R. Schrock, at that time a researcher at DuPont, was inspired by Wilkinson’s synthesis of $W(CH_3)_6$, a homoleptic alkyl complex that was stable at room temperature. This compound was an exception, as methyl complexes based on Ti^{+IV} , Zr^{+IV} , or Hf^{+IV} are typically unstable

at room temperature. Since tantalum is positioned adjacent to tungsten in the periodic table, Schrock concluded that he could potentially prepare stable alkyl complexes of tantalum.^[170, 180]

Initial experiments involved the reaction of the literature-known $\text{TaCl}_2(\text{CH}_3)_3$ with MeLi, eventually yielding the targeted homoleptic species $\text{Ta}(\text{CH}_3)_5$.^[181] To probe the limits of steric hindrance in such alkyl complexes, Schrock attempted an analogous synthesis of $\text{Ta}(\text{CH}_2\text{CMe}_3)_5$, starting from $\text{TaCl}_2(\text{CH}_2\text{CMe}_3)_3$ (**182**).^[20] However, this reaction did not yield the desired penta-alkyl species. Instead, it led to the discovery of an entirely unprecedented class of compounds: the Schrock alkylidenes.

Although the exact mechanism remains uncertain, studies by Schrock indicate that the formation of the alkylidene **183** likely does not involve transient $\text{Ta}(\text{CH}_2\text{CMe}_3)_5$. Instead, it appears to involve a hitherto unknown inter- or intramolecular α -hydrogen abstraction starting from $\text{TaCl}(\text{CH}_2\text{CMe}_3)_4$. This is followed by salt metathesis with $\text{LiCH}_2\text{CMe}_3$ (**34**), ultimately yielding $(\text{Me}_3\text{CH}_2\text{C})_3\text{Ta}=\text{CHCMe}_3$ (**183**) (Scheme 82).^[182]

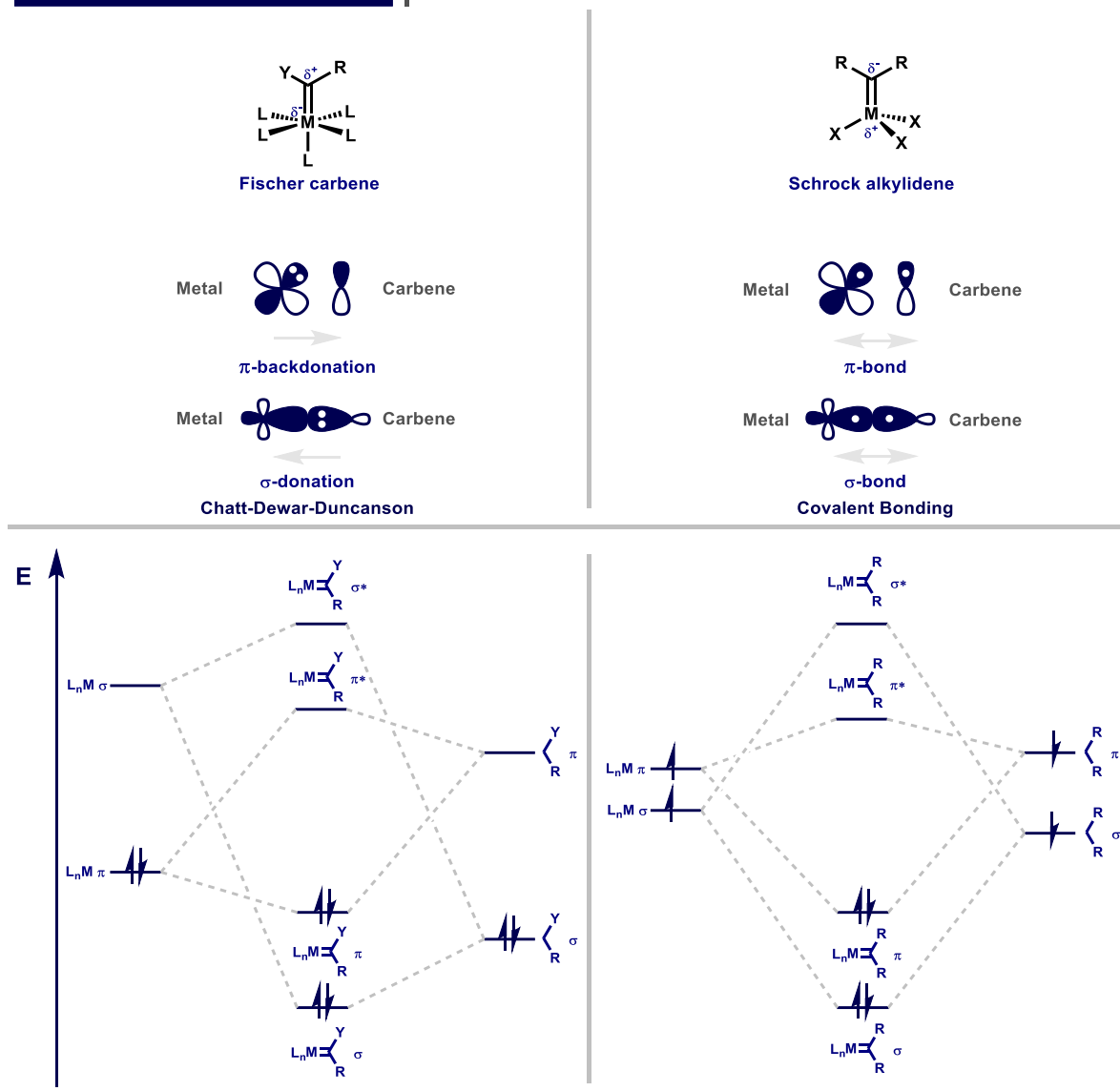
The first Schrock alkylidene



Scheme 82. The synthesis of the first Schrock alkylidene **183**.

The classes of carbenes discovered by Fischer and Schrock represent two distinct extremes (Scheme 83). Fischer carbenes feature a nucleophilic metal atom and an electrophilic carbene carbon, which is typically bound to a heteroatom fragment Y.^[179] As mentioned above, the co-ligands in these complexes are generally neutral L-type ligands and the carbene ligand is considered as a neutral ligand in a singlet state. Bonding is best described by interactions with a singlet metal fragment using the Chatt-Dewar-Duncanson model. The metal in Fischer carbenes is usually a middle or late transition metal.^[157, 183-184]

Conversely, Schrock alkylidenes comprise an electrophilic metal center and a nucleophilic carbene carbon.^[182] Here, the term *alkylidene* is generally used instead of *carbene*, as the alkylidene fragment is considered to be a R_2C^{2-} ligand (with R = H, alkyl). Schrock alkylidenes are typically found for early or middle transition-metal complexes (Ti, Zr, V, Nb, Ta, Mo, W, ...) that bear X-type ligands in which the metal center is in its highest possible oxidation state. Because the metal-carbene bond is stronger than in Fischer carbenes, bonding in these complexes is best described in terms of covalent bonding interactions between a triplet metal fragment and a triplet carbene.^[157, 183-184] The relative energies depicted in Scheme 83 are taken from Hall's theoretical investigation on bonding in transition metal carbene complexes.^[183]

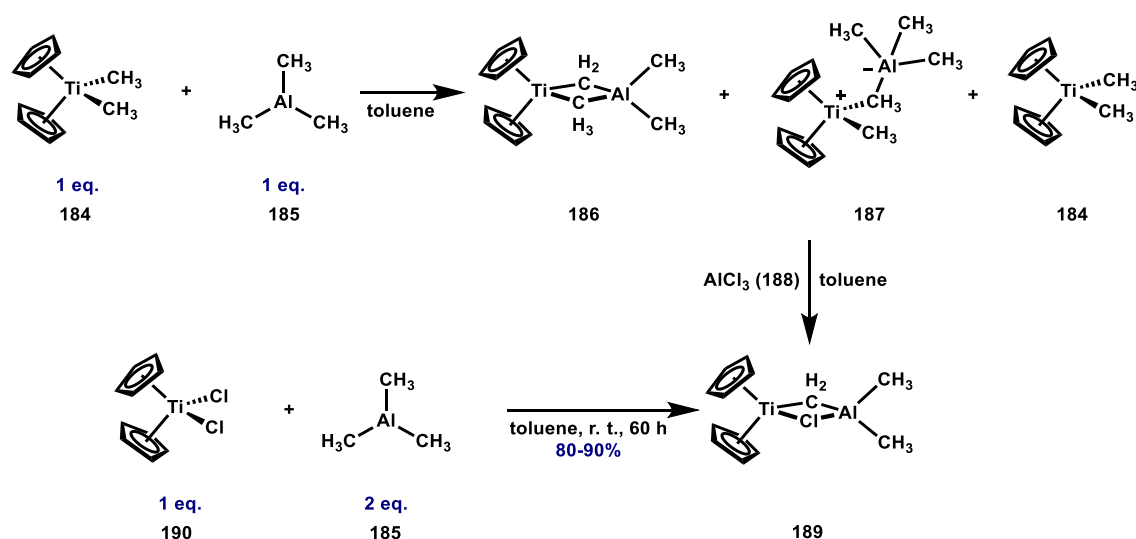


Scheme 83. Top: Characteristics of Fischer and Schrock carbenes. Bottom: Qualitative MO schemes of Fischer and Schrock carbenes. Relative energies were taken from Hall's theoretical study on transition metal carbenes.^[183]

In the 1970s, DuPont was home to numerous chemists, including both established scientists and those who would later rise to prominence. Among the former was Fred N. Tebbe who at the time shared his lab space with Richard Schrock. Tebbe's research was initially centered on developing a deeper understanding of the Ziegler process using homogenous and well-defined organometallic complexes. This approach was necessary, as the original Ziegler process is heterogenous in nature and its mechanism difficult to study.^[185]

In 1974, the same year Schrock that published the first transition-metal alkylidene, Tebbe began investigating the combination of Cp_2TiMe_2 (**184**) and $AlMe_3$ (**185**).^[185] This reaction led to the formation of a bridged carbene $Cp_2Ti(\mu-CH_2)(\mu-CH_3)AlMe_2$ (**186**), which was contaminated with $Cp_2Ti(CH_3)_2$ (**184**) and $Cp_2Ti(CH_3)_2AlMe_3$ (**187**).^[186] Treatment of this mixture with $AlCl_3$ (**188**) generated the bridging carbene $Cp_2Ti(\mu-CH_2)(\mu-Cl)AlMe_2$ (**189**). An optimized procedure for synthesizing $Cp_2Ti(\mu-CH_2)(\mu-Cl)AlMe_2$ (**189**) involved the reaction of Cp_2TiCl_2 (**190**) with two equivalents of $AlMe_3$ (**185**) (Scheme 84).

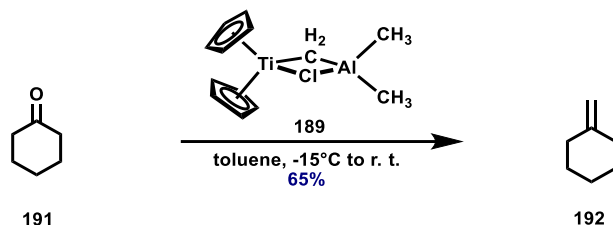
The Tebbe reagent



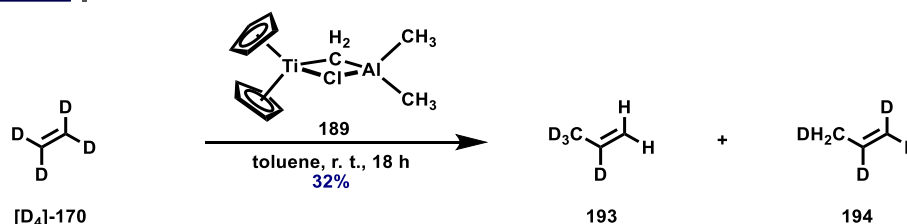
Scheme 84. The synthesis of the Tebbe reagent **189**.

In the same publication, Tebbe confirmed that **189** is a Schrock alkylidene; accordingly, it reacted with ketones *via* nucleophilic attack at the carbonyl carbon, ultimately furnishing the methylenation product **192**. Moreover, **189** reacted with ethylene, resulting in olefin homologation (Scheme 85). Notably, Tebbe stated that isobutylene did not react with **189** under standard conditions. However, the addition of NEt₃ or THF promoted cyclopropanation, albeit in low yield, to afford 1,1-dimethylcyclopropane.

Carbonyl methenylation



Olefin homologation



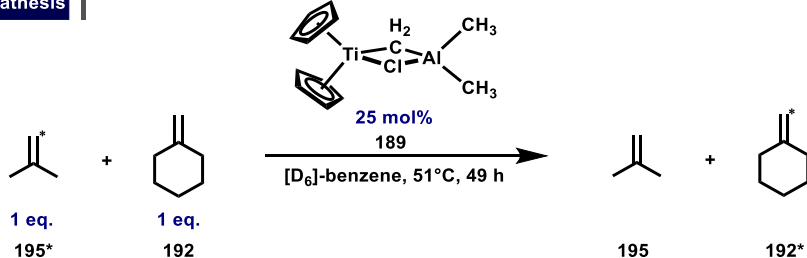
Scheme 85. The Tebbe reagent is a viable methylenation transfer reagent.

In a subsequent publication, Tebbe demonstrated that **189** catalyzes the metathesis of isobutylene and methylenecyclohexane.^[187] While the direct reaction with isobutylene had been missed previously, the metathesis reaction was unambiguously confirmed by ¹³C labeling studies. These revealed that isobutylene binds selectively through its terminal H₂C group to the metal center, leading to reformation of the methylenide and concomitant release of isobutylene. This work stands among the earliest reported examples of olefin metathesis catalyzed by a well-defined transition metal alkylidene (Scheme 86).^[145]

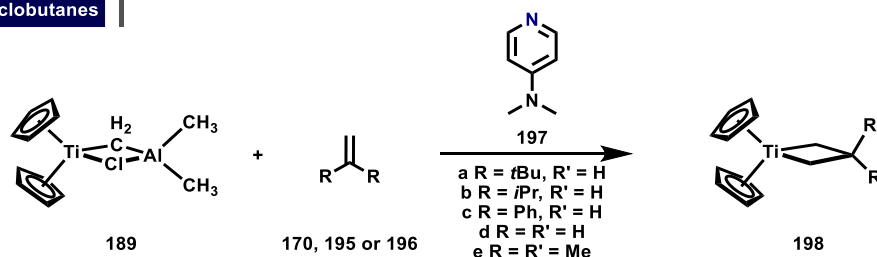
At the outset of his career, Robert H. Grubbs became deeply intrigued by the mechanism of olefin metathesis. When he became aware of Tebbe's finding, he set out to study the metathesis of **189** with

isobutylene in the presence of Lewis-basic ligands. He discovered that the use of DMAP (**191**) as an additive leads to the formation of metallacyclobutane **198**, which was subsequently characterized by NMR spectroscopy and X-ray diffraction analysis.^[188] Through the influential work of Grubbs, complex **189** gained prominence as the “Tebbe reagent” within the organic chemistry community. Both the Tebbe reagent and metallacycle **198**, often referred to as the “Tebbe-Grubbs reagent”, have since found pervasive utility in organic chemistry.^[185, 189-191] Remarkably, methylenation/RCM cascades using the Tebbe reagent have also proven feasible for polyether synthesis, as vividly exemplified in the total syntheses of Maitotoxin by Nicolaou and Prorcocentin by Fürstner.^[161, 192-194]

Catalytic olefin metathesis



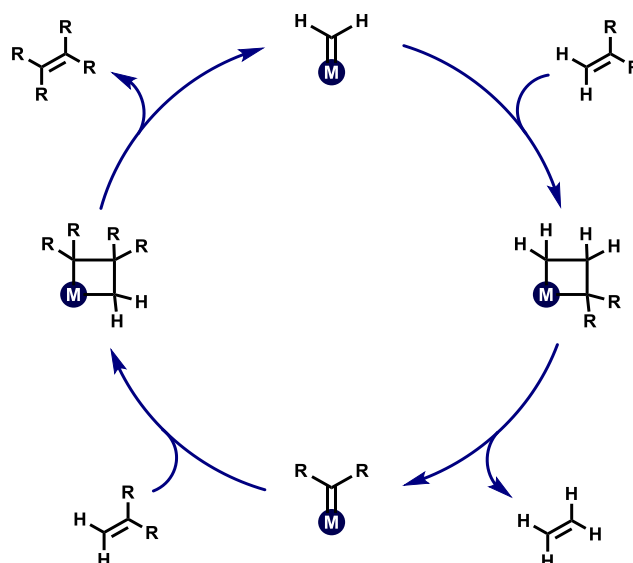
Ti^{IV} metallacyclobutanes



Scheme 86. The Tebbe reagent was one of the first well-defined alkylidene based catalyst systems for olefin metathesis.

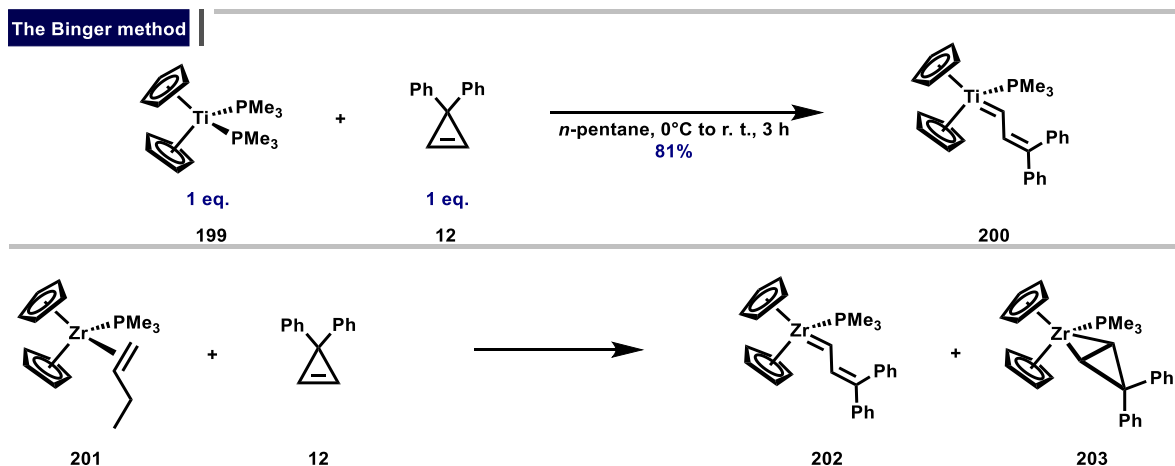
The isolation and characterization of a stable metallacyclobutane by Grubbs, achieved through the use of an active olefin metathesis catalyst system, marked a landmark accomplishment in the field. As such, this work provided compelling experimental validation of the olefin metathesis mechanism proposed by Chauvin in 1970,^[163] although supporting evidence had emerged earlier (Scheme 87).^[164-168] In this mechanism, a metallacyclobutane intermediate is formed through [2+2] cycloaddition, followed by [2+2] cycloreversion to release the olefin product and regeneration of a transition metal carbene.

The Chauvin mechanism



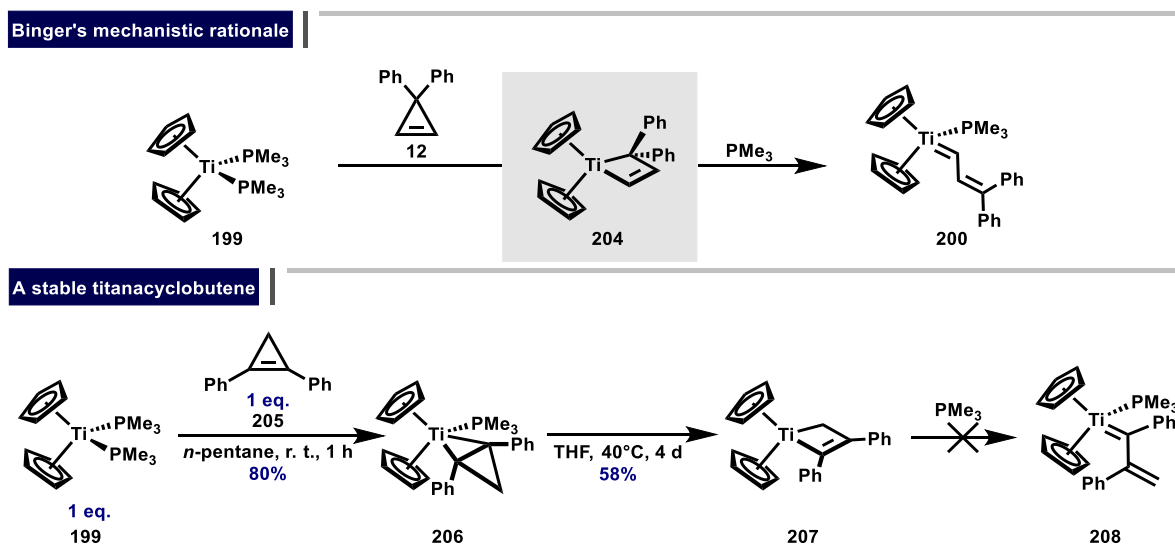
Scheme 87. The Chauvin mechanism for olefin metathesis.

Several years after the discoveries by Tebbe and Grubbs, Paul Binger at the Max-Planck-Institut für Kohlenforschung explored the use of 3,3-disubstituted cyclopropenes as viable carbene initiators using the metallocene-based Ti^{II} precursor $\text{Cp}_2\text{Ti}(\text{PMe}_3)_2$ (**199**). Fortunately, during the reaction, the anticipated vinylic carbene $\text{Cp}_2\text{TiPMe}_3=\text{CH}-\text{CH}=\text{CPh}_2$ (**200**) was formed (Scheme 88). However, when using a Zr^{II} -based precursor **201**, Binger obtained a mixture of the analogous Zr^{IV} alkylidene **202** and the cyclopropene complex **203**, which did not thermally convert to the alkylidene.^[4] Notably, this method had been previously tested with a different cyclopropene and Fe_2CO_9 , also yielding a vinylic carbene together with other species.^[195] The Binger strategy was subsequently expanded to other transition-metal complexes, including ruthenium,^[196-198] tungsten,^[199-201] molybdenum,^[201] cobalt,^[202] rhenium,^[203] gold,^[204] and tantalum.^[205]



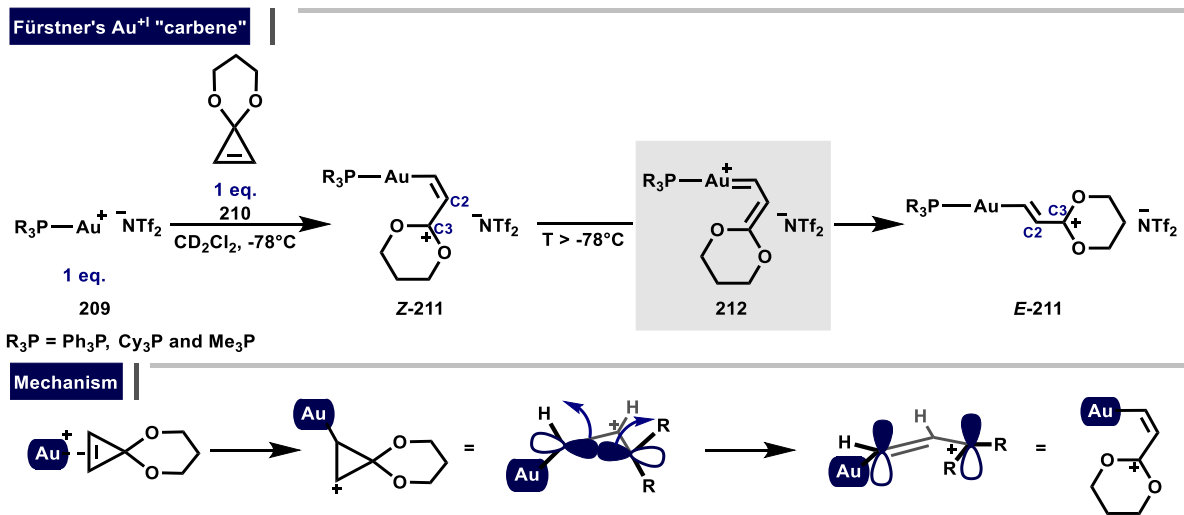
Scheme 88. A method for the synthesis of vinylic carbenes starting from 3,3-disubstituted cyclopropenes by Binger.

Mechanistically, Binger suggested that, after initial oxidative addition of the cyclopropene **12** to the Ti^{II} center, the resulting metallacyclobutene **204** undergoes a [2+2] cycloreversion to furnish the desired vinylic carbene **200** (Scheme 89). This proposal was based on the experimental observation that sterically hindered cyclopropenes undergo oxidative addition to form metallacyclobutene **207**, a compound initially discovered by Tebbe.^[206] However, the resulting sterically congested metallacyclobutene **207** fails to undergo [2+2]-cycloreversion, likely due to the prohibitory steric demands of the substituents.^[207] A similar mechanistic pathway was later proposed by Grubbs.^[208]



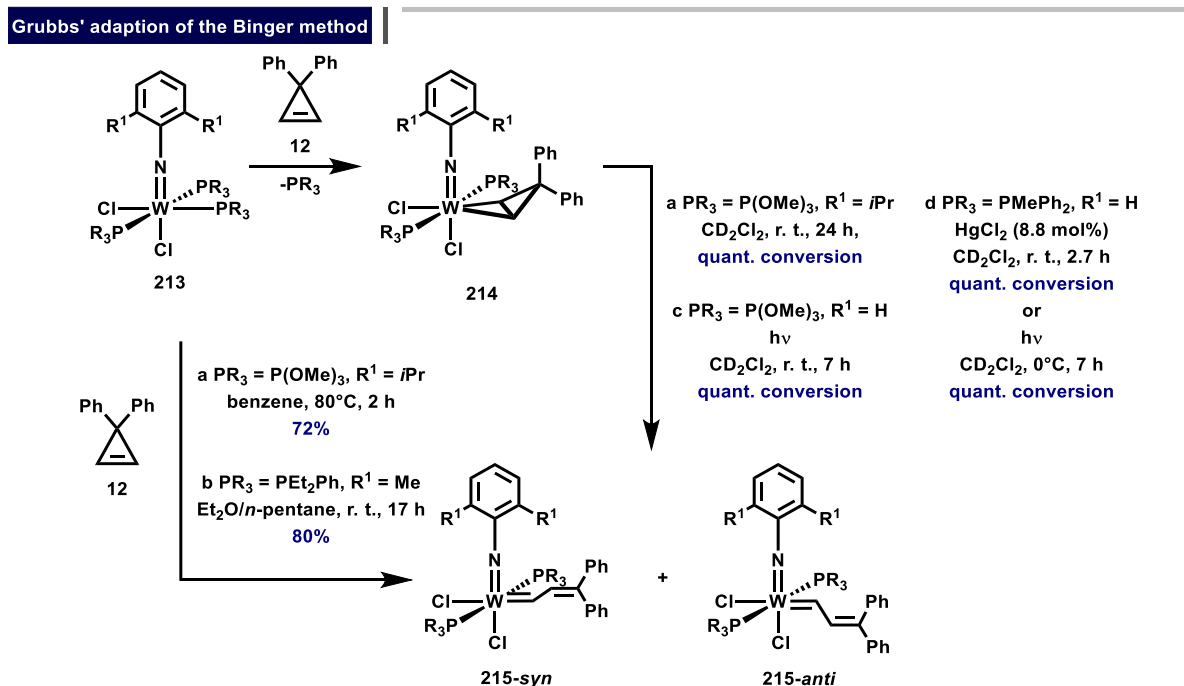
Scheme 89. Binger's mechanistic proposal for the rearrangement of the cyclopropene to yield a vinylic carbene.

However, alternative mechanisms may also be operative, depending on the nature of the transition metal involved. This is vividly illustrated by Fürstner's work on gold(I) "carbenes".^[204] In this case, reaction of precursor **209** with ketalcyclopropene **210** led to the selective formation of **Z-211**, which, upon warming, isomerizes to **E-211**, likely by transient formation of the elusive carbene **212**. In this system, it was possible to unambiguously establish that the resonance extremes **Z-211** and **E-211** represent ground state species, as a rotation around the C2–C3 bond was directly observed. In contrast to Binger's proposed mechanism, this transformation likely proceeds *via* a thermal, disrotatory, and torquoselective electrocyclic ring opening of a cyclopropyl cation, selectively furnishing **Z-211** (Scheme 90).^[209]



Scheme 90. Fürstner's gold(I) "carbene".

Grubbs adapted Binger's procedure, using it to explore the synthesis of vinylic W^{+VI} alkylidenes.^[199, 210] In contrast to Binger's report, Grubbs observed thermal, photochemical, and metal-catalyzed conversion of the cyclopropene adducts **214** to vinylic carbenes **215**, which were formed as a mixture of *syn* and *anti* conformers (Scheme 91).

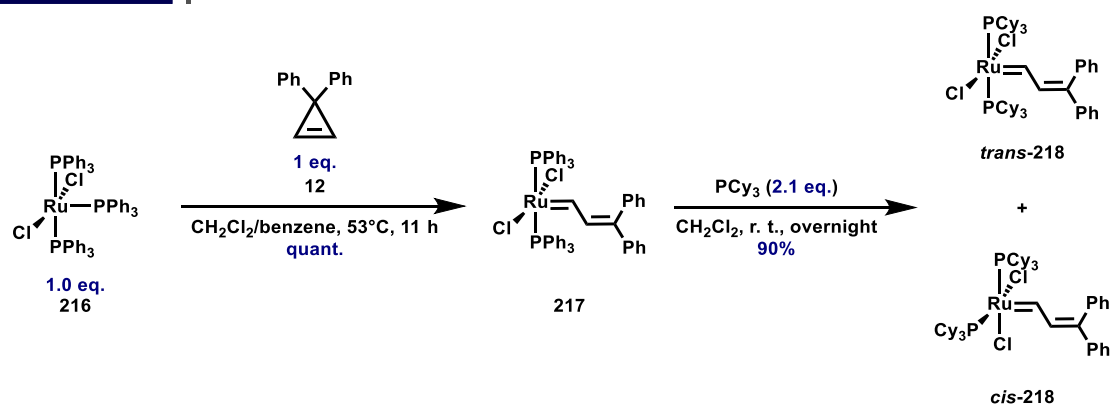


Scheme 91. Grubbs' adaption of the Binger method.

Based on the observation that $\text{Ru}(\text{H}_2\text{O})_6(\text{OTf})_2$ is an active catalyst system for the ROMP of strained monomers,^[211] Grubbs anticipated that the synthesis of a well-defined ruthenium-based carbene *via* Binger's method might be feasible, and that the resulting carbene could also be active in olefin metathesis. It was subsequently discovered that $\text{RuCl}_2(\text{PPh}_3)_3$ (**216**) reacts efficiently with cyclopropene **12** to generate the corresponding vinylic carbene **217** in quantitative yield (Scheme 92). This carbene exhibited remarkable properties: it was stable under acidic conditions and could be handled in air for short periods. These traits stand in stark contrast to early transition metal based carbenes, which are extremely sensitive to air and moisture.^[196]

However, this carbene displayed catalytic activity only in the ROMP of norbornene, a strained monomer, thereby limiting its utility. Following extensive screening of a broad range of ligands, it was found that exchange to the bulkier and more electron-donating phosphine PCy_3 afforded a much more active catalyst system. It did not only catalyze the ROMP norbornene, but also enabled the ring-closing metathesis (RCM) of dienes.^[198, 212] The high functional group tolerance of ruthenium-based carbenes ultimately led to their recognition as catalysts of strategic importance in the total synthesis of (macrocyclic) natural products.^[161, 213-218]

Grubbs' breakthrough



Scheme 92. The synthesis of the first well-defined ruthenium carbene, which is an active catalyst system for olefin metathesis.

This breakthrough triggered a veritable explosion in the field. Numerous research groups in both organic and inorganic chemistry around the world initiated research programs dedicated to the development of even more efficient ruthenium-based olefin metathesis catalysts. New synthetic strategies toward ruthenium based carbenes were developed, as the limited availability of the cyclopropene on significantly larger scale restricted the scope of the original method.^[219] Selected methods for the synthesis of ruthenium carbenes starting from $\text{RuCl}_2(\text{PPh}_3)_3$ (**216**) are presented in Scheme 93.

The Grubbs group was the first to develop an alternative approach based on the use of diazo compounds. This method not only enabled the synthesis of benzylidene **220a**, but also allowed for facile variation of substitution patterns on the carbene moiety. Notably, $(\text{Cy}_3\text{P})_2\text{Cl}_2\text{Ru}=\text{CHPh}$ (**226**) was later popularized and is now commercially available as the “Grubbs I” catalyst.^[220-221]

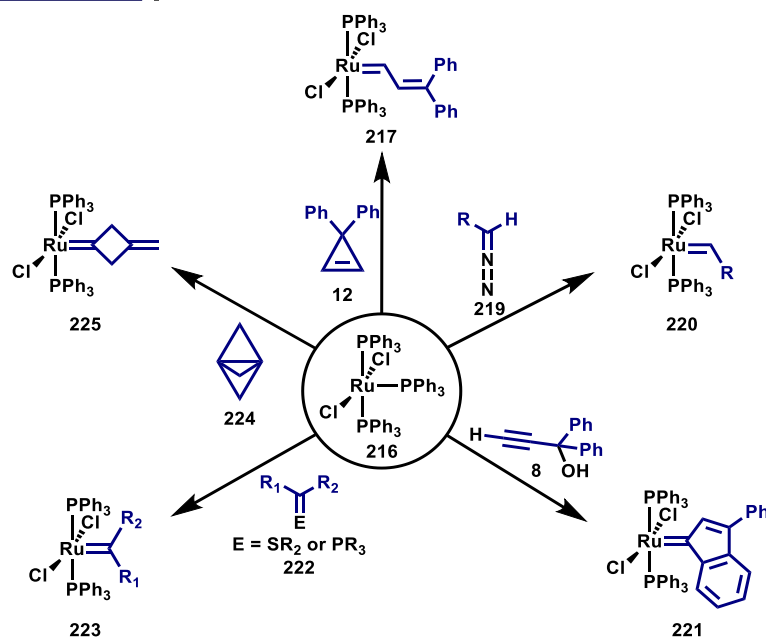
Another approach was developed by Fürstner, based on the synthesis of ruthenium allenylidenes originally discovered by Selegue.^[222-223] In this strategy, the reaction of precursor **216** unexpectedly leads to the formation of the ruthenium indenylidene complex **221**. Notably, this complex was initially misassigned as a ruthenium allenylidene by Hill.^[224] In light of this, both experimental and theoretical studies indicate that trace amounts of acid are required to promote the rearrangement from the corresponding allenylidene to the indenylidene **221**, whereas a direct thermal rearrangement under

neutral conditions is not feasible.^[225-227] Notably, the Fürstner group demonstrated that cationic ruthenium allenylidenes are also highly active catalysts for olefin metathesis.^[228]

The groups of Milstein and Grubbs developed approaches based on the use of sulfur or phosphorous ylides, respectively. In these methods, the carbene moiety is directly transferred to the ruthenium center, yielding the desired carbene complex **223** along with the corresponding sulfide or phosphine by-product.^[210, 229-230]

More recently, Wolczanski and co-workers reported on the utilization of propellanes as synthons for the generation of ruthenium-based carbenes **225**.^[230]

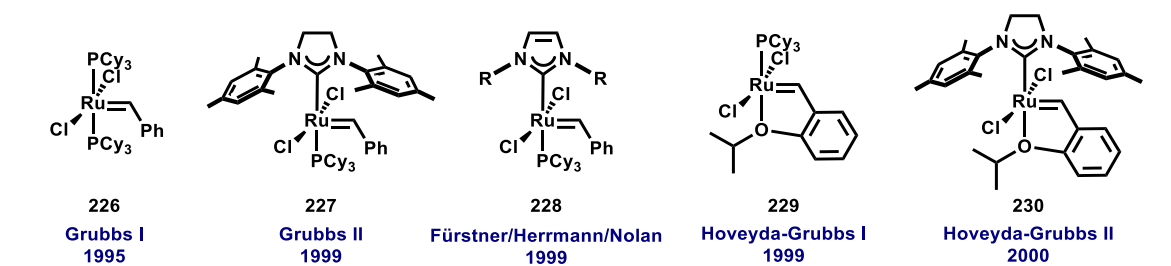
Selected strategies to Ru^{II}carbenes



Scheme 93. Selected methods for the synthesis of ruthenium carbenes starting from $\text{RuCl}_2(\text{PPh}_3)_3$ (**216**).

Besides exploring alternative synthesis procedures, the effect of other neutral ligands was investigated, as metallacyclobutane formation requires dissociation of one phosphine ligand to form a trigonal bipyramidal intermediate.^[231-233] In 1999, Fürstner, Herrmann, Nolan, and Grubbs discovered that substituting one PCy_3 ligand by a N-heterocyclic carbene (NHC) ligand significantly improved catalytic activity (Scheme 94). Fürstner and Herrmann as well as Nolan independently developed versions with an unsaturated NHC backbone, while Grubbs utilized NHC ligands with a saturated backbone, now commonly referred to as the “Grubbs II” catalyst.^[234-237] Additionally, Hoveyda developed Ru^{II} carbenes with enhanced stability by replacing one of the phosphine ligands with an ether ligand tethered to the benzylidene moiety. These carbenes can even be purified by flash chromatography and are recyclable after catalysis.^[238-241]

Selected Grubbs-type carbenes

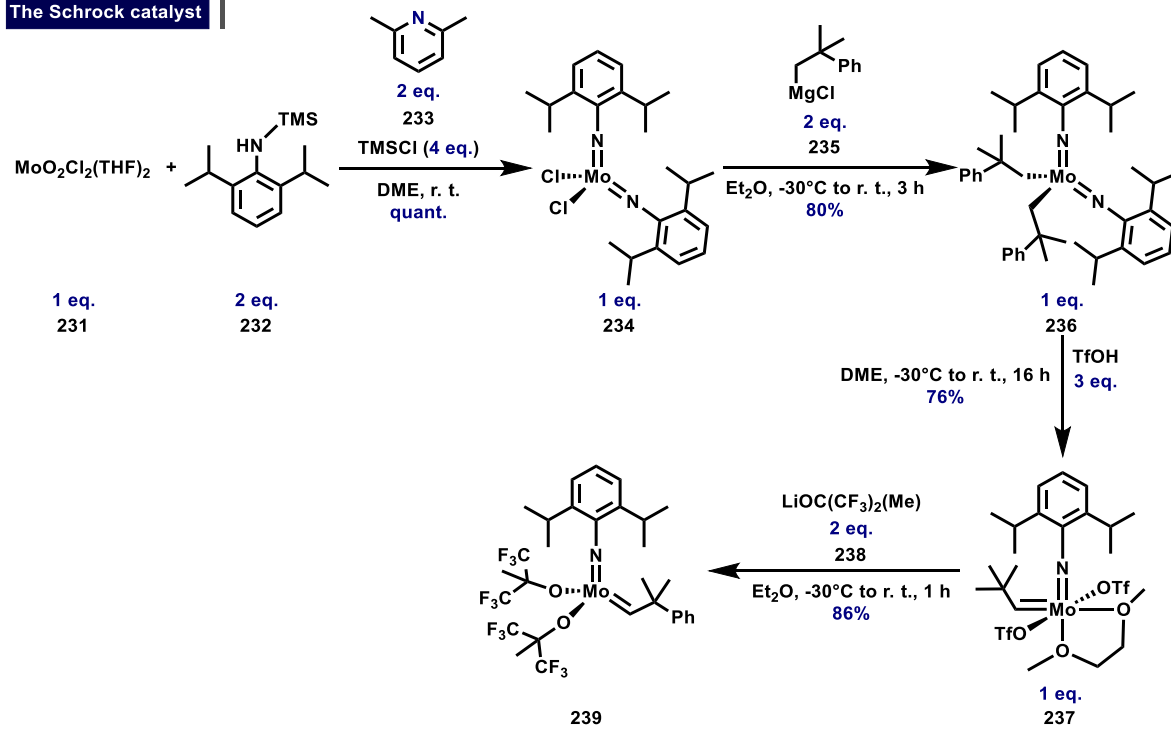


Scheme 94. Selected Grubbs-type carbenes developed by Grubbs, Fürstner, Herrmann, and Hoveyda.

Shortly before Grubbs-type Ru^{II} carbenes gained popularity in the organic chemistry community, Richard Schrock introduced molybdenum-based alkylidene complexes. These exhibit higher reactivity, but are significantly more sensitive compared to Grubbs' Ru^{II} carbenes. The synthesis of Schrock's system follows a general synthetic blueprint, and various derivatives with different alkoxide ligands or alkylidene units are known (Scheme 95).^[242]

Initially, MoO₂Cl₂(THF)₂ (**231**) is reacted with aniline **232**, 2,6-lutidine (**233**), and TMSCl to afford complex **234**. This intermediate is then converted to the bis-alkyl species **236** via treatment with the Grignard reagent **235**. Protonolysis with triflic acid in dimethoxyethane, followed by ligand exchange, ultimately furnishes the 12-VE Schrock catalyst **239**.^[243-244]

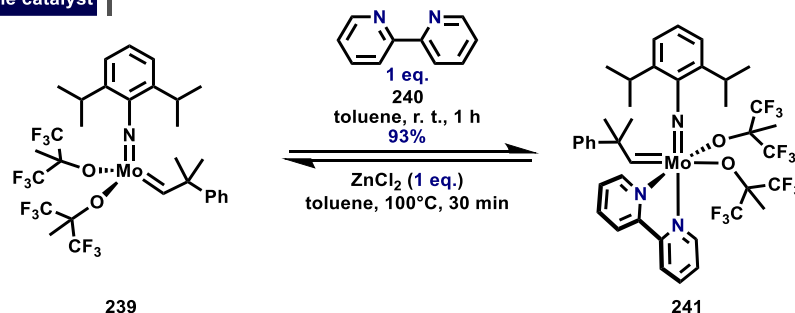
The Schrock catalyst



Scheme 95. Synthesis of the Schrock catalyst **239**.

Notably, Fürstner developed air-stable variants of the Schrock catalyst by forming adducts with phenanthroline and bipyridine. The original catalyst can be regenerated by the addition ZnCl₂ as a Lewis acid (Scheme 96).^[245]

Fürstner's air stable catalyst



Scheme 96. Fürstner's strategy to render Schrock-type alkylidenes air stable.

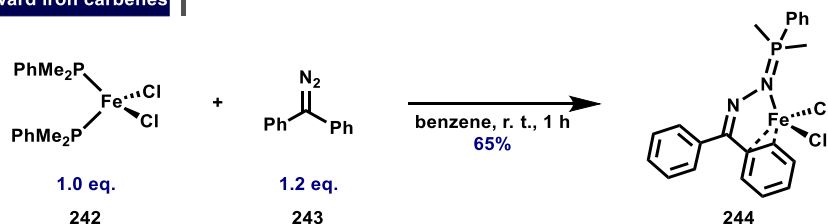
Olefin metathesis has emerged into a tool that has become indispensable with applications ranging from synthetic organic chemistry (including homo-metathesis, cross-metathesis, and ring-closing metathesis) to material science (ring-opening metathesis polymerization and acyclic diene metathesis polymerization). For their groundbreaking contributions to the development of the metathesis method, Grubbs, Schrock, and Chauvin were jointly awarded the Nobel Prize in Chemistry in 2005.^[145, 170, 246]

2.2 Introduction: Toward Iron-Catalyzed Olefin Metathesis

Olefin metathesis *catalyzed* by a well-defined iron carbene has not yet been achieved. Numerous experimental and theoretical studies in the literature have emphasized the desirability of an iron-based carbene catalyst, not only because iron is an inexpensive and earth-abundant base metal, but also because it presents a fundamentally intriguing challenge in organometallic chemistry.^[247]

The hurdle with accessing a well-defined iron-based olefin metathesis catalyst has two major reasons. Firstly, the synthesis of iron-based carbenes is difficult. For instance, Grubbs attempted the preparation of iron carbenes analogous to his ruthenium carbenes by reacting **242** with various diazo compounds. However, the reaction did not result in the formation of an iron carbene but rather led to the insertion of the diazo compounds into the Fe–P bond (Scheme 97).^[248]

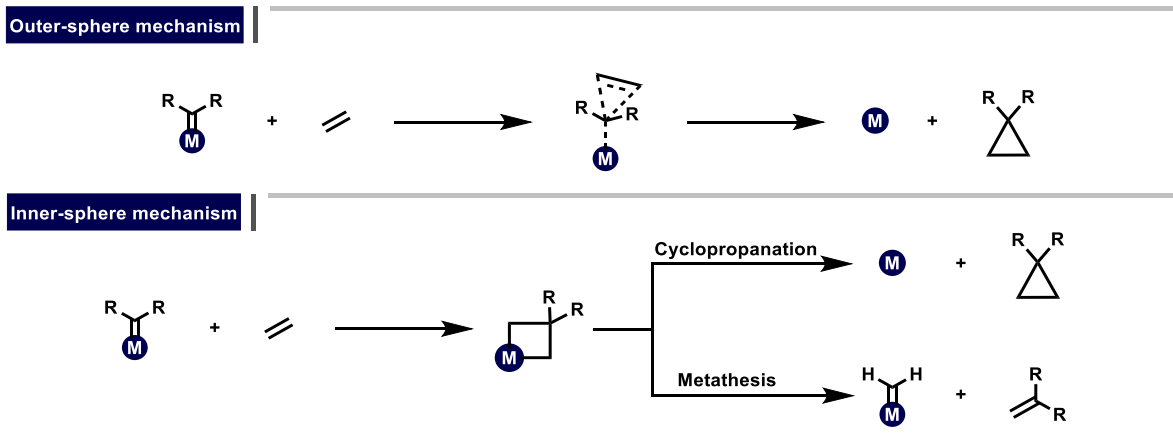
Grubbs' efforts toward iron carbenes



Scheme 97. Grubbs' attempt to prepare an iron carbene.

Secondly, only cyclopropanation has been reported with iron carbenes. For this transformation, two distinct mechanistic pathways are possible: cyclopropanation *via* an outer-sphere mechanism or cyclopropanation by reductive elimination from a metallacyclobutane intermediate (inner-sphere mechanism). Cyclopropanation, proceeding *via* an outer-sphere mechanism has been reported experimentally and studied computationally for a variety of iron carbenes.^[249-254]

The inner-sphere mechanism has been the subject to several computational studies.^[247, 255-259] Starting from the metallacyclobutane, the cyclopropanation pathway (*via* reductive elimination) or the metathesis pathway (*via* [2+2] cycloreversion) are possible. It has been proposed that the intermediate metallacyclobutane must possess a singlet ground state in order to undergo metathesis (Scheme 98).^[255]



Scheme 98. Cyclopropanation vs. metathesis.

Scheme 99 highlights selected milestones in iron carbene chemistry, as well as key studies relevant to iron-catalyzed olefin metathesis.

The first iron carbene reported by Pettit and Jolly in 1966, was formed *in situ* by protonation of $\text{Cp}(\text{CO})_2\text{FeCH}_2\text{OMe}$ with HBF_4 . Although this particular cationic methyldiene complex **245** could not be isolated, the addition of cyclohexene to the reaction mixture strongly suggested the presence of a carbene intermediate, as the cyclopropanation product norcarane was obtained.^[249] Later, Lapinte, Brookhart and Meyer succeeded in isolating related iron carbenes by replacing the CO ligands with other neutral ligands such as phosphines and varying the non-coordinating anion or the carbene unit.^[251-252, 260-261]

In 1997, Floriani and co-workers synthesized a high-spin iron carbene **246** ($S = 5/2$) by reaction of a calixarene-based precursor with Ph_2CN_2 . This carbene exhibited reactivity toward O_2 , affording a bridged oxo-complex and benzophenone as the products.^[262]

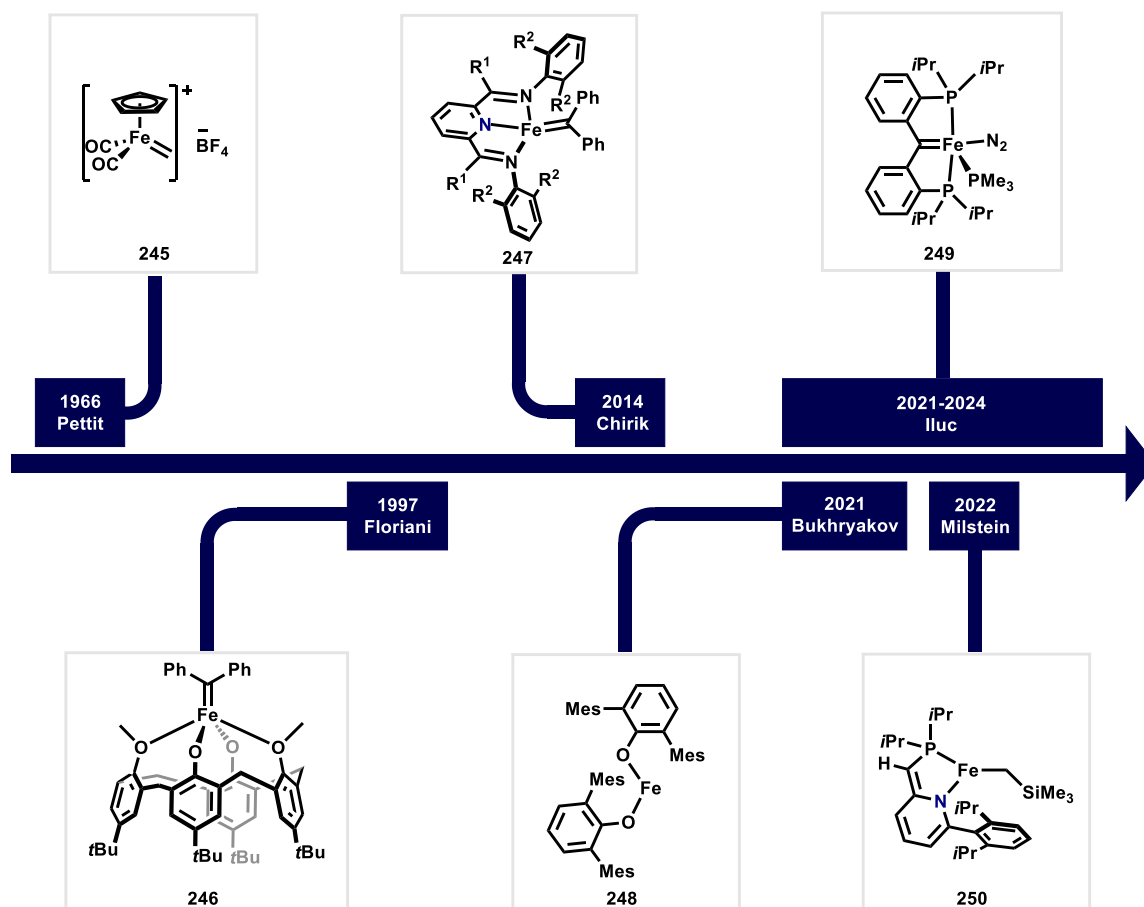
Several years later, Paul Chirik and co-workers made seminal contributions to the synthesis of iron carbenes.^[263] They discovered that reaction of appropriately tailored PDI-based (pyridine diimine) Fe precursors with $\text{Ph}_2\text{C}=\text{N}_2$ led to the formation of a carbene complex with the general formula $\text{PDIFe}=\text{CPh}_2$ (**247**). Notably, Chirik had previously reported the reaction of a PDI-based Fe complex with the diazoalkane $(\text{TMS})(\text{H})\text{CN}_2$,^[264] as well as the isolation of isolobal imido complexes of the general type $\text{PDIFe}=\text{N}-\text{R}$.^[265-266] Of particular interest, imido complexes featuring an $=\text{N}-\text{Ar}$ substituent were found to deviate markedly from the ideal square planar geometry and exhibit an $S = 1$ state. In contrast, $=\text{N}-\text{Alkyl}$ analogues adopt geometries much closer to square planar and are diamagnetic. The divergence in structure is attributed primarily to steric effects. A similar distortion is observed in $\text{PDIFe}=\text{CPh}_2$ (**247**), whose carbene fragment similarly departs from the square planar plane defined by the PDI ligand. Mößbauer and X-ray absorption spectroscopy revealed that **247** is a Fe^{II} species with four unpaired electrons, two of which are antiferromagnetically coupled to a PDI-based radical anion and a carbene radical, resulting in an overall $S = 1$ spin state. Despite possessing an open coordination site, the complex does not react with olefins. This lack of reactivity is likely due to the spatial orientation of the bulky $=\text{CPh}_2$ moiety. While a $[2+2]$ cycloaddition would necessitate the Ph substituents to lie parallel to the plane defined by the PDI ligand,^[267] the substituents are oriented perpendicular to this plane and therefore prevent any reaction with olefins. As with the imido complexes, the particular orientation of the $=\text{CPh}_2$ ligand is likely governed by unfavorable interactions with the PDI-based ligand.

A key finding was reported in 2021 by Bukhryakov, who revealed that the sterically encumbered phenoxide complex **248** catalyzes the stereospecific ROMP of norbornene to yield *cis, syndiotactic*

polynorbornene. Although the exact mechanism remains unclear, comparisons can be drawn to the earlier observations that certain Ziegler-type catalyst systems are also able to catalyze the ROMP of norbornene (*vide supra*).^[160, 268]

Shortly thereafter, Iluc and co-workers presented their work on stoichiometric ene-yne metathesis.^[269] Notably, this work provided the first example of a well-defined iron carbene undergoing a [2+2] cycloaddition/cycloreversion sequence. More recently, Iluc and co-workers extended this work to a stoichiometric metathesis with strained olefins, demonstrating that [2+2] cycloaddition/cycloreversion is indeed possible with an iron carbene.^[270] In this study, the intermediate metallacyclobutane was characterized crystallographically. Given the high importance of these findings, Iluc's system will be discussed in detail below.

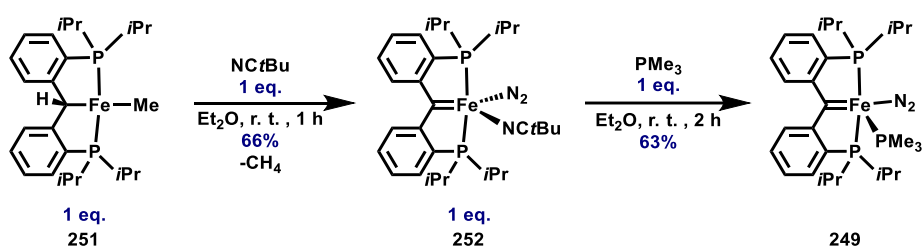
David Milstein and co-workers unveiled a complex that serves as a highly active catalyst for the ROMP of norbornene, achieving a remarkable TON of up to 880. Although complex **250** is not a carbene, it was proposed that it could rearrange to a carbene. This carbene would subsequently undergo [2+2]-cycloaddition with norbornene, followed by a [2+2] cycloreversion.^[271]



Scheme 99. Selected highlights pertinent to iron carbene chemistry and olefin metathesis with iron complexes.

The synthesis of Iluc's system commenced with the reaction of the bis-alkyl complex **251** with NCtBu , resulting in a coordination-induced α -hydrogen abstraction to give carbene **252** as the product. The nitrile ligand was subsequently substituted with a PMe_3 ligand to give carbene **249** (Scheme 100).

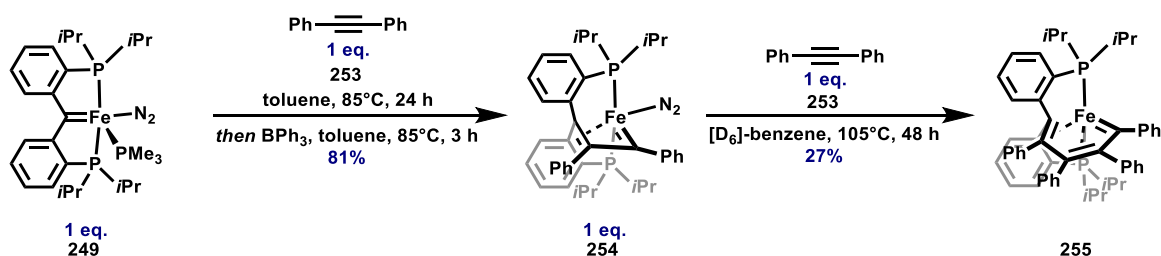
The Iluc system



Scheme 100. The Iluc system enabled the first stoichiometric ene-yne metathesis of an iron carbene.

A landmark discovery in iron carbene chemistry emerged when carbene **249** was reacted with stoichiometric diphenylacetylene in the presence of BPh₃ as a phosphine scavenger (Scheme 101). Building on this finding, Iluc showcased that the resulting carbene **254** could be driven, at higher temperatures, to react with a second equivalent of diphenylacetylene, realizing a second ene-yne metathesis step.^[269]

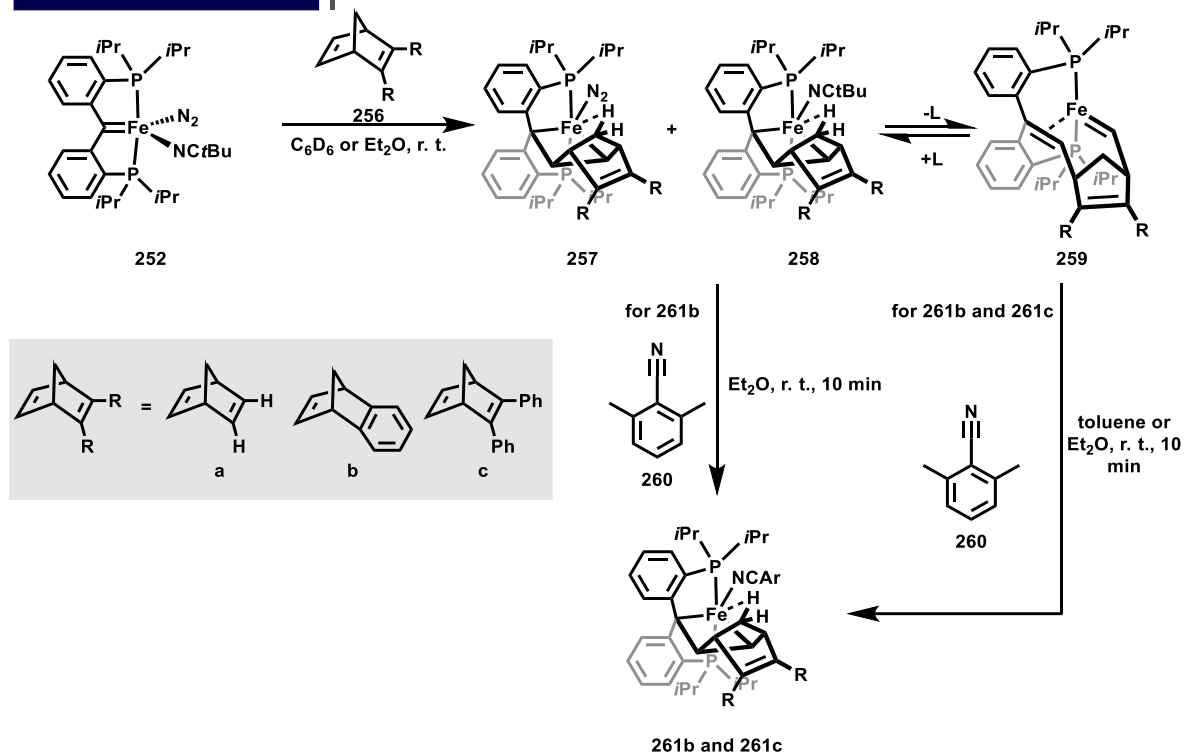
Stoichiometric ene-yne metathesis



Scheme 101. Stoichiometric ene-yne metathesis with carbene **249**.

Carbene **249** showed no reactivity toward olefins, likely because the PMe₃ ligand was not labile enough to be displaced by a more electron-deficient π -system. In contrast, its analogue **252**, equipped with a more labile nitrile ligand, readily reacted with strained norbornadiene derivatives to give a mixture of the diamagnetic metallacyclobutanes (**257** and **258**) and the paramagnetic [2+2]-cycloreversion product **259** (Scheme 102). Loss of either the nitrile or the N₂ ligand *in vacuo* triggered a [2+2]-cycloreversion, leading to clean conversion to the paramagnetic product **259**. Moreover, Iluc and co-workers revealed that the [2+2]-cycloreversion is fully reversible. Thus, when a bulky nitrile ligand **260** was added, the metallacyclobutanes **261b** and **261c** were formed, one of which was characterized crystallographically. Notably, treatment of **259b** with PMe₃ regenerated one of the original carbenes **249**, with concomitant release of norbornadiene derivative **256b**.^[270] Truly catalytic olefin metathesis remains beyond the scope of Iluc's system, mainly because the carbene unit is part of the tridentate PCP pincer ligand. However, Iluc's pioneering discovery serves as a model system and could thus pave the way for the design of catalytically active iron carbenes.

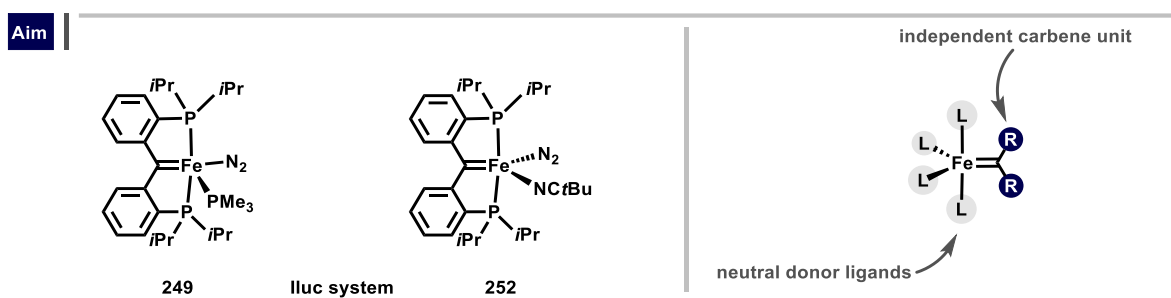
Stoichiometric olefin metathesis



Scheme 102. Iluc's stoichiometric olefin metathesis with strained olefins.

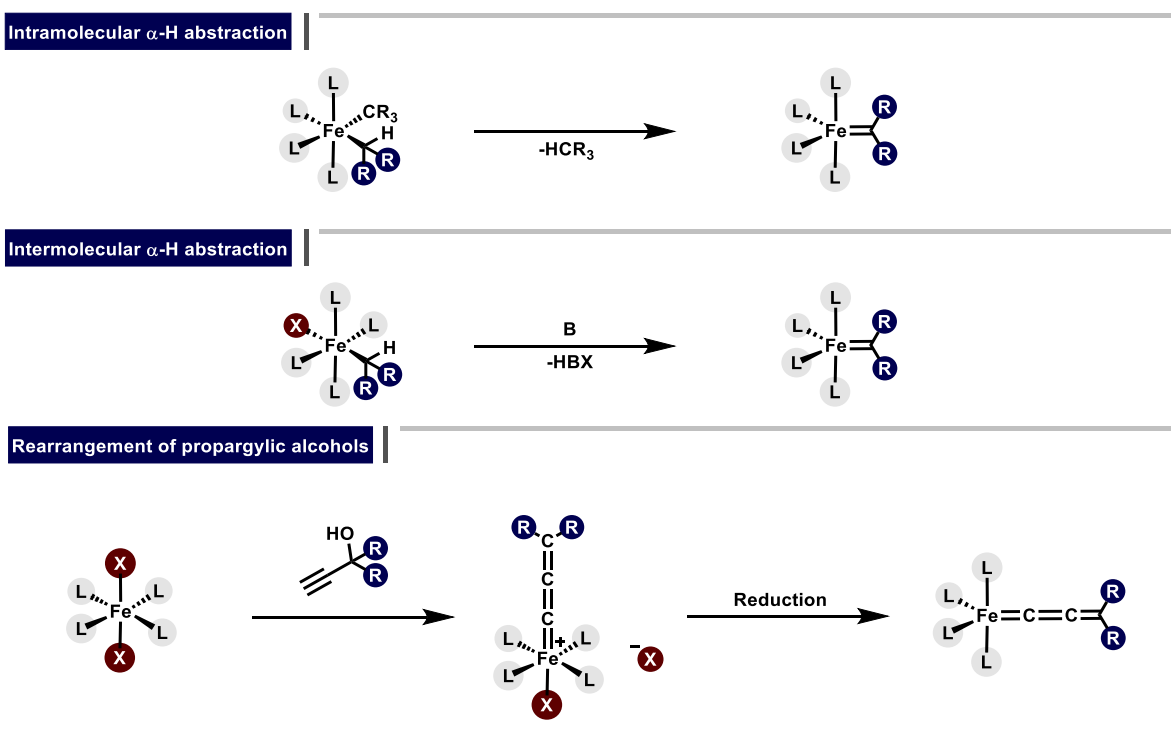
2.3 Aim

The aim of the second section of this PhD thesis was to explore synthetic methods toward iron carbenes and the evaluation of the resulting complexes as potential catalysts for olefin metathesis. Inspired by the stoichiometric metathesis reactivity of the Iluc system, it was hypothesized that an iron carbene mirroring its key characteristics could serve as a viable starting point for such investigations. Thus a five-coordinate, diamagnetic iron carbene surrounded by four neutral donor ligands and a standalone carbene ligand was selected as a promising motif. As the Iluc system features a carbene unit embedded within a rigid tridentate PCP pincer framework, it cannot function as an active olefin metathesis catalyst. Therefore, the goal here was to construct an iron complex featuring a discrete and independently coordinated carbene moiety (Scheme 103).



Scheme 103. Left: carbenes **249** and **252** as reported by Iluc. Right: features of the envisioned carbene.

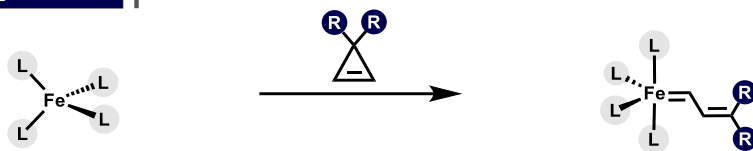
Initial synthetic efforts toward such a hypothetical carbene should focus on inter- or intramolecular α -hydrogen abstractions, since the intramolecular approach had previously proven effective in the Iluc system (Scheme 104). In addition, the rearrangement of propargylic alcohols to allenylidene or indenylidene species was evaluated, as this method not only allows for the facile preparation of catalytically active ruthenium indenylidenes and allenylidenes for olefin metathesis,^[222, 228] but has also been employed in the preparation of certain iron allenylidene complexes.^[272-273]



Scheme 104. α -Hydrogen abstraction as a strategy toward novel iron carbenes. B = Base, X = leaving group.

In addition, this work set out to move beyond established synthetic blueprints for iron carbenes by exploring strategies that are well established for other metals, yet remain uncharted for iron. Among these, particular attention was given to the Binger method, an elegant transformation involving the formal electrocyclic ring-opening of 3,3-substituted cyclopropenes (Scheme 105).

Iron carbenes *via* Binger's method

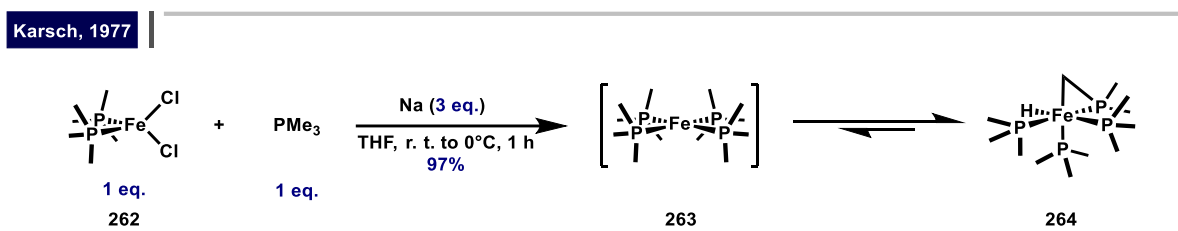


Scheme 105. Envisaged application of the Binger method for the synthesis of iron carbenes.

2.4 Results

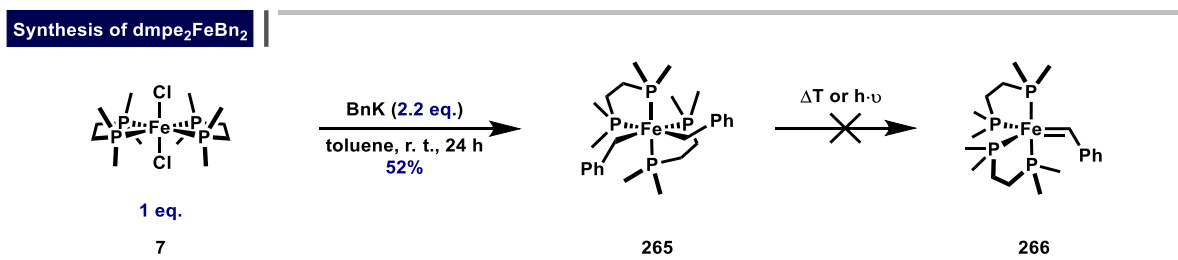
Attempted α -H abstraction

Our efforts began with the search for viable neutral ligands capable of stabilizing both the precursor alkyl species and the resulting carbene product. Formally, the targeted iron complexes can be described either as iron(0) carbenes or iron(+II) alkylidenes, depending on the nature of the carbene ligand. Iron(0) complexes ligated by monodentate ligands such as phosphines are rare. For example, Karsch and co-workers reported the synthesis of $\text{Fe}(\text{PMe}_3)_4$ (**264**); although this species might intuitively be classified as an iron(0) complex, it is, in fact, an octahedral Fe^{II} species **264**, formed *via* β -H oxidative addition from one of the PMe_3 methyl groups.^[274] Notably, this complex exists in equilibrium with the elusive zero-valent iron species **263**. However, such iron complexes are extremely sensitive, as the PMe_3 ligands are highly labile (Scheme 106).



Scheme 106. Karsch's synthesis of $\text{Fe}(\text{PMe}_3)_4$ (**264**).

Therefore, we turned our attention to the closely related bidentate *dmpe* ligand. Due to the chelate effect, this ligand binds more tightly to the iron center, and its derivatives are known to exhibit rich and diverse reactivity.^[275-279] The reaction of $\text{dmpe}_2\text{FeCl}_2$ (**7**) with various alkylating reagents was explored, among which benzyl potassium emerged as most effective. Treatment of **7** with a slight excess of BnK furnished the respective bis-benzyl species **265** (Scheme 107). Complex **265** is diamagnetic and was characterized *via* NMR spectroscopy and X-ray crystal structure analysis. Notably, the NMR spectra of **265** gradually broadened over time, indicating slow decomposition in $[\text{D}_8]$ -toluene solution at room temperature. Due to this sensitivity, mass spectrometry, IR spectroscopy, and elemental analysis were not attempted. Efforts to generate a carbene **266** from **265**, either thermally or photochemically, were unsuccessful, and resulted in decomposition or no reaction, respectively.



Scheme 107. Synthesis of $\text{dmpe}_2\text{FeBn}_2$ (**265**) and attempted generation of carbene **266**.

A single crystal X-ray diffraction analysis of single crystals grown from a toluene/*n*-pentane mixture confirmed the structure of complex **265**. The complex adopts an octahedral geometry, with both benzyl groups oriented *cis* to each other (Figure 30).

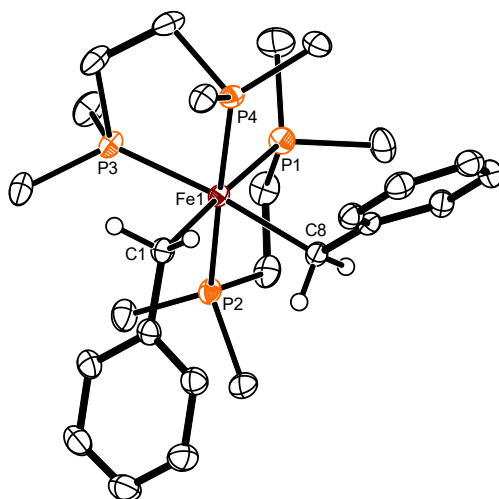
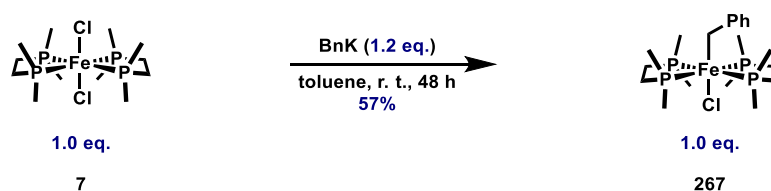


Figure 30. Crystal structure of complex **265**. H-atoms (apart from those on C1 and C8) and solvent molecules are not shown for clarity.

Next, the preparation of the mono-benzyl complex was targeted to test whether this complex could be transformed to carbene **266** on treatment with external bases. Reaction of complex **7** with 1.2 eq. of the benzyl potassium reagent allowed complex **267** to be isolated in 57% yield (Scheme 108). The structure of this complex was assigned using NMR spectroscopy. Additionally, complex **267** was characterized by X-ray diffraction and elemental analysis. Attempted mass spectrometric measurements were unsuccessful. Notably, Bergman and co-workers reported the closely related complex *trans*- $\text{dmpe}_2\text{FeBnH}$.^[280]

Synthesis of $\text{dmpe}_2\text{FeBnCl}$



Scheme 108. Synthesis of $\text{dmpe}_2\text{FeBnCl}$ (**267**).

The X-ray crystallographic analysis of a crystal grown from a toluene/*n*-pentane mixture confirmed the octahedral structure of **267**. In contrast to **265**, complex **267** adopts the *trans* isomeric form (Figure 31).

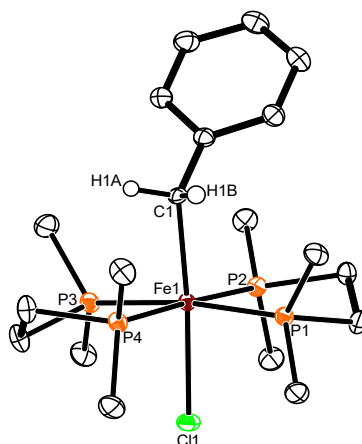
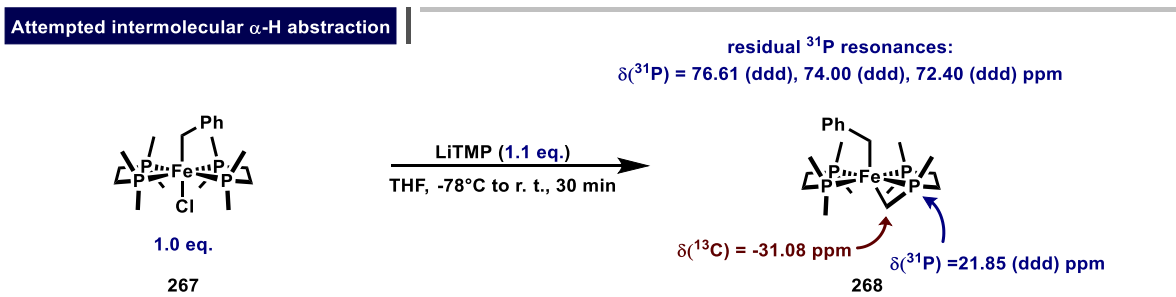


Figure 31. Crystal structure of complex **267**. H-atoms (apart from those on C1) are omitted for clarity.

With complex **267** in hand, we attempted its dehydrohalogenation (intermolecular α -H abstraction) by treating **267** with strong bases. Unfortunately, reaction of **267** with LiTMP did not yield the targeted carbene **266**; instead, NMR data indicated the formation of species **268** derived from deprotonation of one of the methyl groups on the dmpe ligand, followed by salt metathesis with the remaining Fe-Cl moiety (Scheme 109). However, this putative species was not formed cleanly, as several unidentified by-products were also present in the mixture. All attempts at purifying the mixture were met with failure, and mass spectrometric investigations were likewise unsuccessful.

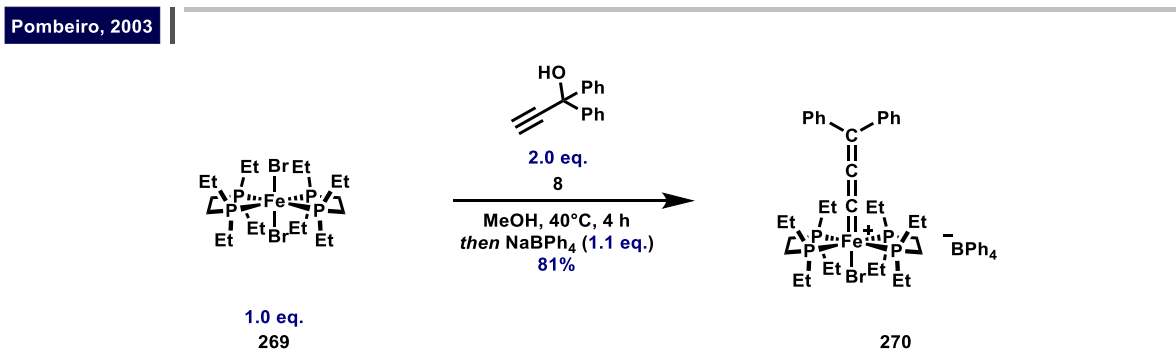
In any case, the NMR spectroscopic fingerprints strongly indicate the formation of the proposed species **268**. The ^{31}P NMR spectrum shows four signals (ddd), consistent with four inequivalent phosphorus nuclei. Notably, three of these signals lie within a very narrow range (72.40–76.61 ppm), while the fourth signal is significantly upfield-shifted (21.85 ppm), suggesting a distinct chemical environment for this phosphorus atom. Additionally, the ^{13}C NMR spectrum shows a notably upfield-shifted signal at -31.08 ppm, which we tentatively assign to the presumed cyclopropylic Fe-P-CH₂ moiety. Comparison with a closely related, literature-known system further supports the proposed structure of **268**.^[281]



Scheme 109. Attempted intermolecular α -H abstraction for the synthesis of carbene **266**. NMR data indicates deprotonation in the undesired position. NMR measurements in [D₆]-benzene at 298 K.

Synthesis of Fe allenylidenes

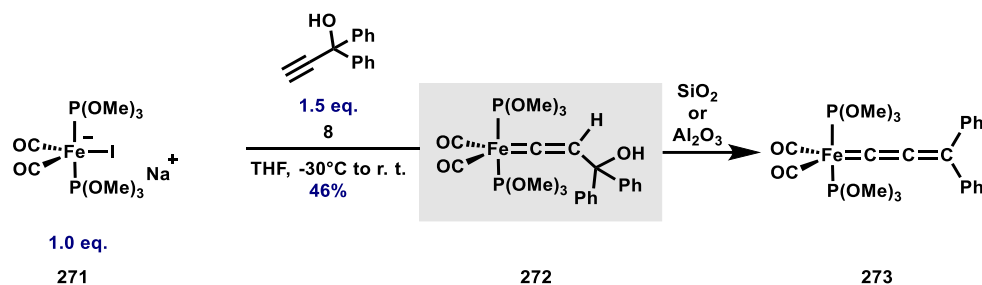
As the envisioned α -H abstraction strategy proved ineffective for the synthesis of a dmpe-ligated iron(o) carbene **266**, alternative methods for accessing a carbene with the substructure $\text{dmpe}_2\text{Fe}=\text{CR}_2$ were explored. Particular attention was given to the synthesis of a cationic allenylidene reported by Pombeiro, which was obtained by reacting the closely related precursor $\text{depe}_2\text{FeBr}_2$ (**269**) with propargylic alcohol **8** in MeOH, followed by anion exchange with NaBPh_4 (Scheme 110).^[272] We hypothesized that a similar reaction would yield the corresponding dmpe analogue. Subsequent reduction of the resulting cationic allenylidene was expected to afford an iron(o) allenylidene, closely resembling the initially targeted carbene structure.



Scheme 110. Pombeiro's allenylidene synthesis.

A related system was also reported by Berke.^[273] Here, complex **271** reacted with propargylic alcohol **8** to give a hydroxy vinylidene complex **272**; upon treatment with Al₂O₃ or SiO₂ these complexes eliminated water to furnish the expected allenylidene **273**.

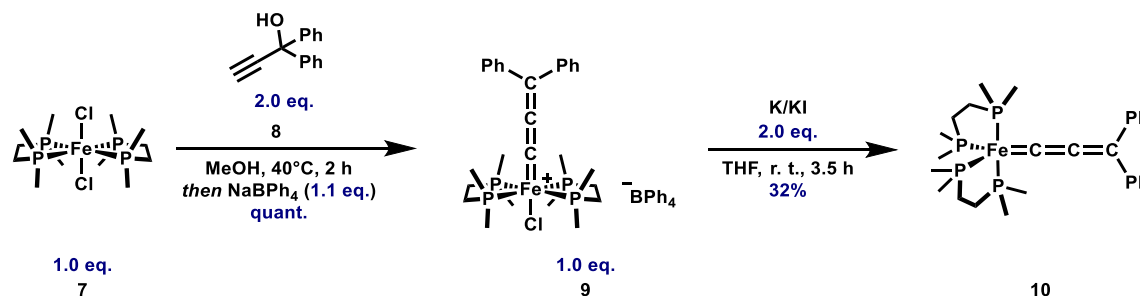
Berke, 1997



Scheme 111. Berke's approach to iron allenylidenes.

The analogous reaction of dmpe₂FeCl₂ (**7**) with the propargylic alcohol **8** in MeOH proceeded smoothly in our case, furnishing the envisaged cationic allenylidene **9** in quantitative yield. Subsequent reduction with K/KI^[282] resulted in the formation of allenylidene **10**, which was isolated in 32% yield after two subsequent recrystallizations from toluene/*n*-pentane to minimize contamination with an unknown impurity. However, the sharp signals of the unknown species are still visible in the ³¹P NMR spectrum. Unfortunately, the dmpe ligand are too tightly bound to the iron center so that **10** did not react with an excess of norbornene, even at elevated temperatures (30 h at 80°C).

Synthesis of iron allenylidenes



Scheme 112. Synthesis of the allenylidenes **9** and **10**.

An X-ray crystallographic analysis of a single crystal grown from *n*-pentane solution confirmed the structure of **10** in the solid state. One of the distinct features is the nearly linear allenylidene unit. The Fe1–C13–C14 (176.17(14)°) and the C13–C14–C15 angles (173.67(17)°) indicate a slight deviation from ideal linearity, possibly caused by crystal packing effects. The Fe1–C13 carbene bond length (1.8287(14) Å) is relatively short compared to those in other iron carbenes with the same oxidation state, but longer than in a related allenylidene system reported by Berke.^[269, 273, 283]

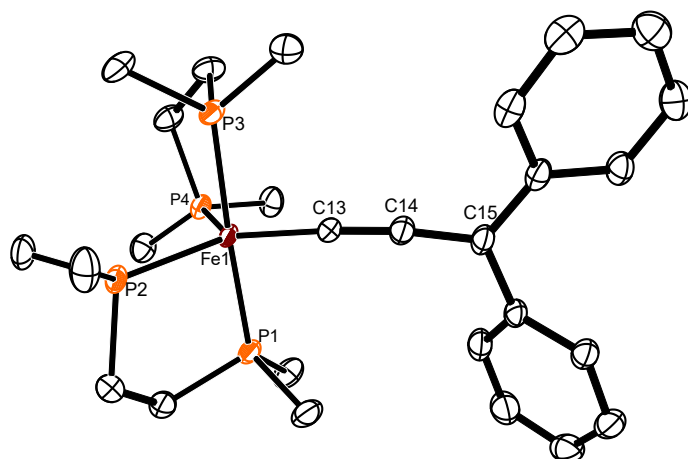


Figure 32. Crystal structure of complex **10**. H-atoms are omitted for clarity.

Notably, complex **10** adopts a trigonal bipyramidal geometry, with the allenylidene moiety and one arm of each dmpe ligand lying in the equatorial plane, while the remaining two dmpe arms occupy the axial positions of the trigonal bipyramid. Based on this structure, one would expect two distinct triplet signals in the ^{31}P NMR spectrum. However, at 298 K only a single broad ^{31}P NMR signal was observed, indicating rapid exchange between the phosphorus nuclei, rendering them equivalent on the NMR timescale. This exchange is likely caused by a Berry pseudorotation, as the broad signal coalesces into two triplet signals at temperatures below 253 K in the ^{31}P NMR spectrum (Figure 33). Using the Eyring expression, it was possible to determine that the barrier of this exchange is $\Delta G^{\ddagger}_{\text{TC}} \approx 11.4$ kcal/mol.

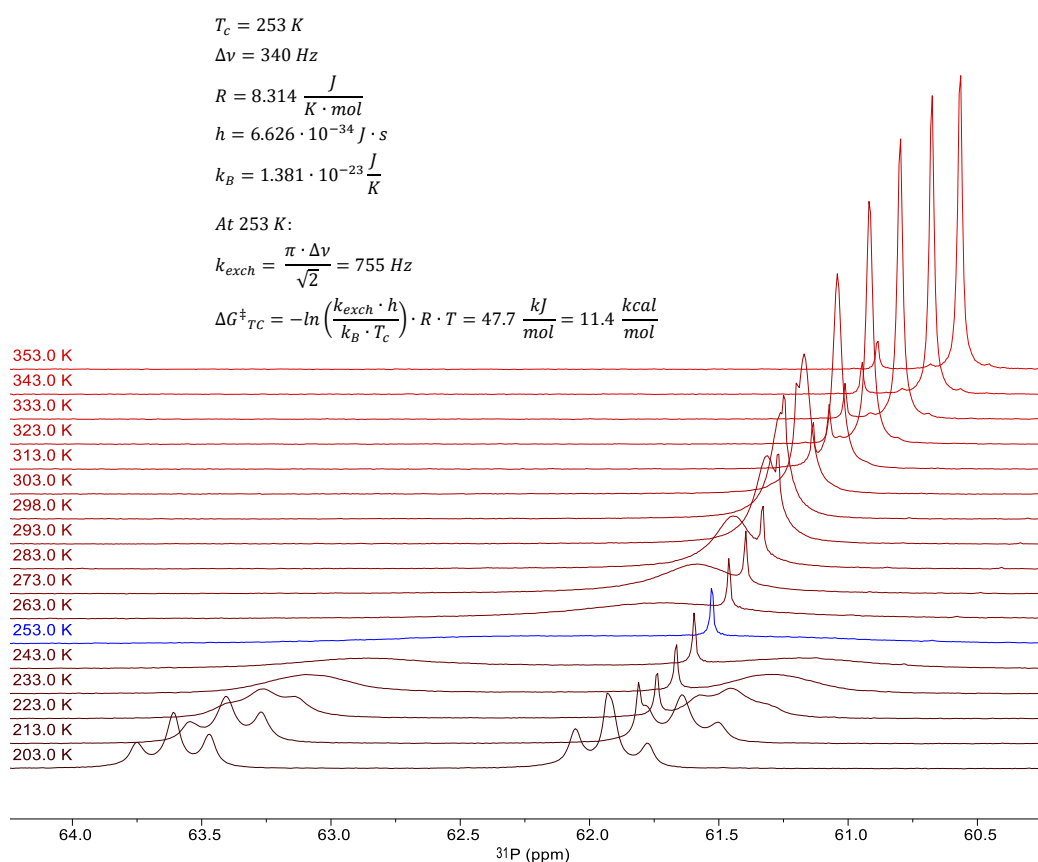
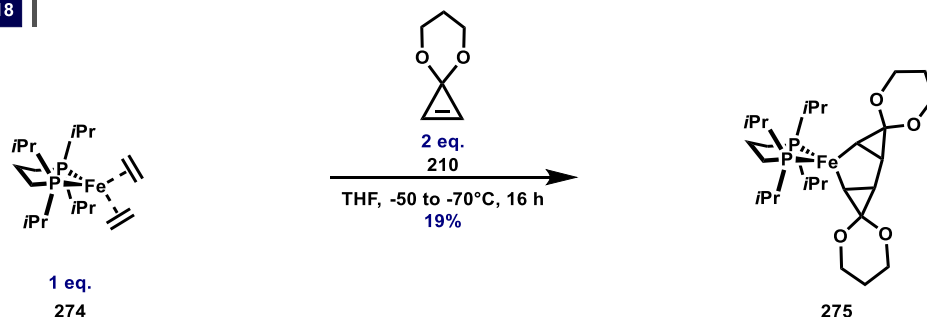


Figure 33. VT ^{31}P NMR spectrum of complex **10** in $[\text{D}_8]$ -toluene from 203 K to 353 K. In collaboration with Dr. Markus Leutzsch.

Accessing Iron Carbenes via the Binger Rearrangement Strategy

Our group previously investigated the Binger rearrangement strategy as a potential route for generating iron carbenes, using an iron(0) complex **274** as the precursor. However, these experiments led exclusively to the formation of complex **275**, the product of an oxidative cyclization (Scheme 113).^[284]

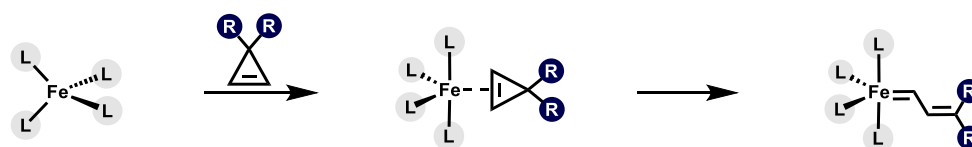
Füstrner, 2018



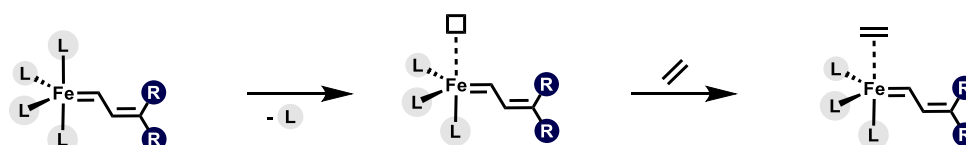
Scheme 113. Füstrner's investigations toward iron-based carbenes *via* Binger's method led exclusively to oxidative cyclization of two molecules of cyclopropene **210** with iron complex **274**.

From this experimental outcome, a major drawback of the Binger method becomes evident: if more than one cyclopropene coordinates to the transition-metal complex, oxidative cyclization will preferentially occur. For the successful synthesis of an iron carbene using this strategy, it is therefore necessary to control the coordination of the cyclopropene so precisely that only a single cyclopropene binds to the metal center. However, this control comes at a price. After coordination and subsequent vinylic carbene formation, the resulting complex would formally be considered a coordinatively saturated 18-VE species. As a result, it would become unreactive toward olefins and other substrates, as observed with the dppe-ligated allenylidene **10**. The loss of at least one ligand would be necessary to enable olefin coordination and allow metathesis to proceed. The key challenge lies in identifying a precursor system that is selective enough to permit single cyclopropene coordination initially, yet flexible enough to allow ligand dissociation after carbene formation, ultimately yielding a potential iron-based catalyst for olefin metathesis. Notably, a single example of an iron carbene formed *via* electrocyclic ring-opening of a cyclopropene exists in the literature; however, in this case, the reported method yielded a mixture of different species, thus preventing clean access to a single vinylic carbene product.^[195] In any case, the generation of transition metal carbenes *via* Binger's method also offers a significant advantage over other approaches since no by-products are formed. For instance, propargylic alcohols cannot be used in iron-based systems that are sensitive to protonolysis.

Single cyclopropene coordination

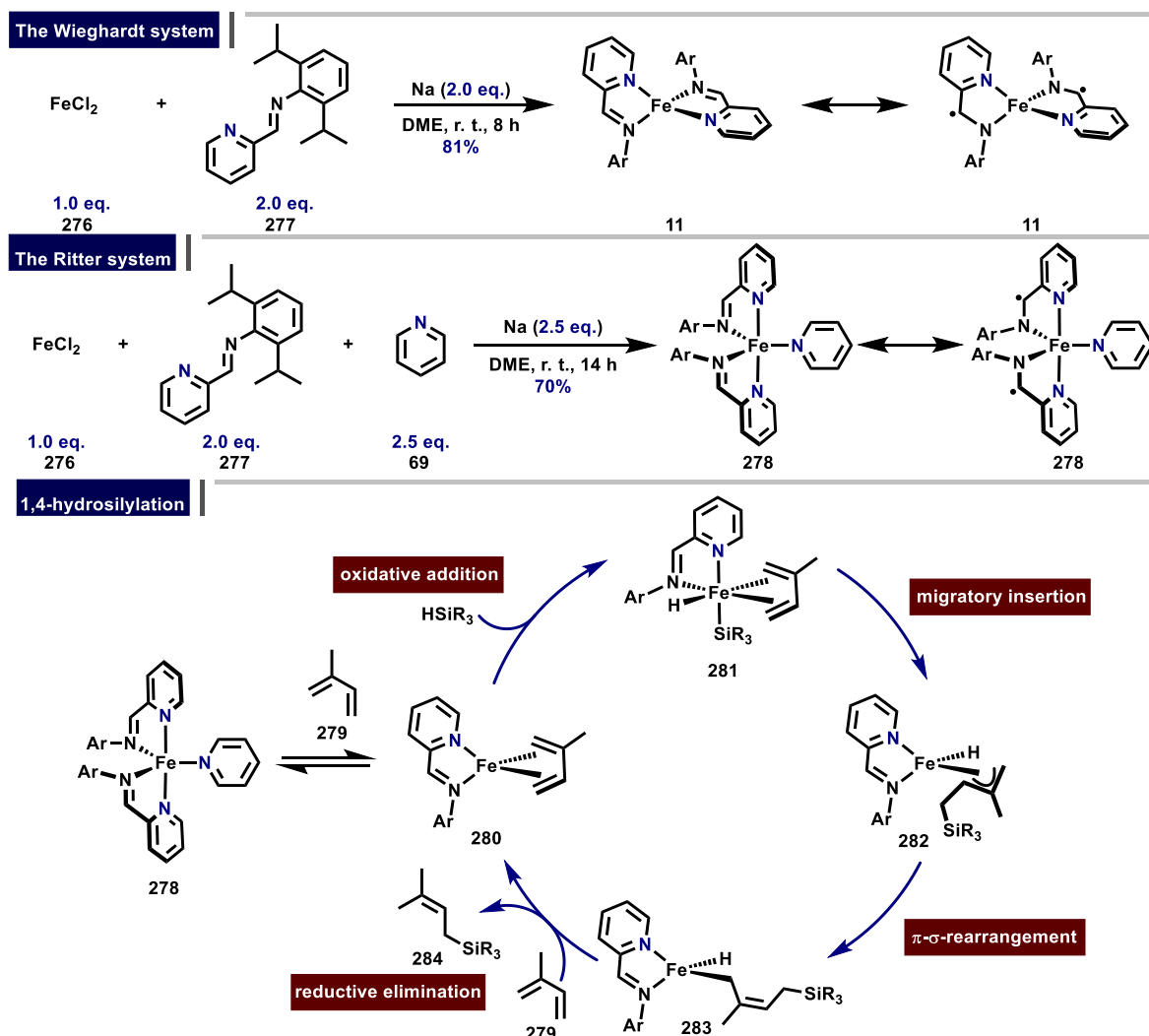


Ligand dissociation enables olefin coordination



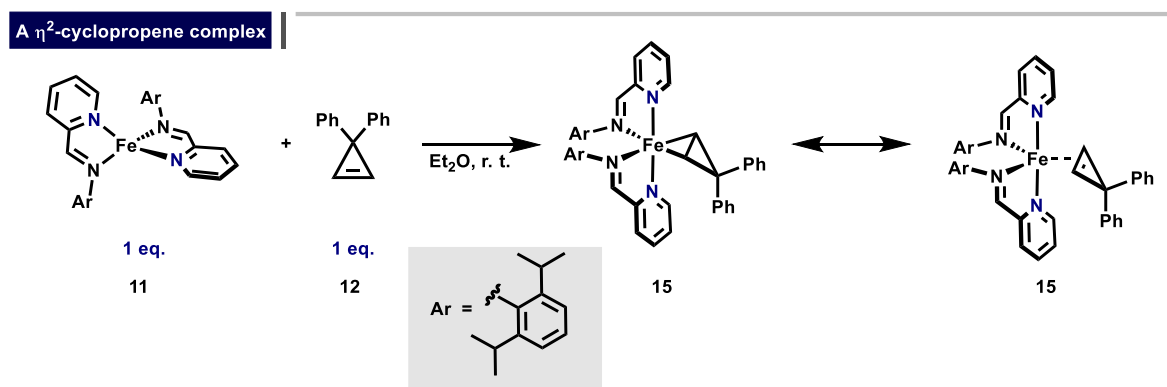
Scheme 114. Strategy toward an iron-based olefin metathesis catalyst.

After an extensive literature search, it became evident that only a handful of known iron complexes might fulfill these criteria. One such system is based on an iminopyridine ligand, initially popularized by Wieghardt and co-workers and later applied in organometallic catalysis by Ritter and co-workers (Scheme 115).^[285-288] Variations of the prototypical IP ligand were also investigated by Chirik and co-workers in iron catalyzed [4+4]-cycloadditions of 1,3-dienes.^[289] More specifically, Wieghardt discovered that the reaction of FeCl₂ and iminopyridine **277**, followed by reduction with sodium in 1,2-dimethoxyethane, yields the four-coordinate species IP₂Fe (**11**). In the same study it was established *via* Mößbauer spectroscopy that **11** is, in fact, an Fe^{II} species with a S = 1 spin state. This interpretation was further supported by calculations on the electronic structure of this complex, which indicated that the iron center features four unpaired electrons, two of which are antiferromagnetically coupled to two monoanionic iminopyridine radicals. Notably, Wieghardt and co-workers not only prepared IP₂Fe (**11**), but also succeeded in preparing IP₂M (M = Cr, Mn, Co, Ni, Zn) as well as the one-electron oxidation products thereof. Ritter and co-workers later demonstrated that IP₂Fe (**11**) selectively binds one equivalent of pyridine to form IP₂FePy (**278**). Mößbauer data indicated redox participation of the IP ligands. It was shown that IP₂FePy (**278**) serves as a highly efficient catalyst for the 1,4-hydrosilylation of 1,3-dienes. The mechanistic proposal involves the initial dissociation of the pyridine and the IP ligand, enabling the coordination of the diene. Following an oxidative addition of the silane, the resulting complex **281** undergoes migratory insertion to form an iron-allyl intermediate **282**. This allyl species undergoes π - σ rearrangement, followed by reductive elimination, ultimately closing the catalytic cycle.



Scheme 115. Wieghardt's and Ritter's systems.

The fact that IP_2Fe (**11**) selectively binds one molecule of pyridine, yet exhibits catalytic activity upon loss of one iminopyridine ligand, renders this system adequate for studying the formation of a potentially metathesis-active iron-based carbene *via* Binger's strategy. We initially performed small-scale reactions using a 1:1 mixture of IP_2Fe (**11**) and cyclopropene **12** at room temperature in Et_2O . Notably, the recorded NMR spectra indicated full conversion of the paramagnetic precursor IP_2Fe (**11**). However, no well-defined new species could be identified, as the spectrum was broad and otherwise featureless. Upon solvent removal and crystallization from *n*-pentane, single crystals suitable for single crystal X-ray diffraction were obtained. The analysis revealed that the η^2 -cyclopropene complex **15** had been formed (Scheme 116).



Scheme 116. Synthesis of a η^2 -cyclopropene complex **15**.

The X-ray structure analysis of **15** warrants a more detailed discussion (Figure 34). According to the Chatt-Dewar-Duncanson formalism, complex **15** can be interpreted either as a metallacyclopropane or as a simple olefin adduct. Particularly indicative is the C1–C2 bond length (1.435(4) Å) of complex **15**, which is significantly elongated compared to the C2–C3 bond length (1.285(4) Å) in the related free 3,3-substituted cyclopropane shown in Figure 34. Moreover, the C1–C3–C2 bond angle (56.28(17)°) of complex **15** is notably larger than the analogous C2–C1–C3 bond angle (50.34(18)°) in this cyclopropene. Both parameters suggest strong π -backdonation from a filled iron-based d-orbital into an empty π^* orbital of the cyclopropene ligand, consistent with a significant contribution from the metallacyclopropane resonance structure.

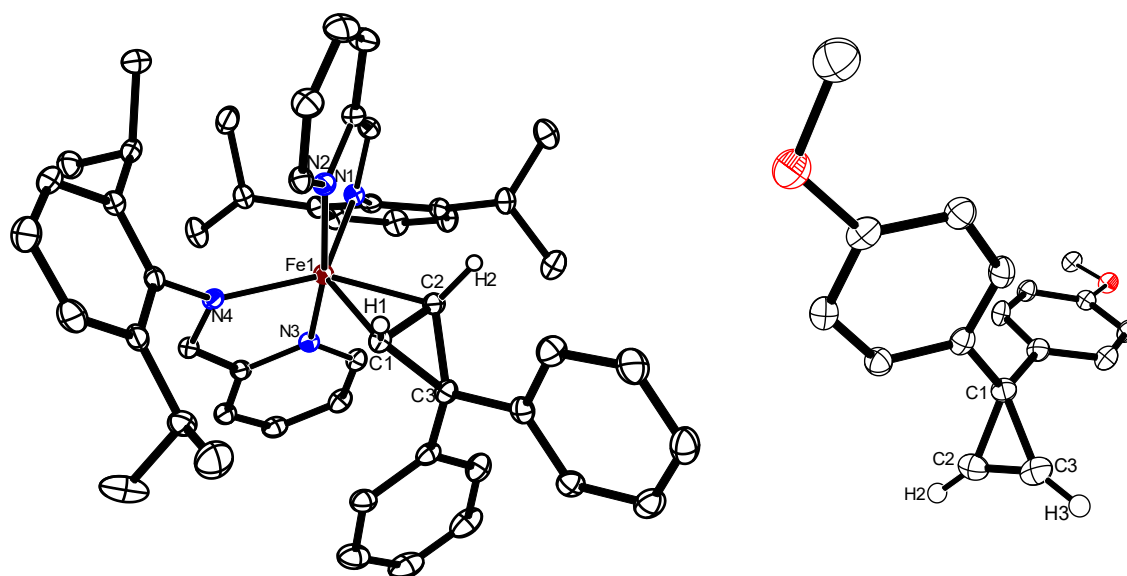


Figure 34. Left: Crystal structure of complex **15**. H-atoms apart from H1 and H2 are omitted for clarity. Right: Literature known crystal structure of a related cyclopropene; the data was taken from the CSD (refcode : JEPZOX).^[290]

Although carbene formation could be further enhanced by optimizing the reaction conditions, the paramagnetic side product **14** was consistently formed in small amounts. In one case, a crude mixture, obtained after a 2 h addition at 80°C was evaporated and extracted with *n*-pentane instead of Et₂O. The resulting black filtrate solution was stored at -20°C, leading to the formation of single crystals suitable for X-ray diffraction. Structural analysis confirmed a nearly square-planar complex **14**, formed *via* initial loss of one IPFe ligand, followed by oxidative cyclization with two equivalents of cyclopropene **12** (Figure 37). The metallacyclopentane moiety shows a marked deviation from the plane defined by the nine atoms of the IPFe moiety. This is particularly evident in the distances from the C3 (0.555 Å) and the C4 (0.496 Å) atoms to this plane. The iminopyridine ligand features bond lengths (N1–C31 (1.319(3) Å), C31–C32 (1.413(3) Å), and N2–C32 (1.383(3) Å)) indicative for the presence of a monoanionic radical ligand.^[285] This nearly square-planar geometry contrasts sharply to Fürstner and co-workers discovery, that the related complex **275**, similarly formed through oxidative cyclization of two cyclopropenes with an iron-center, is a tetrahedral Fe^{+II} species.^[284]

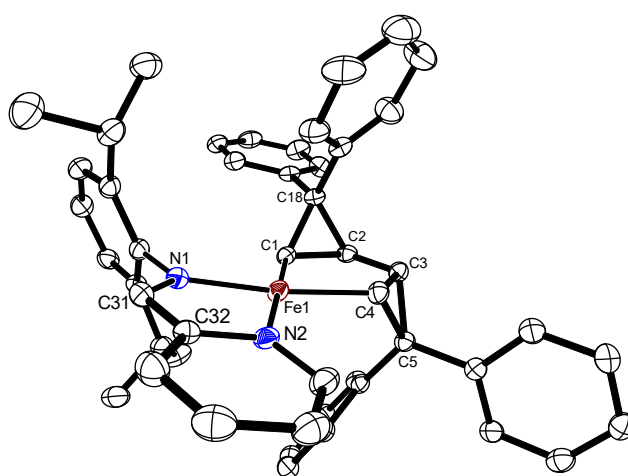
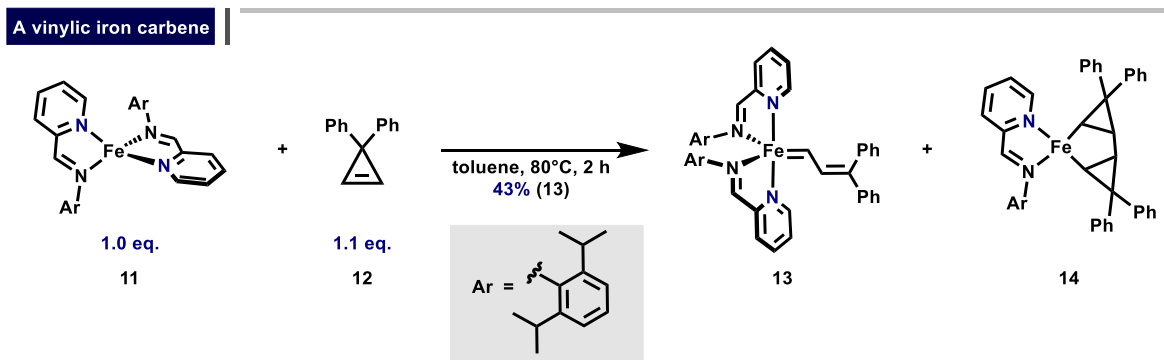


Figure 37. Crystal structure of square-planar complex **14**. H-atoms and solvent molecules are not shown for clarity.

Notably, scaling up the reaction allowed purification of carbene **13** from the side products. Additionally, a higher concentration appeared to positively influence carbene formation, as previously observed by Grubbs.^[199] Washing the crude material with minimal amounts of toluene and drying the filter cake *in vacuo* at 60°C for 30 min yielded analytically pure carbene **13** in 43% yield (Scheme 117).

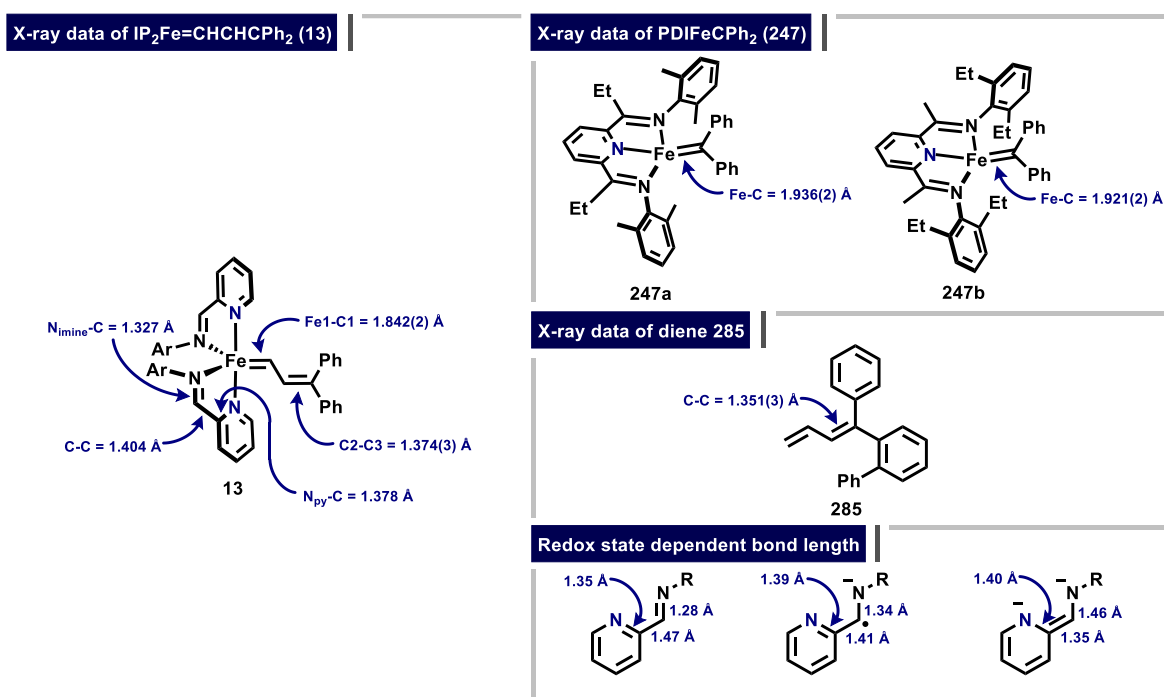


Scheme 117. The reaction of IP₂Fe (**11**) and cyclopropene **12** under optimized conditions allows for the isolation of carbene **13** in analytically pure form.

The geometrical features of carbene **13** warrant a detailed discussion. The carbene bond length Fe1–C1 (1.842(2) Å) is notably shorter than the analogous bond lengths Fe–C (1.936(2) Å and 1.921(2) Å) observed in the crystal structures of Chirik’s PDI-based carbenes **247a** and **247b**. It should be noted

that Chirik's PDI-based carbenes have been shown to be Fe^{II} species with an $S = 1$ spin state, in which the carbene ligand is best described as a monoanionic carbene radical.^[263] In contrast, the significantly shorter Fe1-C1 bond in carbene **13** may indicate a greater degree of covalent, Schrock-like character.

Furthermore, the C2-C3 bond length ($1.374(3) \text{ \AA}$) is slightly elongated compared to the corresponding C-C bond length ($1.351(3) \text{ \AA}$, CSD refcode: ZATHUZ) in the known organic reference compound **285**.^[291] The bond lengths within the iminopyridine backbone are also informative. Based on X-ray crystallographic data, Wieghardt proposed typical bond lengths for such ligand systems depending on their redox states.^[285] The average bond lengths in carbene **13**, $\text{N}_{\text{imine}}\text{-C}_{\text{imine}}$ (1.327 \AA), $\text{C}_{\text{imine}}\text{-C}_{\text{py}}$ (1.404 \AA), and $\text{N}_{\text{py}}\text{-C}_{\text{py}}$ (1.378 \AA), are very close to the bond lengths proposed for a monoanionic iminopyridine radical ligand: $\text{N}_{\text{imine}}\text{-C}_{\text{imine}}$ (1.34 \AA), $\text{C}_{\text{imine}}\text{-C}_{\text{py}}$ (1.41 \AA), and $\text{N}_{\text{py}}\text{-C}_{\text{py}}$ (1.39 \AA) (Scheme 118).



Scheme 118. Comparison of the geometrical features of carbene **13** with the metrical parameters of literature known compounds.

Compound **13** was also fully characterized by NMR spectroscopy. At 298 K, the signals of the iminopyridine ligand appeared broadened, likely due to hindered rotation around the Fe-C bond. Therefore, assignments were carried out at 233 K, where these signals appeared significantly sharper (Figure 38).

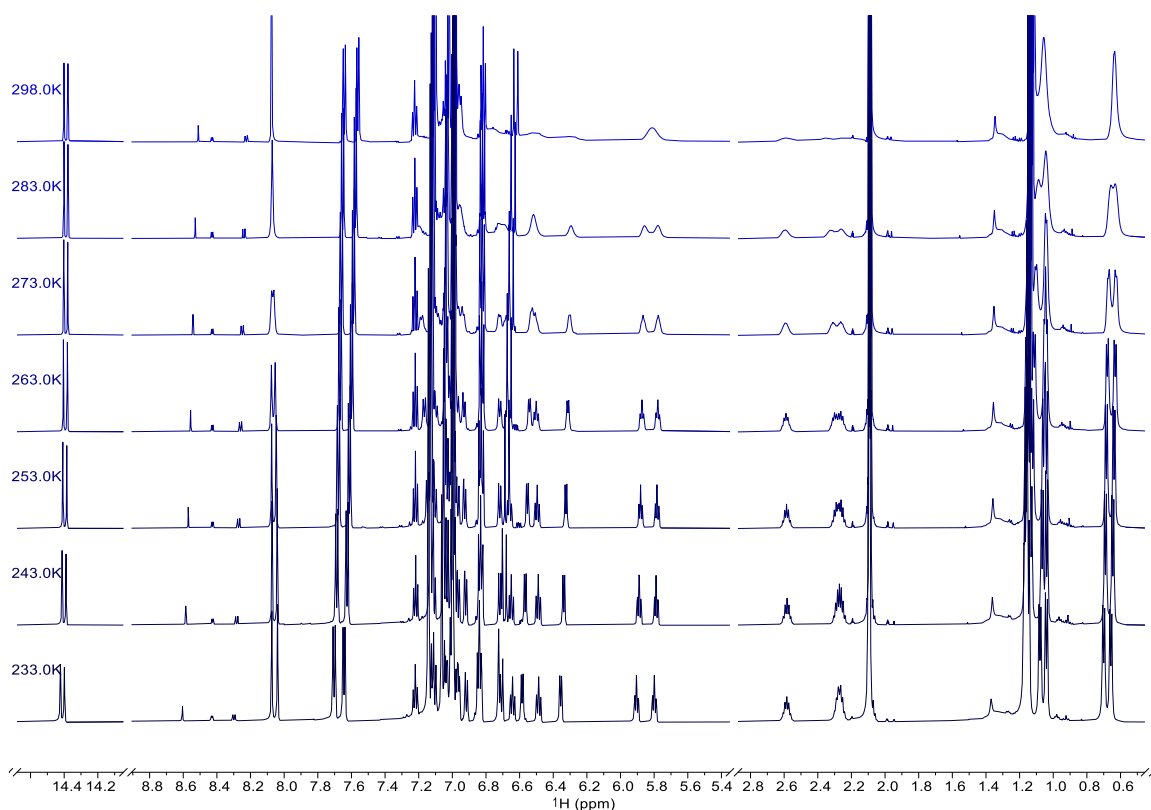


Figure 38. VT ^1H NMR data of complex **13** in $[\text{D}_8]$ -toluene from 233 to 298 K. In collaboration with Dr. Markus Leutzsch.

Key to the NMR structural assignment of **13** as a vinylic carbene were the ^1H - ^{13}C HSQC and HMBC spectra. HSQC cross peak between H-1 \leftrightarrow C-1 were observed. Both, the deshielded NMR signals for H-1 ($\delta_{\text{H}} = 14.39$ ppm) and C-1 ($\delta_{\text{C}} = 230.9$ ppm) together with the large coupling constant ($J = 14.1$ Hz) are characteristic of *trans*-isomers of transition metal vinyl carbenes (Figure 39).

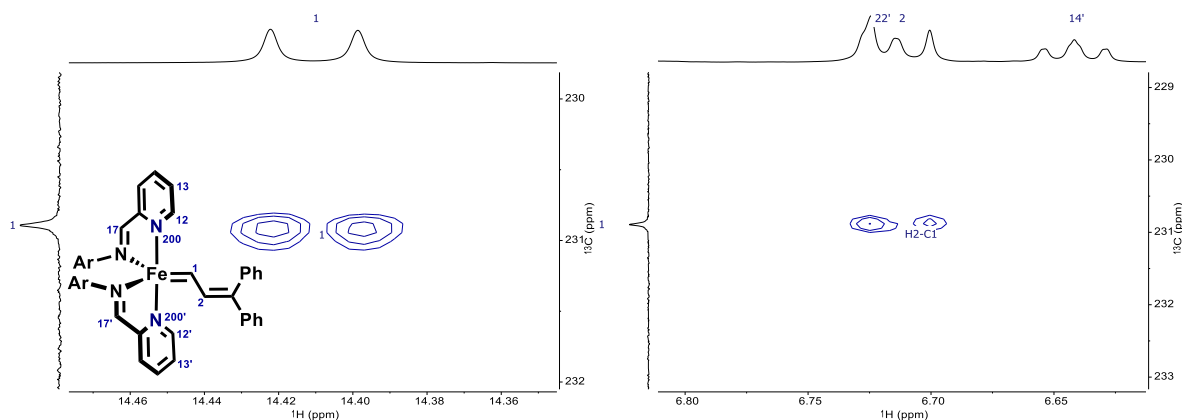


Figure 39. Left: ^1H - ^{13}C HSQC NMR spectrum of **13**. Right: ^1H - ^{13}C HMBC NMR spectrum of **x**. Measurements at 233 K in $[\text{D}_8]$ -toluene. In collaboration with Dr. Markus Leutzsch.

As complex **13** is diamagnetic, we next aimed to study this species *via* ^{57}Fe NMR spectroscopy in collaboration with Dr. Markus Leutzsch. *A priori*, the ^{57}Fe nucleus exhibits unfavorable properties: it is an $S = 1/2$ nucleus with a low natural abundance of 2.2% and a low receptivity of $4.19 \cdot 10^{-3}$ compared to the ^{13}C nucleus.^[292-294] Owing to these parameters, the ^{57}Fe nucleus is among the least sensitive nuclei in NMR spectroscopy.^[295] Furthermore, the chemical shift range spans approximately 12000 ppm.^[296] Notably, attempts have been made to correlate the ^{57}Fe NMR shielding of diamagnetic Fe^{II} porphyrin complexes with the quadrupole splitting $|\Delta E_{\text{Q}}|$ obtained from Mößbauer spectroscopy.^[297]

As no ^{57}Fe NMR shift for a system related to **13** is known in the literature, we initially resorted to calculations to predict the expected chemical shift of this iron carbene. To benchmark these calculations, we selected the following reference systems with experimentally known ^{57}Fe NMR shifts: $\text{Fe}(\text{CO})_5$,^[294] $\text{Fe}(\text{CO})_3(\text{cyclobutadiene})$,^[294] $\text{Fe}(\text{CO})_3(\text{butadiene})$,^[294] $\text{Fe}(\text{CO})_3(\text{norbornadiene})$,^[294] $\text{CpFeCl}(\text{CO})_2$,^[298] and $\text{CpFeCl}(\text{PMe}_2\text{Ph})_2$,^[299] all of which were reported in $[\text{D}_8]$ -toluene or benzene, excluding $\text{CpFeCl}(\text{CO})_2$, which was reported in CH_2Cl_2 . Cp_2Fe was re-measured in $[\text{D}_8]$ -toluene ($\delta_{\text{Fe}} = 1532$ ppm), closely matching the previously reported value in CDCl_3 ($\delta_{\text{Fe}} = 1538$ ppm).^[292]

The conformational space of the complexes was initially explored based on known data or explored based on a GOAT conformer sampling on the GFN2-xTB level of theory. For Cp_2Fe , two conformers, the eclipsed and the staggered forms, were considered based on X-ray crystallographic data. The geometries of the conformers were then optimized at the $\text{r}^2\text{SCAN-3c/CPCM}(\text{toluene})$ level of theory. With the optimized geometries in hand, ^{57}Fe NMR isotropic shieldings were calculated on the $\text{PBE0/def2-TZVPP/CPCM}(\text{toluene})$ level of theory. For Cp_2Fe , $\text{CpFeCl}(\text{PMe}_2\text{Ph})_2$, $\text{Fe}(\text{CO})_3(\text{C}_4\text{H}_4)$, and the carbene **13**, the ^{57}Fe NMR shieldings were calculated for multiple conformers and Boltzmann averaged following Grimme's CENSO workflow.^[300]

This protocol yielded an excellent correlation ($R^2 = 0.9958$) between the computed isotropic ^{57}Fe NMR shieldings and the corresponding experimental ^{57}Fe NMR chemical shifts (Figure 40).

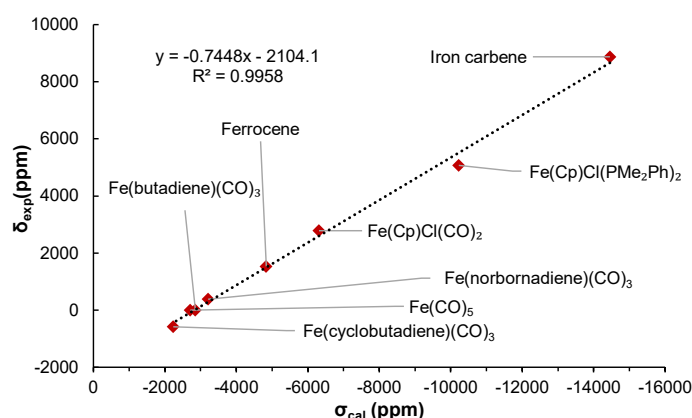


Figure 40. Correlation between the calculated ^{57}Fe NMR shielding and the experimental ^{57}Fe NMR chemical shift. In collaboration with Dr. Markus Leutzsch.

With this correlation in hand, it was possible to estimate where the ^{57}Fe NMR shift of carbene **13** might appear. Consistent with the prediction ($\sigma_{\text{cal}} = -14455$ ppm), the ^{57}Fe NMR signal was successfully detected *via* a ^1H - ^{57}Fe HMBC experiment at $\delta_{\text{exp}} = 8873.0$ ppm, showing HMBC cross peaks between $\text{Fe-1} \leftrightarrow \text{H-1}$, $\text{Fe-1} \leftrightarrow \text{H-17}$, and $\text{Fe-1} \leftrightarrow \text{H-17}'$ (Figure 41). Selected Fe porphyrin complexes exhibit similar isotropic shieldings.^[301] Note that the correlation shown in Figure 40 already includes the ^{57}Fe NMR chemical shift of the iron carbene.

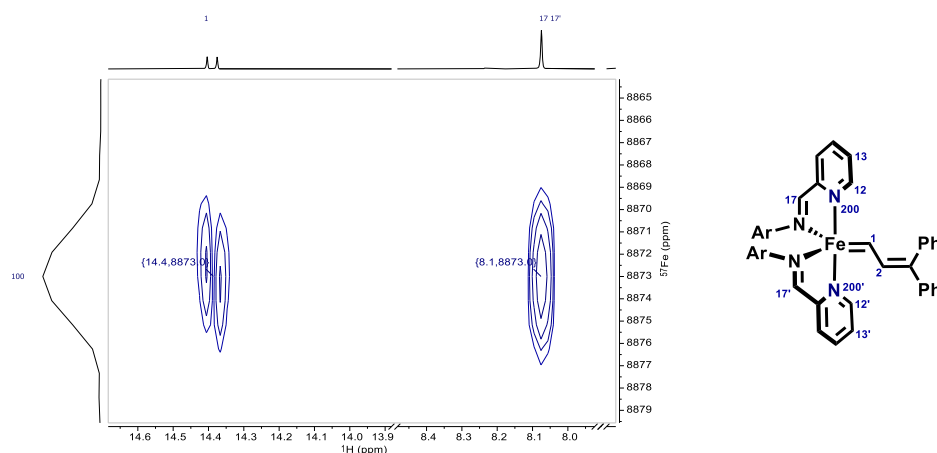


Figure 41. ^1H - ^{57}Fe HMBC NMR spectrum of **13** in $[\text{D}_8]$ -toluene at 298 K. In collaboration with Dr. Markus Leutzsch.

To determine the oxidation state of $\text{IP}_2\text{Fe}=\text{CH}-\text{CH}=\text{CPh}_2$ (**13**), zero-field Mössbauer spectra were recorded. The spectra confirmed the purity of carbene **13**; however, an unambiguous assignment of the oxidation state was not possible based on the data alone. According to the literature, the observed isomer shift $\delta = 0.08 \text{ mm s}^{-1}$ and quadrupole splitting $|\Delta E_Q| = 1.02 \text{ mm s}^{-1}$ are consistent with several possibilities: $\text{Fe}^{+\text{II}}$, $S = 0$; $\text{Fe}^{+\text{III}}$, $S = 1/2$; or $\text{Fe}^{+\text{IV}}$, $S = 1$.^[302-304]

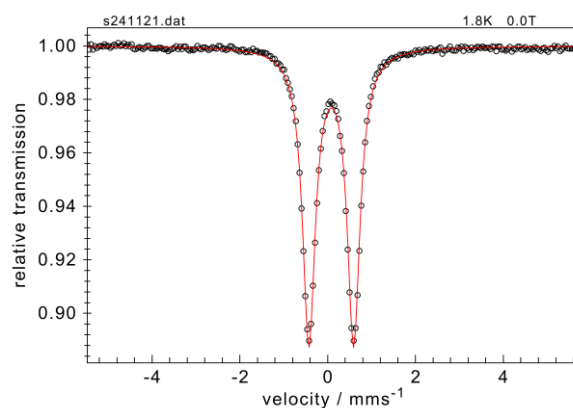


Figure 42. Zero-field Mössbauer spectrum of **13** at 1.8 K. The fitted spectrum (red line) reveals an isomer shift of $\delta = 0.08 \text{ mm s}^{-1}$ and a quadrupole splitting $|\Delta E_Q| = 1.02 \text{ mm s}^{-1}$. In collaboration with Derya Demirbas.

The three scenarios suggested by the Mössbauer parameters can be rationalized by invoking different redox states of the iminopyridine ligand. In the $\text{Fe}^{+\text{II}}$, $S = 0$ case, two neutral iminopyridine ligands and a dianionic Schrock-type R_2C^{2-} ligand would be involved. In contrast, the $\text{Fe}^{+\text{IV}}$, $S = 1$ scenario would require two monoanionic iminopyridine radical ligands and a dianionic Schrock-type R_2C^{2-} ligand. Since carbene **13** is diamagnetic, the two ligand-based radicals must be antiferromagnetically coupled with the two unpaired electrons on the $\text{Fe}^{+\text{IV}}$ center.

For the $\text{Fe}^{+\text{III}}$, $S = 1/2$ case, two possibilities arise. First, a dianionic Schrock-type R_2C^{2-} ligand along with one neutral and one monoanionic iminopyridine radical could be present, with the iminopyridine radical antiferromagnetically coupled to the unpaired electron on the $\text{Fe}^{+\text{III}}$ center. Alternatively, the $\text{Fe}^{+\text{III}}$, $S = 1/2$ center could be antiferromagnetically coupled to a monoanionic carbene radical, while the iminopyridine radicals would themselves be monoanionic radicals antiferromagnetically coupled to each other (Figure 43).

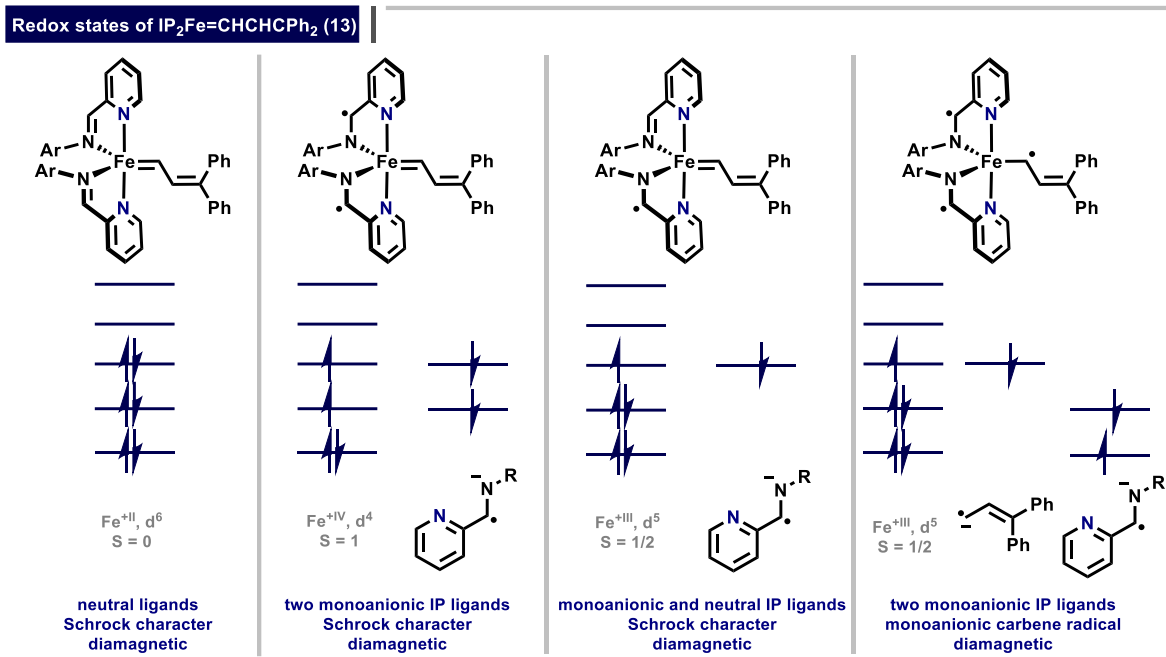
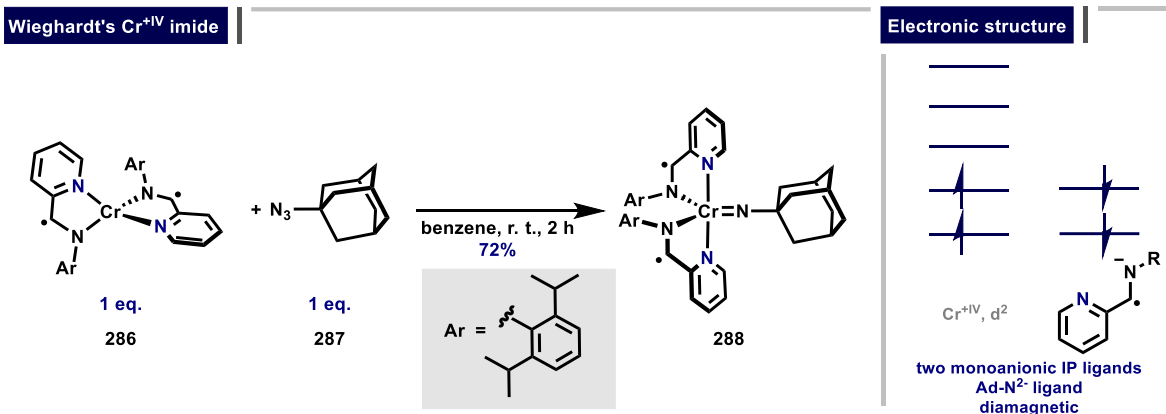


Figure 43. The possible redox states of $\text{IP}_2\text{Fe}=\text{CH}-\text{CH}=\text{CPh}_2$ (**13**) as determined by Mößbauer spectroscopy.

It is worth noting that the closely related diamagnetic compound $\text{IP}_2\text{Cr}=\text{NAd}$ (**288**) was reported by Wieghardt and co-workers (Scheme 119).^[305] This complex also features a trigonal bipyramidal geometry. X-ray absorption measurements, together with broken-symmetry calculations, established that **288** is a Cr^{IV} species with two monoanionic iminopyridine radical ligands, both of which are antiferromagnetically coupled to the two unpaired electrons on the Cr^{IV} atom.



Scheme 119. Wieghardt's Cr^{IV} imide **288**.

As Wieghardt and co-workers reported UV-Vis data for $\text{IP}_2\text{Cr}=\text{NAd}$ (**288**), we also recorded the UV-Vis spectrum of a solution of complex **13** in toluene (Figure 44). The complex exhibits absorption bands at ca. 475, 660, and 820 nm, along with a very broad band at ca. 1480 nm. The overall features of the UV-Vis spectrum of $\text{IP}_2\text{Fe}=\text{CH}-\text{CH}=\text{CPh}_2$ (**13**) closely resemble those observed in the UV-Vis spectrum of $\text{IP}_2\text{Cr}=\text{NAd}$ (**288**).^[305]

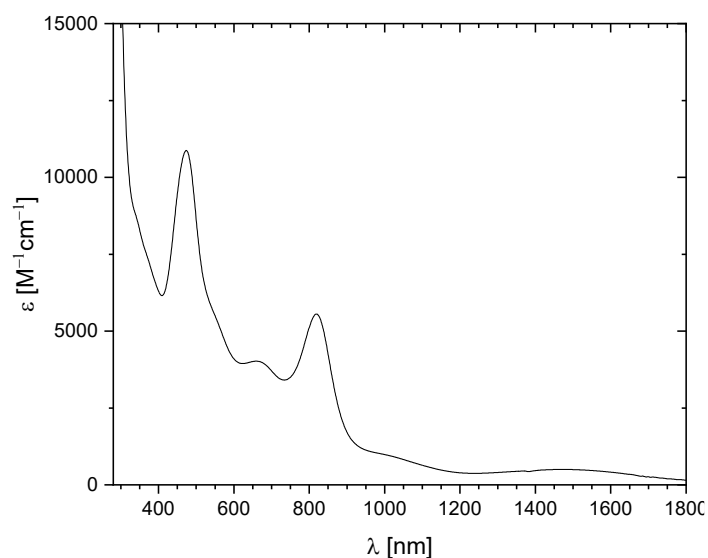


Figure 44. UV-Vis spectrum complex **13** in toluene. In collaboration with Dr. Maurice van Gastel.

We also conducted cyclic voltammetry studies in collaboration with Dr. Alexios Stamoulis. As evident from the CV data, complex **13** exhibits three redox features: a fully reversible Fe^+/Fe^0 redox couple **A** ($E^0([\text{Fe}]^{+/0}) = -0.872 \text{ V vs. Fc}^{+/0}$), an irreversible $\text{Fe}^{2+}/\text{Fe}^+$ redox couple **B**, and a quasi-reversible Fe^0/Fe^- redox couple **C** ($E^0([\text{Fe}]^{0/-}) = -2.20 \text{ V vs. Fc}^{+/0}$) (Figure 45). It should be noted that the charges reflect the charge of the complex and not oxidation state of the metal center.

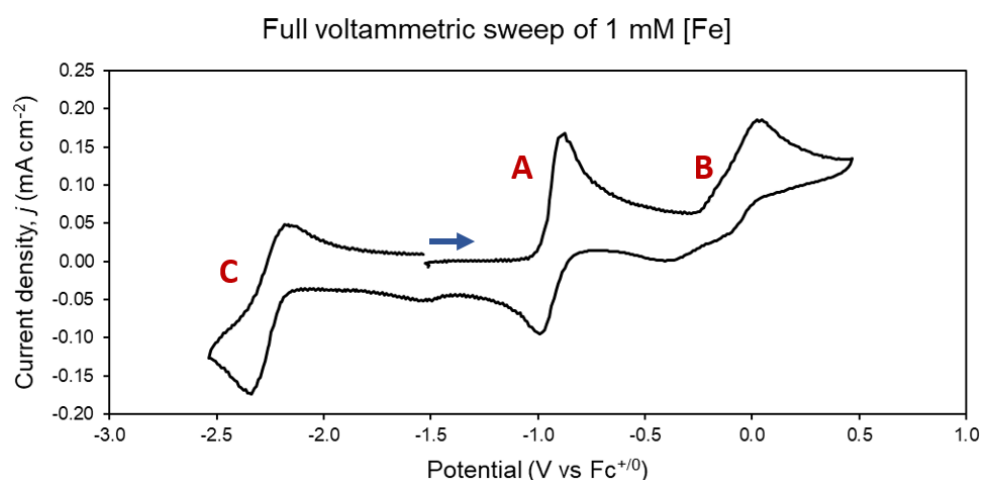
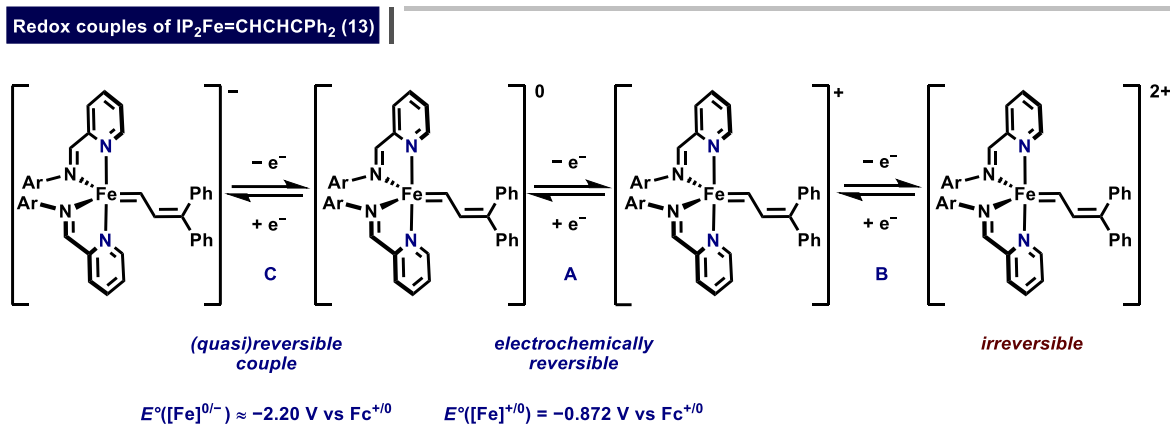


Figure 45. Top: The redox couples of complex **13**. Charges reflect charge of the complex, not oxidation state of the metal center. Bottom: Cyclic voltammogram of **13** (0.1 M $[\text{N}(\text{nBu})_4(\text{PF}_6)]$) in THF, working electrode: 1.6 mm GC disk, reference electrode: Ag wire pseudoreference. In collaboration with Dr. Alexios Stamoulis.

Further CV studies of the Fe^+/Fe^0 redox couple **A** at different scan rates confirmed its reversibility (Figure 46). A Randles-Sevcik-Plot, presented in the Experimental Section, indicates that the redox process involves freely diffusing species. Future investigations will be devoted to isolating the one-electron oxidation product of carbene **13**.

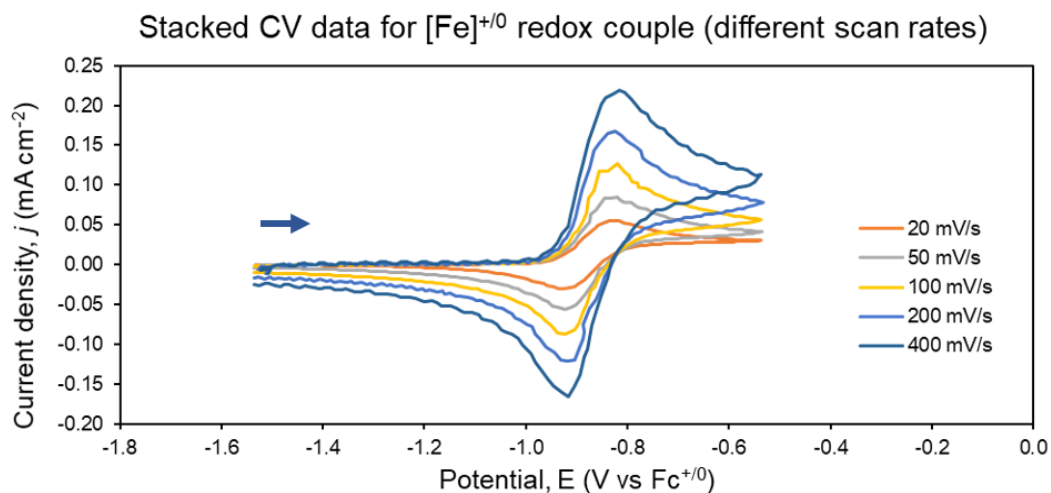


Figure 46. Stacked cyclic voltammogram **13** for redox couple **A** (0.1 M $[\text{N}(\text{nBu})_4(\text{PF}_6)]$ in THF, working electrode:1.6 mm GC disk, reference electrode: Ag wire pseudoreference. $D_{[\text{Fe}]^0} = 1.88 \times 10^{-6} \text{ cm}^2 \text{ s}^{-1}$ and $D_{[\text{Fe}]^+} = 1.23 \times 10^{-6} \text{ cm}^2 \text{ s}^{-1}$. In collaboration with Dr. Alexios Stamoulis.

The quasi-reversibility of the Fe^0/Fe^- redox couple **C** was evident by more detailed CV studies of this redox couple at different scan rates (Figure 47). A Randles-Sevcik-Plot, presented in the Experimental Section, indicates that the redox process involves freely diffusing species.

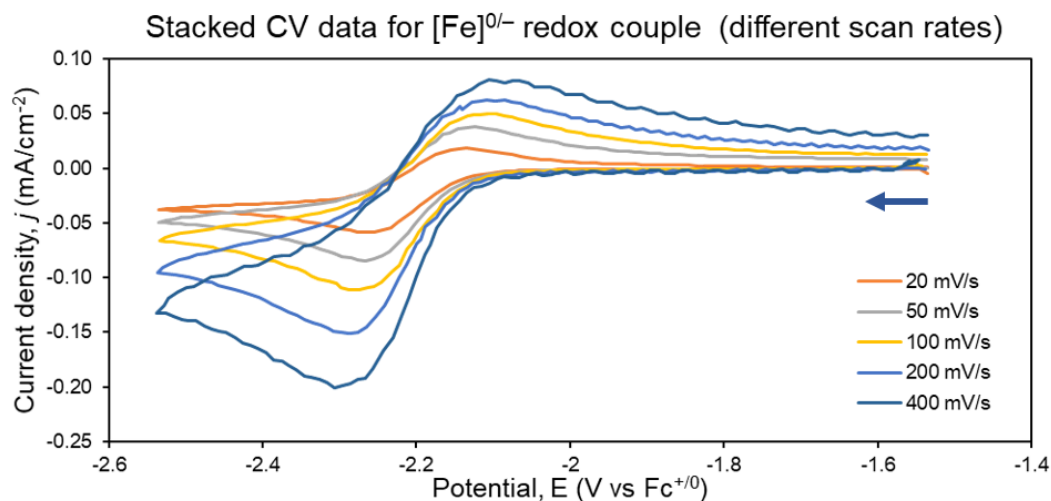
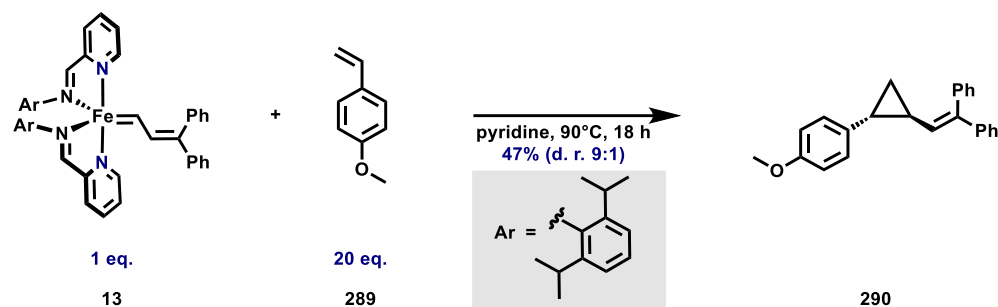


Figure 47. Stacked cyclic voltammogram **13** for redox couple **C** (0.1 M $[\text{N}(\text{nBu})_4(\text{PF}_6)]$ in THF, working electrode:1.6 mm GC disk, reference electrode: Ag wire pseudoreference. In collaboration with Dr. Alexios Stamoulis.

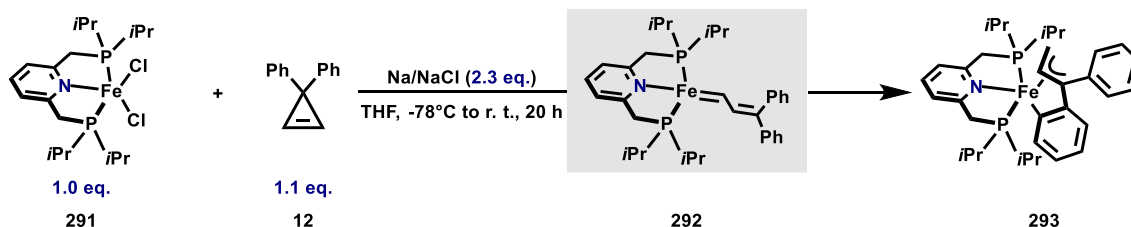
Next, we investigated whether **13** reacts with olefins such as diallylmalonate, norbornene, or styrene in toluene. However, no reaction was observed under these conditions, even at elevated temperatures. Dr. William Parisot, however, demonstrated that the styrene derivative **289** reacts with carbene **13** in pyridine at 90°C to furnish the cyclopropanation product **290**, likely formed *via* an outer-sphere mechanism (Scheme 120). Olefin metathesis is not observed, possibly because the iminopyridine ligand is too tightly coordinated once carbene **13** has formed.

Cyclopropanation with **13**

Scheme 120. Carbene **13** reacts with styrene derivative **289** in pyridine to give the cyclopropanation product **290**. Result by Dr. William Parisot.

In order to obtain an iron carbene featuring an open coordination site, an initial exploration into the reaction of cyclopropene **12** with alternative iron complexes was undertaken. It quickly became evident that IP_2Fe (**11**) is a particularly privileged system for the formation of carbenes by Binger's rearrangement strategy. This is illustrated by the reaction of complex **291**, carrying a PNP pincer ligand, with cyclopropene **12** in the presence of Na/NaCl. Although NMR spectroscopy indicated the formation of multiple species, single crystals suitable for X-ray diffraction were obtained by removing the solvent *in vacuo*, followed by crystallization from an $\text{Et}_2\text{O}/n$ -pentane mixture at -20°C . A crystal structure analysis confirmed the formation of allyl complex **293**, which likely arises from the decomposition of initially formed carbene **292** *via* activation of the *ortho* C–H bond of one of the phenyl groups in the vinyl carbene moiety (Scheme 121 and Figure 48).

An allyl iron species



Scheme 121. The reaction of iron complex **291** with cyclopropene **12** results in formation of the allyl species **293**.

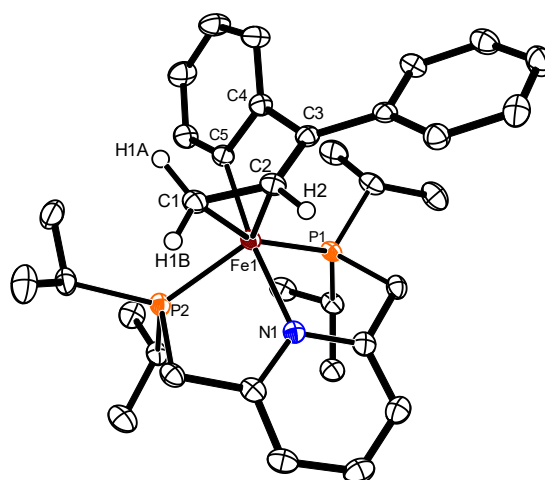
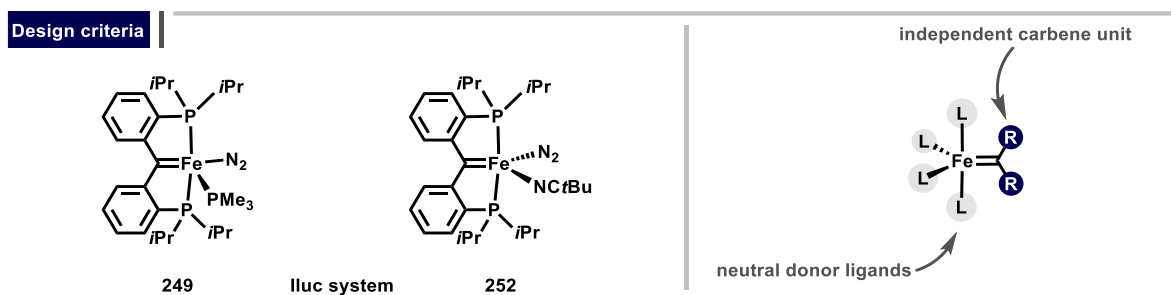


Figure 48. Crystal structure of **293**. H-atoms (except H1 and H2) and solvent molecules are not shown for clarity.

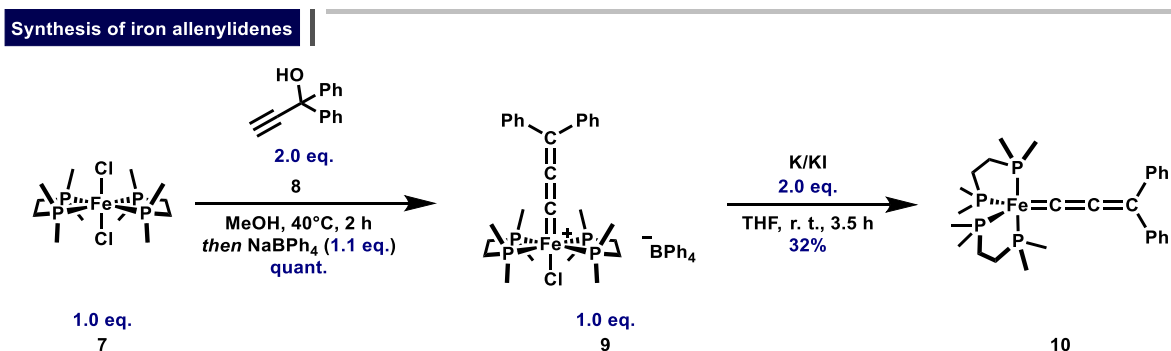
2.5 Summary (Part II)

The catalytic metathesis of olefins, commonly achieved using Mo- or Ru-based carbenes, is beyond the scope of iron carbenes. Such application would be highly desirable, as iron is an earth abundant and inexpensive transition-metal, but also as a fundamentally intriguing challenge in organometallic chemistry. So far, iron carbenes tend to favor a competitive pathway, the cyclopropanation of olefins. However, recent landmark studies by Iluc and co-workers on the stoichiometric metathesis of olefins and alkynes highlight the potential of iron carbenes to serve as catalysts for the metathesis of olefins (Scheme 122). It was anticipated that an iron carbene that mirrors the key features of the carbenes reported by Iluc and co-workers could serve as a feasible starting point for such investigations. Thus a five-coordinate, diamagnetic iron carbene surrounded by four neutral donor ligands and a standalone carbene ligand was selected as a promising motif (Scheme 122).



Scheme 122. Left: Iron carbenes reported by Iluc and co-workers. Right: Key characteristics of the targeted iron carbene.

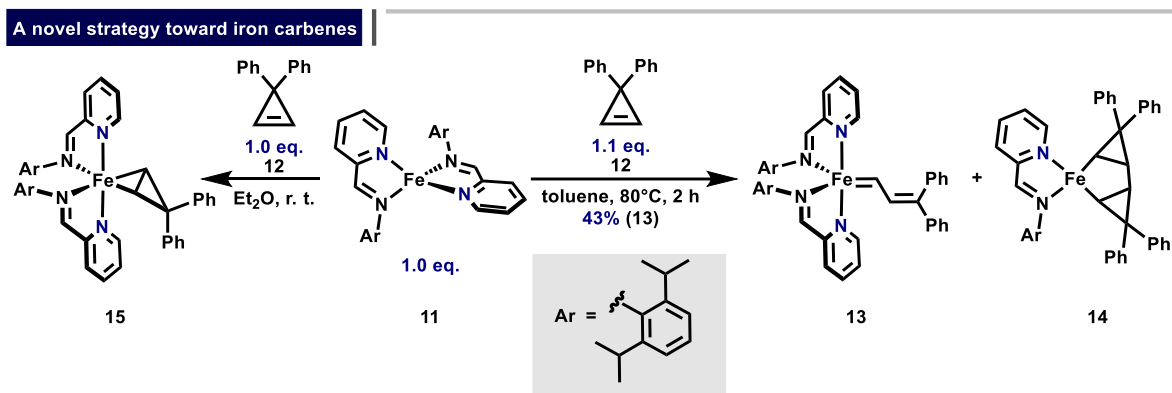
Various methods for the synthesis of iron carbenes with such characteristics were explored within this doctoral thesis. Initial efforts focused on the utilization of a α -H abstraction, but proved unsuccessful for benzyl-substituted complexes. Therefore, we turned our attention to the activation of propargylic alcohols with $\text{dmppe}_2\text{FeCl}_2$ (**7**), followed by reduction with K/KI. Although the activation of propargylic alcohols by the related complex $\text{depe}_2\text{FeBr}_2$ (**269**) had been reported previously, the reduction of the resulting cationic allenylidene has no precedent. This strategy ultimately enabled the isolation of a rare example of a phosphine-ligated formally Fe^0 allenylidene **10**. Complex **10** was analyzed using X-ray crystallography, NMR spectroscopy, elemental analysis, and mass spectrometry (Scheme 123).



Scheme 123. Synthesis of the allenylidenes **9** and **10**.

We next established a novel approach for the synthesis of iron carbenes: the Binger rearrangement strategy. This approach involves the formal electrocyclic ring-opening of a strained cyclopropane to generate an iron carbene. Although this method had previously been explored for iron complexes, it was found to suffer from a dominant side reaction: oxidative cyclization of two cyclopropenes with an iron center to form a metallacyclopentane. This limitation was overcome through the judicious choice of the iron precursor IP_2Fe (**11**), first reported by Wiegardt and co-workers. Depending on the reaction

conditions, either the η^2 -cyclopropene complex **15** or the vinylic carbene **13** was obtained (Scheme 124). Notably, carbene formation competes with oxidative cyclization, as both complexes **13** and **14** were identified in the reaction mixture. While complex **13** does not mediate or catalyze the metathesis of olefins, it was found to cyclopropanate olefins under specific conditions.



Scheme 124. The Binger rearrangement strategy enabled the synthesis of the vinylic carbene **13**.

The iron carbene **13** was characterized using a wide array of analytical techniques, including X-ray crystallography, elemental analysis, IR spectroscopy, UV-Vis spectroscopy, mass spectrometry, Mößbauer spectroscopy, cyclic voltammetry, and NMR spectroscopy. Notably, conventional NMR analysis was complemented by ^{57}Fe NMR spectroscopy, a technique that is highly challenging due to the unfavorable properties of the ^{57}Fe nucleus and often requires isotopically enriched samples. Guided by ^{57}Fe NMR calculations, the ^{57}Fe resonance at 8873.0 ppm was successfully detected *via* a ^1H - ^{57}Fe HMBC NMR experiment performed at natural abundance (Figure 49).

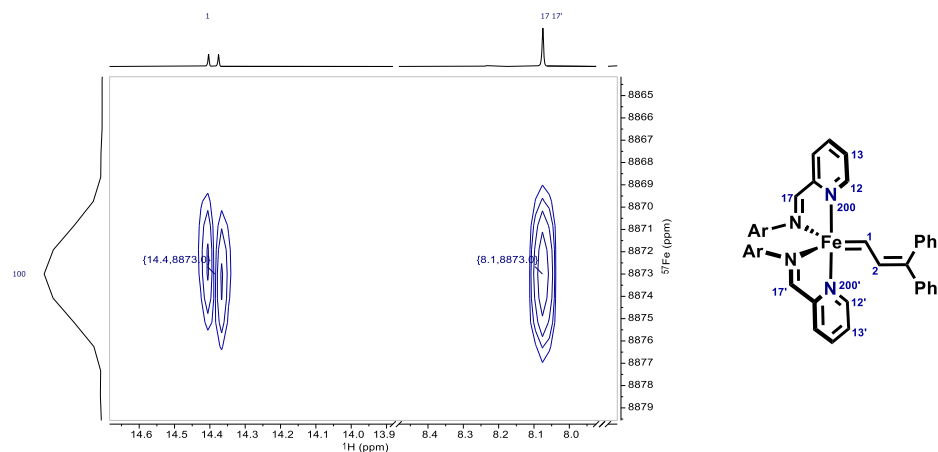


Figure 49. ^1H - ^{57}Fe HMBC NMR spectrum of **13** in $[\text{D}_8]$ -toluene at 298 K. In collaboration with Dr. Markus Leutzsch.

3 Experimental Section

3.1 General

Manipulations of air and hydrolysis sensitive substances were carried out using standard Schlenk techniques. Unless stated otherwise, all reactions were carried out in glassware which had been heated in high vacuum with a Bunsen burner, cooled to ambient temperature and filled with argon prior to use. Likewise, all cannulas and syringes were carefully flushed with argon before use.

The solvents used were distilled after drying over the indicated reagents and stored under an argon atmosphere over molecular sieves (3 Å): tetrahydrofuran (magnesium/anthracene), benzene (CaH₂), dichloromethane (CaH₂), diethyl ether (Na/K), toluene (sodium tetraethylaluminium), *n*-pentane (Na/K). Hexamethyldisiloxane (HMDSO), [D₆]-benzene and [D₈]-toluene were degassed by three freeze-pump-thaw cycles and then stored over molecular sieves (3 Å).

Molecular sieves were activated at 180 °C for 3 d under high vacuum (10⁻³ mbar) and stored under argon.

Commercially available chemicals were used without further purification unless otherwise noted. The following compounds were prepared according to the literature: complex **1**,^[3, 70, 88, 306] complex **7**,^[279] IP₂Fe (**11**),^[285] cyclopropene **12**,^[307] complex **91**,^[119] complex **94**,^[75] ligands **141**,^[115-116], compound **148**,^[116] complex **167**,^[75] complex **168**,^[76] complex **291**,^[308] BnK,^[309] K/KI.^[282]

All ligands used were dried by the following method: The ligand was dissolved in toluene and then powdered molecular sieves (4 Å) were added. The resulting suspension was stirred overnight, filtered *via* cannula and all volatile components were removed *in vacuo* (10⁻³ mbar).

Flash chromatographic separations were performed on silica gel (Merck, type 9385, 230-400 mesh, 60 Å pore diameter) as stationary phase. Reaction control was performed on ready-to-use films for thin-layer chromatography (40 x 80 mm, Polygram® SIL G/UV254). Detection was achieved under UV-light (254 nm) and/or by staining with either acidic *p*-anisaldehyde, cerium ammonium molybdate, or basic KMnO₄ solution.

Nuclear magnetic resonance spectroscopy (NMR)

Spectra were recorded on Bruker Avance III HD 400 MHz or Avance Neo 600 MHz NMR spectrometers in the indicated solvents; chemical shifts (δ) are given in ppm relative to tetramethylsilane (TMS), coupling constants (J) in Hz. The multiplicities of the signals are described by the following abbreviations: s: singlet, d: doublet, t: triplet, q: quartet, pent: quintet, sept: septet, m: multiplet, bs: broad signal. Solvent signals were used as reference and chemical shifts were converted to the TMS scale ([D₆]-benzene: δ_C = 128.06 ppm, residual ¹H: δ_H = 7.16 ppm; CD₂Cl₂: δ_C = 53.84 ppm, residual ¹H: δ_H = 5.32 ppm; [D₈]-toluene: δ_C = 20.43 ppm, residual ¹H: δ_H = 2.09 ppm). 1D ²⁹Si NMR spectra were acquired with a polarisation transfer pulse sequence (refocussed INEPT) and broadband proton decoupling. ⁹⁵Mo NMR spectra were acquired using the Bruker aring pulse sequence to minimize acoustic ringing from the NMR probe at 333 K unless noted otherwise. The $\pi/2$ ⁹⁵Mo pulse was calibrated with a Na₂MoO₄ (2 M in D₂O) sample and had a typical length of 22.5 μ s. ¹⁵N NMR shifts were extracted from cross peaks in a ¹H-¹⁵N-HMBC experiments. ²⁹Si and ⁹⁵Mo chemical shifts were referenced indirectly to the ¹H chemical shift of the solvent according to IUPAC recommendations using the *xiref* macro in Bruker Topspin.^[310] ¹⁵N chemical shifts are reported relative to CH₃NO₂ (δ = 0 ppm; Ξ = 10.136767%), ²⁹Si chemical shifts are reported relative to Me₄Si (δ = 0 ppm; Ξ = 19.867187%), ⁹⁵Mo chemical shifts relative to Na₂MO₄ (δ = 0 ppm; Ξ = 6.516926%) and ⁵⁷Fe chemical shifts are reported relative to Fe(CO)₅ (δ = 0 ppm; Ξ = 3.237778%).

Single-crystal structure analysis

Single-crystal structure determinations were conducted at the Max-Planck-Institut für Kohlenforschung in the department for “Chemical crystallography and electron microscopy”. Structure determinations were performed on either a Bruker AXS D8-Venture diffractometer with an I μ S Diamond Mo-anode or a Bruker-AXS Kappa Mach3 with an APEX-II detector and an I μ S microfocus Mo-anode.

Infrared spectroscopy (IR)

IR spectra were measured on a Spectrum One (Perkin-Elmer) spectrometer at room temperature. Absorption bands are reported in wavenumbers (cm⁻¹).

Mass spectrometry (MS)

High-resolution mass spectra (HRMS) were measured with a Finnigan MAT 95 spectrometer (EI) or a Bruker APEX III FT-ICR-MS (ESI). All values are given in mass units per elementary charge (m/z).

Magnetometry

Variable temperature direct current (DC) magnetic susceptibility data for **6b** was measured using a MPMS3 Quantum Design SQUID magnetometer at the Max Planck Institute for Chemical Energy Conversion (MPI CEC) in the Joint Workspace with the Max-Planck-Institut für Kohlenforschung (MPI KoFo).

UV-Vis spectroscopy

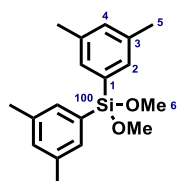
UV-vis spectra were recorded in 2 mm quartz cuvettes at room temperature on a Cary6000i UV-vis-NiR spectrometer.

Elemental analysis

Elemental analysis were performed by Mikroanalytisches Laboratorium H. Kolbe, Oberhausen, Germany.

3.2 Tripodal Silanolate Ligands Expand MoX₃ Chemistry Beyond Its Traditional Borders

Bis(3,5-dimethylphenyl)dimethoxysilane (151)



A solution of 5-bromo-*m*-xylene (15 mL, 0.11 mol) in THF (75 mL) was added dropwise over a period of 1 h to a suspension of Mg turnings (2.9 g, 0.12 mol) and LiCl (4.7 g, 0.11 mol) in THF (40 mL). After 5 min, heat evolution was observed. Stirring was continued for 30 min before the mixture was transferred *via* cannula into the dropping funnel used in the reaction described below.

This solution of (3,5-dimethylphenyl)magnesium bromide in THF was added dropwise over a period of 10 min to a solution of Si(OMe)₄ (7.5 mL, 51 mmol) in THF (135 mL) at 0 °C. Once the addition was complete, stirring was continued for 2 h at ambient temperature before water (150 mL) was carefully added to quench the reaction. The mixture was transferred into a separatory funnel and the aqueous phase extracted with EtOAc (3 x 100 mL). The combined organic layers were dried over MgSO₄, and all volatile components were removed *in vacuo* to give a colorless oil. The crude product was purified by distillation in high vacuum (10⁻³ mbar, bath temperature: 185 °C; b. p. 145-147 °C) to give the title compound as a colorless solid (7.6 g, 50%).

¹H NMR (600 MHz, CD₂Cl₂, 298 K): δ = 7.24–7.23 (m, 4H; H-2), 7.08–7.07 (m, 2H; H-4), 3.59 (s, 6H; H-6), 2.30 ppm (q, *J* = 0.6 Hz, 12H; H-5).

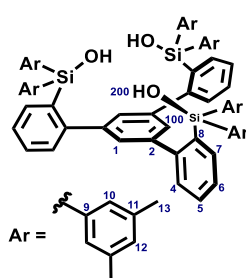
¹³C NMR (151 MHz, CD₂Cl₂, 298 K): δ = 137.7 (C-3), 132.69 (C-1), 132.68 (C-2), 132.4 (C-4), 51.0 (C-6), 21.5 ppm (C-5).

²⁹Si NMR (119 MHz, CD₂Cl₂, 298 K): δ = –28.9 ppm.

IR (ATR): $\tilde{\nu}$ = 2934, 2857, 2834, 1594, 1455, 1404, 1379, 1273, 1182, 1139, 1072, 991, 938, 870, 851, 799, 720, 696, 569, 547, 532, 485, 447, 431, 417 cm⁻¹.

HRMS (EI⁺): *m/z* calculated for C₁₈H₂₄O₂Si [M]⁺: 300.15401, found: 300.15412.

Ligand 141a



A solution of *tert*-butyllithium (1.7 M in *n*-pentane, 17 mL, 28 mmol) was added dropwise over a period of 10 min to a suspension of 1,3,5-tris-2'-bromophenylbenzene (**148**) (2.4 g, 4.4 mmol) in Et₂O (48 mL) at -110 °C. Stirring was continued for 1 h at that ambient temperature before the mixture was cooled again to -110 °C and a solution of compound **151** (3.4 g, 14 mmol) in Et₂O (12 mL) was slowly introduced. Stirring was continued for 2 h at ambient temperature before water (30 mL) was carefully added to quench the reaction.

The mixture was transferred into a separatory funnel and the organic phase was separated. The aqueous phase was extracted with CH₂Cl₂ (3 x 50 mL) and the combined organic layers were dried over MgSO₄. All volatile components were removed *in vacuo* to give a light yellow foam (4.6 g), which was used without further purification in the next step.

Conc. aq. HCl (30 mL, 37 mmol) was added to a solution of this crude material (4.6 g, 4.2 mmol) in THF (100 mL) at 0 °C under air. Stirring was continued for 2 h at ambient temperature before aq. NaOH solution (3 M, 130 mL) was carefully added. The mixture was transferred into a separatory funnel and the organic phase was separated. The aqueous phase was extracted with CH₂Cl₂ (5 x 50 mL) and the combined organic layers were dried over MgSO₄. All volatile components were removed *in vacuo* to give a light yellow crystalline solid, which was washed with CH₂Cl₂ (1 x 10 mL, 1 x 5 mL) and dried under high vacuum (10⁻³ mbar) to give the title compound as a white powder (2.7 g, 57% over two steps).

¹H NMR (600 MHz, CD₂Cl₂, 298 K): δ = 7.41–7.39 (m, 3H; H-7), 7.25–7.20 (m, 6H; H-5 and H-6), 7.13–7.12 (m, 12H; H-10), 7.07 (s, 3H; H-1), 6.91–6.90 (m, 6H; H-12), 6.84–6.83 (m, 3H; H-4), 3.96 (s, 3H; H-200), 2.12 ppm (s, 36H; H-13).

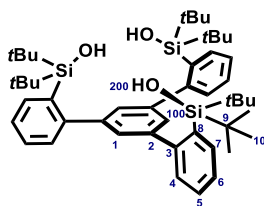
¹³C NMR (151 MHz, CD₂Cl₂, 298 K): δ = 148.9 (C-3), 144.1 (C-2), 137.8 (C-7), 137.5 (C-11), 134.5 (C-8), 132.2 (C-10), 131.6 (C-12), 130.0 (C-5), 129.2 (C-4), 129.0 (C-1), 126.3 (C-6), 21.4 ppm (C-13).

²⁹Si NMR (119 MHz, CD₂Cl₂, 298 K): δ = -12.4 ppm.

IR (ATR): $\tilde{\nu}$ = 3415, 3013, 2916, 2857, 1584, 1557, 1469, 1437, 1402, 1376, 1269, 1168, 1138, 1088, 1064, 1037, 989, 939, 896, 860, 845, 800, 761, 739, 714, 696, 666, 652, 637, 622, 553, 537, 520, 491, 475, 411x cm⁻¹.

HRMS (ESI⁺): *m/z* calculated for C₇₂H₇₂NaO₃Si₃ [M+Na]⁺: 1091.46815, found: 1091.46797.

Ligand **141e**



*m*CPBA (77% *w/w*, 1.23 g, 5.50 mmol) was added in portions to a solution of silane **149e** (671 mg, 0.915 mmol) in THF (9 mL) at 0 °C in air. The mixture was stirred at ambient temperature for 3 d before sat. aq. Na₂S₂O₃ (10 mL) was added. The mixture was transferred into a separatory funnel and diluted with *tert*-butyl methyl ether (100 mL), and the aqueous phase was separated. The organic phase was washed with sat. aq. Na₂CO₃ solution (3 x 50 mL) and dried over MgSO₄ before all volatile components were removed *in vacuo* to give a colorless oil. The residue was dissolved in THF (40 mL) and aq. NaOH solution (3 M, 40 mL) was added. The resulting mixture was vigorously stirred for 30 min, transferred into a separatory funnel and diluted with *tert*-butyl methyl ether (50 mL). The aqueous phase was separated and the organic phase was washed with brine (50 mL). The organic layer was dried over MgSO₄ before all volatile components were removed *in vacuo* to give a colorless oil.

The oil was dissolved in *n*-pentane (15 mL) and the solution stored over 3 Å MS for 16 h. All volatile components were removed *in vacuo* (10⁻³ mbar) to give a colorless oil. The oil was dissolved in toluene (1 mL), which was then evaporated to give a white foam. The foam was dried at 120 °C for 30 min under high vacuum (10⁻³ mbar) whereupon it started to melt. While cooling to ambient temperature, ligand **141e** started to crystallize as a white solid (617 mg, 86%). Colorless single crystals of the monohydrate of complex **141e** suitable for X-ray diffraction were obtained by storing a solution of the compound in hexamethyldisiloxane (HMDSO) at -20 °C.

¹H NMR (600 MHz, [D₈]-toluene, 353 K): δ = 7.64 (dd, *J* = 7.4, 1.5 Hz, 3H; H-7), 7.45 (s, 3H; H-1), 7.32 (bs, 3H; H-4), 7.17 (td, *J* = 7.5, 1.5 Hz, 3H; H-5), 7.13 (td, *J* = 7.4, 1.4 Hz, 3H; H-6), 1.68 (bs, 3H; H-200), 1.06 ppm (s, 54H; H-10).

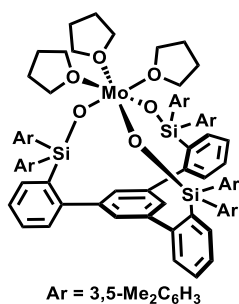
¹³C NMR (151 MHz, [D₈]-toluene, 353 K): δ = 149.3 (C-3), 144.7 (C-2), 135.1 (C-7), 135.0 (C-8), 131.0 (C-4), 128.9 (C-5), 126.2 (C-6), 28.9 (C-10), 21.4 ppm (C-9). The signal of C-1 is broad and overlaps with a [D₈]-toluene peak at 129.0 ppm.

²⁹Si NMR (119 MHz, [D₈]-toluene, 353 K): δ = 3.7 ppm.

IR (ATR): $\tilde{\nu}$ = 3644, 3607, 3051, 2932, 2889, 2856, 1583, 1558, 1471, 1429, 1409, 1388, 1363, 1259, 1121, 1096, 1063, 1012, 935, 885, 820, 760, 738, 727, 714, 683, 629, 577, 529, 479, 437, 413 cm⁻¹.

HRMS (ESI⁺): *m/z* calculated for C₄₈H₇₂NaO₃Si₃ [M+Na]⁺: 803.46815, found: 803.46838.

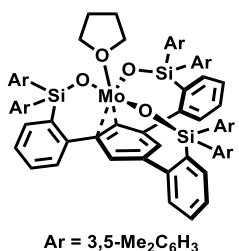
Complex **2·3THF**



A dark red solution of complex **1** (312 mg, 0.499 mmol) in THF (27 mL) was added to a colorless solution of ligand **141a** (484 mg, 0.453 mmol) in THF (27 mL). After the addition was complete, the dark red solution was concentrated under high vacuum (10^{-3} mbar) to ca. 1/4 of its volume to give a dark red-brown suspension, which was filtered under Ar to give a first crop of complex **2·3THF** as the pale orange filter cake. The dark red-brown filtrate was stored for 1 d at -20°C , causing the precipitation of additional **2·3THF** as pale orange crystals. Complex **2·3THF** decomposes upon application of high vacuum; therefore no elemental analysis was obtained.

Complex **2·3THF** can be stored as a suspension in THF to avoid decomposition. Although it has a limited solubility in THF, diluted solutions can be prepared, from which single crystals suitable for X-ray diffraction were grown upon storage at -20°C .

Complex **2·THF**



A dark red solution of complex **1** (312 mg, 0.499 mmol) in THF (27 mL) was added to a colorless solution of ligand **141a** (484 mg, 0.453 mmol) in THF (27 mL). The resulting dark red solution was concentrated under high vacuum (10^{-3} mbar) to ca. 1/4 of its volume to give a dark red-brown suspension, which was filtered to give complex **2·3THF** as the pale orange filter cake.

The pale orange filter cake was dissolved in *n*-pentane (9 mL) to form a deep red solution, which was vigorously stirred for a few minutes until a large amount of a red microcrystalline solid started to precipitate. Once the precipitation was complete as indicated by the loss of the red color of the solution, the solvent was filtered off and the resulting red filter cake was dried under high vacuum (10^{-3} mbar) to give complex **2·THF** as a red microcrystalline solid material (259 mg). The pale orange filtrate was stored for at least 1 d at -20°C causing the formation of a second crop of pale orange crystals, which were collected and dissolved in *n*-pentane (9 mL) to form again a deep red solution. After vigorous stirring for a few minutes, a second crop of red microcrystalline solid material started to precipitate, which was filtered off and dried under high vacuum (10^{-3} mbar) to give a second crop (46.7 mg). Combined yield of the dark red complex **2·THF**: 306 mg, 55%.

Complex **2·THF** has a broad and featureless ^1H NMR spectrum.

Elemental analysis (%) calculated for $\text{C}_{76}\text{H}_{77}\text{MoO}_4\text{Si}_3$: C 73.93, H 6.29, Mo 7.77, Si 6.82; found: C 73.72, H 6.34, Mo 7.75, Si 6.81.

The crystallization of this complex proved to be extremely challenging, as SC-XRD revealed that all the crystals examined were multicomponent, containing complex **2·THF** as the major species, along with two minor constituents. These minor species were identified as a η^6 species **2** devoid of any THF ligands and a third species, which could not be unambiguously assigned.

Single crystals were obtained using different methods in numerous attempts at isolating the η^2 species **2·THF** in pure form. A typical crystallization experiment is described below:

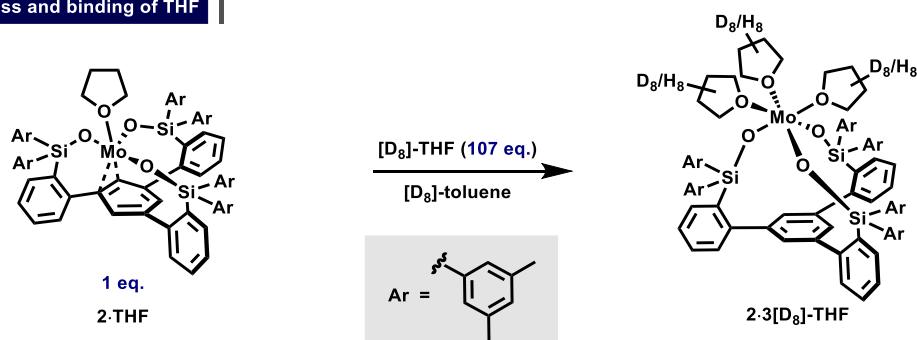
To a colorless solution of ligand **141a** (158 mg, 0.147 mmol) in THF (9 mL) was added a dark red solution of complex **1** (98.3 mg, 0.157 mmol) in THF (9 mL). The resulting dark red solution was concentrated to ca. 1/4 of its volume to give a dark red-brown suspension, which was filtered under Ar. The pale orange filter cake was dissolved in *n*-pentane (3 mL) to form a deep red solution, from which

red crystals precipitated after some minutes. The solvent was filtered off, and the resulting red filter cake was dissolved in toluene (1.5 mL; added in 0.5 mL increments). The solution was carefully layered with *n*-pentane (4.5 mL). Short vigorous stirring was necessary to initiate the precipitation of a red solid. The mixture was then left standing for approximately 1 h before the supernatant solution was filtered off and discarded. The red filter cake was dissolved again in toluene (1 mL; added in 0.5 mL increments) and the resulting solution was again carefully layered with *n*-pentane (3 mL). Over time, red single crystals began to form, which were used for numerous XRD analyses.

Notably, after precipitation from *n*-pentane, the crystals no longer dissolve in *n*-pentane.

Reversibility of THF binding between complex **2**·THF and complex **2**·3THF

Reversible loss and binding of THF



$[D_8]$ -THF (0.4 mL) was added to a dark red solution of complex **2**·THF (56.6 mg, 0.0458 mmol) in $[D_8]$ -toluene (0.4 mL). The resulting solution was transferred into a J-Young NMR tube and spectra were recorded at different temperatures. Over time, crystals started to precipitate from this solution. Some of these crystals were transferred to a microscope slide, where the crystalline batch appeared homogeneous. Determination of the unit cell of these crystals proved that the tris-THF adduct **2**·3THF had formed.

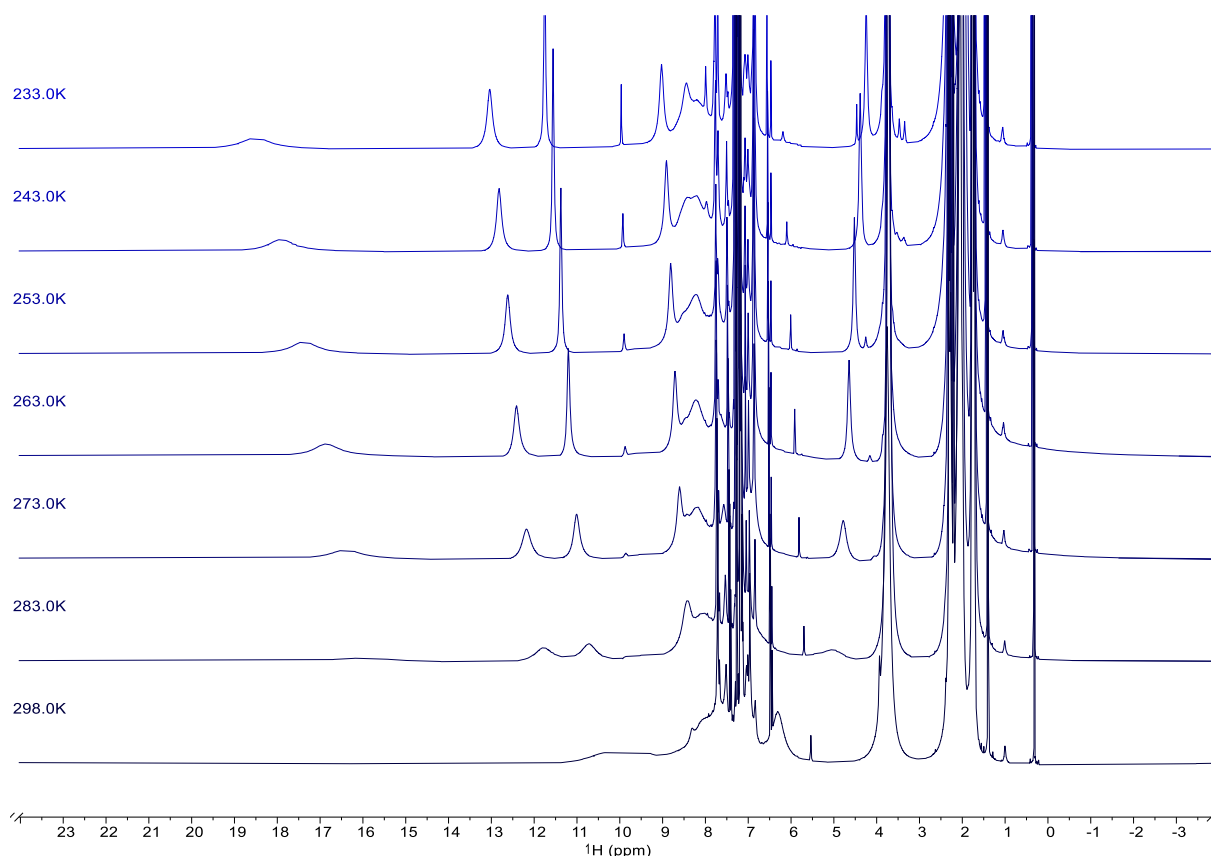


Figure 50. 1H NMR spectra of the reaction between complex **2**·THF and $[D_8]$ -THF: $[D_8]$ -toluene, 233 K–298 K, 600 MHz.

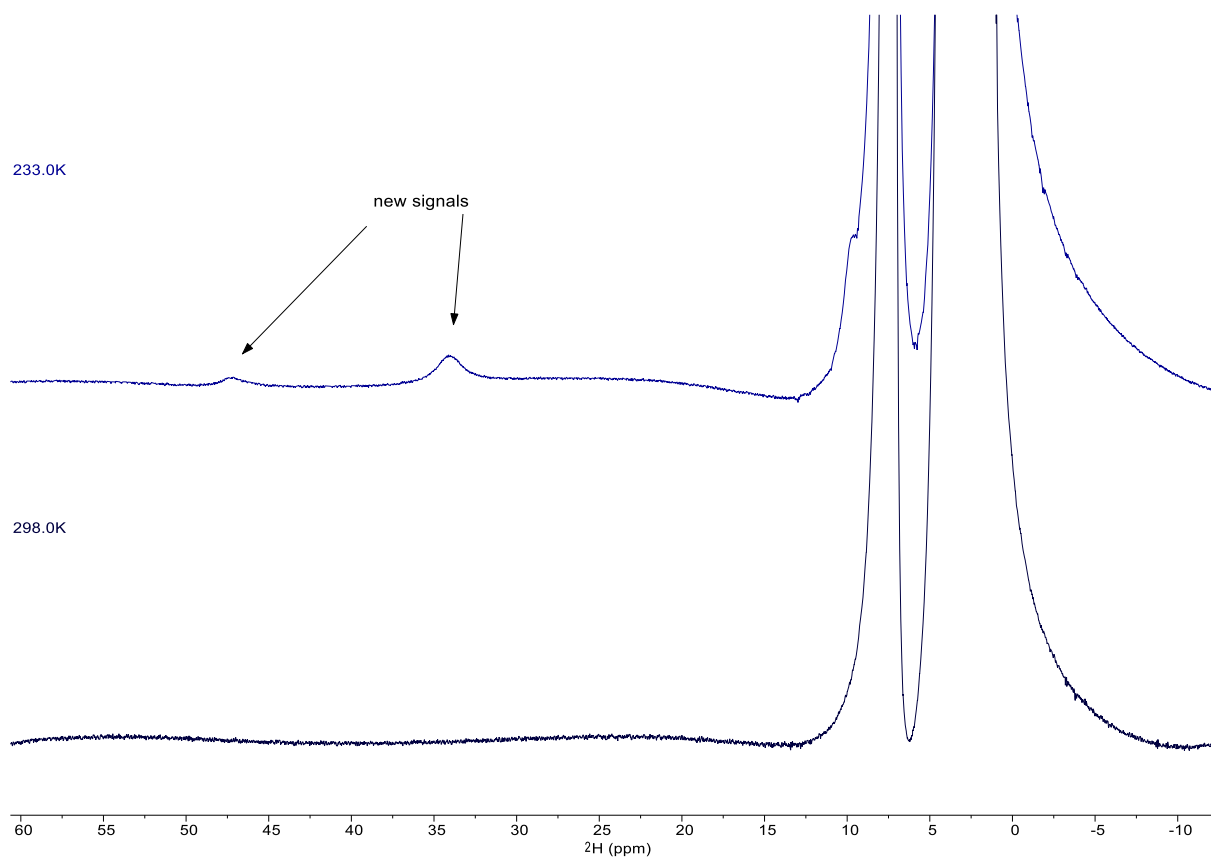
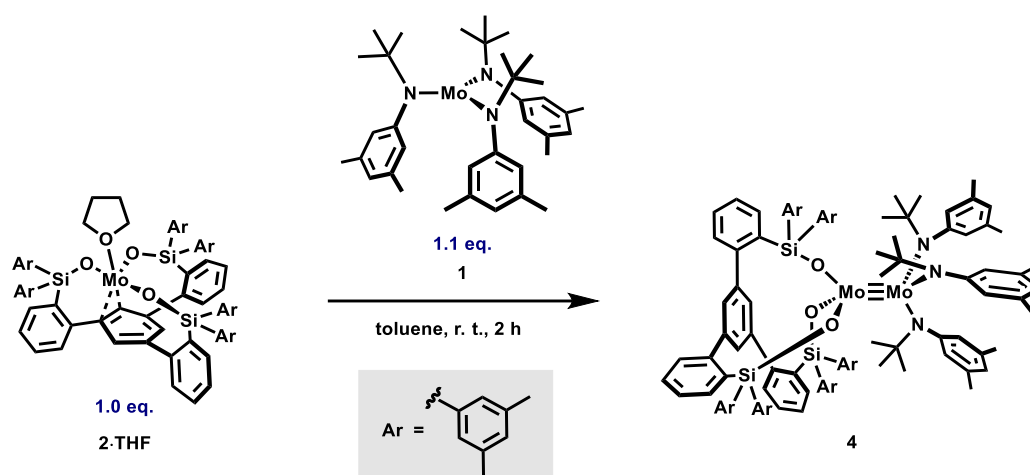


Figure 51. ^2H NMR spectra of the reaction between complex **2**·THF and $[\text{D}_8]$ -THF: $[\text{D}_8]$ -toluene, 233 K–298 K, 92 MHz.

Reaction of complex 2·THF with complex 1

A Mo^{III} heterodimer with a tripodal silanolate ligand



Toluene (1.2 mL) was added to a solid mixture of **2**·THF (19.5 mg, 0.0158 mmol) and the Cummins complex **1** (10.8 mg, 0.0173 mmol). The resulting dark brown mixture was stirred at room temperature for 1 h 45 min, before all volatile components were removed *in vacuo* (10^{-3} mbar). An NMR analysis of this crude product showed that the heterodimer **4** had been cleanly formed. In addition to **4**, excess of Cummins complex **1** and trace quantities of [HN(*t*Bu)Ar] (Ar = 3,5-dimethylphenyl) were detected (which was trace impurity in sample of **1** used to perform this experiment).

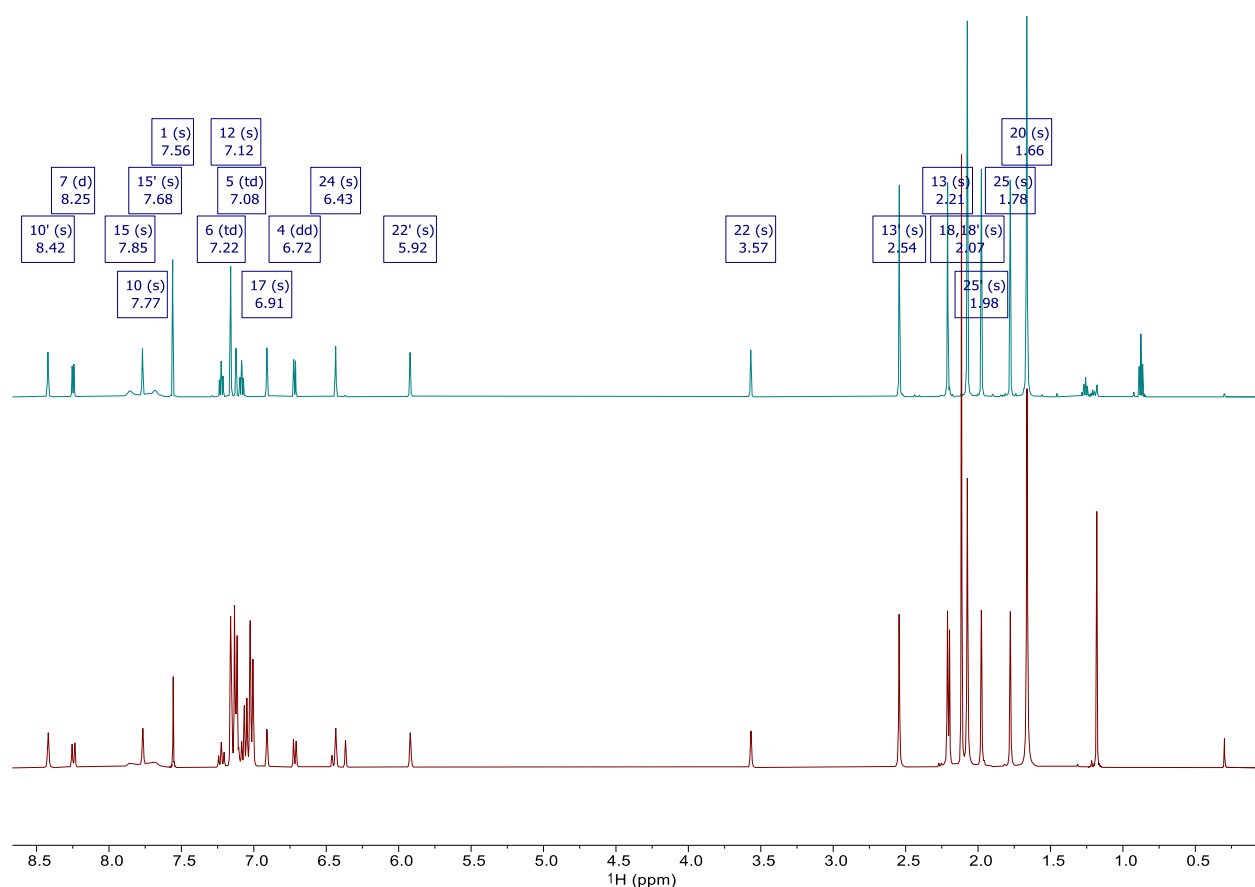
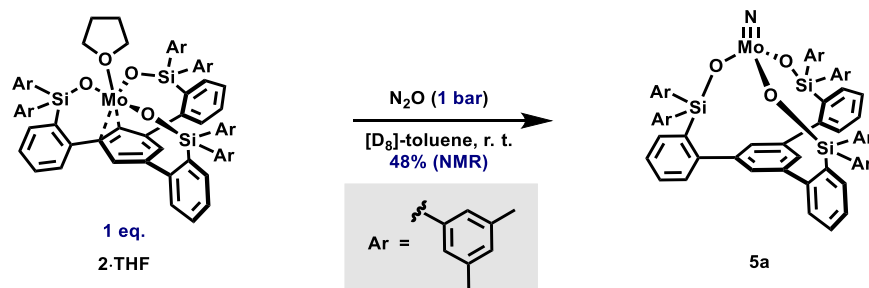


Figure 52. Top: ¹H NMR spectrum of complex **4**: [D₆]-benzene, 298 K, 600 MHz. Bottom: ¹H NMR spectrum of the reaction between complex **2**·THF and **1**: [D₆]-benzene, 298 K, 400 MHz.

Reaction of complex **2**·THF with N₂O

N₂O cleavage



Complex **2**·THF (37.3 mg, 0.0302 mmol) was weighed into a flame-dried 10-mL Schlenk flask under argon. The flask was capped with a rubber septum and the atmosphere was exchanged for N₂O (1 bar). A solution of 1,2,4,5-tetramethylbenzene in [D₈]-toluene (1 mL, 0.1431 M) was then added, causing the immediate formation of a golden solution. After 2 min the solution was transferred into a J-Young NMR tube and spectra of the mixture were recorded. It was determined *via* quantitative NMR studies that the nitrido complex **5a** had been formed in 38% yield (against 1,2,4,5-tetramethylbenzene as the internal standard). While no other species besides the nitrido complex **5a** were detected, the sample exhibited a broad background, suggesting possible oligomer formation. The nitrido complex **5a** was also the only species identified by mass spectrometry, which gave no evidence for any nitrosyl containing species.

	Integral	#H	yield
H7	1.11	3	37.0%
H10	4.71	12	39.3%
H1	1.09	3	36.3%
H12	2.46	6	41.0%
			<u>38.4% ±2.1%</u>

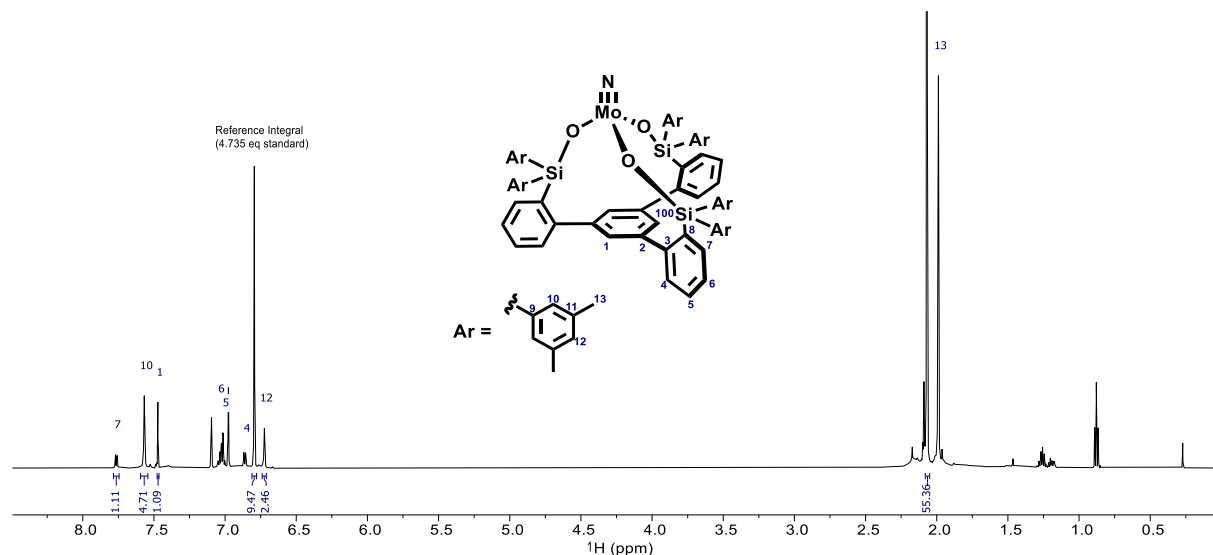
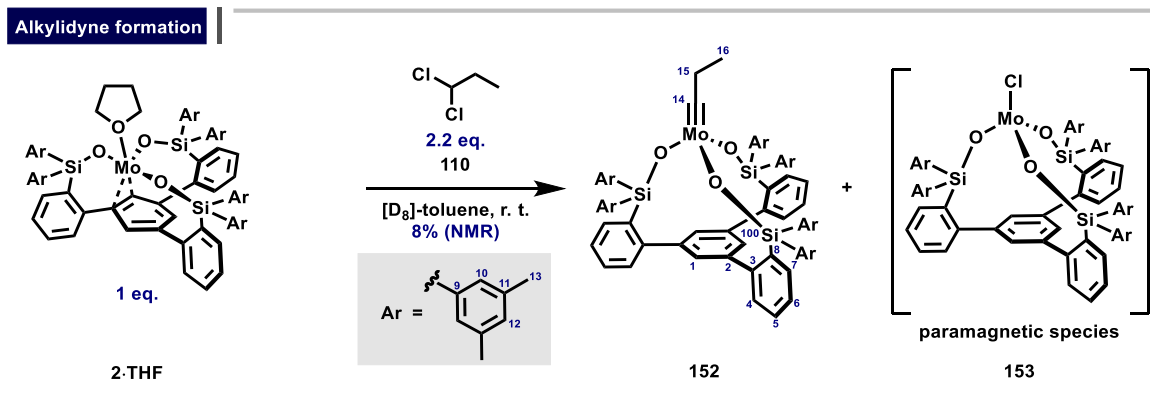


Figure 53. Quantitative ¹H NMR spectrum of the reaction between complex **2**·THF and N₂O: [D₈]-toluene, 298 K, 600 MHz.

Reaction of complex 2·THF with 1,1-dichloropropane



1,1-Dichloropropane (10 μ L, 0.10 mmol) was added to a stirred red solution of complex **2·THF** (55.3 mg, 0.0448 mmol) in $[D_8]$ -toluene (0.7 mL). The resulting dark brown solution was transferred into a J-Young NMR tube and spectra were recorded, which showed that the alkyidyne **152** had been formed. Additionally, the NMR spectra indicated the presence of a paramagnetic species, which might be the corresponding Mo^{IV} chloro complex **153**. When 1,2,4,5-tetramethylbenzene was used as an internal standard, it was possible to determine the yield of alkyidyne **152** to be in the range of 10%.

NMR data of the alkyidyne **152**:

1H NMR (600 MHz, $[D_8]$ -toluene, 298 K): δ = 7.83 (d, J = 7.1 Hz, 3H; H-7), 7.58 (s, 12H; H-10), 7.47 (s, 3H; H-1), 7.04 (t, J = 7.4 Hz, 3H; H-5), 6.87 (d, J = 7.4 Hz, 3H; H-4), 6.79 (s, 6H; H-12), 2.84 (q, J = 7.4 Hz, 2H; H-15), 2.04 (s, 36H; H-13), 0.66 ppm (t, J = 7.4 Hz, 3H; H-16). The signal of H-6 overlapped with one of the solvent signals at 7.09 ppm.

^{13}C NMR (151 MHz, $[D_8]$ -toluene, 298 K): δ = 322.8 (C-14), 149.4 (C-3), 143.8 (C-2), 138.6 (C-9), 137.2 (C-11), 136.3 (C-8), 132.7 (C-10), 131.6 (C-12), 130.1 (C-4), 129.7 (C-5), 129.5 (C-1), 126.1 (C-6), 44.5 (C-15), 21.4 (C-13), 13.7 ppm (C-16). The signal of C-7 overlapped with one of the solvent signals at 137.5 ppm.

^{29}Si NMR (119 MHz, $[D_8]$ -toluene, 298 K): δ = -10.5 ppm (Si-100),

MS analysis of the crude mixture revealed the presence of a cationic species possibly resulting from the loss of a chloride ligand from the chloro complex **153**: HRMS (ESI⁺): m/z calculated for $C_{72}H_{69}MoO_3Si_3$ $[M]^+$: 1163.36031, found: 1163.36019.

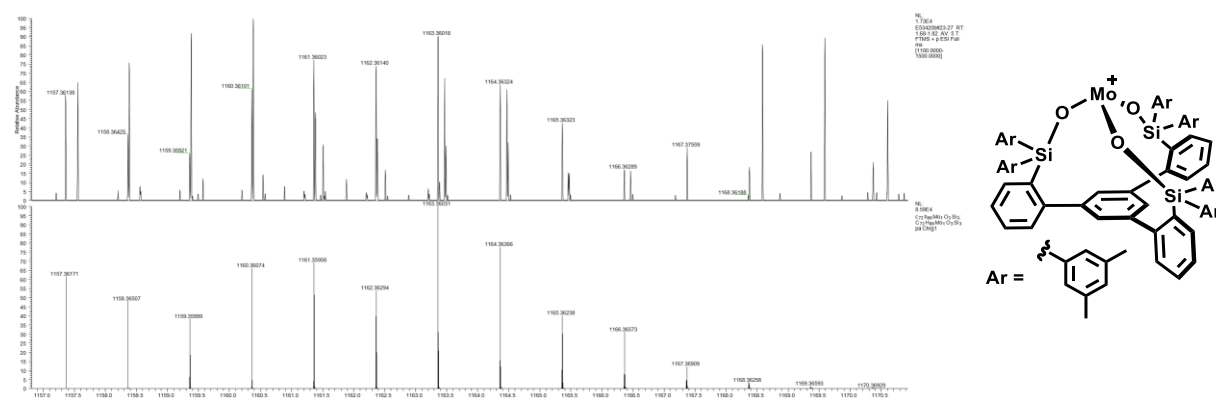
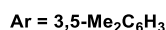
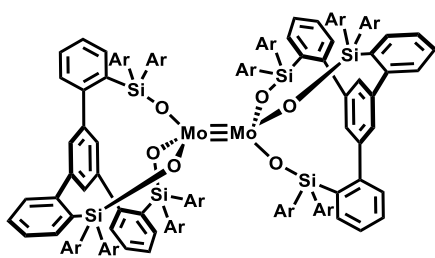


Figure 54. Recorded (top) and simulated (bottom) ESI⁺-MS spectrum of a cationic molybdenum-containing species corresponding to a molecular formula of $C_{72}H_{69}MoO_3Si_3$.

Complex 3



A dark red solution of complex **1** (190 mg, 0.304 mmol) in THF (18 mL) was added to a colorless solution of ligand **141a** (313 mg, 0.292 mmol) in THF (18 mL). The resulting dark red solution was concentrated to ca. 1/4 of its volume to give a dark red-brown suspension, which was filtered under Ar to give complex **2·3THF** as the pale orange filter cake. The pale orange filter cake was dissolved in *n*-pentane (8 mL) to form a deep red solution, which was vigorously stirred for a few minutes to cause precipitation of a large amount of a red microcrystalline solid. The supernatant solvent was filtered off and the resulting red filter cake was dried under high vacuum to give complex **2·THF** as a red microcrystalline solid.

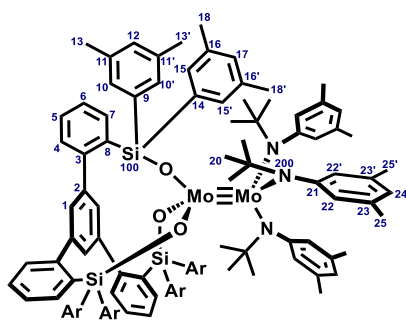
This product was dissolved in toluene (2 mL) and *n*-pentane (6 mL) was added while stirring, which led to the precipitation of a red crystalline material. All volatile components were removed *in vacuo* (10⁻³ mbar). The residual solid was again dissolved in toluene (15 mL) and then all volatile components were removed under high vacuum at RT to give a dark red oil. This dissolution/drying procedure was repeated two more times, before the residue was dissolved in toluene (2 mL) and the resulting red solution was filtered *via* cannula and left standing for 11 d, leading to the formation of orange single crystals. The supernatant solvent was filtered off *via* cannula and the large crystals were collected and used for crystal structure analysis. Drying of the crystals under high vacuum (10⁻³ mbar) afforded the title complex as a purple powder (13.1 mg, 4%).

The title compound is almost insoluble in toluene, THF or CD₂Cl₂; therefore, no NMR data could be recorded.

Elemental analysis (%) calculated for C₁₄₄H₁₃₈Mo₂O₆Si₆: C 74.39, H 5.98, Mo 8.25, Si 7.25; found: C 74.27 H 6.02, Mo 8.21, Si 7.29.

HRMS (ESI⁺): *m/z* calculated for C₁₄₈H₁₄₆Mo₂O₇Si₆ [M+THF]⁺: 2398.77868, found: 2398.78455.

Complex 4



A colorless solution of ligand **141a** (162 mg, 0.152 mmol) in Et₂O (15 mL) was added *via* cannula over a period of 2 min to a dark red solution of complex **1** (207 mg, 0.331 mmol) in Et₂O (15 mL) at -78 °C. Stirring was continued for 30 min at -78 °C before the red brown suspension was allowed to reach ambient temperature. After a total reaction time of 1 h and 10 min, all volatile components were removed *in vacuo* (10⁻³ mbar) to give a brown sticky solid. This residue was triturated with *n*-pentane (3 x 10 mL) and the filter cake was dried under high vacuum (10⁻³ mbar) to give

the title complex as a dark green-brown solid (143 mg, 53%). Orange single crystals suitable for X-ray diffraction were grown by slow evaporation of a solution of **4** in Et₂O.

¹H NMR (600 MHz, [D₆]-benzene, 298 K): δ = 8.42 (s, 3H; H-10'), 8.25 (d, *J* = 7.4 Hz, 3H; H-7), 7.85 (bs, 3H; H-15), 7.77 (s, 3H; H-10), 7.68 (bs, 3H; H-15'), 7.56 (s, 3H; H-1), 7.22 (td, *J* = 7.6, 1.0 Hz, 3H; H-6), 7.12 (s, 3H; H-12), 7.08 (td, *J* = 7.5, 1.1 Hz, 3H; H-5), 6.91 (s, 3H; H-17), 6.72 (dd, *J* = 7.6, 1.5 Hz, 3H; H-4), 6.43 (s, 3H; H-24), 5.92 (s, 3H; H-22'), 3.57 (s, 3H; H-22), 2.54 (s, 9H; H-13'), 2.21 (s, 9H; H-13), 2.07 (s, 18H; H-18 and H-18'), 1.98 (s, 9H; H-25'), 1.78 (s, 9H; H-25), 1.66 (s, 27H; H-20).

¹³C NMR (151 MHz, [D₆]-benzene, 298 K): δ = 151.9 (C-21), 150.2 (C-3), 143.9 (C-2), 140.0 (C-14), 139.5 (C-10'), 139.1 (C-10), 139.0 (C-7), 138.6 (C-9), 138.4 (C-8), 136.6 (bs, C-16'), 136.0 (bs, C-16), 135.5 (C-11), 135.2 (bs, C-15), 135.1 (C-23), 134.7 (C-23'), 134.6 (C-11'), 134.5 (bs, C-15'), 132.3 (C-22'), 131.8 (C-12), 130.9 (C-17), 130.4 (C-22), 130.0 (C-4), 129.6 (C-5), 127.0 (C-24), 126.1 (C-6), 63.7 (C-19), 36.2 (C-20), 21.68 (C-13), 21.66 (C-25 and C13'), 21.5 (bs, C-18 and C-18'), 20.6 (C-25') ppm.

²⁹Si NMR (119 MHz, [D₆]-benzene, 298 K): δ = -5.0 ppm.

¹⁵N NMR (61 MHz, [D₆]-benzene, 298 K): δ = -129 ppm.

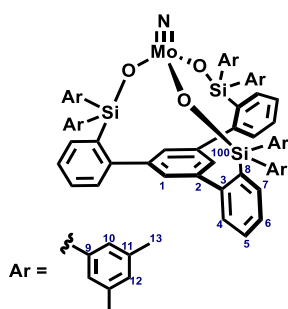
⁹⁵Mo NMR (26 MHz, [D₈]-toluene, 333 K): 3314.1 ppm

IR (ATR): $\tilde{\nu}$ = 2915, 1598, 1584, 1456, 1413, 1375, 1355, 1266, 1177, 1142, 1087, 1042, 960, 928, 866, 823, 765, 741, 723, 699, 685, 636, 624, 584, 551, 536 cm⁻¹.

HRMS (ESI⁺): *m/z* calculated for C₁₀₈H₁₂₃Mo₂N₃O₃Si₃ [M]⁺: 1789.69749, found: 1789.69813.

Elemental analysis (%) calculated for C₁₀₈H₁₂₃Mo₂N₃O₃Si₃: C 72.58, H 6.94, Mo 10.74, N 2.35, Si 4.71; found: C 72.15, H 6.89, Mo 10.61, N 2.33, Si 4.66.

Complex 5a



A solution of complex **94** (112 mg, 0.340 mmol) in toluene (6 mL) was added *via* cannula to a solution of ligand **141a** (361 mg, 0.338 mmol) in toluene (33 mL). The resulting colorless mixture was stirred for 2 h at ambient temperature before all volatile components were removed *in vacuo* (10^{-3} mbar) to give a white solid. The residue was extracted with toluene (2 x 2 mL) and insoluble material filtered off *via* cannula. The filtrate was evaporated *in vacuo* (10^{-3} mbar) at ambient temperature to give a white solid, which was suspended in *n*-pentane (5 mL). All volatile components were removed *in vacuo* (10^{-3} mbar) to give a white solid. This trituration with *n*-pentane was performed three times in total. The residue was dried in high vacuum (10^{-3} mbar) at 60 °C for 1 h to give the title complex as a white solid material (354 mg, 89%).

^1H NMR (600 MHz, $[\text{D}_6]$ -benzene, 298 K): δ = 7.86 (d, J = 7.2 Hz, 3H; H-7), 7.67 (s, 12H; H-10), 7.61 (s, 3H; H-1), 7.05 (td, J = 7.4, 1.5 Hz, 3H; H-6), 7.02 (td, J = 7.4, 1.7 Hz, 3H; H-5), 6.96 (d, J = 7.5 Hz, 3H; H-4), 6.75 (s, 6H; H-12), 1.98 ppm (s, 36H; H-13).

^{13}C NMR (151 MHz, $[\text{D}_6]$ -benzene, 298 K): δ = 149.2 (C-3), 144.2 (C-2), 137.73 (C-11), 137.70 (C-7), 137.5 (C-9), 135.2 (C-8), 132.6 (C-10), 132.1 (C-12), 130.1 (C-5), 129.9 (C-4), 129.6 (C-1), 126.3 (C-6), 21.4 ppm (C-13).

^{29}Si NMR (119 MHz, $[\text{D}_6]$ -benzene, 298 K): δ = -7.4 ppm.

^{95}Mo NMR (26 MHz, $[\text{D}_6]$ -benzene, 298 K): δ = 114 ppm.

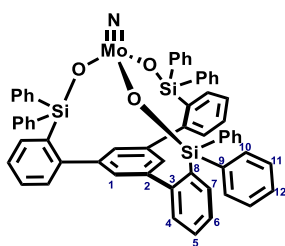
^{95}Mo NMR (26 MHz, $[\text{D}_8]$ -toluene, 298 K): δ = 116 ppm.

IR (ATR): $\tilde{\nu}$ = 3010, 2916, 2856, 1584, 1557, 1469, 1437, 1405, 1377, 1268, 1136, 1089, 1022, 995, 928, 862, 842, 764, 740, 717, 695, 665, 651, 638, 623, 578, 558, 549, 528, 520, 508, 475, 463, 443, 422, 408 cm^{-1} .

HRMS (ESI⁺): m/z calculated for $\text{C}_{72}\text{H}_{70}\text{MoNO}_3\text{Si}_3$ $[\text{M}+\text{H}]^+$: 1178.37121, found: 1178.37152.

Elemental analysis (%) calculated for $\text{C}_{72}\text{H}_{69}\text{MoNO}_3\text{Si}_3$: C 73.50, H 5.91, Mo 8.16, N 1.19, Si 7.16; found: C 72.44, H 5.87, Mo 8.07, N 1.17, Si 7.09.

Complex 5b



A solution of complex **9a** (75.0 mg, 0.228 mmol) in toluene (1 mL) was added *via* cannula to a solution of ligand **141b** (205 mg, 0.228 mmol) in toluene (20 mL). The resulting colorless solution was stirred for 4 h before all volatile components were removed *in vacuo* (10^{-3} mbar) at ambient temperature to give a light yellow sticky solid. The residue was washed with *n*-pentane (5 mL) and the filter cake dried *in vacuo* (10^{-3} mbar) to give the title complex as a white solid material (226 mg, 99%).

^1H NMR (600 MHz, $[\text{D}_6]$ -benzene, 333 K): δ = 7.79 (d, J = 6.7 Hz, 12H; H-10), 7.70 – 7.65 (m, 3H; H-7), 7.27 (s, 3H, 1), 7.11 – 7.02 (m, 24H; H-5, H-6, H-11 & H-12), 6.95 – 6.89 ppm (m, 3H; H-4).

^{13}C NMR (151 MHz, $[\text{D}_6]$ -benzene, 333 K): δ = 149.4 (C-3), 144.4 (bs, C-2), 137.5 (C-7), 137.5 (bs, C-9), 135.1 (C-10), 134.6 (bs, C-8), 130.4 (bs, C-4), 130.2 (C-5), 130.1 (C-12), 129.2 (bs, C-1), 126.4 ppm (C-6).

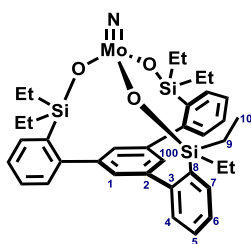
^{95}Mo NMR (26 MHz, $[\text{D}_6]$ -benzene, 298 K): δ = 117 ppm.

IR (ATR): $\tilde{\nu}$ = 3049, 1585, 1470, 1428, 1407, 1115, 1088, 1064, 1029, 1019, 997, 926, 916, 829, 765, 740, 711, 693, 637, 622, 563, 537, 510, 496, 451, 436, 408 cm^{-1} .

HRMS (EI⁺): m/z calculated for $\text{C}_{60}\text{H}_{45}\text{MoNO}_3\text{Si}_3$ $[\text{M}]^+$ 1009.17569, found: 1009.17660.

Elemental analysis (%) calculated for $\text{C}_{60}\text{H}_{45}\text{MoNO}_3\text{Si}_3$: C 71.48, H 4.50, Mo 9.52, N 1.39, Si 8.36; found: C 71.13, H 4.54, Mo 9.49, N 1.37, Si 8.31.

Complex 5c



A solution of complex **94** (250 mg, 0.758 mmol) in toluene (8 mL) was added *via* cannula to a solution of ligand **141c** (465 mg, 0.759 mmol) in toluene (78 mL). The resulting solution was stirred for 10 min before all volatile components were removed *in vacuo* (10^{-3} mbar) at ambient temperature over a period of 1 h to leave a light yellow foam. This residue was dissolved in toluene (2 mL) and *n*-pentane (40 mL), the resulting mixture was filtered *via* cannula and the filtrate stored at -78 °C overnight to form a white precipitate. The supernatant solution was syphoned off *via* cannula at -78 °C and the filter cake was dried under high vacuum (10^{-3} mbar) to give a first crop of the title complex as a white solid (325 mg, 60%). The filtrate was evaporated *in vacuo* (10^{-3} mbar) and the residue dissolved in toluene (0.4 mL) and *n*-pentane (8 mL). The resulting mixture was filtered *via* cannula and the filtrate stored at -78 °C overnight to yield a white precipitate. The supernatant solution was removed *via* cannula at -78 °C and the filter cake dried under high vacuum (10^{-3} mbar) to give a second crop of the complex as a white solid (127 mg, 23%). Overall yield: 452 mg, 83 %

^1H NMR (600 MHz, $[\text{D}_8]$ -toluene, 298 K): δ = 7.36 (bs, 3H; H-1), 7.34–7.33 (m, 3H; H-7), 7.21–7.20 (m, 3H; H-4), 7.17–7.12 (m, 6H; H-5 and H-6), 1.06 (t, J = 7.8 Hz, 18H; H-10), 0.98–0.84 ppm (m, 12H; H-9).

^{13}C NMR (151 MHz, $[\text{D}_8]$ -toluene, 298 K): δ = 149.3 (C-3), 144.6 (C-2), 135.9 (C-8), 134.6 (C-7), 130.7 (C-4), 129.3 (C-5), 128.2 (C-1), 126.8 (C-6), 9.4 (C-9), 7.2 ppm (C-10).

^{29}Si NMR (119 MHz, $[\text{D}_8]$ -toluene): δ = 13.7 ppm.

^{95}Mo NMR (26 MHz, $[\text{D}_8]$ -toluene, 298 K): δ = 120 ppm.

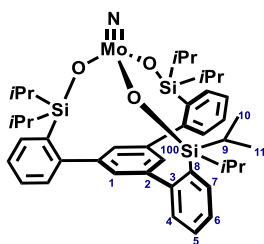
^{14}N NMR (29 MHz, $[\text{D}_8]$ -toluene, 333 K): δ = 468 ppm; $\Delta\nu_{1/2}$ = 1425 Hz.

IR (ATR): $\tilde{\nu}$ = 3051, 2954, 2910, 2874, 1583, 1557, 1460, 1409, 1378, 1260, 1233, 1124, 1098, 1061, 1043, 1004, 861, 759, 711, 624, 507, 462 cm^{-1} .

HRMS (ESI⁺): m/z calculated for $\text{C}_{36}\text{H}_{46}\text{MoNO}_3\text{Si}_3$ $[\text{M}+\text{H}]^+$: 722.18341, found: 722.18272.

Elemental analysis (%) calculated for $\text{C}_{36}\text{H}_{45}\text{MoNO}_3\text{Si}_3$: C 60.06, H 6.30, Mo 13.33, N 1.95, Si 11.70; found: C 59.88, H 6.22, Mo 13.09, N 1.92, Si 11.51.

Complex 5d



A solution of complex **94** (173 mg, 0.526 mmol) in toluene (8 mL) was added *via* cannula to a solution of ligand **141d** (367 mg, 0.527 mmol) in toluene (52 mL). The resulting colorless solution was stirred for 5 min before all volatile components were removed *in vacuo* (10^{-3} mbar) at ambient temperature over a period of 2 h to give a beige solid residue. *n*-pentane (40 mL) was added before all volatile components were removed *in vacuo* (10^{-3} mbar) to give the title complex as a white solid material (419 mg, 99%).

Colorless single crystals suitable for X-ray diffraction were grown by slow cooling of a saturated solution of the complex in Et₂O from 20 °C to 5 °C.

¹H NMR (600 MHz, [D₈]-toluene, 298 K): δ = 7.38 (s, 3H; H-1), 7.36–7.33(m, 3H; H-7), 7.21–7.20 (m, 3H; H-4), 7.15–7.12 (m, 6H; H-5 and H-6), 1.33–1.26 (m, 6H; H-9), 1.23 (d, J = 7.0 Hz, 18H; H-11), 1.08 ppm (d, J = 7.3 Hz, 18H; H-10).

¹³C NMR (151 MHz, [D₈]-toluene, 298 K): δ = 149.7 (C-3), 144.1 (C-2), 134.6 (C-8), 134.4 (C-7), 131.1 (C-4), 129.0 (C-5) [signal overlaps with a solvent peak (confirmed by DEPT-135)], 128.0 (C-1), 126.5 (C-6), 18.3 (C-10), 17.9 (C-11), 15.6 ppm (C-9).

²⁹Si NMR (119 MHz, [D₈]-toluene, 298 K): δ = 13.3 ppm.

⁹⁵Mo NMR (26 MHz, [D₈]-toluene, 298 K): δ = 121 ppm.

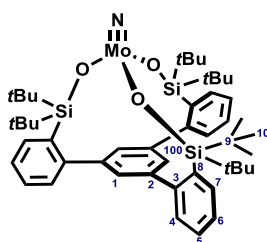
¹⁴N NMR (29 MHz, [D₈]-toluene, 333 K): δ = 472 ppm; $\Delta\nu_{1/2}$ = 1500 Hz.

IR (ATR): $\tilde{\nu}$ = 3052, 2956, 2939, 2889, 2861, 1585, 1461, 1433, 1411, 1382, 1242, 1126, 1093, 1065, 1015, 1004, 908, 876, 773, 760, 738, 724, 698, 667, 653, 628, 531, 471, 417 cm⁻¹.

HRMS (ESI⁺): m/z calculated for C₄₂H₅₈MoNO₃Si₃ [M+H]⁺: 806.27731, found: 806.27669.

Elemental analysis (%) calculated for C₄₂H₅₇MoNO₃Si₃: C 62.73, H 7.15, Mo 11.93, N 1.74, Si 10.48; found: C 62.42, H 7.11, Mo 11.80, N 1.73, Si 10.27.

Complex 5e



Ligand **141e** is extremely hygroscopic. Therefore, a mixture of ligand **141e** (117 mg, 0.150 mmol) and 4 Å MS in *o*-xylene (5 mL) was vigorously stirred for 7 h at ambient temperature before it was filtered *via* cannula into a suspension of complex **167** (36.7 mg, 0.150 mmol) in *o*-xylene (5 mL). The cannula was washed with *o*-xylene (4 mL). The resulting white suspension was stirred at 140 °C (bath temperature), leading to the formation of a colorless solution. After 14 h at 140 °C, the mixture was allowed to reach ambient temperature before it was filtered *via* cannula into a flame-dried 25-mL Schlenk flask. All volatile components were removed *in vacuo* (10⁻³ mbar) to give a colorless foam. Hexamethyldisiloxane (10 mL) was added which resulted in the formation of a white suspension. The suspension was vigorously stirred and then concentrated *in vacuo* (10⁻³ mbar) to ca. 1/4 of its original volume. The supernatant was filtered off *via* cannula. The residue was dissolved in *n*-pentane (2 mL) before all volatile components were removed *in vacuo* (10⁻³ mbar) to give the title complex as a white solid (99.2 mg, 75%). Yellow single crystals suitable for X-ray diffraction were grown by slow cooling of a saturated solution of the complex in Et₂O from 20 °C to -20 °C.

¹H NMR (600 MHz, [D₈]-toluene, 298 K): δ = 7.60–7.58 (m, 3H; H-7), 7.19 (s, 3H; H-1), 7.16–7.10 (m, 9H; H-4, H-5 and H-6), 1.24 ppm (s, 54H; H-10).

¹³C NMR (151 MHz, [D₈]-toluene, 298 K): δ = 149.8 (C-3), 144.7 (C-2), 134.6 (C-8), 134.1 (C-7), 131.8 (C-4), 128.6 (C-5), 126.9 (C-1), 125.9 (C-6), 29.5 (C-10), 22.4 ppm (C-9).

²⁹Si NMR (119 MHz, [D₈]-toluene, 298 K): δ = 10.2 ppm.

⁹⁵Mo NMR (26 MHz, [D₈]-toluene, 298 K): δ = 116 ppm.

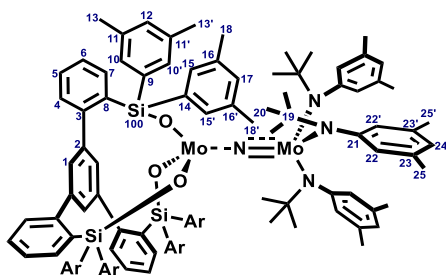
¹⁴N NMR (29 MHz, [D₈]-toluene, 333 K): δ = 476 ppm; Δ*v*_{1/2} = 1724 Hz.

IR (ATR): $\tilde{\nu}$ = 3045, 2966, 2947, 2856, 1582, 1558, 1473, 1428, 1408, 1395, 1364, 1256, 1121, 1087, 1064, 1045, 994, 891, 820, 759, 738, 725, 716, 635, 594, 525, 482, 420 cm⁻¹.

HRMS (ESI⁺): *m/z* calculated for C₄₈H₇₀MoNO₃Si₃ [M+H]⁺: 890.37121, found: 890.37107.

Elemental analysis (%) calculated for C₄₈H₆₉MoNO₃Si₃: C 64.90, H 7.83, Mo 10.80, N 1.58, Si 9.49; found: C 64.81, H 7.85, Mo 10.68, N 1.57, Si 9.51.

Complex 6a



A dark red solution of complex **1** (115 mg, 0.184 mmol) in toluene (1 mL) was added *via* cannula to a light yellow suspension of complex **5a** (206 mg, 0.175 mmol) in toluene (10 mL), causing an immediate color change to dark turquoise. After stirring for 5 min, all volatile components were removed *in vacuo* (10^{-3} mbar) to give a black solid. The residue was washed with *n*-pentane (3 x 3 mL) and the filter cake dried under high vacuum (10^{-3} mbar) at 60 °C to give the title

compound as a black solid material (270 mg, 86%). Green single crystals suitable for X-ray diffraction were grown by slow vapor diffusion of *n*-pentane into a solution of the complex in toluene.

Due to its high sensitivity, ^1H and ^{13}C NMR spectra contained small amounts of free aniline $\text{HN}(t\text{Bu})(\text{Ar})$ and the terminal nitrido complex $\text{N}\equiv\text{Mo}(\text{N}(t\text{Bu})(\text{Ar}))_3$ (**91**).

^1H NMR (600 MHz, $[\text{D}_6]$ -benzene, 283 K): δ = 11.42 (s, 3H; H-1), 8.96 (bs, 3H; H-22), 8.30 (d, J = 7.8 Hz, 3H; H-4), 7.86–7.81 (m, 6H; H-6 and H-24), 7.79 (d, J = 6.9 Hz, 3H; H-7), 7.44 (t, J = 7.3 Hz, 3H; H-5), 6.69 (bs; H-15), 6.59 (s, 3H; H-12), 6.02 (s, 3H; H-17), 5.87 (bs; H-15'), 5.70 (bs, 3H; H-22'), 4.83 (s, 27H; H-20), 3.47 (bs, 9H; H-25), 2.33 (bs, 9H; H-25'), 1.78 (s, 18H; H-13 and H-13'), 1.67 (bs; H-18'), 1.49 ppm (bs; H-18) (Note: the signals for H-10 and H-10' were not found at 283 K due to their broad linewidths at this temperature).

^{13}C NMR (151 MHz, $[\text{D}_6]$ -benzene, 283 K): δ = 520.3 (bs, C-19), 289.7, 270.9, 244.6 (C-8), 170.0, 164.3 (bs), 161.2 (bs), 156.5 (bs), 153.2 (C-2), 149.3 (C-7), 147.6 (C-3), 142.1 (bs, C-15), 139.2 (bs), 138.0, 137.9 (bs), 135.5, 134.9 (bs), 134.1 (bs), 133.2, 133.1, 132.2 (bs, C-10 and C10'), 131.8 (C-6), 131.0 (C-12), 130.2 (C-5), 127.2 (C-1), 81.5 (C-20), 26.6 (bs, C-25), 22.5 (C-18), 21.9 (C-13 and C-13'), 21.4, 20.2 ppm (Note: not all signals could assigned based on the 2D NMR data due line broadening at 283 K.).

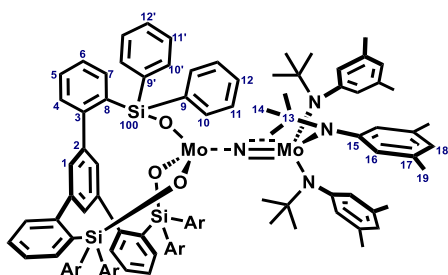
^{29}Si NMR (119 MHz, $[\text{D}_6]$ -benzene, 283 K): δ = -117.7 ppm.

IR (ATR): $\tilde{\nu}$ = 2967, 2918, 1585, 1555, 1411, 1385, 1357, 1286, 1266, 1178, 1138, 1087, 1045, 1000, 985, 941, 921, 902, 846, 763, 728, 717, 698, 689, 635, 623, 580, 558, 551, 535 cm^{-1} .

HRMS (ESI⁺): m/z calculated for $\text{C}_{108}\text{H}_{123}\text{Mo}_2\text{N}_4\text{O}_3\text{Si}_3$ $[\text{M}]^+$: 1803.70057, found: 1803.70276.

Elemental analysis (%) calculated for $\text{C}_{108}\text{H}_{123}\text{Mo}_2\text{N}_4\text{O}_3\text{Si}_3$: C 72.01, H 6.88, Mo 10.65, N 3.11, Si 4.68; found: C 71.90, H 6.84, Mo 10.59, N 3.07, Si 4.61.

Complex 6b



A dark red solution of complex **1** (132 mg, 0.211 mmol) in toluene (1.3 mL) was added *via* syringe to a light yellow suspension of complex **5b** (189 mg, 0.188 mmol) in toluene (19 mL), causing an immediate color change to dark purple. The syringe was washed with toluene (0.2 mL). After stirring for 5 min, all volatile components were removed *in vacuo* (10^{-3} mbar) to give a black solid. This residue was washed with *n*-pentane (3 x 3 mL) and the filter cake dried under high

vacuum (10^{-3} mbar) at 60 °C to give the title complex as a black solid material (242 mg, 79%). Orange single crystals suitable for X-ray diffraction were grown by slow vapor diffusion of *n*-pentane into a solution of the complex in [D₆]-benzene.

Due to the high sensitivity of the complex, ¹H and ¹³C NMR spectra showed small amounts of free aniline HN(*t*Bu)(Ar) (Ar = 3,5-dimethylphenyl) and the terminal nitrido complex N≡Mo(N(*t*Bu)(Ar))₃ (**91**).

¹H NMR (600 MHz, [D₆]-benzene, 298 K): δ = 10.02 (s, 3H; H-1), 7.94 (d, *J* = 7.7 Hz, 3H; H-4), 7.78 (t, *J* = 7.3 Hz, 3H; H-6), 7.70 (d, *J* = 6.8 Hz, 3H; H-7), 7.54 (s, 3H; H-18), 7.36 (t, *J* = 7.4 Hz, 3H; H-5), 7.21 (t, *J* = 7.3 Hz, 6H; H-11), 6.89 (d, *J* = 6.3 Hz, 6H; H-10), 6.86 (t, *J* = 7.4 Hz, 3H; H-12'), 6.77 (bs, 6H; H-11'), 6.56 (t, *J* = 7.5 Hz, 3H; H-12), 4.78 (s, 27H; H-14), 2.68 ppm (s, 18H; H-19) (Note: Signals for H-10' and H16 were not observed at 298 K due to the hindered rotation of the Ar groups. However, it was possible to assign them at 333 K and 343 K, see the VT NMR data).

¹³C NMR (151 MHz, [D₆]-benzene, 298 K): δ = 484.4 (bs, C-13), 269.0 (C-15), 257.3 (C-9), 240.8 (C-8), 178.4 (C-9'), 161.4 (C-16), 150.4 (C-2), 148.6 (C-7), 148.1 (C-3), 146.8 (bs; C-17), 145.0 (bs; C-17), 140.1 (C-10), 136.4 (bs; C-10'), 134.7 (C-1), 132.8 (C-4), 131.4 (C-12), 131.3 (C-6), 130.5 (C-5), 129.5 (C-12'), 129.2 (bs; C-11 and C11'), 127.4 (C-18), 95.7 (bs; C-14), 23.3 ppm (bs; C-19).

²⁹Si NMR (119 MHz, [D₆]-benzene, 298 K): δ = -93.2 ppm.

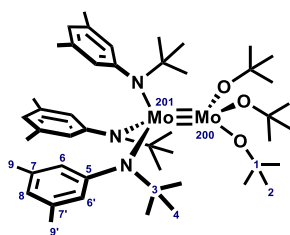
Magnetic Susceptibility (Evans method, 600 MHz, [D₆]-benzene, 298 K): $\mu_{\text{eff}} = 2.16(6) \mu_{\text{B}}$ (see below).

IR (ATR): $\tilde{\nu} = 2968, 1585, 1428, 1356, 1177, 1121, 1112, 1086, 1000, 984, 960, 940, 920, 898, 848, 771, 761, 730, 708, 699, 688, 548, 532 \text{ cm}^{-1}$.

HRMS (ESI⁺): *m/z* calculated for C₉₆H₉₉Mo₂N₄O₃Si₃ [M]⁺: 1635.51277, found: 1635.51489.

Elemental analysis (%) calculated for C₉₆H₉₉Mo₂N₄O₃Si₃: C 70.61, H 6.11, Mo 11.75, N 3.43, Si 5.16; found: C 69.89, H 6.05, Mo 11.63, N 3.39, Si 5.11.

Complex 147



A colorless solution of *t*BuOH in toluene (2.1 mL, 1.5 mmol) was added to a dark red solution of complex **1** (580 mg, 0.928 mmol) in toluene (14 mL). The resulting dark red/brown solution was stirred for 3 d at ambient temperature before all volatile components were removed *in vacuo* (10^{-3} mbar). The flask was equipped with a short distillation bridge without a cooling jacket. To remove most of the aniline [(*t*Bu)(Ar)NH] (Ar = 3,5-dimethylphenyl), the residue was heated to 80°C (oil bath) under high vacuum (10^{-3} mbar) for 20 min (the distillation was assisted by occasional heating of the glassware with a heat gun). After cooling to room temperature, the dark red brown residue was extracted with hexamethyldisiloxane (HMDSO, 2 x 20 mL, 1 x 10 mL; *Note*: The amount of HMDSO can vary depending on how effectively the aniline had been removed by distillation) and filtered *via* cannula. The resulting dark red solution was cooled from 20°C to -35°C over the course of 4 h and kept overnight at -35°C, but no crystals were formed at this point. Therefore, the dark red solution was allowed to warm to room temperature; gentle agitation led to the formation of a small amount of a dark red crystalline solid. The resulting dark red mixture was again cooled from 20°C to -35°C over the course of 4 h and then kept at -35°C for 3 d until a large amount of dark red crystals had precipitated. The supernatant solution was filtered off at -35°C and the residue was dissolved in *n*-pentane (5 mL). All volatile components were removed *in vacuo* (10^{-3} mbar) from the dark red solution to give the title complex as a dark red solid (188 mg, 43%). Orange single crystals suitable for X-ray diffraction were grown by slow cooling of a saturated solution of **147** in HMDSO from 20°C to -35°C.

^1H NMR (600 MHz, [D_8]-toluene, 233 K): δ = 7.28 (s, 3H; H-6'), 6.60 (s, 3H; H-8), 4.12 (s, 3H; H-6), 2.28 (s, 9H; H-9'), 2.00 (s, 9H; H-9), 1.84 (s, 27H; H-4), 1.50 ppm (s, 27H; H-2).

^{13}C NMR (151 MHz, [D_8]-toluene, 233 K): δ = 151.2 (C-5), 135.5 (C-7), 134.7 (C-7'), 133.3 (C-6'), 132.4 (C-6), 126.8 (C-8), 79.5 (C-1), 62.3 (C-3), 33.7 (C-2), 33.3 (C-4), 21.9 (C-9), 21.5 ppm (C-9').

^{15}N NMR (61 MHz, [D_8]-toluene, 233 K): δ = -147 ppm.

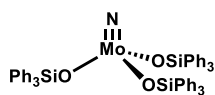
^{95}Mo NMR (26 MHz, [D_8]-toluene, 333 K): δ = 3260 (Mo-200), 3126 ppm (Mo-201).

IR (ATR): $\tilde{\nu}$ = 2969, 2924, 2863, 1597, 1583, 1458, 1379, 1357, 1283, 1225, 1170, 1143, 1040, 1019, 957, 937, 923, 899, 883, 847, 776, 717, 682, 580, 567, 551, 501, 469, 438, 420 cm^{-1} .

HRMS (ESI⁺): m/z calculated for $\text{C}_{48}\text{H}_{81}\text{Mo}_2\text{N}_3\text{O}_3$ [M]⁺: 943.43806, found: 943.43914.

Elemental analysis (%) calculated for $\text{C}_{48}\text{H}_{81}\text{Mo}_2\text{N}_3\text{O}_3$: C 61.33, H 8.69, Mo 20.41, N 4.47; found: C 60.57, H 8.66, Mo 19.99, N 4.38.

Complex 163

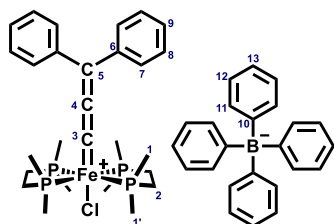


A solution of complex **94** (116 mg, 0.351 mmol) in toluene (5 mL) was added *via* cannula to a solution of Ph_3SiOH (290 mg, 1.05 mmol) in toluene (35 mL). The resulting colorless mixture was stirred for 10 min before all volatile components were removed *in vacuo* (10^{-3} mbar) at ambient temperature over a period of 1 h to give a white solid material (*note*: the slow evaporation was necessary to ensure full conversion in this case). The crude product was dissolved in toluene (10 mL) which was then evaporated (10^{-3} mbar) at ambient temperature to give the title complex as a white solid (322 mg, 98%). The analytical and spectroscopic data is in agreement with the literature.^[137]

Light yellow single crystals suitable for X-ray diffraction were grown by slow vapor diffusion of *n*-pentane into a solution of the complex in benzene.

3.3 Synthetic Strategies for Diamagnetic Iron Carbenes

Complex 9



MeOH (40 mL) was added to solid mixture of $\text{dppe}_2\text{FeCl}_2$ (**7**) (1.17 g, 2.75 mmol) and 1,1-diphenyl-2-propyne-1-ol (**8**) (1.20 g, 5.77 mmol). The resulting deep blue solution was heated to 40°C for 2 h, after which it was allowed to cool to room temperature. NaBPh_4 (1.05 g, 3.07 mmol) was added as a solid. All volatile components were removed *in vacuo* and the resulting dark blue solid was extracted with CH_2Cl_2 (3 x 5 mL). All volatile components were removed *in vacuo* to give an oily residue, which was washed with Et_2O (5 x 20 mL) and dried under high vacuum (10^{-3} mbar) to give complex **9** as a blue solid (2.50 g, quant.).

^1H NMR (600 MHz, CD_2Cl_2 , 298 K): δ = 7.69 (t, J = 7.5 Hz, 2H; H-9), 7.62 (d, J = 7.3 Hz 4H; H-7), 7.41–7.37 (m, 4H; H-8), 7.34–7.29 (m, 8H; H-11), 7.02 (app. t, J = 7.3 Hz, 8H; H-12), 6.87 (t, J = 7.0 Hz, 4H; H-13), 2.08–1.96 (m, 4H; H-2''), 1.88–1.78 (m, 4H; H-2'), 1.44–1.41 (m, 12H; H-1'), 1.22–1.19 ppm (m, 12H; H-1).

^{13}C NMR (151 MHz, CD_2Cl_2 , 298 K): δ = 307.3 (p, J_{PC} = 35.8 Hz; C-3), 239.5 (p, J_{PC} = 4.5 Hz; C-4), 164.4 (q, J_{BC} = 49.3 Hz; C-10), 151.9 (p, J_{PC} = 6.5 Hz; C-5), 145.7 (p, J_{PC} = 3.5 Hz; C-6), 136.3 (q, J_{BC} = 1.4 Hz; C-11), 131.1 (s; C-9), 129.7 (s; C-8), 128.8 (p, J_{PC} = 1.3 Hz; C-7), 126.0 (q, J_{BC} = 2.8 Hz; C-12), 122.1 (s; C-13), 29.1 (p, J_{PC} = 11.9 Hz; C-2), 16.4–16.1 (m; C-1), 13.0–12.6 ppm (m; C-1').

$^{31}\text{P}\{^1\text{H}\}$ NMR (243 MHz, CD_2Cl_2 , 298 K): δ = 51.1 ppm (s).

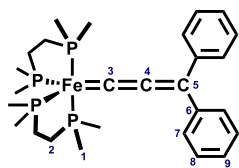
$^{11}\text{B}\{^1\text{H}\}$ NMR (193 MHz, CD_2Cl_2 , 298 K): δ = 6.6 ppm (s).

IR (ATR): $\tilde{\nu}$ = 3052, 3029, 2982, 2906, 1885, 1579, 1478, 1450, 1414, 1301, 1284, 1237, 1177, 1124, 1073, 1031, 998, 928, 888, 840, 796, 774, 732, 702, 691, 651, 622, 602, 468, 454 cm^{-1} .

HRMS (ESI⁺): m/z calculated for $\text{C}_{27}\text{H}_{42}\text{ClFeP}_4[\text{M}]^+$: 581.12694, found: 581.12736.

Elemental analysis (%) calculated for $\text{C}_{51}\text{H}_{62}\text{BClFeP}_4$: C 67.98, H 6.94, B 1.20, Cl 3.93, Fe 6.20, P 13.75; found: C 67.56, H 6.97, B 1.19, Cl 3.96, Fe 6.16, P 13.71.

Complex 10



A solution of complex **9** (740 mg, 0.822 mmol) in THF (25 mL) was added *via* cannula to a suspension of K/KI (5w%, 1.30 g, 1.66 mmol) in THF (25 mL). The cannula was washed with THF (5 mL). After 3.5 h, all volatile components were removed under high vacuum (10^{-3} mbar). The residue was extracted with toluene (4 x 2 mL) and the resulting purple filtrate solution was evaporated under high vacuum (10^{-3} mbar) to give a purple oil. *n*-Pentane (5 mL) was added to this oil to give a red purple suspension. This suspension was cooled to -78°C and filtered *via* cannula. The resulting red purple solid was extracted with a toluene/*n*-pentane mixture (1/5, 2 x 6 mL) and the filtrate was stored at -20°C overnight for crystallization. The supernatant solution was filtered off and the crystalline solid was dried under high vacuum (10^{-3} mbar) to give complex **10** as dark purple solid (144 mg, 32%).

^1H NMR (600 MHz, $[\text{D}_8]$ -toluene, 323 K): δ = 7.86–7.83 (m, 4H; H-7), 7.20–7.16 (m, 2H; H-9), 7.16–7.11 (m, 4H; H-8), 1.52–1.42 (m, 8H; H-2), 1.20 ppm (bs, 24H; H-1).

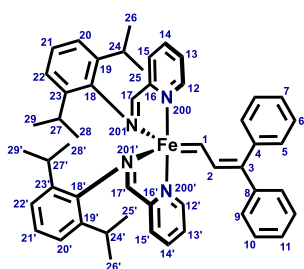
^{13}C NMR (151 MHz, $[\text{D}_8]$ -toluene, 323 K): δ = 225.1 (p, J = 5.7 Hz; C-4), 207.0 (p, J = 18.7 Hz; C-3), 148.3 (p, J = 3.0 Hz; C-6), 128.6 (s; C-8), 127.4 (s; C-7), 123.7 (s; C-9), 110.1 (p, J = 3.7 Hz; C-5), 33.3 (m; C-2), 23.5 ppm (bs; C-1).

$^3\text{P}\{^1\text{H}\}$ NMR (243 MHz, $[\text{D}_8]$ -toluene, 323 K): δ = 60.9 ppm (s).

HRMS (ESI $^+$): m/z calculated for $\text{C}_{27}\text{H}_{43}\text{FeP}_4$ $[\text{M}+\text{H}]^+$: 547.16591, found: 547.16538.

Elemental analysis (%) calculated for $\text{C}_{27}\text{H}_{42}\text{FeP}_4$: C 59.35, H 7.75, Fe 10.22, P 22.68; found: C 58.79, H 7.97, Fe 10.14, P 22.73.

Complex 13



Note: The reproducibility of the synthesis of **13** was found to be highly dependent on the selected conditions. We therefore strongly recommend to follow these conditions closely.

A 25-mL Schlenk flask equipped with a magnetic stir bar was flame dried under vacuum and subsequently filled with argon. The flask was charged with a dark brown mixture of IP_2Fe (**11**) (878 mg, 1.49 mmol) in toluene (10 mL), capped with a rubber septum, and placed in a pre-heated oil bath at 80°C, stirring at 500 rpm. A solution of cyclopropene **12** (310 mg, 1.62 mmol) in toluene (5 mL) was added dropwise over 2 h *via* syringe pump. Upon completion of the addition, heating was stopped immediately. All volatile components were removed *in vacuo* to give a black residue. The black residue was washed with toluene (3 x 1 mL), and the resulting black filter cake was dried under high vacuum (10⁻³ mbar) at 60°C for 30 min to give complex **13** as a black solid (501 mg, 43%).

¹H NMR (600 MHz, [D₈]-toluene, 233 K): δ = 14.41 (d, *J* = 14.1 Hz, 1H; H-1), 8.07 (s, 1H; H-17), 8.04 (s, 1H; H-17'), 7.70 (d, *J* = 7.8 Hz, 2H; H-5), 7.64 (d, *J* = 7.4 Hz, 2H; H-9), 7.22 (t, *J* = 7.4 Hz, 1H; H-7), 7.13–7.09 (m, 2H; H-15' and H-21), 7.05–7.02 (m, 2H; H-11 and H-21'), 6.99–6.95 (m, 2H; H-15 and H-20), 6.92 (d, *J* = 7.8 Hz, 1H; H-20'), 6.86–6.82 (m, 3H; H-6 and H-22), 6.74–6.69 (m, 2H; H-2 and H-22'), 6.66–6.62 (m, 1H; H-14'), 6.58 (d, *J* = 6.3 Hz, 1H; H-12'), 6.51–6.46 (m, 1H; H-14), 6.36 (d, *J* = 6.2 Hz, 1H; H-12), 5.93–5.88 (m, 1H; H-13'), 5.82–5.78 (m, 1H; H-13), 2.62–2.54 (m, 1H; H-27), 2.32–2.23 (m, 2H; H-24' and H-27'), 1.19–1.13 (m, 12H; H-25, H-25', H-26', H-28), 1.08 (d, *J* = 6.8 Hz, 3H; H-28'), 1.04 (d, *J* = 6.9 Hz, 3H; H-26), 0.70 (d, *J* = 6.8 Hz, 3H; H-29), 0.66 (d, *J* = 6.8 Hz, 3H; H-29'). The signals of H-10 (7.00 ppm) and H-24 (2.08 ppm) overlapped with the solvent signal.

¹³C NMR (151 MHz, [D₈]-toluene, 233 K): δ = 230.9 (C-1), 156.8 (C-16), 156.6 (C-16'), 153.2 (C-12'), 152.2 (C-12), 151.1 (C-17), 150.9 (C-18), 150.7 (C-18'), 150.4 (C-17'), 149.5 (C-2), 149.4 (C-4), 146.1 (C-8), 141.8 (C-19 and C19'), 141.74 (C-23), 141.67 (C-23'), 129.7 (C-6), 129.5 (C-3), 128.5 (C-9), 128.4 (C-10), 126.4 (C-11), 126.1 (C-21), 125.9 (C-21'), 125.6 (C-7), 125.36 (C-15'), 125.27 (C-15), 125.0 (C-5), 124.4 (C-14'), 124.2 (C-14), 122.8 (C-20), 122.7 (C-20'), 122.1 (C-22), 121.9 (C-22'), 114.8 (C-13), 114.2 (C-13'), 27.9 (C-27), 27.7 (C-27'), 26.72 (C-24'), 26.71 (C-26'), 26.65 (C-24), 26.3 (C-26), 25.9 (C-28), 25.6 (C-28'), 23.6 (C-25'), 23.4 (C-25), 21.4 (C-29), 21.3 ppm (C-29'). The signals of C-5, C-15, and C-15' overlapped with the solvent signal.

¹⁵N NMR (61 MHz, [D₈]-toluene, 233 K): δ = -119.4 (N-200'), -122.0 ppm (N-200).

⁵⁷Fe NMR (16 MHz, [D₈]-toluene, 298 K): δ = 8873.0 ppm.

IR (ATR): $\tilde{\nu}$ = 3052, 2955, 2921, 2884, 2862, 1587, 1438, 1398, 1380, 1359, 1324, 1298, 1256, 1225, 1202, 1179, 1143, 1114, 1073, 1059, 1039, 1027, 1004, 932, 910, 794, 761, 738, 728, 693, 653, 632, 601, 579, 546, 529, 485, 457, 409 cm⁻¹.

HRMS (ESI⁺): *m/z* calculated for C₅₁H₅₆FeN₄ [M]⁺: 780.38489, found: 780.38502.

Elemental analysis (%) calculated for C₅₁H₅₆FeN₄: C 78.44, H 7.23, N 7.17, Fe 7.15; found: C 77.25, H 7.16, N 7.15, Fe 6.97. Note: The sample always contains trace amounts of free iminopyridine ligand.

Mößbauer spectroscopy (1.8 K, 0.0 T): δ = 0.08 mm s⁻¹ and |ΔE_Q| = 1.02 mm s⁻¹

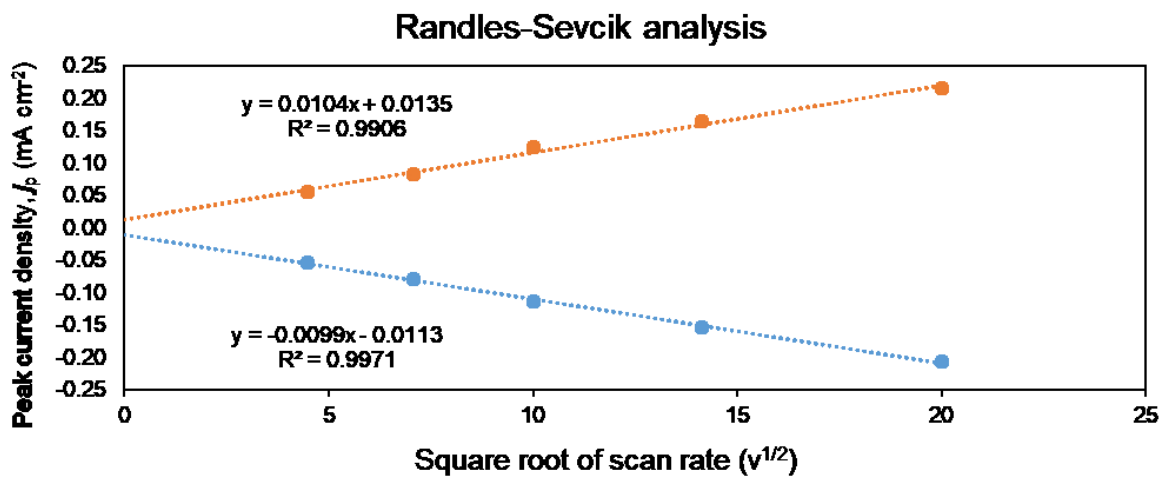


Figure 55. Randles-Sevcik analysis of the $[IP_2Fe=CH-CH=CPh_2]^{+/0}$ redox couple. In collaboration with Dr. Alexios Stamoulis.

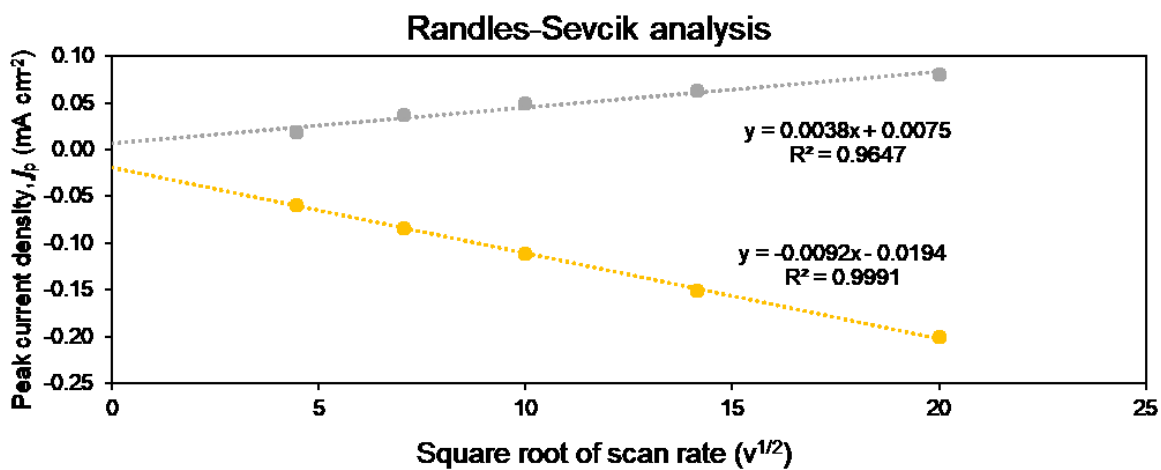
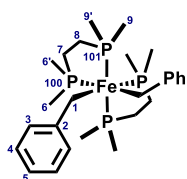


Figure 56. Randles-Sevcik analysis of the $[IP_2Fe=CH-CH=CPh_2]^{0/-}$ redox couple. In collaboration with Dr. Alexios Stamoulis.

Complex 265



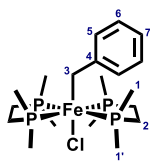
An orange suspension of BnK (273 mg, 2.09 mmol) in toluene (20 mL) was added *via* cannula to a green solution of $\text{dmpe}_2\text{FeCl}_2$ (**7**) (413 mg, 0.966 mmol) in toluene (20 mL). The reaction mixture immediately changed from a green solution to red brown suspension. After 24 h, *n*-pentane (10 mL) was added and the mixture was filtered. The solvent of the resulting dark red-brown filtrate solution was evaporated under high vacuum (10^{-3} mbar) to give a dark red brown oil. The residue was extracted with toluene (3 x 3 mL) and filtered *via* cannula. All volatile components were removed from the filtrate *in vacuo* to give a dark red brown oil. This residue was washed with *n*-pentane (2 x 5 mL), the filtrate was filtered off *via* cannula and discarded. The red filter cake was dried under high vacuum (10^{-3} mbar) to give complex **265** as a red solid (268 mg, 52%).

$^1\text{H}\{^{31}\text{P}\}$ NMR (600 MHz, $[\text{D}_8]$ -toluene, 298 K): δ = 7.60–7.55 (m, 4H; H-3), 7.13–7.08 (m, 4H; H-4), 6.99–6.93 (m, 2H; H-5), 2.21 (d, J = 8.2 Hz, 2H; H-1''), 1.67 (d, J = 8.2 Hz, 2H; H-1'), 1.24 (s, 6H; H-6), 1.15–0.89 (m, 8H; H-7 and H-8), 0.76 (s, 6H; H-6'), 0.74 (s, 6H; H-9'), 0.56 ppm (s, 6H; H-9).

^{13}C NMR (151 MHz, $[\text{D}_8]$ -toluene, 298 K): δ = 162.0 (C-2), 127.94 (C-3), 127.88 (C-4), 120.2 (C-5), 32.9 (C-7), 32.4 (C-8), 22.3 (C-6'), 20.3 (C-6), 18.4 (C-9'), 12.5 (C-1), 9.4 ppm (C-9).

^{31}P NMR (243 MHz, $[\text{D}_8]$ -toluene, 298 K): δ = 60.1 (t, J = 26.2 Hz, P-101), 55.0 ppm (t, J = 26.2 Hz, P-100).

Complex 267



A green solution of $\text{dmpe}_2\text{FeCl}_2$ (**7**) (536 mg, 1.26 mmol) in toluene (20 mL) was added *via* cannula to an orange suspension of BnK (194 mg, 1.49 mmol) in toluene (20 mL). The cannula was washed with toluene (20 mL). The resulting dark red-brown mixture was stirred for 48 h at room temperature and then all volatile components were removed *in vacuo*. The residue was washed with *n*-pentane (4 x 5 mL) during which the residue turned from dark red to dark purple. The residue was then extracted with toluene (2 x 5 mL) and filtered *via* cannula. All volatile components were removed from the filtrate solution to give a purple red solid, which was dissolved in toluene (10 mL) and *n*-pentane (10 mL). The resulting solution was rapidly cooled to -78°C , which resulted in the precipitation of a purple solid. After stirring for 40 min at this temperature, the supernatant solution was filtered off *via* cannula and the filter cake was dried under high vacuum (10^{-3} mbar) to give complex **267** as a purple solid (345.6 mg, 57%).

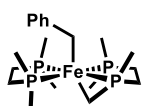
^1H NMR (600 MHz, $[\text{D}_6]$ -benzene, 298 K): δ = 6.96–6.88 (m, 3H; H-6 and H-7), 6.85–6.81 (m, 2H; H-5), 1.82–1.63 (m, 8H; H-2), 1.40–1.38 (m, 12H; H-1'), 1.12–1.09 (m, 12H; H-1), -0.25 ppm (p, $J_{\text{PH}} = 6.6$ Hz, 2H; H-3).

^{13}C NMR (151 MHz, $[\text{D}_6]$ -benzene, 298 K): δ = 161.9 (p, $J_{\text{PC}} = 3.1$ Hz; C-4), 128.0 (s; C-5), 120.7 (s; C-7), 30.5 (m; C-2), 16.1 (m; C-1'), 15.1 (m; C-1), -10.0 ppm (p, $J_{\text{PC}} = 12.7$ Hz; C-3).

$^{31}\text{P}\{^1\text{H}\}$ NMR (243 MHz, $[\text{D}_6]$ -benzene, 298 K): δ = 63.9 ppm (s).

Elemental analysis (%) calculated for $\text{C}_{19}\text{H}_{39}\text{ClFeP}_4$: C 47.28, H 8.14, Cl 7.34, Fe 11.57, P 25.67; found: C 46.84, H 8.09, Cl 7.27, Fe 11.51, P 25.54.

Complex 268



A light yellow solution of LiTMP (8.2 mg, 0.056 mmol) in THF (5 mL) was added *via* syringe to a purple solution of $\text{dmpe}_2\text{FeBnCl}$ (**267**) (25 mg, 0.052 mmol) in THF (5 mL). The red solution was stirred for 1 h at room temperature, before all volatile components were removed *in vacuo* (10^{-3} mbar). The resulting residue was dissolved in $[\text{D}_6]$ -benzene and filtered *via* cannula into a J-Young NMR tube.

It was not possible to isolate the compound or characterize it using tools other than NMR spectroscopy. However, the structure is tentatively proposed based on literature evidence.^[281]

Selected data:

$^3\text{P}\{^1\text{H}\}$ NMR (162 MHz, $[\text{D}_6]$ -benzene, 298 K): $\delta = 76.61$ (ddd, $J = 108.5, 57.7, 39.1$ Hz), 74.00 (ddd, $J = 70.3, 50.9, 39.4$ Hz), 72.41 (ddd, $J = 108.5, 51.0, 29.0$ Hz), 21.85 ppm (ddd, $J = 70.1, 57.5, 28.9$ Hz).

4 Bibliography

- [1] F. A. Cotton, C. A. Murillo, R. A. Walton, *Multiple Bonds Between Metal Atoms.*, 3rd ed., Springer: New York, **2005**.
- [2] M. H. Chisholm, *Acc. Chem. Res.* **1990**, *23*, 419-425.
- [3] C. E. Laplaza, A. L. Odom, W. M. Davis, C. C. Cummins, J. D. Protasiewicz, *J. Am. Chem. Soc.* **1995**, *117*, 4999-5000.
- [4] P. Binger, P. Müller, R. Benn, R. Mynott, *Angew. Chem. Int. Ed. Engl.* **1989**, *28*, 610-611.
- [5] A. Werner, *Z. Anorg. Chem.* **1893**, *3*, 267-330.
- [6] L. H. Gade, *Chem. Unserer Zeit* **2002**, *36*, 168-175.
- [7] E. C. Constable, C. E. Housecroft, *Chem. Soc. Rev.* **2013**, *42*, 1429-1439.
- [8] C. W. Blomstrand, *Chemie der Jetztzeit*, **1869**.
- [9] R. H. Crabtree, *The Organometallic Chemistry of the Transition Metals*, 6th ed., John Wiley & Sons: Hoboken, NJ, **2014**.
- [10] W. R. King, Jr., C. S. Garner, *J. Chem. Phys.* **1950**, *18*, 689-691.
- [11] F. A. Cotton, B. G. DeBoer, M. D. Laprade, J. R. Pipal, D. A. Ucko, *J. Am. Chem. Soc.* **1970**, *92*, 2926-2927.
- [12] J. C. Sheldon, *Nature* **1959**, *184*, 1210-1213.
- [13] J. A. Bertrand, F. A. Cotton, W. A. Dollase, *J. Am. Chem. Soc.* **1963**, *85*, 1349-1350.
- [14] J. A. Bertrand, F. A. Cotton, W. A. Dollase, *Inorg. Chem.* **1963**, *2*, 1166-1171.
- [15] F. A. Cotton, C. B. Harris, *Inorg. Chem.* **1965**, *4*, 330-333.
- [16] V. G. Kuznetsov, P. A. Koz'min, *J. Struct. Chem.* **1963**, *4*, 49-55.
- [17] F. Huq, W. Mowat, A. Shortland, A. C. Skapski, G. Wilkinson, *J. Chem. Soc. D* **1971**, 1079-1080.
- [18] G. Yagupsky, W. Mowat, A. Shortland, G. Wilkinson, *J. Chem. Soc. D* **1970**, 1369-1370.
- [19] R. A. Andersen, M. H. Chisholm, J. F. Gibson, W. W. Reichert, I. P. Rothwell, G. Wilkinson, *Inorg. Chem.* **1981**, *20*, 3934-3936.
- [20] R. R. Schrock, *J. Am. Chem. Soc.* **1974**, *96*, 6796-6797.
- [21] J. Hillenbrand, J. N. Korber, M. Leutzsch, N. Nöthling, A. Fürstner, *Chem. Eur. J.* **2021**, *27*, 14025-14033.
- [22] L. Chamberlain, J. Keddington, I. P. Rothwell, *Organometallics* **1982**, *1*, 1098-1100.
- [23] S. M. Beshouri, I. P. Rothwell, K. Folting, J. C. Huffman, W. E. Streib, *Polyhedron* **1986**, *5*, 1191-1195.
- [24] T. M. Gilbert, A. M. Landes, R. D. Rogers, *Inorg. Chem.* **1992**, *31*, 3438-3444.
- [25] D. C. Bradley, M. H. Chisholm, *J. Chem. Soc. A* **1971**, 2741-2744.
- [26] J. Hillenbrand, M. van Gastel, E. Bill, F. Neese, A. Fürstner, *J. Am. Chem. Soc.* **2020**, *142*, 16392-16402.
- [27] M. Chisholm, F. A. Cotton, B. A. Frenz, L. Shive, *J. Chem. Soc., Chem. Commun.* **1974**, 480-481.
- [28] M. H. Chisholm, W. Reichert, *J. Am. Chem. Soc.* **1974**, *96*, 1249-1251.
- [29] M. H. Chisholm, F. A. Cotton, B. A. Frenz, W. W. Reichert, L. W. Shive, B. R. Stults, *J. Am. Chem. Soc.* **1976**, *98*, 4469-4476.
- [30] M. H. Chisholm, F. A. Cotton, C. A. Murillo, W. W. Reichert, *Inorg. Chem.* **1977**, *16*, 1801-1808.
- [31] M. H. Chisholm, W. W. Reichert, F. A. Cotton, C. A. Murillo, *J. Am. Chem. Soc.* **1977**, *99*, 1652-1654.
- [32] C. E. Laplaza, A. R. Johnson, C. C. Cummins, *J. Am. Chem. Soc.* **1996**, *118*, 709-710.
- [33] M. H. Chisholm, F. A. Cotton, M. Extine, B. R. Stults, *J. Am. Chem. Soc.* **1976**, *98*, 4477-4485.
- [34] M. H. Chisholm, B. W. Eichhorn, K. Folting, J. C. Huffman, C. D. Ontiveros, W. E. Streib, W. G. Van der Sluys, *Inorg. Chem.* **1987**, *26*, 3182-3186.
- [35] M. H. Chisholm, I. P. Rothwell, *J. Chem. Soc., Chem. Commun.* **1980**, 985-987.
- [36] M. H. Chisholm, K. Folting, J. C. Huffman, I. P. Rothwell, *Organometallics* **1982**, *1*, 251-259.
- [37] H. Schulz, K. Folting, J. C. Huffman, W. E. Streib, M. H. Chisholm, *Inorg. Chem.* **1993**, *32*, 6056-6066.
- [38] M. H. Chisholm, R. J. Tatz, *Organometallics* **1986**, *5*, 1590-1598.
- [39] M. H. Chisholm, J. C. Huffman, R. J. Tatz, *J. Am. Chem. Soc.* **1984**, *106*, 5385-5386.
- [40] M. H. Chisholm, D. R. Click, J. C. Huffman, *Organometallics* **2000**, *19*, 3916-3924.
- [41] T. A. Budzichowski, S. T. Chacon, M. H. Chisholm, F. J. Feher, W. Streib, *J. Am. Chem. Soc.* **1991**, *113*, 689-691.
- [42] K. J. Ahmed, M. H. Chisholm, K. Folting, J. C. Huffman, *Inorg. Chem.* **1985**, *24*, 4039-4044.

- [43] M. H. Chisholm, E. R. Davidson, J. C. Huffman, K. B. Quinlan, *J. Am. Chem. Soc.* **2001**, *123*, 9652-9664.
- [44] M. H. Chisholm, W. W. Reichert, P. Thornton, *J. Am. Chem. Soc.* **1978**, *100*, 2744-2748.
- [45] M. H. Chisholm, F. A. Cotton, M. W. Extine, W. W. Reichert, *Inorg. Chem.* **1978**, *17*, 2944-2946.
- [46] M. H. Chisholm, C. C. Kirkpatrick, J. C. Huffman, *Inorg. Chem.* **1981**, *20*, 871-876.
- [47] M. H. Chisholm, J. C. Huffman, I. P. Rothwell, *J. Am. Chem. Soc.* **1981**, *103*, 4245-4246.
- [48] M. H. Chisholm, K. Folting, J. C. Huffman, I. P. Rothwell, *J. Am. Chem. Soc.* **1982**, *104*, 4389-4399.
- [49] R. R. Schrock, M. L. Listemann, L. G. Sturgeoff, *J. Am. Chem. Soc.* **1982**, *104*, 4291-4293.
- [50] M. L. Listemann, R. R. Schrock, *Organometallics* **1985**, *4*, 74-83.
- [51] M. H. Chisholm, M. Extine, *J. Am. Chem. Soc.* **1975**, *97*, 5625-5627.
- [52] M. Akiyama, M. H. Chisholm, F. A. Cotton, M. W. Extine, D. A. Haitko, D. Little, P. E. Fanwick, *Inorg. Chem.* **1979**, *18*, 2266-2270.
- [53] P. R. Sharp, R. R. Schrock, *J. Am. Chem. Soc.* **1980**, *102*, 1430-1431.
- [54] F. A. Cotton, W. Schwotzer, E. S. Shamshoum, *Organometallics* **1983**, *2*, 1340-1343.
- [55] F. A. Cotton, E. S. Shamshoum, *J. Am. Chem. Soc.* **1985**, *107*, 4662-4667.
- [56] H. Strutz, R. R. Schrock, *Organometallics* **1984**, *3*, 1600-1601.
- [57] M. H. Chisholm, R. L. Kelly, F. A. Cotton, M. W. Extine, *J. Am. Chem. Soc.* **1978**, *100*, 2256-2257.
- [58] M. H. Chisholm, F. A. Cotton, M. W. Extine, R. L. Kelly, *J. Am. Chem. Soc.* **1979**, *101*, 7645-7650.
- [59] B. E. Bursten, F. A. Cotton, J. C. Green, E. A. Seddon, G. G. Stanley, *J. Am. Chem. Soc.* **1980**, *102*, 4579-4588.
- [60] F. A. Cotton, G. G. Stanley, B. J. Kalbacher, J. C. Green, E. Seddon, M. H. Chisholm, *Proc. Natl. Acad. Sci. U. S. A.* **1977**, *74*, 3109-3113.
- [61] T. A. Albright, R. Hoffmann, *J. Am. Chem. Soc.* **1978**, *100*, 7736-7738.
- [62] C. C. Cummins, *Chem. Commun.* **1998**, 1777-1786.
- [63] D. C. Bradley, M. H. Chisholm, *Acc. Chem. Res.* **1976**, *9*, 273-280.
- [64] J. S. Basi, D. C. Bradley, *Proc. Chem. Soc.* **1963**, 305.
- [65] J. S. Basi, D. C. Bradley, M. H. Chisholm, *J. Chem. Soc. A* **1971**, 1433-1436.
- [66] E. C. Alyea, J. S. Basi, D. C. Bradley, M. H. Chisholm, *Chem. Commun. (London)* **1968**, 495-495.
- [67] D. C. Bradley, M. B. Hursthouse, C. W. Newing, *J. Chem. Soc. D* **1971**, 411b-412.
- [68] C. E. Laplaza, W. M. Davis, C. C. Cummins, *Organometallics* **1995**, *14*, 577-580.
- [69] C. E. Laplaza, C. C. Cummins, *Science* **1995**, *268*, 861-863.
- [70] C. E. Laplaza, M. J. A. Johnson, J. C. Peters, A. L. Odom, E. Kim, C. C. Cummins, G. N. George, I. J. Pickering, *J. Am. Chem. Soc.* **1996**, *118*, 8623-8638.
- [71] J. J. Curley, T. R. Cook, S. Y. Reece, P. Müller, C. C. Cummins, *J. Am. Chem. Soc.* **2008**, *130*, 9394-9405.
- [72] Q. Cui, D. G. Musaev, M. Svensson, S. Sieber, K. Morokuma, *J. Am. Chem. Soc.* **1995**, *117*, 12366-12367.
- [73] G. J. Leigh, *Science* **1995**, *268*, 827-828.
- [74] J. C. Peters, J.-P. F. Cherry, J. C. Thomas, L. Baraldo, D. J. Mindiola, W. M. Davis, C. C. Cummins, *J. Am. Chem. Soc.* **1999**, *121*, 10053-10067.
- [75] D. M. T. Chan, M. H. Chisholm, K. Folting, J. C. Huffman, N. S. Marchant, *Inorg. Chem.* **1986**, *25*, 4170-4174.
- [76] M. J. A. Johnson, P. M. Lee, A. L. Odom, W. M. Davis, C. C. Cummins, *Angew. Chem. Int. Ed. Engl.* **1997**, *36*, 87-91.
- [77] M.-M. Rohmer, M. Bénard, *Inorg. Chem.* **2002**, *41*, 892-900.
- [78] T. Agapie, A. L. Odom, C. C. Cummins, *Inorg. Chem.* **2000**, *39*, 174-179.
- [79] D. Rütter, M. van Gastel, M. Leutzsch, N. Nöthling, D. SantaLucia, F. Neese, A. Fürstner, *Inorg. Chem.* **2024**, *63*, 8376-8389.
- [80] Y.-C. Tsai, M. J. A. Johnson, D. J. Mindiola, C. C. Cummins, W. T. Klooster, T. F. Koetzle, *J. Am. Chem. Soc.* **1999**, *121*, 10426-10427.
- [81] E. Solari, C. Da Silva, B. Iacono, J. Hesschenbrouck, C. Rizzoli, R. Scopelliti, C. Floriani, *Angew. Chem. Int. Ed.* **2001**, *40*, 3907-3909.

- [82] J.-P. F. Cherry, A. R. Johnson, L. M. Baraldo, Y.-C. Tsai, C. C. Cummins, S. V. Kryatov, E. V. Rybak-Akimova, K. B. Capps, C. D. Hoff, C. M. Haar, S. P. Nolan, *J. Am. Chem. Soc.* **2001**, *123*, 7271-7286.
- [83] N. C. Zanetti, R. R. Schrock, W. M. Davis, *Angew. Chem. Int. Ed. Engl.* **1995**, *34*, 2044-2046.
- [84] C. E. Laplaza, W. M. Davis, C. C. Cummins, *Angew. Chem. Int. Ed. Engl.* **1995**, *34*, 2042-2044.
- [85] F. H. Stephens, M. J. A. Johnson, C. C. Cummins, O. P. Kryatova, S. V. Kryatov, E. V. Rybak-Akimova, J. E. McDonough, C. D. Hoff, *J. Am. Chem. Soc.* **2005**, *127*, 15191-15200.
- [86] J. C. Peters, A. L. Odom, C. C. Cummins, *Chem. Commun.* **1997**, 1995-1996.
- [87] A. Fürstner, C. Mathes, C. W. Lehmann, *J. Am. Chem. Soc.* **1999**, *121*, 9453-9454.
- [88] A. Fürstner, C. Mathes, C. W. Lehmann, *Chem. Eur. J.* **2001**, *7*, 5299-5317.
- [89] A. Fürstner, *J. Am. Chem. Soc.* **2021**, *143*, 15538-15555.
- [90] A. Fürstner, P. W. Davies, *Chem. Commun.* **2005**, 2307-2320.
- [91] A. Fürstner, *Angew. Chem. Int. Ed.* **2013**, *52*, 2794-2819.
- [92] W. Zhang, S. Kraft, J. S. Moore, *Chem. Commun.* **2003**, 832-833.
- [93] W. Zhang, S. Kraft, J. S. Moore, *J. Am. Chem. Soc.* **2004**, *126*, 329-335.
- [94] W. Zhang, Y. Lu, J. S. Moore, *Org. Synth.* **2007**, *84*, 163-176.
- [95] J.-P. F. Cherry, Dissertation, Massachusetts Institute of Technology, **2001**.
- [96] Y.-C. Tsai, P. L. Diaconescu, C. C. Cummins, *Organometallics* **2000**, *19*, 5260-5262.
- [97] J. M. Blackwell, J. S. Figueroa, F. H. Stephens, C. C. Cummins, *Organometallics* **2003**, *22*, 3351-3353.
- [98] D.-D. Zhai, S.-Q. Zhang, S.-J. Xie, R.-K. Wu, F. Liu, Z.-F. Xi, X. Hong, Z.-J. Shi, *J. Am. Chem. Soc.* **2022**, *144*, 14071-14078.
- [99] D.-d. Zhai, S.-j. Xie, Y. Xia, H.-y. Fang, Z.-j. Shi, *Natl. Sci. Rev.* **2020**, *8*.
- [100] C. C. Cummins, J. Lee, R. R. Schrock, W. D. Davis, *Angew. Chem. Int. Ed. Engl.* **1992**, *31*, 1501-1503.
- [101] D. V. Yandulov, R. R. Schrock, *Science* **2003**, *301*, 76-78.
- [102] D. V. Yandulov, R. R. Schrock, *J. Am. Chem. Soc.* **2002**, *124*, 6252-6253.
- [103] D. V. Yandulov, R. R. Schrock, A. L. Rheingold, C. Ceccarelli, W. M. Davis, *Inorg. Chem.* **2003**, *42*, 796-813.
- [104] D. V. Yandulov, R. R. Schrock, *Inorg. Chem.* **2005**, *44*, 1103-1117.
- [105] F. Neese, *Angew. Chem. Int. Ed.* **2006**, *45*, 196-199.
- [106] W. Thimm, C. Gradert, H. Broda, F. Wennmohs, F. Neese, F. Tuczek, *Inorg. Chem.* **2015**, *54*, 9248-9255.
- [107] Y. Nishibayashi, *Nitrogen Fixation*, Springer, **2017**.
- [108] S. J. K. Forrest, B. Schluschaß, E. Y. Yuzik-Klimova, S. Schneider, *Chem. Rev.* **2021**, *121*, 6522-6587.
- [109] D. S. Kuiper, R. E. Douthwaite, A.-R. Mayol, P. T. Wolczanski, E. B. Lobkovsky, T. R. Cundari, O. P. Lam, K. Meyer, *Inorg. Chem.* **2008**, *47*, 7139-7153.
- [110] D. S. Kuiper, P. T. Wolczanski, E. B. Lobkovsky, T. R. Cundari, *J. Am. Chem. Soc.* **2008**, *130*, 12931-12943.
- [111] M. Pucino, F. Allouche, C. P. Gordon, M. Wörle, V. Mougél, C. Copéret, *Chem. Sci.* **2019**, *10*, 6362-6367.
- [112] K. M. Wampler, R. R. Schrock, *Inorg. Chem.* **2008**, *47*, 10226-10228.
- [113] B. S. Buyuktas, P. P. Power, *Chem. Commun.* **1998**, 1689-1690.
- [114] J. Hillenbrand, M. Leutzsch, A. Fürstner, *Angew. Chem. Int. Ed.* **2019**, *58*, 15690-15696.
- [115] J. Hillenbrand, M. Leutzsch, C. P. Gordon, C. Copéret, A. Fürstner, *Angew. Chem. Int. Ed.* **2020**, *59*, 21758-21768.
- [116] J. Hillenbrand, M. Leutzsch, E. Yiannakas, C. P. Gordon, C. Wille, N. Nöthling, C. Copéret, A. Fürstner, *J. Am. Chem. Soc.* **2020**, *142*, 11279-11294.
- [117] A. Haack, J. Hillenbrand, M. van Gastel, A. Fürstner, F. Neese, *ACS Catal.* **2021**, *11*, 9086-9101.
- [118] A. Haack, J. Hillenbrand, M. Leutzsch, M. van Gastel, F. Neese, A. Fürstner, *J. Am. Chem. Soc.* **2021**, *143*, 5643-5648.
- [119] J. J. Curley, E. L. Sceats, C. C. Cummins, *J. Am. Chem. Soc.* **2006**, *128*, 14036-14037.
- [120] D. Rütter, Master Thesis, Heinrich-Heine-Universität Düsseldorf, **2021**.
- [121] J. N. Korber, Master Thesis, Ludwig-Maximilians-Universität München, **2021**.
- [122] C. Beemelmans, R. Husmann, D. K. Whelligan, S. Özçubukçu, C. Bolm, *Eur. J. Org. Chem.* **2012**, *2012*, 3373-3376.
- [123] C. P. Gordon, R. A. Andersen, C. Copéret, *Helv. Chim. Acta* **2019**, *102*, e1900151.

- [124] Z. J. Berkson, L. Lätsch, J. Hillenbrand, A. Fürstner, C. Copéret, *J. Am. Chem. Soc.* **2022**, *144*, 15020-15025.
- [125] J. Malito, *Annu. Rep. NMR Spectrosc.* **1996**, *33*, 151-206.
- [126] C. G. Young, E. M. Kober, J. H. Enemark, *Polyhedron* **1987**, *6*, 255-259.
- [127] T. M. Gilbert, C. B. Bauer, A. H. Bond, R. D. Rogers, *Polyhedron* **1999**, *18*, 1293-1301.
- [128] C. Bittner, H. Ehrhorn, D. Bockfeld, K. Brandhorst, M. Tamm, *Organometallics* **2017**, *36*, 3398-3406.
- [129] A. Chapovetsky, R. R. Langeslay, G. Celik, F. A. Perras, M. Pruski, M. S. Ferrandon, E. C. Wegener, H. Kim, F. Dogan, J. Wen, N. Khetrapal, P. Sharma, J. White, A. J. Kropf, A. P. Sattelberger, D. M. Kaphan, M. Delferro, *Organometallics* **2020**, *39*, 1035-1045.
- [130] R. R. Thompson, M. E. Rotella, X. Zhou, F. R. Fronczek, O. Gutierrez, S. Lee, *J. Am. Chem. Soc.* **2021**, *143*, 9026-9039.
- [131] A. M. Geyer, E. S. Wiedner, J. B. Gary, R. L. Gdula, N. C. Kuhlmann, M. J. A. Johnson, B. D. Dunietz, J. W. Kampf, *J. Am. Chem. Soc.* **2008**, *130*, 8984-8999.
- [132] R. L. Gdula, M. J. A. Johnson, *J. Am. Chem. Soc.* **2006**, *128*, 9614-9615.
- [133] M. Bindl, R. Stade, E. K. Heilmann, A. Picot, R. Goddard, A. Fürstner, *J. Am. Chem. Soc.* **2009**, *131*, 9468-9470.
- [134] J. Heppekausen, R. Stade, R. Goddard, A. Fürstner, *J. Am. Chem. Soc.* **2010**, *132*, 11045-11057.
- [135] J. Heppekausen, R. Stade, A. Kondoh, G. Seidel, R. Goddard, A. Fürstner, *Chem. Eur. J.* **2012**, *18*, 10281-10299.
- [136] J. N. Korber, C. Wille, M. Leutzsch, A. Fürstner, *J. Am. Chem. Soc.* **2023**, *145*, 26993-27009.
- [137] E. S. Wiedner, K. J. Gallagher, M. J. A. Johnson, J. W. Kampf, *Inorg. Chem.* **2011**, *50*, 5936-5945.
- [138] R. Hoffmann, *Angew. Chem. Int. Ed. Engl.* **1982**, *21*, 711-724.
- [139] J. Mason, L. F. Larkworthy, E. A. Moore, *Chem. Rev.* **2002**, *102*, 913-934.
- [140] W. Beck, T. M. Klapötke, J. Knizek, H. Nöth, T. Schütt, *Eur. J. Inorg. Chem.* **1999**, *1999*, 523-526.
- [141] S. Gaemers, J. Groenevelt, Cornelis J. Elsevier, *Eur. J. Inorg. Chem.* **2001**, *2001*, 829-835.
- [142] Y. Li, A. Turnas, J. T. Ciszewski, A. L. Odom, *Inorg. Chem.* **2002**, *41*, 6298-6306.
- [143] M.-J. Crawford, P. Mayer, H. Nöth, M. Suter, *Inorg. Chem.* **2004**, *43*, 6860-6862.
- [144] P. Kofod, *Magn. Reson. Chem.* **2003**, *41*, 531-534.
- [145] R. H. Grubbs, *Angew. Chem. Int. Ed.* **2006**, *45*, 3760-3765.
- [146] M. T. Reetz, *Angew. Chem. Int. Ed.* **2014**, *53*, 8562-8586.
- [147] G. Wilke, *Angew. Chem. Int. Ed.* **2003**, *42*, 5000-5008.
- [148] K. Ziegler, E. Holzkamp, H. Breil, H. Martin, *Angew. Chem.* **1955**, *67*, 541-547.
- [149] K. Ziegler, *Angew. Chem.* **1952**, *64*, 323-329.
- [150] K. Fischer, K. Jonas, P. Misbach, R. Stabba, G. Wilke, *Angew. Chem. Int. Ed. Engl.* **1973**, *12*, 943-953.
- [151] H. Martin, *Karl Ziegler, das Team, 1953-1998 ; Zur wirtschaftlichen Verwertung akademischer Forschung*, Wiley-VCH: Weinheim, **2002**.
- [152] P. Cossee, *Tetrahedron Lett.* **1960**, *1*, 12-16.
- [153] P. Cossee, *J. Catal.* **1964**, *3*, 80-88.
- [154] E. J. Arlman, P. Cossee, *J. Catal.* **1964**, *3*, 99-104.
- [155] E. J. Arlman, *J. Catal.* **1964**, *3*, 89-98.
- [156] D. S. Breslow, N. R. Newburg, *J. Am. Chem. Soc.* **1959**, *81*, 81-86.
- [157] J. F. Hartwig, *Organotransition Metal Chemistry: From Bonding to Catalysis*, University Science Books, Sausalito, **2010**.
- [158] R. H. Grubbs, G. W. Coates, *Acc. Chem. Res.* **1996**, *29*, 85-93.
- [159] C. A. Jolly, D. S. Marynick, *J. Am. Chem. Soc.* **1989**, *111*, 7968-7974.
- [160] W. L. Truett, D. R. Johnson, I. M. Robinson, B. A. Montague, *J. Am. Chem. Soc.* **1960**, *82*, 2337-2340.
- [161] A. Fürstner, *Angew. Chem. Int. Ed.* **2000**, *39*, 3012-3043.
- [162] K. J. Ivin, J. J. Rooney, C. D. Stewart, M. L. H. Green, R. Mahtab, *J. Chem. Soc., Chem. Commun.* **1978**, 604-606.
- [163] P. J. L. Hérisson, Y. Chauvin, *Makromol. Chem.* **1970**, *141*, 161-176.
- [164] R. H. Grubbs, P. L. Burk, D. D. Carr, *J. Am. Chem. Soc.* **1975**, *97*, 3265-3267.
- [165] R. H. Grubbs, D. D. Carr, C. Hoppin, P. L. Burk, *J. Am. Chem. Soc.* **1976**, *98*, 3478-3483.
- [166] E. I. Muettterties, *Inorg. Chem.* **1975**, *14*, 951-953.

- [167] T. J. Katz, J. McGinnis, *J. Am. Chem. Soc.* **1975**, *97*, 1592-1594.
- [168] T. J. Katz, R. Rothchild, *J. Am. Chem. Soc.* **1976**, *98*, 2519-2526.
- [169] R. H. Grubbs, T. K. Brunck, *J. Am. Chem. Soc.* **1972**, *94*, 2538-2540.
- [170] R. R. Schrock, *Angew. Chem. Int. Ed.* **2006**, *45*, 3748-3759.
- [171] R. L. Banks, G. C. Bailey, *I&EC Product Research and Development* **1964**, *3*, 170-173.
- [172] N. Calderon, H. Y. Chen, K. W. Scott, *Tetrahedron Lett.* **1967**, *8*, 3327-3329.
- [173] G. Wilkinson, M. Rosenblum, M. C. Whiting, R. B. Woodward, *J. Am. Chem. Soc.* **1952**, *74*, 2125-2126.
- [174] E. O. Fischer, W. Pfab, *Z. Naturforsch.* **1952**, *B7*, 377-379.
- [175] P. F. Eiland, R. Pepinsky, *J. Am. Chem. Soc.* **1952**, *74*, 4971-4971.
- [176] J. D. Dunitz, L. E. Orgel, *Nature* **1953**, *171*, 121-122.
- [177] J. D. Dunitz, L. E. Orgel, A. Rich, *Acta Cryst.* **1956**, *9*, 373-375.
- [178] E. O. Fischer, A. Maasböl, *Angew. Chem. Int. Ed. Engl.* **1964**, *3*, 580-581.
- [179] D. J. Cardin, B. Cetinkaya, M. F. Lappert, *Chem. Rev.* **1972**, *72*, 545-574.
- [180] A. J. Shortland, G. Wilkinson, *J. Chem. Soc., Dalton Trans.* **1973**, 872-876.
- [181] R. R. Schrock, P. Meakin, *J. Am. Chem. Soc.* **1974**, *96*, 5288-5290.
- [182] R. R. Schrock, J. D. Fellmann, *J. Am. Chem. Soc.* **1978**, *100*, 3359-3370.
- [183] T. E. Taylor, M. B. Hall, *J. Am. Chem. Soc.* **1984**, *106*, 1576-1584.
- [184] W. A. Nugent, J. M. Mayer, *Metal-Ligand Multiple Bonds: The Chemistry of Transition Metal Complexes Containing Oxo, Nitrido, Imido, Alkylidene, or Alkylidyne Ligands*, John Wiley & Sons: New York, **1988**.
- [185] J. Scott, D. J. Mindiola, *Dalton Trans.* **2009**, 8463-8472.
- [186] F. N. Tebbe, G. W. Parshall, G. S. Reddy, *J. Am. Chem. Soc.* **1978**, *100*, 3611-3613.
- [187] F. N. Tebbe, G. W. Parshall, D. W. Ovenall, *J. Am. Chem. Soc.* **1979**, *101*, 5074-5075.
- [188] T. R. Howard, J. B. Lee, R. H. Grubbs, *J. Am. Chem. Soc.* **1980**, *102*, 6876-6878.
- [189] J. R. Stille, R. H. Grubbs, *J. Am. Chem. Soc.* **1983**, *105*, 1664-1665.
- [190] S. H. Pine, R. Zahler, D. A. Evans, R. H. Grubbs, *J. Am. Chem. Soc.* **1980**, *102*, 3270-3272.
- [191] L. R. Gilliom, R. H. Grubbs, *J. Am. Chem. Soc.* **1986**, *108*, 733-742.
- [192] R. J. Zachmann, K. Yahata, M. Holzheimer, M. Jarret, C. Wirtz, A. Fürstner, *J. Am. Chem. Soc.* **2023**, *145*, 2584-2595.
- [193] K. C. Nicolaou, M. H. D. Postema, E. W. Yue, A. Nadin, *J. Am. Chem. Soc.* **1996**, *118*, 10335-10336.
- [194] K. C. Nicolaou, M. H. D. Postema, C. F. Claiborne, *J. Am. Chem. Soc.* **1996**, *118*, 1565-1566.
- [195] J. Klimes, E. Weiss, *Angew. Chem., Int. Ed. Engl.* **1982**, *21*, 477-482.
- [196] S. T. Nguyen, L. K. Johnson, R. H. Grubbs, J. W. Ziller, *J. Am. Chem. Soc.* **1992**, *114*, 3974-3975.
- [197] M. R. Gagne, R. H. Grubbs, J. Feldman, J. W. Ziller, *Organometallics* **1992**, *11*, 3933-3935.
- [198] S. T. Nguyen, R. H. Grubbs, J. W. Ziller, *J. Am. Chem. Soc.* **1993**, *115*, 9858-9859.
- [199] L. K. Johnson, R. H. Grubbs, J. W. Ziller, *J. Am. Chem. Soc.* **1993**, *115*, 8130-8145.
- [200] F. J. de la Mata, R. H. Grubbs, *Organometallics* **1996**, *15*, 577-584.
- [201] Y. Ning, R. D. J. Froese, P. Margl, E. L. Lee, S. T. Nguyen, T. H. Peterson, N. Wagner, C. L. Stern, A. A. Sarjeant, *Organometallics* **2014**, *33*, 1120-1125.
- [202] J. Foerstner, A. Kakoschke, D. Stellfeldt, H. Butenschön, R. Wartchow, *Organometallics* **1998**, *17*, 893-896.
- [203] B. T. Flatt, R. H. Grubbs, R. L. Blanski, J. C. Calabrese, J. Feldman, *Organometallics* **1994**, *13*, 2728-2732.
- [204] G. Seidel, R. Mynott, A. Fürstner, *Angew. Chem. Int. Ed.* **2009**, *48*, 2510-2513.
- [205] J.-H. Huang, T.-Y. Lee, D. C. Swenson, L. Messerle, *Inorg. Chim. Acta* **2003**, *345*, 209-215.
- [206] F. N. Tebbe, R. L. Harlow, *Journal of the American Chemical Society* **1980**, *102*, 6149-6151.
- [207] P. Binger, P. Müller, A. T. Herrmann, P. Philipps, B. Gabor, F. Langhauser, C. Krüger, *Chem. Ber.* **1991**, *124*, 2165-2170.
- [208] R. T. Li, S. T. Nguyen, R. H. Grubbs, J. W. Ziller, *J. Am. Chem. Soc.* **1994**, *116*, 10032-10040.
- [209] W. Kirmse, N. G. Rondan, K. N. Houk, *J. Am. Chem. Soc.* **1984**, *106*, 7989-7991.
- [210] S. T. Nguyen, Dissertation, Caltech, **1995**.
- [211] B. M. Novak, R. H. Grubbs, *J. Am. Chem. Soc.* **1988**, *110*, 7542-7543.
- [212] G. C. Fu, S. T. Nguyen, R. H. Grubbs, *J. Am. Chem. Soc.* **1993**, *115*, 9856-9857.
- [213] B. C. Borer, S. Deerenberg, H. Bieräugel, U. K. Pandit, *Tetrahedron Lett.* **1994**, *35*, 3191-3194.
- [214] A. Fürstner, K. Langemann, *J. Org. Chem.* **1996**, *61*, 3942-3943.

- [215] A. Fürstner, *Top. Catal.* **1997**, *4*, 285-299.
- [216] A. Fürstner, T. Gastner, H. Weintritt, *J. Org. Chem.* **1999**, *64*, 2361-2366.
- [217] S. F. Martin, Y. Liao, Y. Wong, T. Rein, *Tetrahedron Lett.* **1994**, *35*, 691-694.
- [218] S. F. Martin, J. M. Humphrey, A. Ali, M. C. Hillier, *J. Am. Chem. Soc.* **1999**, *121*, 866-867.
- [219] T. M. Trnka, R. H. Grubbs, *Acc. Chem. Res.* **2001**, *34*, 18-29.
- [220] P. Schwab, M. B. France, J. W. Ziller, R. H. Grubbs, *Angew. Chem. Int. Ed. Engl.* **1995**, *34*, 2039-2041.
- [221] P. Schwab, R. H. Grubbs, J. W. Ziller, *J. Am. Chem. Soc.* **1996**, *118*, 100-110.
- [222] A. Fürstner, O. Guth, A. Düffels, G. Seidel, M. Liebl, B. Gabor, R. Mynott, *Chem. Eur. J.* **2001**, *7*, 4811-4820.
- [223] J. P. Selegue, *Organometallics* **1982**, *1*, 217-218.
- [224] K. J. Harlow, A. F. Hill, J. D. E. T. Wilton-Ely, *J. Chem. Soc., Dalton Trans.* **1999**, 285-292.
- [225] E. A. Shaffer, C.-L. Chen, A. M. Beatty, E. J. Valente, H.-J. Schanz, *Journal of Organometallic Chemistry* **2007**, *692*, 5221-5233.
- [226] E. Pump, C. Slugovc, L. Cavallo, A. Poater, *Organometallics* **2015**, *34*, 3107-3111.
- [227] R. Castarlenas, C. Vovard, C. Fischmeister, P. H. Dixneuf, *J. Am. Chem. Soc.* **2006**, *128*, 4079-4089.
- [228] A. Fürstner, M. Liebl, C. W. Lehmann, M. Picquet, R. Kunz, C. Bruneau, D. Touchard, P. H. Dixneuf, *Chem. Eur. J.* **2000**, *6*, 1847-1857.
- [229] M. Gandelman, K. M. Naing, B. Rybtchinski, E. Poverenov, Y. Ben-David, N. Ashkenazi, R. M. Gauvin, D. Milstein, *J. Am. Chem. Soc.* **2005**, *127*, 15265-15272.
- [230] G. M. George, P. T. Wolczanski, S. N. MacMillan, *Organometallics* **2021**, *40*, 3389-3396.
- [231] M. S. Sanford, J. A. Love, R. H. Grubbs, *J. Am. Chem. Soc.* **2001**, *123*, 6543-6554.
- [232] C. P. Gordon, K. Yamamoto, W.-C. Liao, F. Allouche, R. A. Andersen, C. Copéret, C. Raynaud, O. Eisenstein, *ACS Central Science* **2017**, *3*, 759-768.
- [233] P. E. Romero, W. E. Piers, *J. Am. Chem. Soc.* **2005**, *127*, 5032-5033.
- [234] L. Ackermann, A. Fürstner, T. Weskamp, F. J. Kohl, W. A. Herrmann, *Tetrahedron Lett.* **1999**, *40*, 4787-4790.
- [235] J. Huang, E. D. Stevens, S. P. Nolan, J. L. Petersen, *J. Am. Chem. Soc.* **1999**, *121*, 2674-2678.
- [236] M. Scholl, S. Ding, C. W. Lee, R. H. Grubbs, *Org. Lett.* **1999**, *1*, 953-956.
- [237] T. Weskamp, F. J. Kohl, W. Hieringer, D. Gleich, W. A. Herrmann, *Angew. Chem. Int. Ed.* **1999**, *38*, 2416-2419.
- [238] J. P. A. Harrity, M. S. Visser, J. D. Gleason, A. H. Hoveyda, *J. Am. Chem. Soc.* **1997**, *119*, 1488-1489.
- [239] J. P. A. Harrity, D. S. La, D. R. Cefalo, M. S. Visser, A. H. Hoveyda, *J. Am. Chem. Soc.* **1998**, *120*, 2343-2351.
- [240] J. S. Kingsbury, J. P. A. Harrity, P. J. Bonitatebus, A. H. Hoveyda, *J. Am. Chem. Soc.* **1999**, *121*, 791-799.
- [241] S. B. Garber, J. S. Kingsbury, B. L. Gray, A. H. Hoveyda, *J. Am. Chem. Soc.* **2000**, *122*, 8168-8179.
- [242] R. R. Schrock, *Chem. Rev.* **2002**, *102*, 145-180.
- [243] R. R. Schrock, J. S. Murdzek, G. C. Bazan, J. Robbins, M. DiMare, M. O'Regan, *J. Am. Chem. Soc.* **1990**, *112*, 3875-3886.
- [244] H. H. Fox, J. K. Lee, L. Y. Park, R. R. Schrock, *Organometallics* **1993**, *12*, 759-768.
- [245] J. Heppekausen, A. Fürstner, *Angew. Chem. Int. Ed.* **2011**, *50*, 7829-7832.
- [246] Y. Chauvin, *Angew. Chem. Int. Ed.* **2006**, *45*, 3740-3747.
- [247] B. W. Grau, A. Neuhauser, S. Aghazada, K. Meyer, S. B. Tsogoeva, *Chem. Eur. J.* **2022**, *28*, e202201414.
- [248] J. Louie, R. H. Grubbs, *Organometallics* **2001**, *20*, 481-484.
- [249] P. W. Jolly, R. Pettit, *J. Am. Chem. Soc.* **1966**, *88*, 5044-5045.
- [250] Y. Wei, A. Tinoco, V. Steck, R. Fasan, Y. Zhang, *J. Am. Chem. Soc.* **2018**, *140*, 1649-1662.
- [251] M. Brookhart, J. R. Tucker, G. R. Husk, *J. Am. Chem. Soc.* **1981**, *103*, 979-981.
- [252] M. Brookhart, J. R. Tucker, G. R. Husk, *J. Am. Chem. Soc.* **1983**, *105*, 258-264.
- [253] J. R. Wolf, C. G. Hamaker, J.-P. Djukic, T. Kodadek, L. K. Woo, *J. Am. Chem. Soc.* **1995**, *117*, 9194-9199.
- [254] Y. Li, J.-S. Huang, Z.-Y. Zhou, C.-M. Che, X.-Z. You, *J. Am. Chem. Soc.* **2002**, *124*, 13185-13193.
- [255] É. de Brito Sá, L. Rodríguez-Santiago, M. Sodupe, X. Solans-Monfort, *Organometallics* **2016**, *35*, 3914-3923.

- [256] É. de Brito Sá, L. Rodríguez-Santiago, M. Sodupe, X. Solans-Monfort, *Organometallics* **2018**, *37*, 1229-1241.
- [257] M. Vasiliu, A. J. Arduengo, III, D. A. Dixon, *J. Phys. Chem. C* **2014**, *118*, 13563-13577.
- [258] M. Mauksch, S. B. Tsogoeva, *Chem. Eur. J.* **2017**, *23*, 10264-10269.
- [259] A. Poater, E. Pump, S. V. C. Vummaleti, L. Cavallo, *Chem. Phys. Lett.* **2014**, *610-611*, 29-32.
- [260] C. Roger, C. Lapinte, *J. Chem. Soc., Chem. Commun.* **1989**, 1598-1600.
- [261] S. Aghazada, D. Munz, F. W. Heinemann, A. Scheurer, K. Meyer, *J. Am. Chem. Soc.* **2021**, *143*, 17219-17225.
- [262] M. Giusti, E. Solari, L. Giannini, C. Floriani, A. Chiesi-Villa, C. Rizzoli, *Organometallics* **1997**, *16*, 5610-5612.
- [263] S. K. Russell, J. M. Hoyt, S. C. Bart, C. Milsmann, S. C. E. Stieber, S. P. Semproni, S. DeBeer, P. J. Chirik, *Chem. Sci.* **2014**, *5*, 1168-1174.
- [264] S. C. Bart, A. C. Bowman, E. Lobkovsky, P. J. Chirik, *J. Am. Chem. Soc.* **2007**, *129*, 7212-7213.
- [265] S. C. Bart, E. Lobkovsky, E. Bill, P. J. Chirik, *J. Am. Chem. Soc.* **2006**, *128*, 5302-5303.
- [266] A. C. Bowman, C. Milsmann, E. Bill, Z. R. Turner, E. Lobkovsky, S. DeBeer, K. Wieghardt, P. J. Chirik, *J. Am. Chem. Soc.* **2011**, *133*, 17353-17369.
- [267] O. Eisenstein, R. Hoffmann, A. R. Rossi, *J. Am. Chem. Soc.* **1981**, *103*, 5582-5584.
- [268] D. S. Belov, L. Mathivathanan, M. J. Beazley, W. B. Martin, K. V. Bukhryakov, *Angew. Chem. Int. Ed.* **2021**, *60*, 2934-2938.
- [269] M. R. Hoffbauer, V. M. Iluc, *J. Am. Chem. Soc.* **2021**, *143*, 5592-5597.
- [270] Z. S. Lincoln, V. M. Iluc, *J. Am. Chem. Soc.* **2024**, *146*, 17595-17599.
- [271] S. Takebayashi, M. A. Iron, M. Feller, O. Rivada-Wheelaghan, G. Leitus, Y. Diskin-Posner, L. J. W. Shimon, L. Avram, R. Carmieli, S. G. Wolf, I. Cohen-Ofri, R. A. Sanguramath, R. Shenhar, M. Eisen, D. Milstein, *Nat. Catal.* **2022**, *5*, 494-502.
- [272] A. I. F. Venâncio, L. s. M. D. R. S. Martins, A. J. L. Pombeiro, *J. Organomet. Chem.* **2003**, *684*, 315-321.
- [273] C. Gauss, D. Veghini, O. Orama, H. Berke, *J. Organomet. Chem.* **1997**, *541*, 19-38.
- [274] H. H. Karsch, H.-F. Klein, H. Schmidbaur, *Chem. Ber.* **1977**, *110*, 2200-2212.
- [275] C. A. Tolman, S. D. Ittel, A. D. English, J. P. Jesson, *J. Am. Chem. Soc.* **1978**, *100*, 4080-4089.
- [276] S. D. Ittel, C. A. Tolman, A. D. English, J. P. Jesson, *J. Am. Chem. Soc.* **1978**, *100*, 7577-7585.
- [277] C. A. Tolman, S. D. Ittel, A. D. English, J. P. Jesson, *J. Am. Chem. Soc.* **1979**, *101*, 1742-1751.
- [278] A. Hills, D. L. Hughes, M. Jimenez-Tenorio, G. J. Leigh, A. T. Rowley, *J. Chem. Soc., Dalton Trans.* **1993**, 3041-3049.
- [279] G. S. Girolami, G. Wilkinson, A. M. R. Galas, M. Thornton-Pett, M. B. Hursthouse, *J. Chem. Soc., Dalton Trans.* **1985**, 1339-1348.
- [280] D. J. Fox, R. G. Bergman, *Organometallics* **2004**, *23*, 1656-1670.
- [281] M. V. Baker, L. D. Field, *Organometallics* **1986**, *5*, 821-823.
- [282] J. Hicks, M. Juckel, A. Paparo, D. Dange, C. Jones, *Organometallics* **2018**, *37*, 4810-4813.
- [283] C. H. Arnett, T. Agapie, *J. Am. Chem. Soc.* **2020**, *142*, 10059-10068.
- [284] A. Casitas, H. Krause, S. Lutz, R. Goddard, E. Bill, A. Fürstner, *Organometallics* **2018**, *37*, 729-739.
- [285] C. C. Lu, E. Bill, T. Weyhermüller, E. Bothe, K. Wieghardt, *J. Am. Chem. Soc.* **2008**, *130*, 3181-3197.
- [286] J. Y. Wu, B. Moreau, T. Ritter, *J. Am. Chem. Soc.* **2009**, *131*, 12915-12917.
- [287] J. Y. Wu, B. N. Stanzl, T. Ritter, *J. Am. Chem. Soc.* **2010**, *132*, 13214-13216.
- [288] E. McNeill, T. Ritter, *Acc. Chem. Res.* **2015**, *48*, 2330-2343.
- [289] C. R. Kennedy, H. Zhong, R. L. Macaulay, P. J. Chirik, *J. Am. Chem. Soc.* **2019**, *141*, 8557-8573.
- [290] S. Meyer, L. Göbel, K. Livingstone, C. Roblick, C. G. Daniliuc, R. Gilmour, *Tetrahedron* **2022**, *126*, 132925.
- [291] L. Zhou, F. Ye, Y. Zhang, J. Wang, *Org. Lett.* **2012**, *14*, 922-925.
- [292] B. Wrackmeyer, O. L. Tok, M. Herberhold, *Organometallics* **2001**, *20*, 5774-5776.
- [293] R. Benn, A. Ruffinska, M. S. Kralik, R. D. Ernst, *Journal of Organometallic Chemistry* **1989**, *375*, 115-121.
- [294] T. Jenny, W. von Philipsborn, J. Kronenbitter, A. Schwenk, *J. Organomet. Chem.* **1981**, *205*, 211-222.
- [295] R. Benn, H. Brenneke, A. Frings, H. Lehmkühl, G. Mehler, A. Ruffinska, T. Wildt, *J. Am. Chem. Soc.* **1988**, *110*, 5661-5668.
- [296] W. v. Philipsborn, *Pure Appl. Chem.* **1986**, *58*, 513-528.

- [297] J. R. Polam, J. L. Wright, K. A. Christensen, F. A. Walker, H. Flint, H. Winkler, M. Grodzicki, A. X. Trautwein, *J. Am. Chem. Soc.* **1996**, *118*, 5272-5276.
- [298] A. A. Koridze, N. M. Astakhova, P. V. Petrovskii, *J. Organomet. Chem.* **1983**, *254*, 345-360.
- [299] R. Benn, A. Ruffinska, *Magn. Reson. Chem.* **1988**, *26*, 895-902.
- [300] S. Grimme, F. Bohle, A. Hansen, P. Pracht, S. Spicher, M. Stahn, *J. Phys. Chem. A* **2021**, *125*, 4039-4054.
- [301] L. Baltzer, M. Landergren, *J. Chem. Soc., Chem. Commun.* **1987**, 32-34.
- [302] P. Gütllich, E. Bill, A. X. Trautwein, *Mössbauer Spectroscopy and Transition Metal Chemistry*, Springer, **2011**.
- [303] C. Gallenkamp, U. I. Kramm, J. Proppe, V. Krewald, *Int. J. Quantum Chem.* **2021**, *121*, e26394.
- [304] D. J. SantaLucia, *Introduction to Mössbauer Spectroscopy*, unpublished results.
- [305] C. C. Lu, S. DeBeer George, T. Weyhermüller, E. Bill, E. Bothe, K. Wieghardt, *Angew. Chem. Int. Ed.* **2008**, *47*, 6384-6387.
- [306] J. J. Curley, Dissertation, Massachusetts Institute of Technology, **2009**.
- [307] A. V. Nizovtsev, *Org. Prep. Proced. Int.* **2020**, *52*, 537-542.
- [308] J. Zhang, M. Gandelman, D. Herrman, G. Leitius, L. J. W. Shimon, Y. Ben-David, D. Milstein, *Inorg. Chim. Acta* **2006**, *359*, 1955-1960.
- [309] S. Kundu, S. Sinhababu, M. M. Siddiqui, A. V. Luebben, B. Dittrich, T. Yang, G. Frenking, H. W. Roesky, *J. Am. Chem. Soc.* **2018**, *140*, 9409-9412.
- [310] R. K. Harris, E. D. Becker, S. M. C. d. Menezes, P. Granger, R. E. Hoffman, K. W. Zilm, *Pure Appl. Chem.* **2008**, *80*, 59-84.

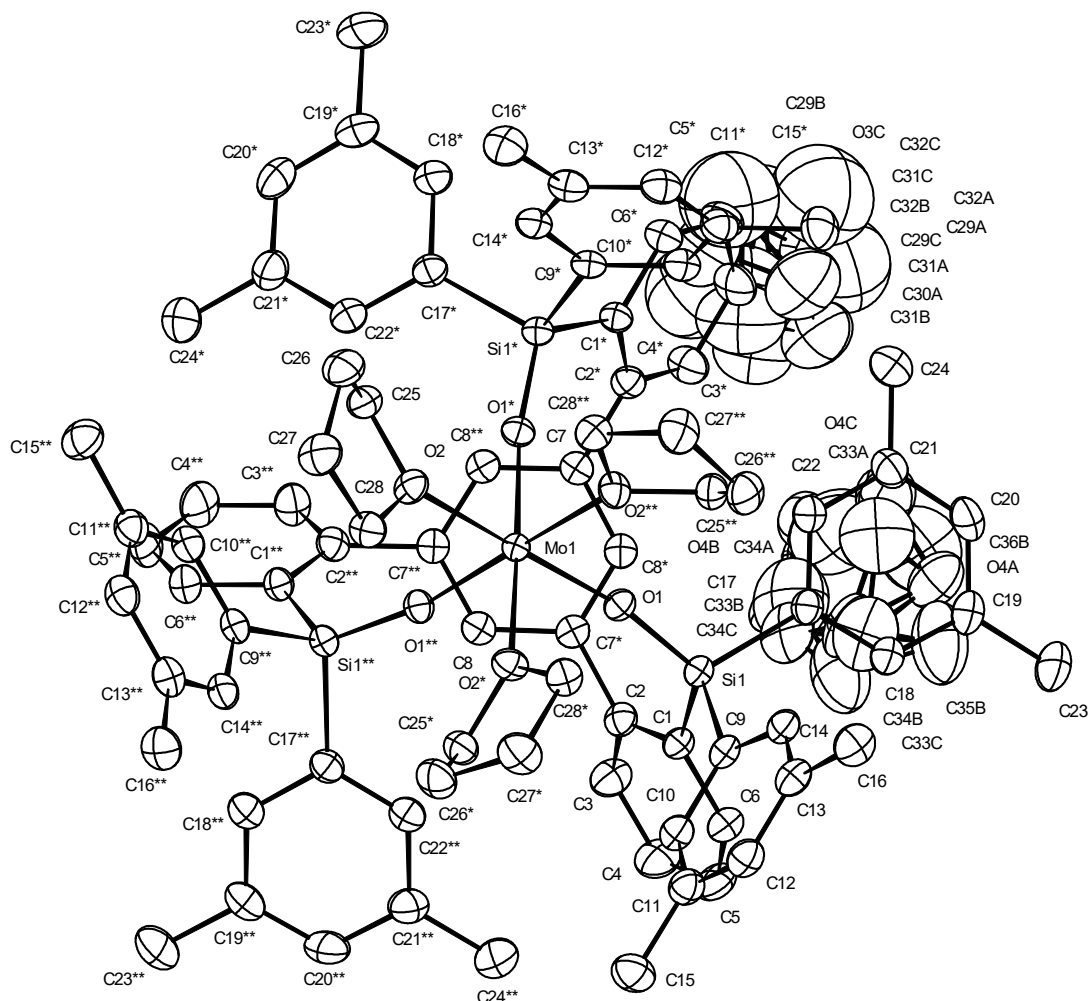
5 Appendix

5.1 Overview of Tools

This thesis was independently written by the author. The language tools DeepL and ChatGPT were used to assist with proofreading of grammar and language, resulting in minor modifications.

5.2 Supporting Crystallographic Information

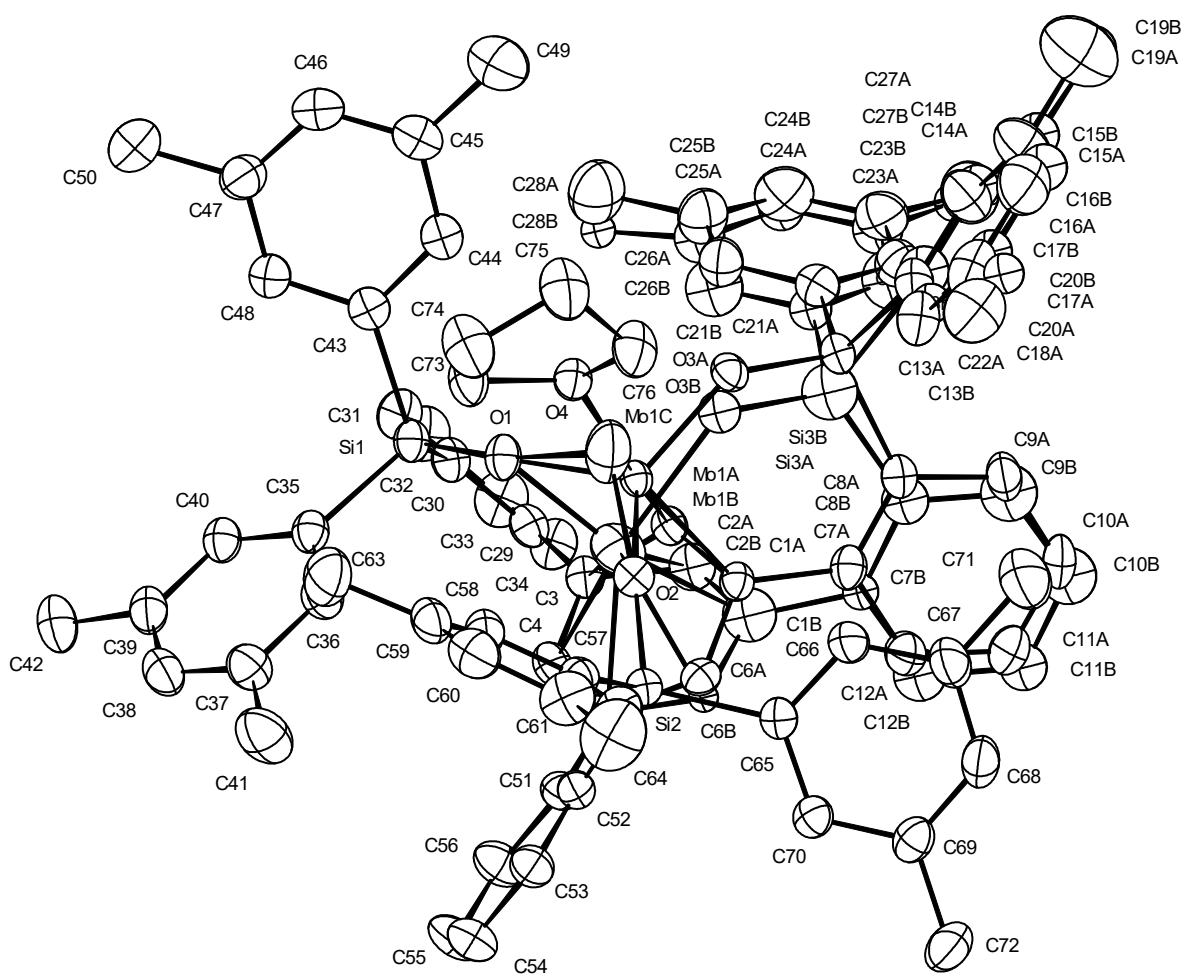
Single Crystal Structure Analysis of Complex 2 3THF



Identification code	15546	
Empirical formula	$C_{113} H_{149} Mo O_{13.25} Si_3$	
Color	yellow	
Formula weight	$1899.52 \text{ g}\cdot\text{mol}^{-1}$	
Temperature	150(2) K	
Wavelength	0.71073 \AA	
Crystal system	Cubic	
Space group	$P2_13$, (no. 198)	
Unit cell dimensions	$a = 21.9285(6) \text{ \AA}$	$\alpha = 90^\circ$
	$b = 21.9285(6) \text{ \AA}$	$\beta = 90^\circ$
	$c = 21.9285(6) \text{ \AA}$	$\gamma = 90^\circ$
Volume	$10544.5(9) \text{ \AA}^3$	
Z	4	
Density (calculated)	$1.197 \text{ Mg}\cdot\text{m}^{-3}$	
Absorption coefficient	0.218 mm^{-1}	

F(000)	4068 e	
Crystal size	0.147 x 0.090 x 0.088 mm ³	
θ range for data collection	2.077 to 28.303°.	
Index ranges	-29 \leq h \leq 29, -29 \leq k \leq 29, -29 \leq l \leq 29	
Reflections collected	416339	
Independent reflections	8748 [$R_{int} = 0.1252$]	
Reflections with $I > 2\sigma(I)$	7907	
Completeness to $\theta = 25.242^\circ$	99.5 %	
Absorption correction	Numerical	
Max. and min. transmission	0.9805 and 0.9213	
Refinement method	Full-matrix least-squares on F^2	
Data / restraints / parameters	8748 / 631 / 560	
Goodness-of-fit on F^2	1.089	
Final R indices [$I > 2\sigma(I)$]	$R_1 = 0.0331$	$wR^2 = 0.0812$
R indices (all data)	$R_1 = 0.0416$	$wR^2 = 0.0869$
Absolute structure parameter	-0.043(9)	
Extinction coefficient	n/a	
Largest diff. peak and hole	0.316 and -0.307 e \cdot \AA^{-3}	

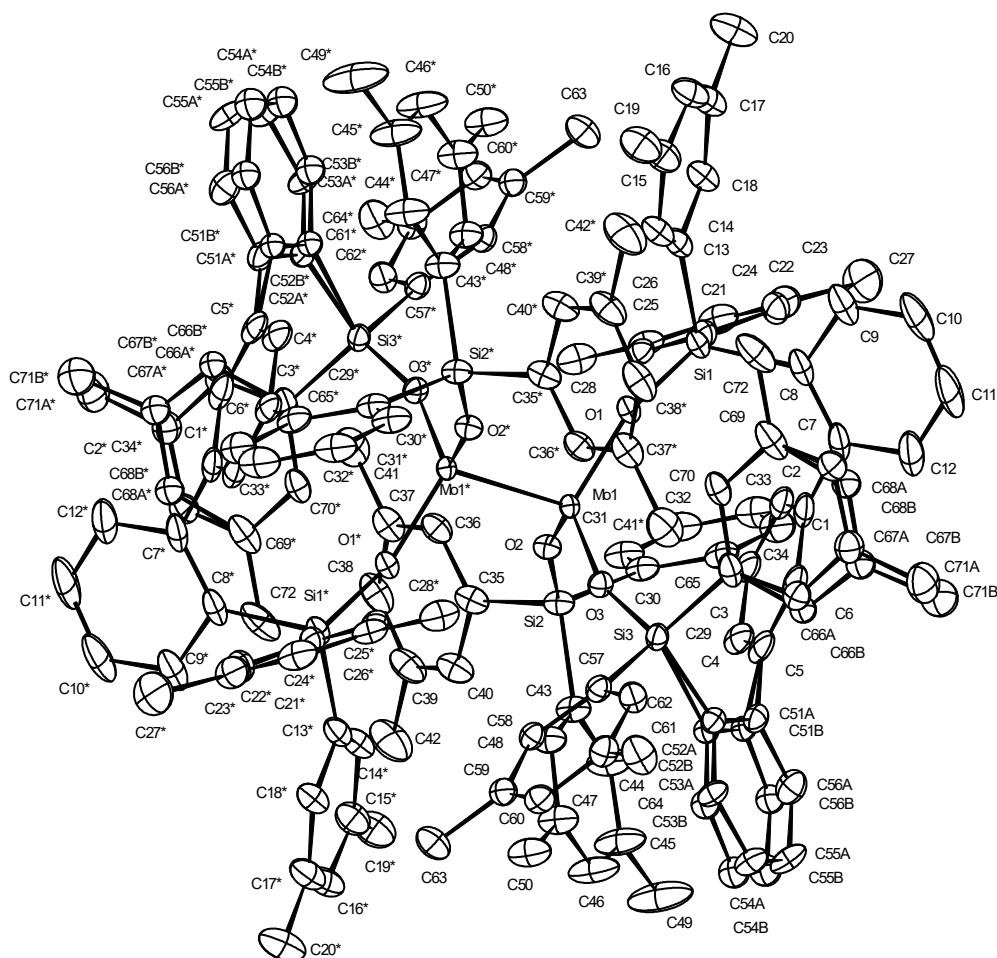
Single Crystal Structure Analysis of Complex 2·THF



Identification code	15585	
Empirical formula	$C_{83.10} H_{94.20} Mo O_{3.90} Si_3$	
Color	orange-brown	
Formula weight	1335.58 $g \cdot mol^{-1}$	
Temperature	150(2) K	
Wavelength	0.71073 Å	
Crystal system	Monoclinic	
Space group	$P2_1/c$, (no. 14)	
Unit cell dimensions	$a = 27.9711(15)$ Å	$\alpha = 90^\circ$
	$b = 16.0465(8)$ Å	$\beta = 106.550(2)^\circ$
	$c = 17.2062(9)$ Å	$\gamma = 90^\circ$
Volume	$7402.9(7)$ Å ³	
Z	4	
Density (calculated)	1.198 $Mg \cdot m^{-3}$	
Absorption coefficient	0.274 mm^{-1}	
F(000)	2832 e	
Crystal size	0.283 x 0.110 x 0.030 mm^3	

θ range for data collection	1.979 to 29.130°.	
Index ranges	-38 \leq h \leq 38, -21 \leq k \leq 21, -23 \leq l \leq 23	
Reflections collected	458250	
Independent reflections	19899 [$R_{\text{int}} = 0.1172$]	
Reflections with $I > 2\sigma(I)$	14760	
Completeness to $\theta = 25.242^\circ$	99.9 %	
Absorption correction	Numerical	
Max. and min. transmission	0.9936 and 0.9491	
Refinement method	Full-matrix least-squares on F^2	
Data / restraints / parameters	19899 / 57 / 866	
Goodness-of-fit on F^2	1.024	
Final R indices [$I > 2\sigma(I)$]	$R_1 = 0.0425$	$wR^2 = 0.1004$
R indices (all data)	$R_1 = 0.0666$	$wR^2 = 0.1129$
Extinction coefficient	n/a	
Largest diff. peak and hole	0.590 and -0.595 $e \cdot \text{\AA}^{-3}$	

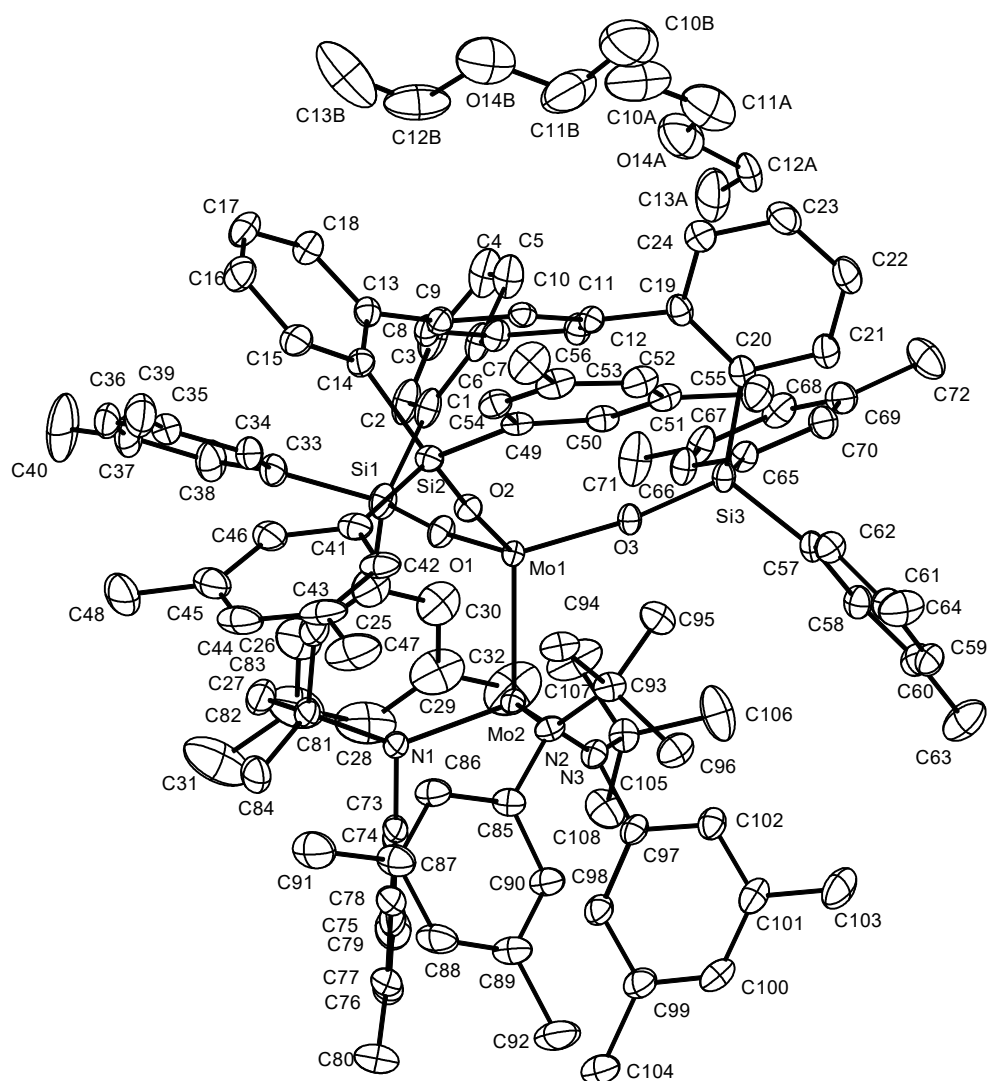
Single Crystal Structure Analysis of Complex 3



Identification code	15549	
Empirical formula	$C_{89.50} H_{89} Mo O_3 Si_3$	
Color	orange	
Formula weight	1392.81 $g \cdot mol^{-1}$	
Temperature	296.15 K	
Wavelength	0.71073 Å	
Crystal system	Triclinic	
Space group	$P-1$, (no. 2)	
Unit cell dimensions	$a = 16.0426(8)$ Å	$\alpha = 82.583(2)^\circ$
	$b = 16.2382(7)$ Å	$\beta = 61.746(2)^\circ$
	$c = 16.4587(8)$ Å	$\gamma = 76.552(2)^\circ$
Volume	$3672.3(3)$ Å ³	
Z	2	
Density (calculated)	1.260 $Mg \cdot m^{-3}$	
Absorption coefficient	0.278 mm^{-1}	
F(000)	1468 e	
Crystal size	0.192 x 0.128 x 0.127 mm^3	

θ range for data collection	1.290 to 30.508°.	
Index ranges	-22 \leq h \leq 22, -23 \leq k \leq 23, -23 \leq l \leq 23	
Reflections collected	113885	
Independent reflections	22393 [$R_{\text{int}} = 0.0613$]	
Reflections with $I > 2\sigma(I)$	16613	
Completeness to $\theta = 25.242^\circ$	100.0 %	
Absorption correction	None	
Max. and min. transmission	1.0000 and 0.9107	
Refinement method	Full-matrix least-squares on F^2	
Data / restraints / parameters	22393 / 60 / 766	
Goodness-of-fit on F^2	1.068	
Final R indices [$I > 2\sigma(I)$]	$R_1 = 0.0444$	$wR^2 = 0.1073$
R indices (all data)	$R_1 = 0.0669$	$wR^2 = 0.1171$
Extinction coefficient	n/a	
Largest diff. peak and hole	0.888 and -1.302 $e \cdot \text{\AA}^{-3}$	

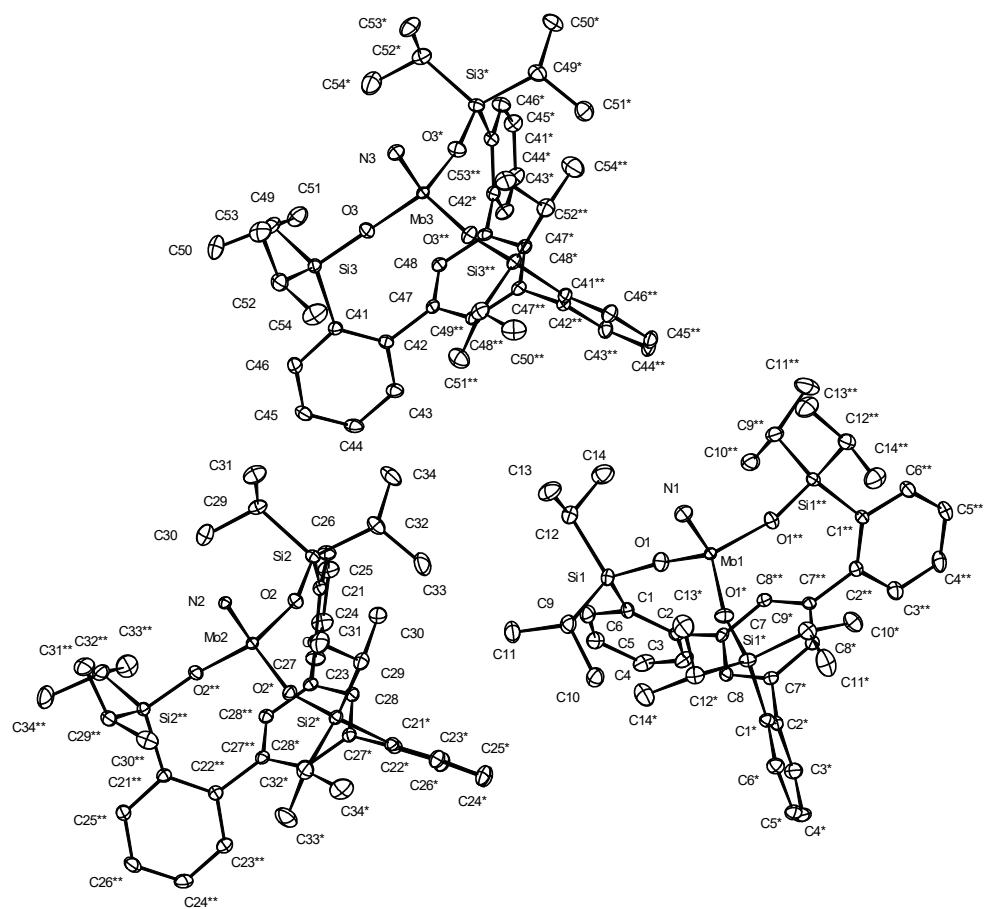
Single Crystal Structure Analysis of Complex 4



Identification code	14506	
Empirical formula	$C_{112} H_{133} Mo_2 N_3 O_4 Si_3$	
Color	orange	
Formula weight	$1861.36 \text{ g}\cdot\text{mol}^{-1}$	
Temperature	100(2) K	
Wavelength	0.71073 \AA	
Crystal system	Monoclinic	
Space group	$P2_1/n$, (no. 14)	
Unit cell dimensions	$a = 14.5704(6) \text{ \AA}$	$\alpha = 90^\circ$.
	$b = 27.4246(13) \text{ \AA}$	$\beta = 90.816(2)^\circ$.
	$c = 25.0257(12) \text{ \AA}$	$\gamma = 90^\circ$.
Volume	$9998.9(8) \text{ \AA}^3$	
Z	4	
Density (calculated)	$1.236 \text{ Mg}\cdot\text{m}^{-3}$	
Absorption coefficient	0.340 mm^{-1}	

F(000)	3936 e	
Crystal size	0.242 x 0.106 x 0.06 mm ³	
θ range for data collection	1.583 to 30.034°.	
Index ranges	-20 \leq h \leq 20, -38 \leq k \leq 38, -35 \leq l \leq 35	
Reflections collected	379265	
Independent reflections	29260 [$R_{\text{int}} = 0.0813$]	
Reflections with $I > 2\sigma(I)$	22287	
Completeness to $\theta = 25.242^\circ$	99.9 %	
Absorption correction	Gaussian	
Max. and min. transmission	0.98820 and 0.95950	
Refinement method	Full-matrix least-squares on F^2	
Data / restraints / parameters	29260 / 0 / 1208	
Goodness-of-fit on F^2	1.062	
Final R indices [$I > 2\sigma(I)$]	$R_1 = 0.0414$	$wR^2 = 0.1011$
R indices (all data)	$R_1 = 0.0662$	$wR^2 = 0.1130$
Extinction coefficient	n/a	
Largest diff. peak and hole	1.373 and -0.704 e $\cdot\text{\AA}^{-3}$	

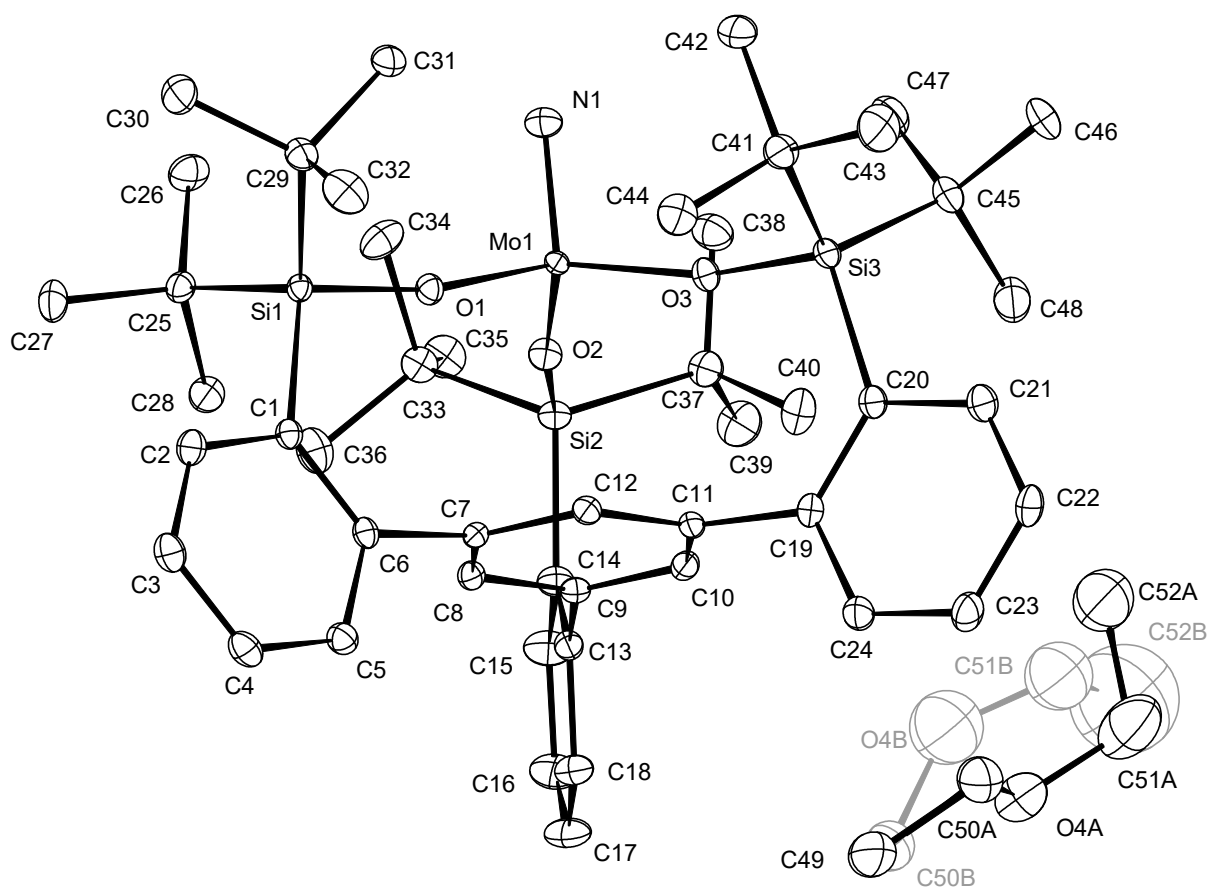
Single Crystal Structure Analysis of Complex **5d**



Identification code	14014
Empirical formula	$C_{42} H_{57} Mo N O_3 Si_3$
Color	colourless
Formula weight	$804.09 \text{ g}\cdot\text{mol}^{-1}$
Temperature	100(2) K
Wavelength	0.71073 \AA
Crystal system	Trigonal
Space group	$P3c1$, (no. 158)
Unit cell dimensions	$a = 20.9695(9) \text{ \AA}$ $\alpha = 90^\circ$. $b = 20.9695(9) \text{ \AA}$ $\beta = 90^\circ$. $c = 16.4975(10) \text{ \AA}$ $\gamma = 120^\circ$.
Volume	$6282.4(7) \text{ \AA}^3$
Z	6
Density (calculated)	$1.275 \text{ Mg}\cdot\text{m}^{-3}$
Absorption coefficient	0.436 mm^{-1}
F(000)	2544 e
Crystal size	$0.101 \times 0.064 \times 0.017 \text{ mm}^3$
θ range for data collection	1.121 to 31.524° .
Index ranges	$-30 \leq h \leq 30$, $-30 \leq k \leq 30$, $-24 \leq l \leq 24$

Reflections collected	206695	
Independent reflections	13714 [$R_{\text{int}} = 0.0471$]	
Reflections with $I > 2\sigma(I)$	11831	
Completeness to $\theta = 25.242^\circ$	100.0 %	
Absorption correction	Gaussian	
Max. and min. transmission	0.99219 and 0.95533	
Refinement method	Full-matrix least-squares on F^2	
Data / restraints / parameters	13714 / 1 / 463	
Goodness-of-fit on F^2	1.029	
Final R indices [$I > 2\sigma(I)$]	$R_1 = 0.0253$	$wR^2 = 0.0560$
R indices (all data)	$R_1 = 0.0363$	$wR^2 = 0.0607$
Absolute structure parameter	-0.013(6)	
Extinction coefficient	n/a	
Largest diff. peak and hole	0.421 and -0.357 $e \cdot \text{\AA}^{-3}$	

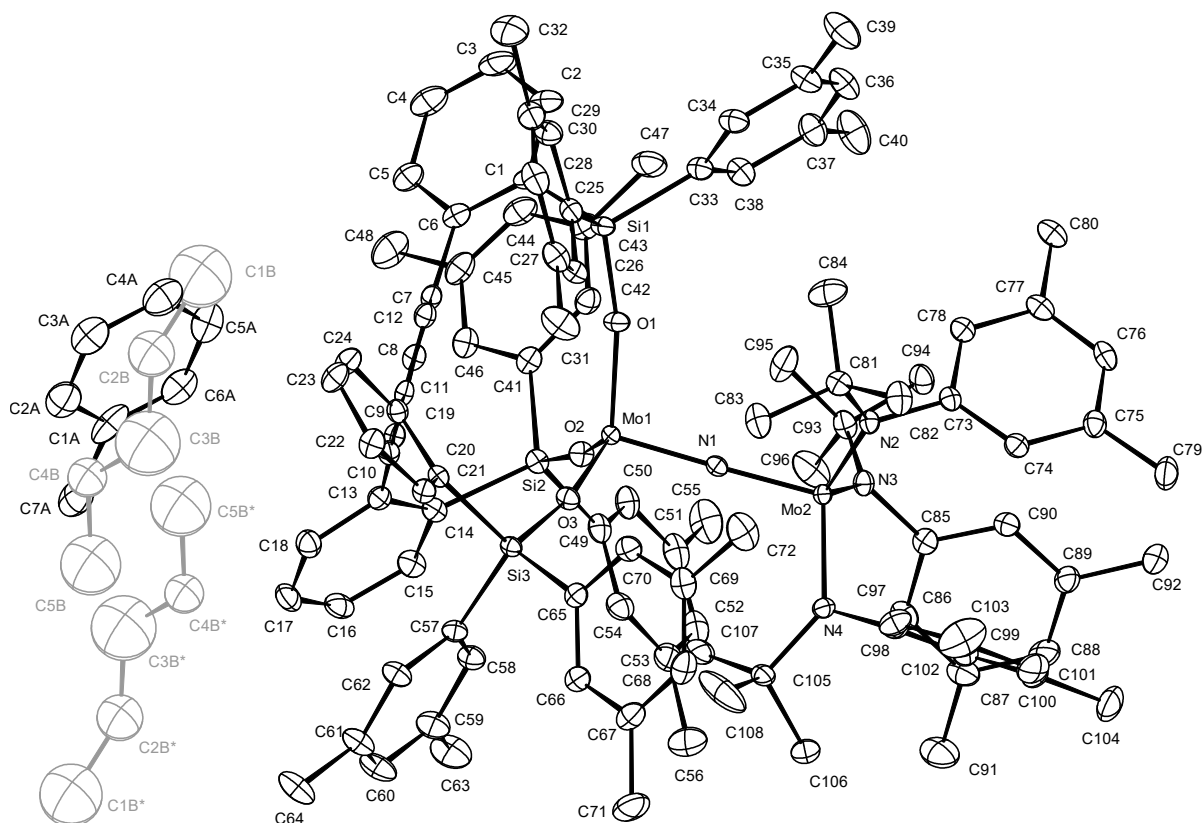
Single Crystal Structure Analysis of Complex **5e**



Identification code	14831	
Empirical formula	$C_{52} H_{79} Mo N O_4 Si_3$	
Color	yellow	
Formula weight	962.37 $g \cdot mol^{-1}$	
Temperature	100(2) K	
Wavelength	0.71073 Å	
Crystal system	Monoclinic	
Space group	$C2/c$, (no. 15)	
Unit cell dimensions	$a = 17.9114(13)$ Å	$\alpha = 90^\circ$.
	$b = 15.0179(10)$ Å	$\beta = 90.702(3)^\circ$.
	$c = 38.283(3)$ Å	$\gamma = 90^\circ$.
Volume	$10297.1(12)$ Å ³	
Z	8	
Density (calculated)	1.242 $Mg \cdot m^{-3}$	
Absorption coefficient	0.367 mm^{-1}	
F(000)	4112 e	
Crystal size	0.132 x 0.131 x 0.102 mm^3	
θ range for data collection	1.064 to 30.998°.	
Index ranges	$-25 \leq h \leq 25$, $-21 \leq k \leq 21$, $-55 \leq l \leq 55$	

Reflections collected	307116	
Independent reflections	16549 [$R_{\text{int}} = 0.0463$]	
Reflections with $I > 2\sigma(I)$	15724	
Completeness to $\theta = 25.242^\circ$	100.0 %	
Absorption correction	Gaussian	
Max. and min. transmission	0.97654 and 0.96327	
Refinement method	Full-matrix least-squares on F^2	
Data / restraints / parameters	16549 / 2 / 588	
Goodness-of-fit on F^2	1.134	
Final R indices [$I > 2\sigma(I)$]	$R_1 = 0.0375$	$wR^2 = 0.0850$
R indices (all data)	$R_1 = 0.0398$	$wR^2 = 0.0862$
Extinction coefficient	n/a	
Largest diff. peak and hole	1.258 and -0.549 $e \cdot \text{\AA}^{-3}$	

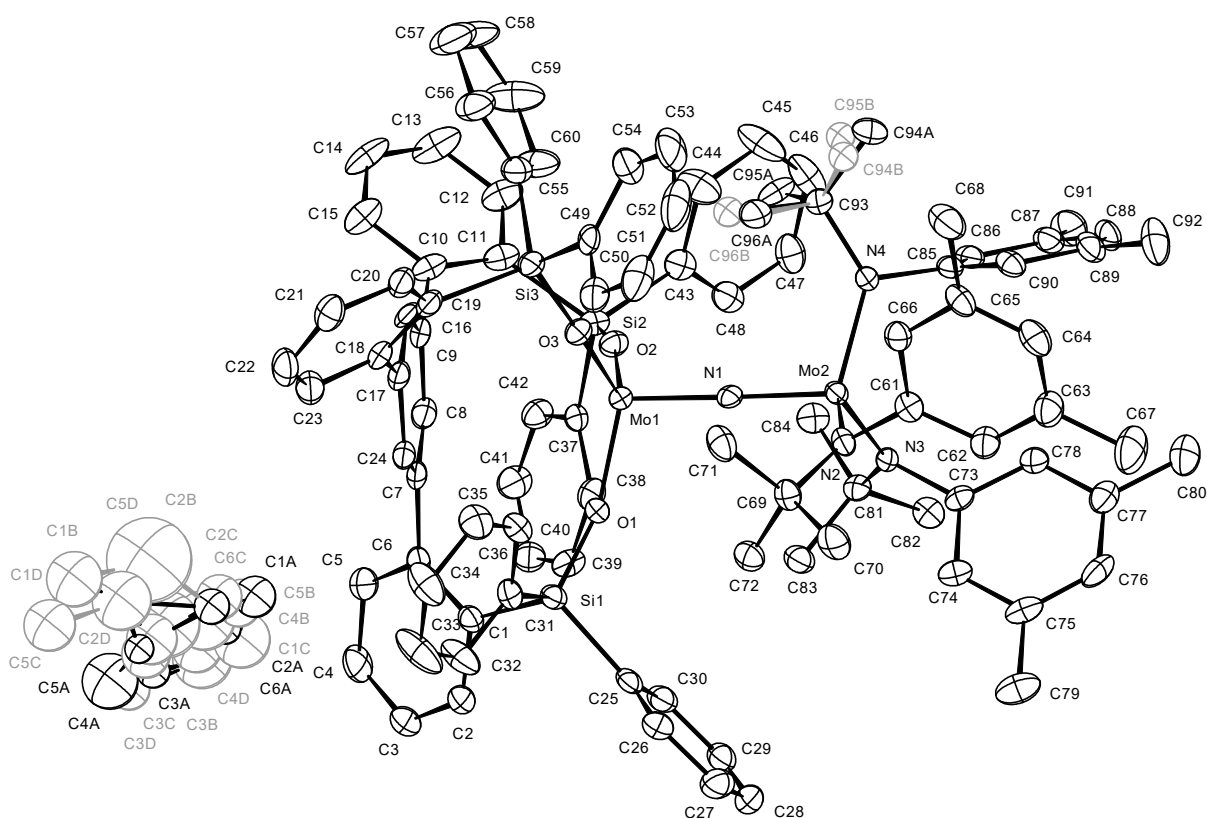
Single Crystal Structure Analysis of Complex **6a**



Identification code	14495
Empirical formula	C ₄₅₈ H ₅₂₈ Mo ₈ N ₁₆ O ₁₂ Si ₁₂
Color	green
Formula weight	7553.53 g·mol ⁻¹
Temperature	100(2) K
Wavelength	0.71073 Å
Crystal system	Monoclinic
Space group	<i>P</i> 2 ₁ / <i>n</i> , (no. 14)
Unit cell dimensions	<i>a</i> = 14.8017(7) Å α = 90°. <i>b</i> = 29.0993(15) Å β = 92.440(2)°. <i>c</i> = 23.9781(12) Å γ = 90°.
Volume	10318.5(9) Å ³
<i>Z</i>	1
Density (calculated)	1.216 Mg·m ⁻³
Absorption coefficient	0.330 mm ⁻¹
<i>F</i> (000)	3988 e
Crystal size	0.197 x 0.143 x 0.04 mm ³
θ range for data collection	1.101 to 30.999°.

Index ranges	$-21 \leq h \leq 21, -42 \leq k \leq 42, -34 \leq l \leq 34$	
Reflections collected	348764	
Independent reflections	32908 [$R_{\text{int}} = 0.0847$]	
Reflections with $I > 2\sigma(I)$	23936	
Completeness to $\theta = 25.242^\circ$	100.0 %	
Absorption correction	Gaussian	
Max. and min. transmission	0.99184 and 0.95295	
Refinement method	Full-matrix least-squares on F^2	
Data / restraints / parameters	32908 / 20 / 1194	
Goodness-of-fit on F^2	1.019	
Final R indices [$I > 2\sigma(I)$]	$R_1 = 0.0398$	$wR^2 = 0.0830$
R indices (all data)	$R_1 = 0.0687$	$wR^2 = 0.0933$
Extinction coefficient	n/a	
Largest diff. peak and hole	0.533 and -0.672 $e \cdot \text{\AA}^{-3}$	

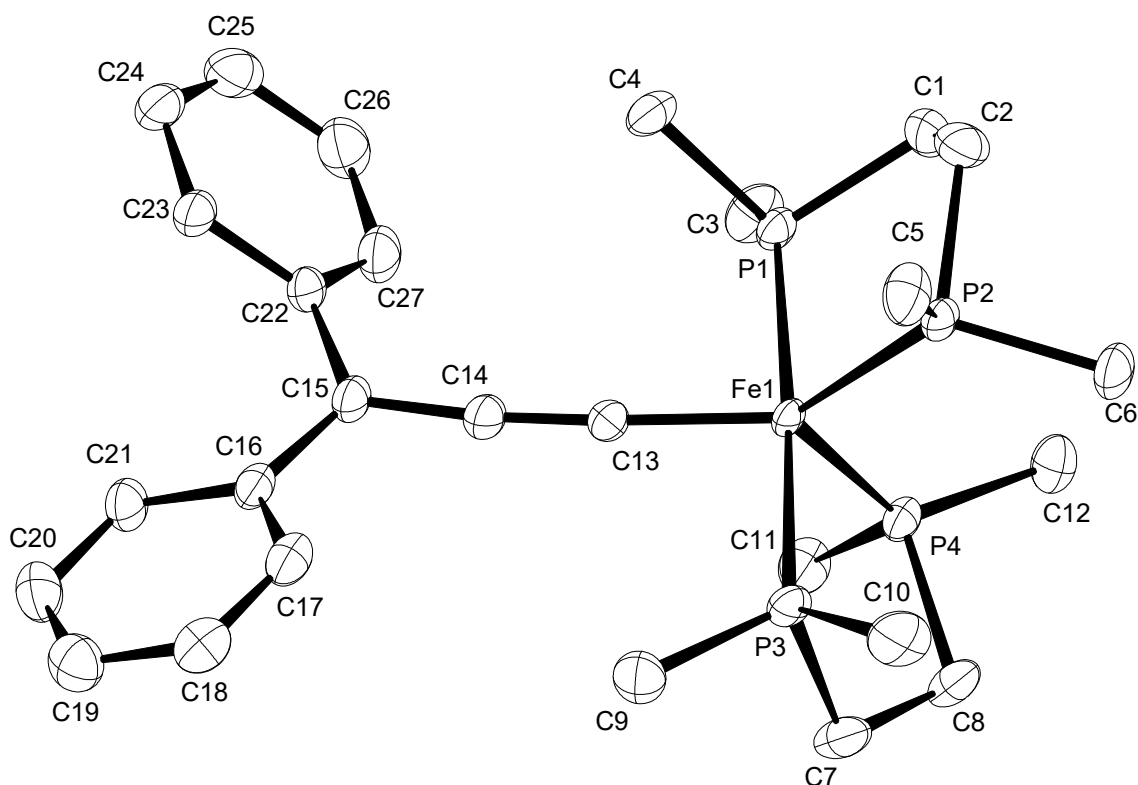
Single Crystal Structure Analysis of Complex **6b**



Identification code	14253	
Empirical formula	$\text{C}_{203} \text{H}_{216} \text{Mo}_4 \text{N}_8 \text{O}_6 \text{Si}_6$	
Color	orange	
Formula weight	$3416.13 \text{ g}\cdot\text{mol}^{-1}$	
Temperature	$100(2) \text{ K}$	
Wavelength	0.71073 \AA	
Crystal system	Monoclinic	
Space group	$P2_1/c$, (no. 14)	
Unit cell dimensions	$a = 14.885(3) \text{ \AA}$	$\alpha = 90^\circ$.
	$b = 28.731(7) \text{ \AA}$	$\beta = 91.244(12)^\circ$.
	$c = 20.650(5) \text{ \AA}$	$\gamma = 90^\circ$.
Volume	$8829(4) \text{ \AA}^3$	
Z	2	
Density (calculated)	$1.285 \text{ Mg}\cdot\text{m}^{-3}$	
Absorption coefficient	0.378 mm^{-1}	
F(000)	3580 e	
Crystal size	$0.061 \times 0.061 \times 0.009 \text{ mm}^3$	
θ range for data collection	1.215 to 26.372° .	
Index ranges	$-18 \leq h \leq 18$, $-35 \leq k \leq 35$, $-25 \leq l \leq 25$	
Reflections collected	161323	

Independent reflections	17891 [$R_{\text{int}} = 0.1752$]	
Reflections with $I > 2\sigma(I)$	10974	
Completeness to $\theta = 25.242^\circ$	99.0 %	
Absorption correction	Gaussian	
Max. and min. transmission	0.99810 and 0.97863	
Refinement method	Full-matrix least-squares on F^2	
Data / restraints / parameters	17891 / 40 / 1071	
Goodness-of-fit on F^2	1.005	
Final R indices [$I > 2\sigma(I)$]	$R_1 = 0.0506$	$wR^2 = 0.0849$
R indices (all data)	$R_1 = 0.1118$	$wR^2 = 0.1018$
Extinction coefficient	n/a	
Largest diff. peak and hole	0.605 and -0.822 $e \cdot \text{\AA}^{-3}$	

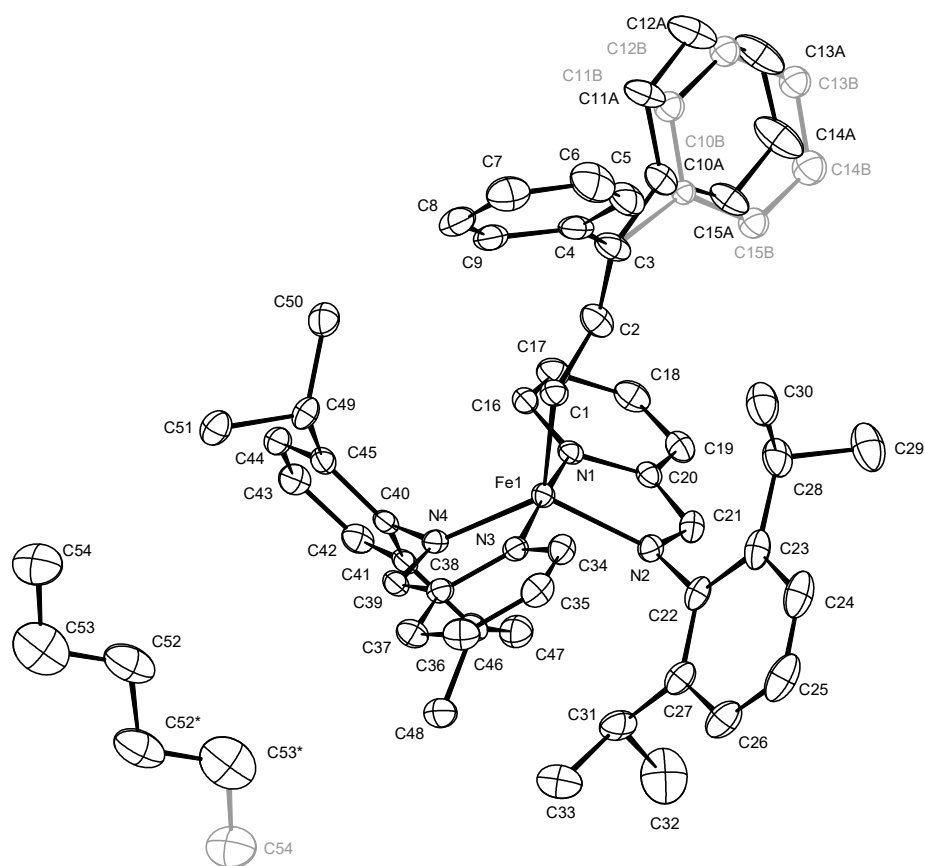
Single Crystal Structure Analysis of Complex 10



Identification code	15582
Empirical formula	$C_{27}H_{42}FeP_4$
Color	purple
Formula weight	$546.33 \text{ g} \cdot \text{mol}^{-1}$
Temperature	150(2) K
Wavelength	0.71073 \AA
Crystal system	MONOCLINIC
Space group	$P2_1/c$, (no. 14)
Unit cell dimensions	$a = 11.9545(5) \text{ \AA}$ $\alpha = 90^\circ$. $b = 12.8023(5) \text{ \AA}$ $\beta = 106.085(2)^\circ$. $c = 19.3140(8) \text{ \AA}$ $\gamma = 90^\circ$.
Volume	$2840.2(2) \text{ \AA}^3$
Z	4
Density (calculated)	$1.278 \text{ Mg} \cdot \text{m}^{-3}$
Absorption coefficient	0.770 mm^{-1}
F(000)	1160 e

Crystal size	0.21 x 0.142 x 0.092 mm ³	
θ range for data collection	1.773 to 31.095°.	
Index ranges	-17 \leq h \leq 17, -18 \leq k \leq 18, -27 \leq l \leq 28	
Reflections collected	89177	
Independent reflections	9105 [$R_{\text{int}} = 0.0521$]	
Reflections with $I > 2\sigma(I)$	7009	
Completeness to $\theta = 25.242^\circ$	100.0 %	
Absorption correction	Gaussian	
Max. and min. transmission	0.96 and 0.89	
Refinement method	Full-matrix least-squares on F^2	
Data / restraints / parameters	9105 / 0 / 297	
Goodness-of-fit on F^2	1.035	
Final R indices [$I > 2\sigma(I)$]	$R_1 = 0.0348$	$wR^2 = 0.0844$
R indices (all data)	$R_1 = 0.0553$	$wR^2 = 0.0942$
Largest diff. peak and hole	0.7 and -0.4 e \cdot Å ⁻³	

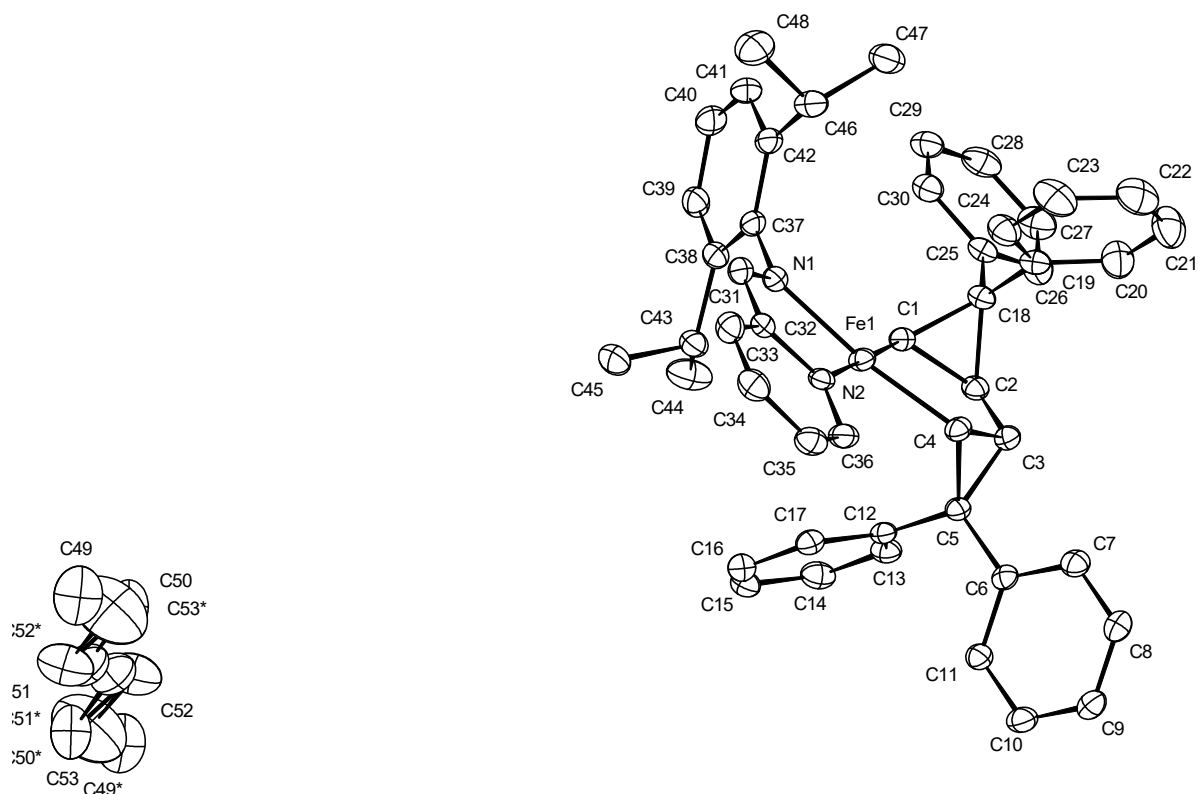
Single Crystal Structure Analysis of Complex 13



Identification code	15910	
Empirical formula	$C_{107} H_{123} Fe_2 N_8$	
Color	black	
Formula weight	1632.83 $g \cdot mol^{-1}$	
Temperature	100(2) K	
Wavelength	0.71073 Å	
Crystal system	Triclinic	
Space group	$P\bar{1}$, (no. 2)	
Unit cell dimensions	$a = 11.2763(5)$ Å	$\alpha = 81.313(3)^\circ$.
	$b = 12.4715(6)$ Å	$\beta = 85.313(3)^\circ$.
	$c = 16.7708(8)$ Å	$\gamma = 79.195(2)^\circ$.
Volume	2286.66(19) Å ³	
Z	1	
Density (calculated)	1.186 $Mg \cdot m^{-3}$	
Absorption coefficient	0.369 mm^{-1}	
F(000)	873 e	
Crystal size	0.094 x 0.035 x 0.031 mm^3	
θ range for data collection	1.230 to 29.130°.	

Index ranges	-15 ≤ h ≤ 15, -17 ≤ k ≤ 17, -22 ≤ l ≤ 22	
Reflections collected	70849	
Independent reflections	12309 [R _{int} = 0.1043]	
Reflections with I > 2σ(I)	7554	
Completeness to θ = 25.242°	100.0 %	
Absorption correction	Gaussian	
Max. and min. transmission	0.99011 and 0.97222	
Refinement method	Full-matrix least-squares on F ²	
Data / restraints / parameters	12309 / 36 / 558	
Goodness-of-fit on F ²	1.008	
Final R indices [I > 2σ(I)]	R ₁ = 0.0518	wR ² = 0.0885
R indices (all data)	R ₁ = 0.1126	wR ² = 0.1058
Extinction coefficient	n/a	
Largest diff. peak and hole	0.343 and -0.484 e·Å ⁻³	

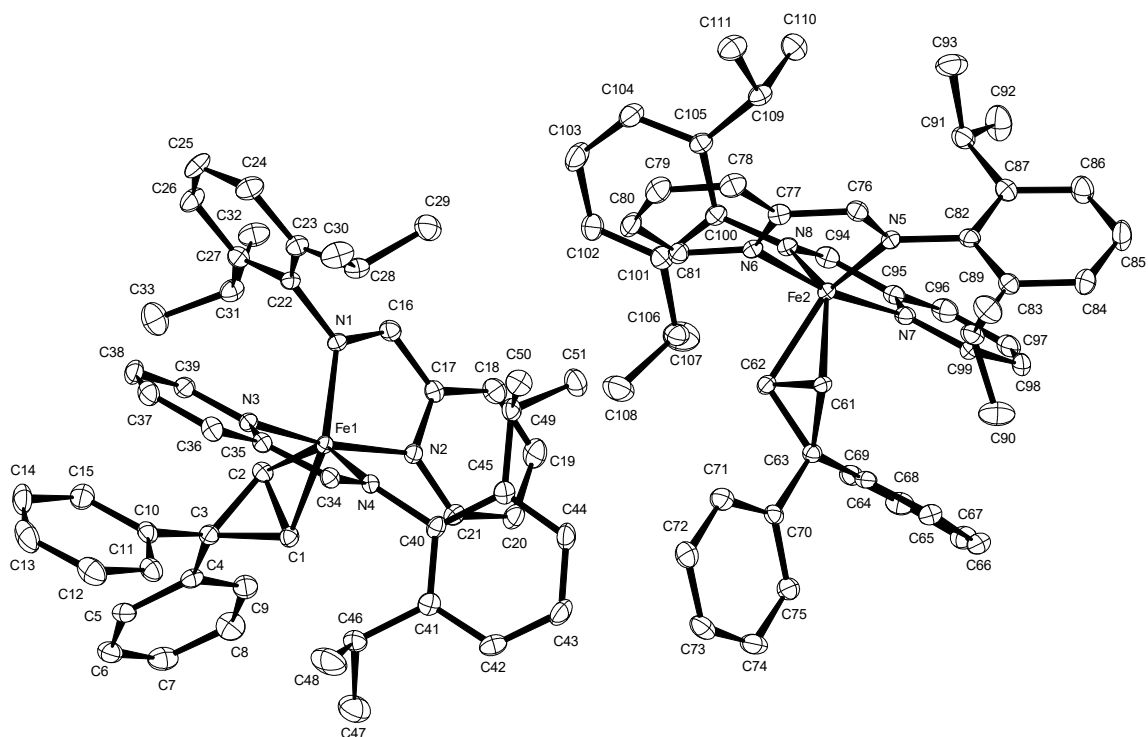
Single Crystal Structure Analysis of Complex 14



Identification code	15915
Empirical formula	$C_{121} H_{152} Fe_2 N_4$
Color	black
Formula weight	$1774.16 \text{ g}\cdot\text{mol}^{-1}$
Temperature	100(2) K
Wavelength	0.71073 \AA
Crystal system	Monoclinic
Space group	$P2_1/n$, (no. 14)
Unit cell dimensions	$a = 12.4996(6) \text{ \AA}$ $\alpha = 90^\circ$. $b = 22.8421(10) \text{ \AA}$ $\beta = 97.135(2)^\circ$. $c = 17.4330(8) \text{ \AA}$ $\gamma = 90^\circ$.
Volume	$4938.9(4) \text{ \AA}^3$
Z	2
Density (calculated)	$1.193 \text{ Mg}\cdot\text{m}^{-3}$
Absorption coefficient	0.346 mm^{-1}
F(000)	1916 e
Crystal size	$0.176 \times 0.126 \times 0.08 \text{ mm}^3$
θ range for data collection	1.477 to 28.698° .

Index ranges	$-16 \leq h \leq 16, -30 \leq k \leq 30, -23 \leq l \leq 23$	
Reflections collected	144846	
Independent reflections	12769 [$R_{\text{int}} = 0.1076$]	
Reflections with $I > 2\sigma(I)$	8694	
Completeness to $\theta = 25.242^\circ$	99.9 %	
Absorption correction	Gaussian	
Max. and min. transmission	0.98113 and 0.96342	
Refinement method	Full-matrix least-squares on F^2	
Data / restraints / parameters	12769 / 73 / 511	
Goodness-of-fit on F^2	1.036	
Final R indices [$I > 2\sigma(I)$]	$R_1 = 0.0609$	$wR^2 = 0.1530$
R indices (all data)	$R_1 = 0.0946$	$wR^2 = 0.1684$
Extinction coefficient	n/a	
Largest diff. peak and hole	0.762 and -0.645 $e \cdot \text{\AA}^{-3}$	

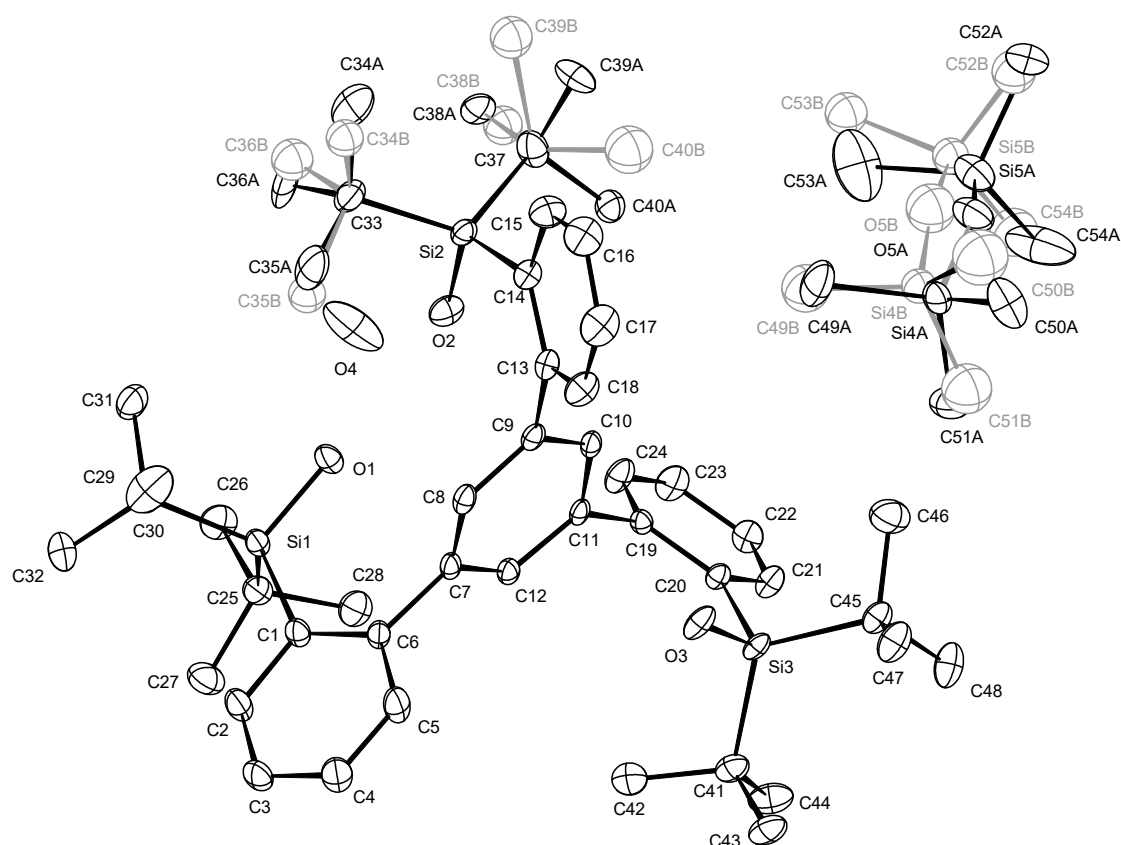
Single Crystal Structure Analysis of Complex 15



Identification code	15875	
Empirical formula	$C_{51}H_{56}FeN_4$	
Color	black	
Formula weight	780.84 $g \cdot mol^{-1}$	
Temperature	100(2) K	
Wavelength	0.71073 Å	
Crystal system	ORTHORHOMBIC	
Space group	Pca2₁, (no. 29)	
Unit cell dimensions	$a = 23.4639(7)$ Å	$\alpha = 90^\circ$.
	$b = 11.3212(3)$ Å	$\beta = 90^\circ$.
	$c = 32.0787(9)$ Å	$\gamma = 90^\circ$.
Volume	$8521.4(4)$ Å ³	
Z	8	
Density (calculated)	1.217 $Mg \cdot m^{-3}$	
Absorption coefficient	0.393 mm^{-1}	
F(000)	3328 e	

Crystal size	0.20 x 0.10 x 0.051 mm ³	
θ range for data collection	1.270 to 31.638°.	
Index ranges	-34 \leq h \leq 33, -16 \leq k \leq 16, -47 \leq l \leq 46	
Reflections collected	208809	
Independent reflections	28325 [$R_{int} = 0.0652$]	
Reflections with $I > 2\sigma(I)$	21597	
Completeness to $\theta = 25.242^\circ$	100.0 %	
Absorption correction	Gaussian	
Max. and min. transmission	0.98 and 0.95	
Refinement method	Full-matrix least-squares on F^2	
Data / restraints / parameters	28325 / 1 / 1026	
Goodness-of-fit on F^2	1.020	
Final R indices [$I > 2\sigma(I)$]	$R_1 = 0.0422$	$wR^2 = 0.0826$
R indices (all data)	$R_1 = 0.0713$	$wR^2 = 0.0920$
Absolute structure parameter	0.463(10)	
Largest diff. peak and hole	0.5 and -0.5 e \cdot Å ⁻³	

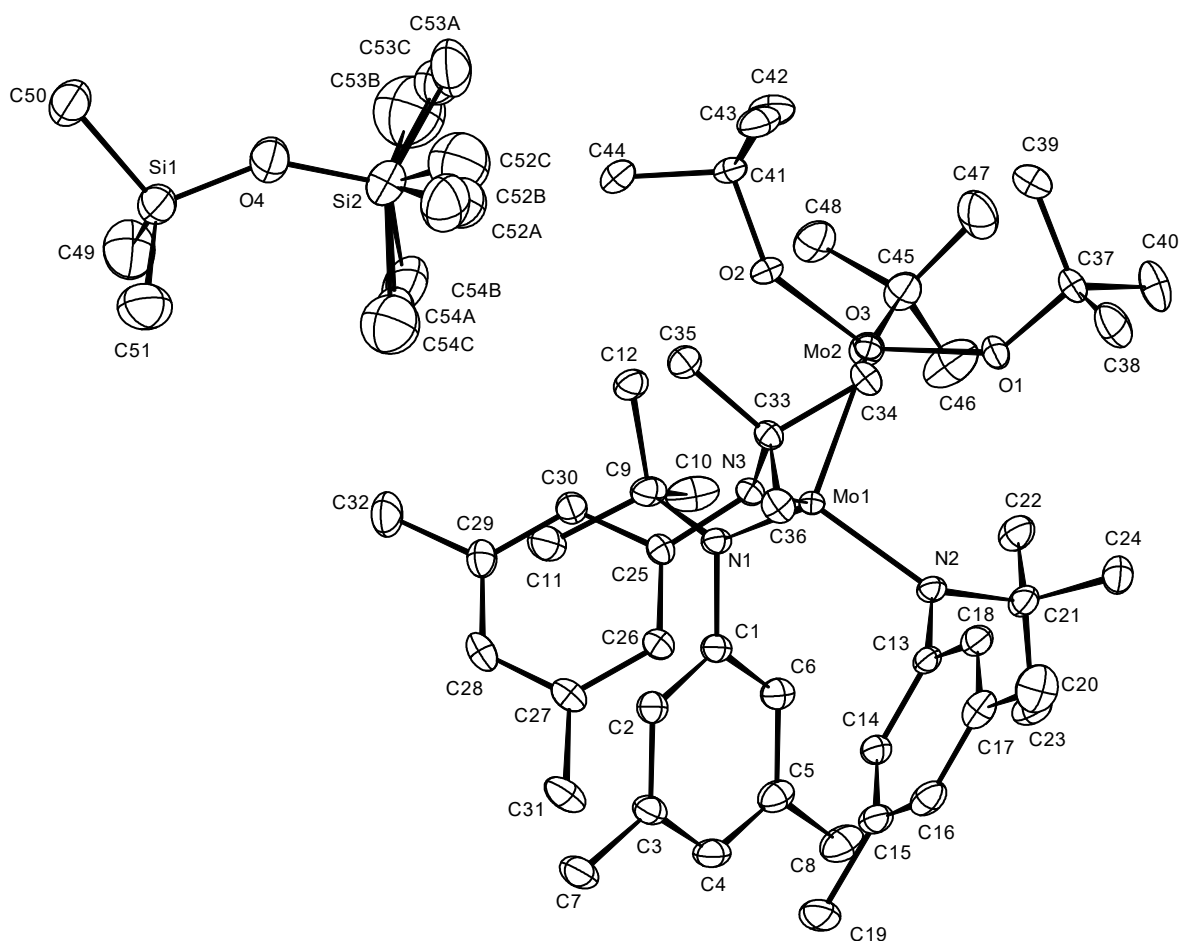
Single Crystal Structure Analysis of Ligand **141e**



Identification code	14724
Empirical formula	$C_{54} H_{92} O_5 Si_5$
Color	colourless
Formula weight	$961.72 \text{ g}\cdot\text{mol}^{-1}$
Temperature	100(2) K
Wavelength	0.71073 \AA
Crystal system	Monoclinic
Space group	$P2_1/c$, (no. 14)
Unit cell dimensions	$a = 23.8929(9) \text{ \AA}$ $\alpha = 90^\circ$. $b = 10.0543(3) \text{ \AA}$ $\beta = 102.301(2)^\circ$. $c = 25.3872(10) \text{ \AA}$ $\gamma = 90^\circ$.
Volume	$5958.7(4) \text{ \AA}^3$
Z	4
Density (calculated)	$1.072 \text{ Mg}\cdot\text{m}^{-3}$
Absorption coefficient	0.160 mm^{-1}
F(000)	2104 e
Crystal size	$0.203 \times 0.108 \times 0.06 \text{ mm}^3$
θ range for data collection	2.017 to 31.506° .
Index ranges	$-35 \leq h \leq 35$, $-14 \leq k \leq 14$, $-37 \leq l \leq 37$
Reflections collected	382203

Independent reflections	19830 [$R_{\text{int}} = 0.0761$]	
Reflections with $I > 2\sigma(I)$	17147	
Completeness to $\theta = 25.242^\circ$	99.9 %	
Absorption correction	Gaussian	
Max. and min. transmission	0.990 and 0.968	
Refinement method	Full-matrix least-squares on F^2	
Data / restraints / parameters	19830 / 0 / 691	
Goodness-of-fit on F^2	1.126	
Final R indices [$I > 2\sigma(I)$]	$R_1 = 0.0590$	$wR^2 = 0.1285$
R indices (all data)	$R_1 = 0.0704$	$wR^2 = 0.1339$
Extinction coefficient	n/a	
Largest diff. peak and hole	0.657 and -0.500 $e \cdot \text{\AA}^{-3}$	

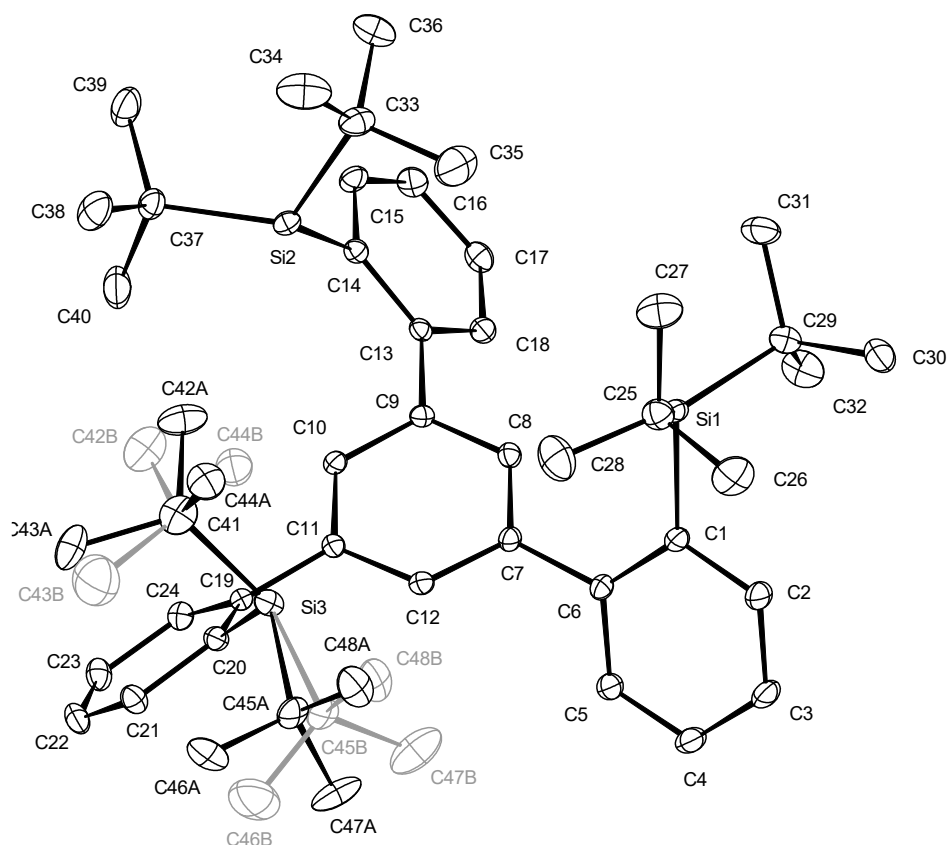
Single Crystal Structure Analysis of Complex 147



Identification code	15175	
Empirical formula	$C_{54} H_{99} Mo_2 N_3 O_4 Si_2$	
Color	orange	
Formula weight	$1102.42 \text{ g}\cdot\text{mol}^{-1}$	
Temperature	100(2) K	
Wavelength	0.71073 \AA	
Crystal system	Triclinic	
Space group	$P\bar{1}$, (no. 2)	
Unit cell dimensions	$a = 13.6675(5) \text{ \AA}$	$\alpha = 65.205(2)^\circ$
	$b = 15.2361(5) \text{ \AA}$	$\beta = 85.004(2)^\circ$
	$c = 15.6598(5) \text{ \AA}$	$\gamma = 88.036(2)^\circ$
Volume	$2949.11(18) \text{ \AA}^3$	
Z	2	
Density (calculated)	$1.241 \text{ Mg}\cdot\text{m}^{-3}$	
Absorption coefficient	0.508 mm^{-1}	
F(000)	1176 e	
Crystal size	$0.225 \times 0.051 \times 0.021 \text{ mm}^3$	
θ range for data collection	2.244 to 31.069°	

Index ranges	$-19 \leq h \leq 19, -22 \leq k \leq 22, -22 \leq l \leq 22$	
Reflections collected	580534	
Independent reflections	18822 [$R_{\text{int}} = 0.1070$]	
Reflections with $I > 2\sigma(I)$	15563	
Completeness to $\theta = 25.242^\circ$	99.9 %	
Absorption correction	Numerical	
Max. and min. transmission	0.9761 and 0.8586	
Refinement method	Full-matrix least-squares on F^2	
Data / restraints / parameters	18822 / 0 / 646	
Goodness-of-fit on F^2	1.074	
Final R indices [$I > 2\sigma(I)$]	$R_1 = 0.0337$	$wR^2 = 0.0681$
R indices (all data)	$R_1 = 0.0472$	$wR^2 = 0.0741$
Extinction coefficient	n/a	
Largest diff. peak and hole	0.691 and -0.698 $e \cdot \text{\AA}^{-3}$	

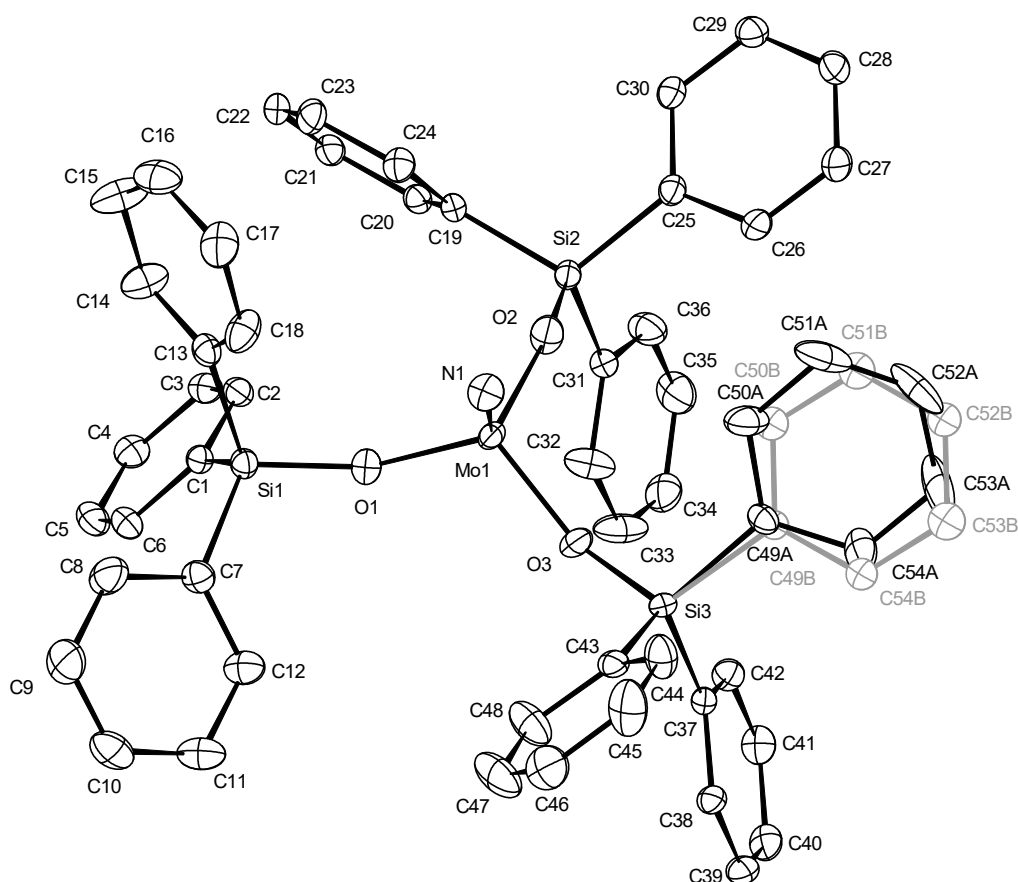
Single Crystal Structure Analysis of Silane **149e**



Identification code	14699	
Empirical formula	$C_{48} H_{72} Si_3$	
Color	colourless	
Formula weight	$733.32 \text{ g}\cdot\text{mol}^{-1}$	
Temperature	100(2) K	
Wavelength	0.71073 Å	
Crystal system	Triclinic	
Space group	$P\bar{1}$, (no. 2)	
Unit cell dimensions	$a = 13.1547(10) \text{ Å}$	$\alpha = 67.763(4)^\circ$.
	$b = 13.1703(10) \text{ Å}$	$\beta = 74.469(4)^\circ$.
	$c = 16.8177(13) \text{ Å}$	$\gamma = 60.595(3)^\circ$.
Volume	$2337.4(3) \text{ Å}^3$	
Z	2	
Density (calculated)	$1.042 \text{ Mg}\cdot\text{m}^{-3}$	
Absorption coefficient	0.131 mm^{-1}	
F(000)	804 e	
Crystal size	$0.224 \times 0.134 \times 0.101 \text{ mm}^3$	
θ range for data collection	1.857 to 30.508° .	
Index ranges	$-18 \leq h \leq 18$, $-18 \leq k \leq 18$, $-24 \leq l \leq 24$	
Reflections collected	193651	

Independent reflections	14245 [$R_{\text{int}} = 0.0480$]	
Reflections with $I > 2\sigma(I)$	12995	
Completeness to $\theta = 25.242^\circ$	100.0 %	
Absorption correction	Gaussian	
Max. and min. transmission	0.987 and 0.971	
Refinement method	Full-matrix least-squares on F^2	
Data / restraints / parameters	14245 / 38 / 563	
Goodness-of-fit on F^2	1.172	
Final R indices [$I > 2\sigma(I)$]	$R_1 = 0.0519$	$wR^2 = 0.1106$
R indices (all data)	$R_1 = 0.0578$	$wR^2 = 0.1132$
Extinction coefficient	n/a	
Largest diff. peak and hole	0.534 and -0.302 $e \cdot \text{\AA}^{-3}$	

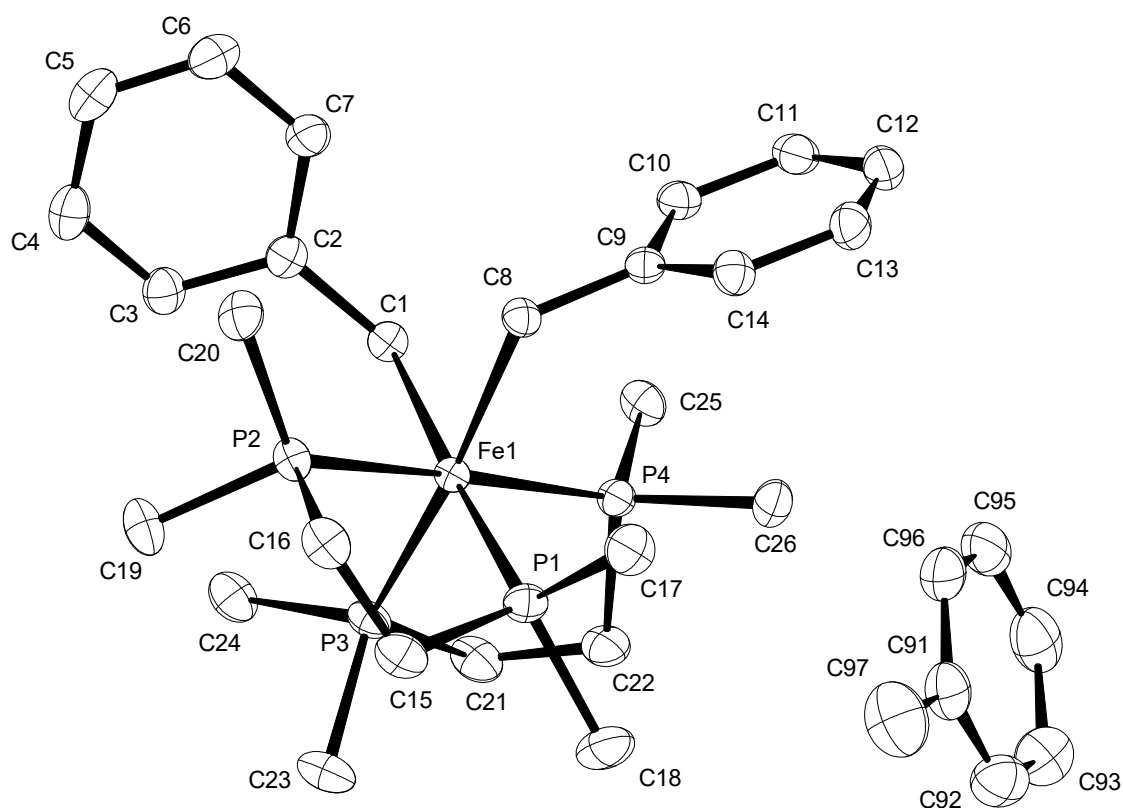
Single Crystal Structure Analysis of Complex **163**



Identification code	13941	
Empirical formula	$C_{54} H_{45} Mo N O_3 Si_3$	
Color	light yellow	
Formula weight	936.12 $g \cdot mol^{-1}$	
Temperature	100(2) K	
Wavelength	0.71073 Å	
Crystal system	Triclinic	
Space group	$P\bar{1}$, (no. 2)	
Unit cell dimensions	$a = 9.8873(6)$ Å	$\alpha = 71.713(2)^\circ$
	$b = 13.6273(8)$ Å	$\beta = 81.406(2)^\circ$
	$c = 18.3370(11)$ Å	$\gamma = 78.354(2)^\circ$
Volume	$2287.7(2)$ Å ³	
Z	2	
Density (calculated)	1.359 $Mg \cdot m^{-3}$	
Absorption coefficient	0.411 mm^{-1}	
F(000)	968 e	
Crystal size	0.094 x 0.080 x 0.041 mm^3	
θ range for data collection	1.175 to 32.576°.	
Index ranges	$-14 \leq h \leq 14, -20 \leq k \leq 20, -27 \leq l \leq 27$	

Reflections collected	112568	
Independent reflections	16644 [$R_{\text{int}} = 0.0406$]	
Reflections with $I > 2\sigma(I)$	14361	
Completeness to $\theta = 25.242^\circ$	100.0 %	
Absorption correction	Gaussian	
Max. and min. transmission	0.98858 and 0.97152	
Refinement method	Full-matrix least-squares on F^2	
Data / restraints / parameters	16644 / 0 / 571	
Goodness-of-fit on F^2	1.074	
Final R indices [$I > 2\sigma(I)$]	$R_1 = 0.0442$	$wR^2 = 0.1033$
R indices (all data)	$R_1 = 0.0539$	$wR^2 = 0.1078$
Extinction coefficient	n/a	
Largest diff. peak and hole	1.858 and -1.689 $e \cdot \text{\AA}^{-3}$	

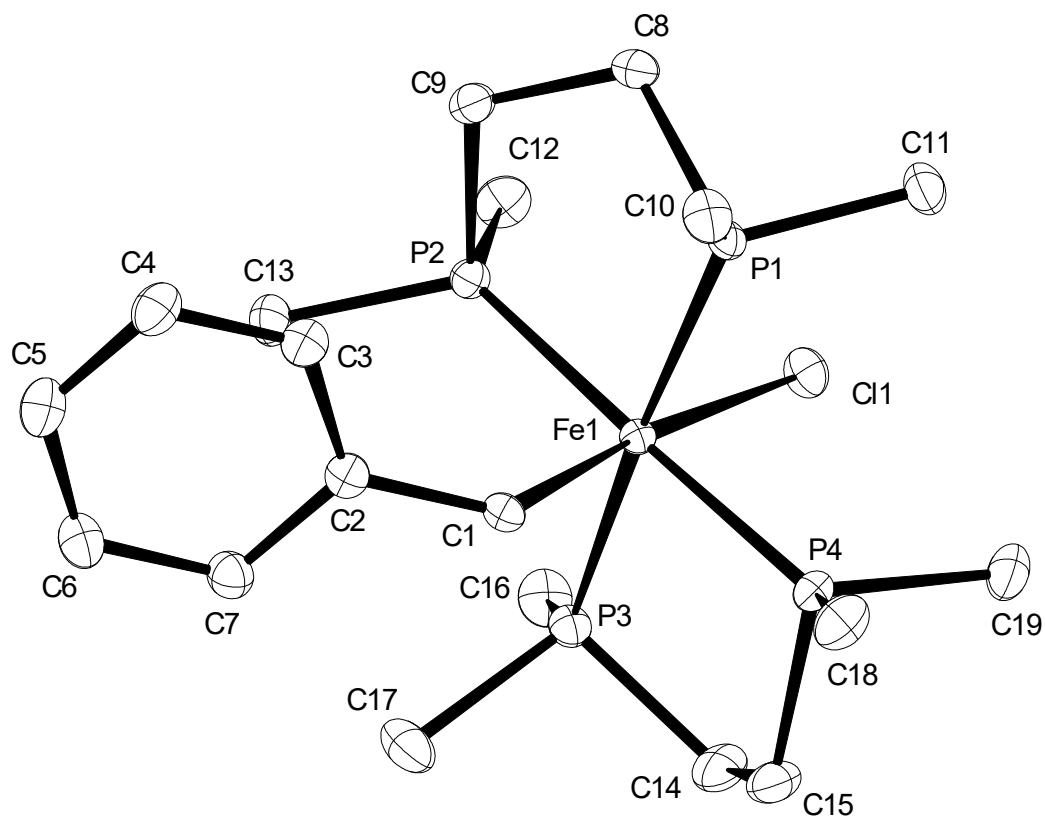
Single Crystal Structure Analysis of Complex **265**



Identification code	15126	
Empirical formula	$C_{33}H_{54}FeP_4$	
Color	orange-yellow	
Formula weight	$630.49 \text{ g}\cdot\text{mol}^{-1}$	
Temperature	150(2) K	
Wavelength	0.71073 \AA	
Crystal system	MONOCLINIC	
Space group	$P2_1/c$, (no. 14)	
Unit cell dimensions	$a = 12.8871(5) \text{ \AA}$	$\alpha = 90^\circ$.
	$b = 27.9377(11) \text{ \AA}$	$\beta = 106.130(2)^\circ$.
	$c = 9.5724(3) \text{ \AA}$	$\gamma = 90^\circ$.
Volume	$3310.7(2) \text{ \AA}^3$	
Z	4	
Density (calculated)	$1.265 \text{ Mg}\cdot\text{m}^{-3}$	
Absorption coefficient	0.670 mm^{-1}	
F(000)	1352 e	

Crystal size	0.278 x 0.131 x 0.101 mm ³	
θ range for data collection	2.198 to 31.066°.	
Index ranges	-18 \leq h \leq 18, -40 \leq k \leq 40, -13 \leq l \leq 13	
Reflections collected	939828	
Independent reflections	10581 [$R_{int} = 0.0753$]	
Reflections with $I > 2\sigma(I)$	9812	
Completeness to $\theta = 25.242^\circ$	99.9 %	
Absorption correction	Semi-empirical from equivalents	
Max. and min. transmission	0.95 and 0.88	
Refinement method	Full-matrix least-squares on F^2	
Data / restraints / parameters	10581 / 0 / 352	
Goodness-of-fit on F^2	1.068	
Final R indices [$I > 2\sigma(I)$]	$R_1 = 0.0233$	$wR^2 = 0.0627$
R indices (all data)	$R_1 = 0.0262$	$wR^2 = 0.0650$
Largest diff. peak and hole	0.4 and -0.2 e \cdot Å ⁻³	

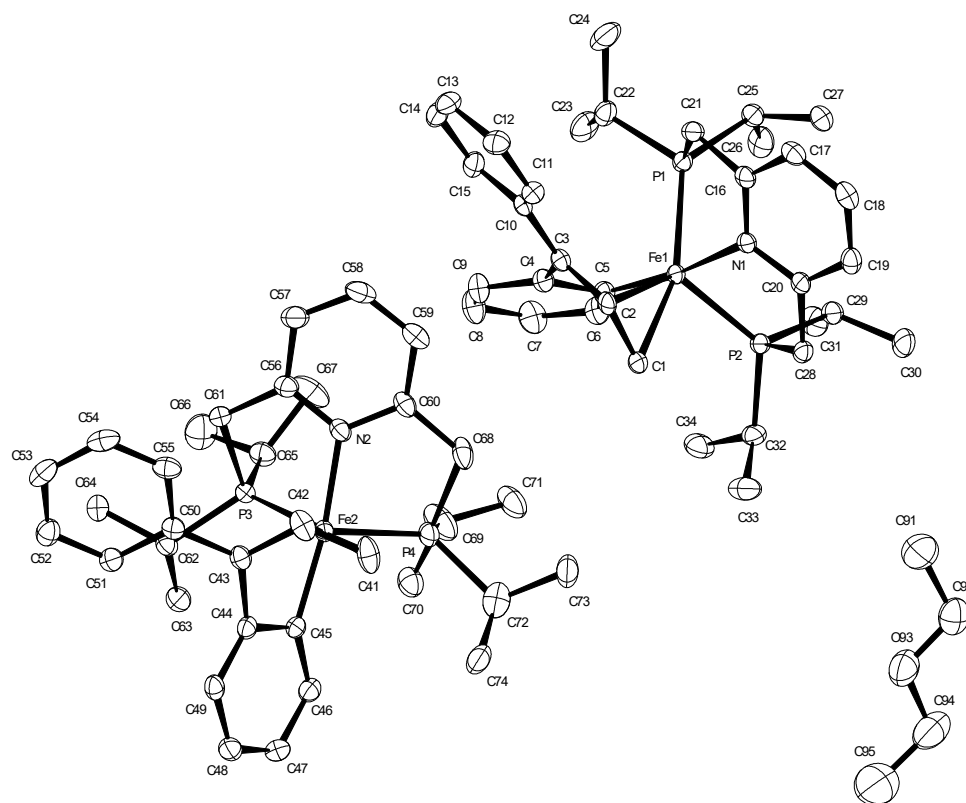
Single Crystal Structure Analysis of Complex **267**



Identification code	15107	
Empirical formula	$C_{19}H_{39}ClFeP_4$	
Color	violet	
Formula weight	482.68 $g \cdot mol^{-1}$	
Temperature	100(2) K	
Wavelength	0.71073 Å	
Crystal system	MONOCLINIC	
Space group	$P2_1/c$, (no. 14)	
Unit cell dimensions	$a = 10.2165(2)$ Å	$\alpha = 90^\circ$.
	$b = 15.7688(3)$ Å	$\beta = 100.8490(10)^\circ$.
	$c = 14.7633(3)$ Å	$\gamma = 90^\circ$.
Volume	$2335.89(8)$ Å ³	
Z	4	
Density (calculated)	1.373 $Mg \cdot m^{-3}$	
Absorption coefficient	1.036 mm^{-1}	
F(000)	1024 e	

Crystal size	0.324 x 0.168 x 0.130 mm ³	
θ range for data collection	1.908 to 33.192°.	
Index ranges	-15 \leq h \leq 15, -24 \leq k \leq 24, -22 \leq l \leq 22	
Reflections collected	461172	
Independent reflections	8937 [$R_{\text{int}} = 0.0682$]	
Reflections with $I > 2\sigma(I)$	8311	
Completeness to $\theta = 25.242^\circ$	100.0 %	
Absorption correction	Semi-empirical from equivalents	
Max. and min. transmission	0.91 and 0.78	
Refinement method	Full-matrix least-squares on F^2	
Data / restraints / parameters	8937 / 0 / 242	
Goodness-of-fit on F^2	1.048	
Final R indices [$I > 2\sigma(I)$]	$R_1 = 0.0204$	$wR^2 = 0.0554$
R indices (all data)	$R_1 = 0.0226$	$wR^2 = 0.0568$
Largest diff. peak and hole	0.7 and -0.4 e \cdot Å ⁻³	

Single Crystal Structure Analysis of Complex **293**



Identification code	15996	
Empirical formula	$C_{72}H_{104}Fe_2N_2O_4P_4$	
Color	black	
Formula weight	1249.15 $g \cdot mol^{-1}$	
Temperature	100(2) K	
Wavelength	0.71073 Å	
Crystal system	ORTHORHOMBIC	
Space group	Pbca, (no. 61)	
Unit cell dimensions	$a = 20.443(3)$ Å	$\alpha = 90^\circ$.
	$b = 18.542(2)$ Å	$\beta = 90^\circ$.
	$c = 34.760(4)$ Å	$\gamma = 90^\circ$.
Volume	$13176(3)$ Å ³	
Z	8	
Density (calculated)	1.259 $Mg \cdot m^{-3}$	
Absorption coefficient	0.582 mm^{-1}	
F(000)	5360 e	

Crystal size	0.172 x 0.097 x 0.09 mm ³	
θ range for data collection	1.172 to 28.947°.	
Index ranges	-27 \leq h \leq 27, -24 \leq k \leq 25, -47 \leq l \leq 47	
Reflections collected	346835	
Independent reflections	17255 [$R_{int} = 0.1294$]	
Reflections with $I > 2\sigma(I)$	11754	
Completeness to $\theta = 25.242^\circ$	100.0 %	
Absorption correction	Gaussian	
Max. and min. transmission	0.97 and 0.95	
Refinement method	Full-matrix least-squares on F^2	
Data / restraints / parameters	17255 / 0 / 748	
Goodness-of-fit on F^2	1.025	
Final R indices [$I > 2\sigma(I)$]	$R_1 = 0.0491$	$wR^2 = 0.1016$
R indices (all data)	$R_1 = 0.0914$	$wR^2 = 0.1196$
Largest diff. peak and hole	2.0 and -1.0 e \cdot Å ⁻³	